

DISSERTATION – DOCTORAL THESIS

On the coupled heat and mass transfer of falling liquid films

ausgeführt zum Zwecke der Erlangung des akademischen Grades
eines Doktors der technischen Wissenschaften

unter der Leitung von

Univ.-Prof. Dr.rer.nat. Hendrik C. Kuhlmann
E322 Institut für Strömungsmechanik und Wärmeübertragung

eingereicht an der

Technischen Universität Wien
Fakultät für Maschinenwesen und Betriebswissenschaften

von

Ernst Hofmann
0430537
Attemsgasse 43/19, 1220 Wien

Wien, im April 2015

Dedicated to Heike for her unconditional support.

"... as Sir Cyril Hinshelwood has observed... fluid dynamicists were divided into hydraulic engineers who observed things that could not be explained and mathematicians who explained things that could not be observed."

James Lighthill

Kurzfassung

Die vorliegende Dissertation ist durch den Absorptionskälteprozess motiviert und behandelt numerisch die durch Oberflächenwellen bedingte Erhöhung des Stoff- und/oder Wärmeübergangs an einem Fallfilm. Aus Sicht der Numerik ist die Aufgabe eine Herausforderung, da die zeitabhängige Strömung der freien Oberfläche und die typischerweise sehr großen Längen-zu-Filmdickenverhältnisse einen enormen Einsatz an Rechnerressourcen bedingen. Um die Untersuchung so systematisch wie möglich zu gestalten, werden nur zweidimensionale, laufende Wellen unter der Annahme, dass das Strömungsfeld vom Absorptionsvorgang unbeeinflusst bleibt, betrachtet. Diese Annahmen reduzieren die Komplexität erheblich, da sich so die Impulsgleichungen und die Gleichungen für den Wärme- und Stofftransport nacheinander lösen lassen. Die laufenden Wellen, als Lösungen der Navier–Stokes-Gleichungen mit scharf definierter freier Oberfläche, folgen schließlich als stationäre Zustände innerhalb eines bewegten Bezugssystems. Die a-priori unbekannte Wellengeschwindigkeit und die unbekannt Form der freien Oberfläche sind ebenso Teil der unter Einbeziehung von zwei zusätzlichen Bedingungen abgeleiteten Lösung. Das System von nichtlinearen Gleichungen wird durch Verwendung des Newton-Verfahrens in der Finiten-Volumen-Formulierung auf einem versetzten Gitter, das durch eine Koordinatentransformation an die freie Oberfläche angepasst ist, gelöst. Ausgewählte Lösungen für das Strömungsfeld dienen weiters als Grundlage für die weiteren Untersuchungen.

Die erste Folgestudie ist erneut im bewegten Bezugssystem durchgeführt und betrachtet den thermischen Film, definiert durch eine isotherme Wand und einer isothermen freien Oberfläche. Der Einfluss der Konvektion wird aus der gemittelten Nusseltzahl ersichtlich, berechnet für einen weiten Bereich der Prandtlzahl. Darüber hinaus sind die lokalen Nusseltzahlen an der Wand und an der freien Oberfläche für verschiedene Prandtlzahlen dargestellt und zeigen die Wirkung der effektiven Filmdickenabnahme (*film-thinning*), den Einfluss des Ablösegebiets innerhalb des primären Wellenberges (im bewegten Bezugssystem) und der Rückströmgebiete (im Laborsystem).

Die finale Studie befasst sich mit dem absorbierenden, welligen Fallfilm. Ausgewählte Lösungen aus der ersten Untersuchung dienen als Basis, um den zeitabhängigen, gekoppelten Wärme- und Stoffübergang mit Hilfe einer einfachen Fortschrittstechnik zu lösen. Die numerische Behandlung der Rückströmgebiete erweist sich als kompliziert, da diese zur Vorwärts-Rückwärts-Wärmeleitungsgleichung führen. Zur Überwindung des Problems wird ein probates Mittel eingesetzt und Lösungen für mehrere Parametersätze vorgestellt. Vorab zu dieser Untersuchung wird zum Vergleich noch der absorbierende, ebene Fallfilm diskutiert, insbesondere wird die Auswirkungen der einseitigen Diffusion im Detail analysiert.

Abstract

The present dissertation is motivated by absorption refrigeration and aims to reveal numerically the source for mass and/or heat transfer enhancement caused by the presence of surface waves on a falling liquid film. The targeted task is a numerical challenge since massive computational cost originate from the transient free surface flow in combination with, typically, vast length-to-film thickness ratios. To make the investigation as systematic as possible, only two-dimensional traveling waves are considered under the assumption that the flow field remains unaffected by the absorption process (one-way-coupling). These preconditions reduce the complexity significantly, since one can solve the momentum equations and the equations for heat and species transport consecutively. Finally, Navier–Stokes sharp-interface traveling-wave solutions are derived as steady states within a co-moving frame of reference. The a priori unknown wave celerity and the unknown shape of the free surface are also part of the solution derived with the inclusion of two additional constraints. The system of non-linear equations is solved by employing Newton’s method in the finite-volume formulation on a staggered grid which is adapted to the free surface by a coordinate transformation. Certain solutions of the flow field then serve as basis for further investigations.

The first subsequent study is again done in the moving frame of reference and accounts for the thermal film, which is defined through an isothermal wall and an isothermal free surface. The influence of convection is deduced from the average Nusselt number, shown for a wide range of Prandtl numbers. In addition, the local Nusselt numbers at wall and free surface, given for different Prandtl numbers, reveal the effect of film-thinning, the influence of the separation zone within the main hump (moving frame) and the backflow regions (laboratory frame).

The final study addresses the absorbing wavy film by choosing certain traveling wave solutions from the initial investigation as input to solve the transient, coupled heat and mass transfer by a simple marching technique. The numerical treatment of the backflow regions turn out to be difficult since the resulting problem leads to the forward-backward heat equation. Nonetheless, a proper remedy is introduced and solutions for several parameter sets are presented. Prior to the study, the absorbing flat film is discussed as benchmark and certain modeling aspects, especially the impact of one-sided diffusion, are discussed in detail.

Acknowledgments

This treatise represents the result of my research activities at the Institute of Fluid Mechanics and Heat Transfer, Vienna University of Technology between 03/2010 and 07/2013. The activity was funded by the Climate and Energy Fund of the Austrian Federal Government through the Austrian Research Promotion Agency (FFG) under grant number 825560.

My utmost gratitude goes to my supervisor Hendrik Kuhlmann who gave me the maximum conceivable freedom to unfold my research interests. Many thanks are also necessary for his encouraging words in tough times. I am also very grateful to my second referee Helfried Steiner for his detailed review.

The Austrian Institute of Technology GmbH is gratefully acknowledged for the project management as well as for the stimulating discussions that have induced the applied component to this work. Many thanks go to Thomas Fleckl, Johann Emhofer, Piotr Dudzinski and Christoph Reichl.

All kinds of fruitful and stimulating discussions with the institute members are gratefully acknowledged. Special thanks go to Daniel Lanzerstorfer, Michael Lukasser and Christoph Buchner for their comprehensive MATLAB and Linux support, Roman Mukin, Christiane Lechner and Željko Tuković (University of Zagreb) for their unrelenting efforts in teaching me OpenFOAM, Mario Aigner for enlightening me with the mathematician's point of view, the Müllner-twins Thomas & Markus and Frank Muldoon for pushing me deeper into the field of numerics and Thomas Loimer for being a very pleasant office mate during the years.

Not to forget, special thanks go to Liebherr-Transportation Systems GmbH & Co KG for giving me the possibility to finalize this thesis.

Contents

Nomenclature	xi
1. Introduction	1
1.1. Motivation	1
1.2. Related work	2
2. Basic considerations	5
2.1. Notation	5
2.2. Nusselt film	7
2.3. Scaling	9
2.4. Boundary layer equations	10
2.5. Stability	11
2.6. Nusselt and Sherwood number	13
3. Governing equations	21
3.1. Bulk equations	21
3.2. Boundary conditions	28
4. The isothermal wavy film	35
4.1. Moving frame	38
4.2. Numerics	44
4.3. Results	60
4.4. Interim summary	81
5. The thermal wavy film	83
5.1. Flow field	83
5.2. Nusselt numbers	85
5.3. Results	86
5.4. Interim summary	94
6. The absorbing flat film	95
6.1. Governing equations	95

6.2. Wall boundary condition	101
6.3. Numerics	106
6.4. Results	108
6.5. Interim summary	118
7. The absorbing wavy film	121
7.1. Governing equations	121
7.2. Numerical approach	123
7.3. Results for the thermal case	130
7.4. Results for the absorbing case	132
8. Summary and Conclusions	145
A. Thermophysical properties of LiBr–H₂O	149
A.1. Transport coefficients, solubility	149
A.2. Gibbs energy equation of state	151
A.3. Vapor pressure P_2	152
Bibliography	156

Nomenclature

To maintain readability, non-dimensional quantities are distinguished from their corresponding dimensional equivalents by an asterisk only if this is necessary. In case that a quantity appears in its dimensional and non-dimensional form, the units in the table below belong to the dimensional one.

Latin letters

Symbol	Quantity	Units
\mathbf{A}	Picard matrix	1
A	apparatus parameter	1
ΔA	surface length increase	m
a	thermal diffusivity	$\text{m}^2 \text{s}^{-1}$
B	non-dimensional enthalpy of evaporation	1
\mathbf{b}	rhs of linearized system	1
C	mass fraction (concentration), $C := C'_1$	1
C_0	reference concentration: $C_0 = C(T_0, P_0)$	1
C_s	film inlet concentration	1
C_α	concentration of constituent α	1
ΔC	characteristic concentration difference	1
ΔC_x	local concentration difference	1
\mathbf{c}	wave celerity	m s^{-1}
c_p	specific heat capacity	$\text{J kg}^{-1} \text{K}^{-1}$
D	binary diffusion coefficient	$\text{m}^2 \text{s}^{-1}$
d	characteristic length	m
f	wave frequency	s^{-1}
f_f	forcing frequency	s^{-1}
\mathbf{f}^n	residual vector at iteration n	1
\mathbf{g}	gravitational acceleration	m s^{-2}
g_x	gravity in streamwise direction	m s^{-2}
H_c	coolant channel width	m
h	height of the liquid film	m

\bar{h}	averaged film thickness	m
h_c	half coolant channel width	m
h_{Nu}	film thickness of Nusselt solution	m
h_s	specific enthalpy of solution	J kg ⁻¹
h_α	specific enthalpy of constituent α	J kg ⁻¹
Δh	enthalpy of absorption	J kg ⁻¹
\mathbf{i}	species flux density of $\alpha = 1$, i.e. $\mathbf{i} := \mathbf{i}_1$	kg m ⁻² s ⁻¹
\mathbf{i}_α	species flux density of constituent α	kg m ⁻² s ⁻¹
\mathbf{J}	Jacobian matrix	1
\mathbf{j}	diffusive flux density	–
k	wavenumber	m ⁻¹
L	length of the wave	m
L_{th}	thermal entrance length	m
L_0	length of the plate	m
M_α	molar mass of constituent α	kg mol ⁻¹
m	mass of solution	kg
m_α	mass of constituent α	kg
\dot{m}	local mass flux density	kg m ⁻² s ⁻¹
\bar{m}	length-averaged mass flux density	kg m ⁻² s ⁻¹
N_A	Avogadro constant	mol ⁻¹
N_α	number of particles of constituent α	1
N_η	number of cells in wall-normal direction	1
N_ξ	number of cells in streamwise direction	1
$\hat{\mathbf{n}}$	unit normal vector	1
n	normalization in unit normal vector	1
n_α	amount of constituent α	mol
P	pressure	Pa
P_0	reference pressure, system pressure	Pa
p	perc. of convectively induced heat transfer enhancement	1
q	source density	–
\dot{q}	local heat flux density	W m ⁻²
\bar{q}	length-averaged heat flux density	W m ⁻²
R	cell aspect ratio	1
r^n	residual at iteration n	1
\mathbf{S}	stress tensor	N m ⁻²
S	placeholder for scalar quantity, i.e. $S = T, C$	–
s	specific entropy of solution	J kg ⁻¹ K ⁻¹
T	temperature field of the liquid film	K

\bar{T}	mixing temperature of liquid film	K
T_0	reference temperature: film inlet temperature	K
ΔT	characteristic temperature difference	K
ΔT_x	local temperature difference	K
u	velocity component, streamwise	m s^{-1}
\mathbf{u}_{Nu}	Nusselt solution	m s^{-1}
\bar{u}_{Nu}	averaged velocity of Nusselt solution	m s^{-1}
V	volume	m^3
v	velocity component, crosswise	m s^{-1}
\mathbf{w}	boundary velocity	m s^{-1}
X	placeholder for any quantity	–
x	Cartesian coordinate, downstream	m
\mathbf{x}^n	solution vector at iteration n	1
y	Cartesian coordinate, wall-normal	m

Greek letters

Symbol	Quantity	Units
α	local heat transfer coefficient	$\text{W m}^{-2} \text{K}^{-1}$
$\bar{\alpha}$	length-averaged heat transfer coefficient	$\text{W m}^{-2} \text{K}^{-1}$
α_{m}	molar mass ratio	1
β	local mass transfer coefficient	m s^{-1}
$\bar{\beta}$	length-averaged mass transfer coefficient	m s^{-1}
β_T	thermal expansion coefficient	K^{-1}
β_C	solubility expansion coefficient	1
Γ	mass flux per unit length in spanwise direction	$\text{kg s}^{-1} \text{m}^{-1}$
γ	concentration coefficient	K^{-1}
Δ_i	cell length at face i	1
δ_S	reduced Reynolds number	1
ε_0	aspect ratio of the domain	1
ε_c	coolant aspect ratio	1
ε_S	viscous dispersion number	1
ζ	deviation of inlet concentration from equilibrium	1
η	surface fitted coordinate, wall normal	1
$\bar{\eta}$	dynamic viscosity	Pa s
Θ	coolant temperature	K
$\bar{\Theta}$	coolant mixing temperature	K
Θ_c	coolant inlet temperature	K

θ	inclination angle of plate	1
κ	curvature of free surface	m^{-1}
Λ	ratio of thermal conductivities	1
λ	thermal conductivity	$\text{W m}^{-1} \text{K}$
μ	chem potential of solution	J kg^{-1}
μ_α	chem potential of constituent α	J kg^{-1}
ν	kinematic viscosity	$\text{m}^2 \text{s}^{-1}$
Ξ	scaled reference concentration	1
ξ	surface fitted coordinate, downstream	1
ρ	density of solution	kg m^{-3}
ρ_α	density of constituent α	kg m^{-3}
ϱ	gas-to-fluid density ratio	1
σ	surface tension	N m^{-1}
$\boldsymbol{\tau}$	viscous part of stress tensor	N m^{-2}
Φ	dissipation function	W m^{-3}
φ_m	non-dimensional mass flux density (linear/linear)	1
ϕ	relative volume flux density	m s^{-1}
ϕ_m	non-dimensional mass flux density (linear/non-linear)	1
ϕ_m^\dagger	non-dimensional mass flux density (non-linear)	1
ϕ_q	non-dimensional heat flux density	1
$\phi_{q,f}$	non-dimensional heat flux density (film/wall)	1
$\phi_{q,i}$	non-dimensional heat flux density (free surface)	1
χ	parameter for arclength continuation	1
ψ	transport quantity in standard transport equation	–

Non-dimensional products

Symbol	Denotation	see Eq.
Fr	Froude number	(2.11a)
Ka	Kapitza number	(2.13)
Le	Lewis number	$Le = a/D$
Nu	Nusselt number (general)	(2.21a)
\overline{Nu}	averaged Nusselt number (general)	(2.21b)
Nu_c	coolant Nusselt number	(2.26b)
Nu_c^*	reduced coolant Nusselt number	(6.18)
Nu_i	Nusselt number free surface	(2.25a)
Nu_f	Nusselt number film/wall	(2.25b)
Nu_w	wall Nusselt number	(6.13)
Pe	Péclet number	$Pe = Re Pr$
Pe_c	coolant Péclet number	$Pe_c = Re_c Pr_c$
Pe_c^*	reduced coolant Péclet number	(6.28)
Pr	Prandtl number	$Pr = \nu/a$
Pr_c	coolant Prandtl number	$Pr_c = \nu_c/a_c$
Re	film Reynolds number	(2.8)
Re_C	film Reynolds number (CFC)	(2.15a)
Re_c	coolant Reynolds number	(2.26a)
Re_S	Reynolds number employed by Salamon <i>et al.</i> (1994)	Tab. 2.2
Sh	Sherwood number	(2.29a)
\overline{Sh}	averaged Sherwood number	(2.29b)
We	Weber number	(2.11b)
We_C	Weber number (CFC)	(2.15b)
We_S	Weber number employed by Salamon <i>et al.</i> (1994)	Tab. 2.2

Abbreviations

Acronym	Denotation
BL	boundary layer
bc	boundary condition
CFC	closed flow condition
LMTD	logarithmic mean temperature difference
ODE	ordinary differential equation
OFC	open flow condition
PDE	partial differential equation

Subscripts

Symbol	Quantity refers to
C	closed flow condition
c	wall/coolant interface, coolant, cooling channel
D	quantity defined by Dietze (2010)
f	film/wall interface
i	liquid free surface
Nu	Nusselt solution
p	plate
S	quantity defined by Salamon <i>et al.</i> (1994)
w	wall
c, n, s, e, w	location within numerical cell: center, north, south, east, west
α	constituent α
$\alpha = 1$	absorbent (e.g. LiBr)
$\alpha = 2$	refrigerant (e.g. H ₂ O)
$\alpha = 3$	non-absorbable gas (e.g. air)

Mathematics

Symbol	Denotation	Definition
∂_x	partial derivative operator	$\partial/\partial x$
∂_n	normal derivative operator	$\hat{\mathbf{n}} \cdot \nabla$
∇_s	tangential derivative operator	$(\mathbf{1} - \hat{\mathbf{n}}\hat{\mathbf{n}}) \cdot \nabla$
D_t	material derivative operator	$\partial_t + \mathbf{u} \cdot \nabla$
\mathcal{D}	bulk normal derivative operator	(4.22b)
$\mathbf{1}$	unity matrix	
$\ \square\ _2$	Euclidian norm	$\sqrt{\sum_i \square_i^2}$
\square^T	matrix/vector transpose	
$[[\square]]$	jump of quantity at an interface	$\square' - \square''$
$[\square]$	ceiling function	
δ_D	Dirac-delta distribution	
θ	Heaviside step function	
\Im	imaginary part of complex number	

1. Introduction

The laminar falling liquid film has attracted the interest of researchers since decades. As simple as the concept of the falling film appears, as complex its characteristics are. Due to the interesting fluid dynamics, the isothermal falling film is an outstanding problem for theoretical studies. Moreover, the thermal falling film represents an important concept for industrial applications and is, therefore, subject to applied research activities. From this applied point of view the falling film is typically subject to heating/cooling, condensation/evaporation or absorption/desorption. The latter case can be further divided into wall-sided absorption and absorption through the liquid free surface which may be either isothermal or coupled to heat transfer.

1.1. Motivation

One important field of application of falling films is absorption refrigeration. The present dissertation aims to numerically investigate the falling film dynamics and the influence of the film waviness on the absorption process. Despite enormous computer power and numerous simulation tools the numerical treatment of this particular problem, even formulated in just two dimensions, is still an enormous challenge. This is primarily due to the well-known inherent instability of the flat film interface. Therefore, one has to necessarily deal with a transient free surface flow. Capturing the free surface position calls for elaborate numerical techniques and since the absorption process (coupled heat and mass transfer) is located at the free surface, the accuracy by which the interface is represented numerically is crucial. Moreover, a tremendous number of cells can be expected resulting from thin concentration boundary layers at the free surface in combination with typically vast length-to-film thickness ratios of the domain. All these conditions already indicate the hopelessness, to perform an accurate numerical simulation (even for 2D) of the absorbing falling film just by using first principles. It is therefore inevitable to reduce the numerical effort by suitable approximations. Authors typically simplify the governing equations by exploiting boundary layer theory or they relax the requirement of having a sharply defined free-surface position. The present treatise aims to avoid both of these common approximations in order to present more accurate results which can be further used as benchmarks. To that end, we compute sharp-interface solutions of the Navier–Stokes equations. How-

ever, to reduce the afore mentioned numerical effort, we firstly search for traveling-wave solutions in a moving frame of reference and employ these as a basis for the subsequently-solved non-stationary absorption problem. To reduce the large parameter space that is related to the setup we shall focus on LiBr–H₂O due to its practical importance. The drawback of this particular fluid, however, is its thermophysical properties, i.e. a very low Kapitza number and a very large Schmidt number ($Ka \approx 500$, $Sc \approx 3000$, definitions to be given below) which represents another difficulty for the numerical treatment.

1.2. Related work

The overwhelming amount of literature regarding the falling liquid film can be primarily divided into theoretical studies of the isothermal and of the thermal film which are especially devoted to stability analysis and applied studies which are focusing on transport mechanisms. The following, non-exhaustive overview, presents selected relevant contributions to the respective sub-fields.

Isothermal wavy film It is widely accepted that the seminal work on the wavy falling film is due to [Kapitza & Kapitza \(1949\)](#) in which the Nobel laureate and his son experimentally characterized the waves appearing on the falling film. This was followed by the important theoretical contribution of [Benjamin \(1957\)](#), showing that the (vertically) falling film is unstable at all Reynolds numbers. Further theoretical investigations are dedicated to the solution-branching behavior and to the stability of boundary-layer-related model equations based on a long-wave assumption. This approach is extensively discussed in [Chang \(1994\)](#); [Chang *et al.* \(1994\)](#); [Chang & Demekhin \(2002\)](#); [Chang *et al.* \(1993\)](#); [Cheng & Chang \(1995\)](#). A recent and comprehensive monograph is given by [Kalliadasis *et al.* \(2012\)](#) with focus on the deduction of several model equations including stability analysis for isothermal and non-isothermal conditions including the Marangoni effect. Preceding works leading to the mentioned monograph are [Scheid *et al.* \(2006\)](#), [Ruyer-Quil *et al.* \(2005\)](#) and [Scheid *et al.* \(2005\)](#) for instance.

Some work is available based on full Navier–Stokes simulations which are typically performed by using the Volume of Fluid (VOF) method, see e.g [Gao *et al.* \(2003\)](#). Recently, [Albert *et al.* \(2012\)](#) applied the VOF method to the falling film and compared several surface-tension models. They conclude that only the *balanced Continuum Surface Force (bCSF)* approach yields correct results for the falling film. Another extensive VOF simulation by employing Fluent is done by [Dietze \(2010\)](#) and [Dietze *et al.* \(2008\)](#) with attention to the backflow region. We shall refer to their results in greater detail below. In [Trifonov \(2012\)](#) two different integral approaches are compared with the results from Navier–Stokes simulations. Sharp-interface Navier–Stokes solutions are rare. Probably the most impor-

tant one is the work by [Salamon *et al.* \(1994\)](#) and [Salamon \(1995\)](#). There, the Finite Element Method (FEM) is used to find stationary solutions within a moving frame of reference. They compare the solution branching with the branching of solutions resulting from the first-order boundary layer equations given by [Chang *et al.* \(1993\)](#) and found a great sensitivity to the parameter that is called *viscous dispersion number* by [Kalliadasis *et al.* \(2012\)](#). Therefrom, [Salamon *et al.* \(1994\)](#) conclude that the predictions of the first-order boundary layer equations would not agree with the Navier–Stokes results for water at moderate Reynolds numbers. This shortcoming was removed in [Kalliadasis *et al.* \(2012\)](#) by using their so-called *simplified second order model*. Prior to [Salamon *et al.* \(1994\)](#), [Bach & Villadsen \(1984\)](#) have already applied the FEM method to the falling film and solved, quite uncommon, for the Lagrangian velocities. Transient FEM-simulations are presented in [Malamataris *et al.* \(2002\)](#) and [Malamataris & Balakotaiah \(2008\)](#).¹

Thermal wavy film The thermal wavy falling film with a constant temperature difference across the film is a very instructive case since it reveals the primary physical effect behind the heat-transfer enhancement that is induced by waves. A numerical investigation was made by [Miyara \(1999\)](#) where he shows the insignificance of convection compared to the so called film thinning effect. The same conclusion is drawn by [Aktershev & Alekseenko \(2013\)](#) for a condensing film at an isothermal wall. In contrast to [Miyara \(1999\)](#) they account for a varying film thickness (due to the condensing mass) and find that the enhancement of the heat transfer is dominated by film thinning. An implementation of the energy equation into OpenFOAM (VOF) and the application to the falling film is provided by [Raach *et al.* \(2011\)](#).

Besides the thermal falling film one can also assume the mathematically equivalent isothermally absorbing falling film. The equivalence holds true for the case of an infinitely dilute (and non-reactive) solute. For this case Henry’s law acts as the species boundary condition at the free surface. Recently, [Albert *et al.* \(2014\)](#) presented a numerical investigation using VOF on the interfacial mass transfer to a wavy falling film. They use a subgrid model to capture the concentration boundary layer at the free surface. Supplementary, wall-sided heat and species transfer to a liquid film on a spinning disc is investigated in [Prieling & Steiner \(2013a,b\)](#) by employing an unsteady integral boundary layer approach.

Absorbing flat film An excellent overview on the strategies in modeling the absorbing falling film until 2001 can be found in [Killion & Garimella \(2001\)](#). They give a detailed review of the most important works and pay particular attention to the assumptions made by each individual publication. Probably, the first substantial investigation was due to

¹Interestingly, [Malamataris & Balakotaiah \(2008\)](#) mention the average time for a simulation to range between 5 to 50 days.

Grigor'eva & Nakoryakov (1977). Some of the approximations introduced by them are still common practice. Grossman (1983) further improved the existing model by replacing the uniform velocity by the parabolic velocity profile. He obtained approximate solutions for the temperature and concentration fields in form of a series expansion considering an adiabatic and an isothermal wall. Since that time the model has been extended by several authors by including film-thickness variations, a non-linear vapor–liquid equilibrium condition, shear stress at the free surface, the Eckert–Schneider condition, a non-isothermal wall, as well as an energy equation including interdiffusion, variable thermophysical properties and the differential enthalpy of solution. Another major factor for the absorption efficiency is the presence of non-absorbable gases as shown by Grossman & Gommed (1997) and Yang & Jou (1998). Recent numerical studies considering the flat film were carried out by Bo *et al.* (2010); Karami & Farhanieh (2009, 2011); Yoon *et al.* (2005). The first and the second work are dealing with a fully dimensional formulation and treat the influence of several operating conditions and variable thermophysical properties, respectively, on the heat- and mass-transfer coefficients. The latter investigators included a transverse velocity component in the flat-film model and studied the dependence of the averaged Sherwood and Nusselt numbers on the Reynolds number and the inclination angle. Most recently, Mittermaier *et al.* (2014) present a detailed numerical study by accounting for interdiffusion, variable thermophysical properties, the differential enthalpy of solution and show that the non-linear equilibrium condition at the interface leads to different results for absorption and desorption.

Absorbing wavy film The particular case of the absorbing wavy film is less represented in the literature so far. Some *early* investigations are summarized by Killion & Garimella (2001) in their table 4, where simplifying assumptions are made regarding the interfacial deformation and the flow field. Morioka & Kiyota (1991), for instance, construct a simple sinusoidal (capillary) wave and predict the absorption to be enhanced by a factor of 1.7–2.4. In turn, Patnaik & Perez-Blanco (1996) use a model for roll waves and finally present values for the averaged Sherwood number that may exceed the corresponding smooth-film values by a factor of 3.75–10. Since they define a complicated formula for the averaged Sherwood number it remains unclear how this averaged Sherwood number correlates with the mass flux. In Yang & Jou (1998) the influence of non-absorbable gases combined with the appearance of waves is given.

The absorbing wavy film is also related to bubble dynamics where the solubility of the gas of a bubble in a surrounding liquid poses a two-phase flow problem with interfacial mass transfer. Numerical work by using VOF can be found, to name just one, in Bothe *et al.* (2003). Additionally, the simulation of a bubble with soluble surfactants is given by Tuković & Jasak (2008) in the framework of OpenFOAM's ALE solver.

2. Basic considerations

The present chapter introduces some basic considerations used throughout this dissertation and discusses some of the most important results which are related to the topic.

2.1. Notation

1. We assume a typical absorber device that works with a binary liquid solution, called mixture in the following. The components of a binary mixture are called solute and solvent in general. However, the terms absorbent and absorbate are more applicable, where the absorbate plays the role of the refrigerant (cooling liquid). Two of the most popular working-pairs are water–ammonia ($\text{H}_2\text{O}\text{--}\text{NH}_3$) and lithium bromide–water ($\text{LiBr}\text{--}\text{H}_2\text{O}$). Note that for these cases H_2O acts either as absorbent or as absorbate (refrigerant).

working pair	absorbent	refrigerant
water–ammonia	H_2O	NH_3
lithium bromide–water	LiBr	H_2O

2. The present model is derived for working pairs with a non-volatile absorbent (e.g. LiBr). This consideration excludes $\text{H}_2\text{O}\text{--}\text{NH}_3$, where both components are volatile.
3. Since we assume the absorbent to be non-volatile, the gaseous phase consists of the vaporized refrigerant (e.g. H_2O , vapor) and in general of some non-absorbable gas (e.g. air). Both gases are assumed to be ideal and the total pressure P_0 (system pressure) is assumed to be constant.
4. We introduce the subscript $\alpha = 1, 2, 3$ for any quantity X_α where $\alpha = 1$ stands for the absorbent, $\alpha = 2$ for the refrigerant and $\alpha = 3$ for the non-absorbable gas. If necessary, quantities from the liquid phase are primed (X'_α) and those of the gaseous phase are double primed (X''_α).
5. The system consists of three components and two phases, where each phase is a binary mixture and only the refrigerant is present in both phases. An intuitive sketch of the penetrability of the free surface is given in Figure 2.1 indicating the

absorbed mass flux density \dot{m} . All concentration variables (to be defined later) are listed in Table 2.1.

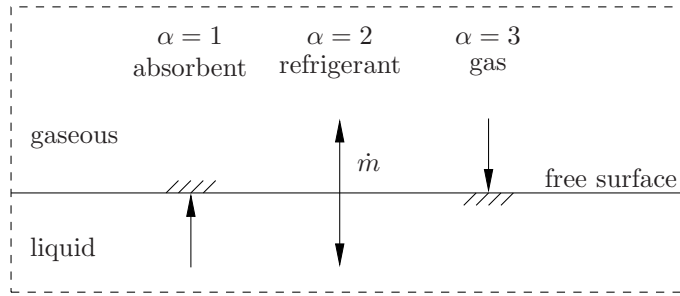


Figure 2.1.: Illustration of the penetrability of the liquid free surface.

Table 2.1.: Concentration variables within the system under consideration.

	$\alpha = 1$	$\alpha = 2$	$\alpha = 3$	mixture
liquid phase C'_α	C'_1	C'_2	0	$C'_1 + C'_2 = 1$
gaseous phase C''_α	0	C''_2	C''_3	$C''_2 + C''_3 = 1$

6. At the liquid free surface we assume local thermodynamic equilibrium. This condition results in a continuous change of temperature and vapor pressure(s).
7. After presenting a general model for film absorption we will concentrate on the particular working pair LiBr–H₂O, since this is of practical importance and numerical correlations for all important material parameters are well documented.
8. For any binary mixture it is convenient to deal with just one concentration variable. Since we are primarily interested in the concentration field of the refrigerant ($\alpha = 2$), it seems to be obvious to define $C' = C'_2$ for the liquid phase. However, since this is more common, we shall employ the concentration field of the absorbent, thus $C' := C'_1$.
9. Whenever necessary we shall distinguish dimensional from non-dimensional quantities by indicating the dimensional ones with an asterisk, thus X^* .

2.2. Nusselt film

The flat film solution, referred to as Nusselt film¹ from now on, is the solution of the steady and incompressible Navier–Stokes equations for a stratified flow over a plate inclined with respect to the horizontal by the angle θ , hence

$$\nu \partial_{yy} u = -g \sin \theta := -g_x, \quad (2.1a)$$

$$v = 0, \quad (2.1b)$$

$$u|_{y=0} = 0, \quad (2.1c)$$

$$(\partial_y u)|_{y=h_{\text{Nu}}} = 0, \quad (2.1d)$$

where the downstream coordinate is denoted by x , the wall-normal coordinate by y and the film thickness by h_{Nu} . In addition we have introduced the kinematic viscosity ν and the gravity in streamwise direction g_x . The boundary conditions are no-slip at the wall ($y = 0$) and no shear stress at the free surface ($y = h_{\text{Nu}}$). Figure 2.2 shows a sketch of the Nusselt film with its most important quantities. The solution of (2.1) is given by

$$\mathbf{u}_{\text{Nu}} = \frac{g_x}{\nu} \left(y h_{\text{Nu}} - \frac{y^2}{2} \right) \mathbf{e}_x. \quad (2.2)$$

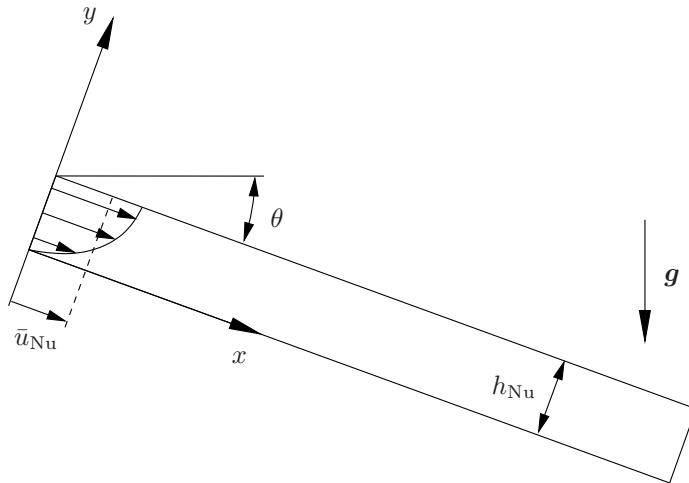


Figure 2.2.: Sketch of the Nusselt film which is inclined by θ with respect to the horizontal.

¹As it is most common we call it Nusselt film or Nusselt solution even though his work (Nusselt, 1916) contains more than just the flat film solution.

The averaged velocity \bar{u}_{Nu} and the maximum velocity at the free surface $u_{\text{Nu,max}}$ are

$$\bar{u}_{\text{Nu}} = \frac{g_x h_{\text{Nu}}^2}{3\nu}, \quad (2.3a)$$

$$u_{\text{Nu,max}} = \frac{g_x h_{\text{Nu}}^2}{2\nu} \quad (2.3b)$$

with the ratio

$$\frac{u_{\text{Nu,max}}}{\bar{u}_{\text{Nu}}} = \frac{3}{2}. \quad (2.4)$$

By using the incoming mass flux Γ (per unit length in spanwise direction)

$$\Gamma = \rho h_{\text{Nu}} \bar{u}_{\text{Nu}}, \quad (2.5)$$

having introduced the fluid density ρ , the Nusselt film thickness h_{Nu} derives as

$$h_{\text{Nu}} = \left(\frac{3\Gamma\nu}{\rho g_x} \right)^{1/3}. \quad (2.6)$$

In the following we will choose, as this is most common, h_{Nu} and \bar{u}_{Nu} as the scales for non-dimensionalization, thus

$$y_0 := h_{\text{Nu}} \quad , \quad u_0 := \bar{u}_{\text{Nu}} \quad (2.7)$$

so that the film Reynolds number is

$$\text{Re} := \frac{u_0 y_0}{\nu} = \frac{\bar{u}_{\text{Nu}} h_{\text{Nu}}}{\nu} = \frac{\Gamma}{\rho\nu}. \quad (2.8)$$

The film thickness can also be written in terms of Re, hence

$$h_{\text{Nu}} = \left(\frac{3\nu^2}{g_x} \text{Re} \right)^{1/3}. \quad (2.9)$$

Other scales are the surface velocity $u_{\text{Nu,max}}$ and $(\nu^2/g_x)^{1/3}$ as the length scale. Note that some authors include the factor 4 in their definition of Re which seems to originate from using the hydraulic diameter of the liquid film as length scale.

2.3. Scaling

The following scaling is applied to the later introduced momentum equations.

$$x = \frac{x^*}{y_0} \quad , \quad y = \frac{y^*}{y_0} \quad , \quad t = t^* \frac{u_0}{y_0} \quad , \quad u = \frac{u^*}{u_0} \quad , \quad v = \frac{v^*}{u_0} \quad , \quad P = \frac{P^*}{\rho u_0^2} \quad (2.10)$$

Here, the pressure P was introduced and the asterisks indicate the dimensional quantities. The given scales lead us to the Reynolds number (2.8) and to the Froude and Weber numbers in their common definitions

$$\text{Fr} := \sqrt{\frac{u_0^2}{gy_0}} \quad (2.11a)$$

$$\text{We} := \frac{\sigma}{\rho y_0 u_0^2} \quad (2.11b)$$

If we employ u_0 and y_0 from the Nusselt solution (2.7), the square of Fr can be expressed through Re and θ as

$$\text{Fr}^2 = \frac{\text{Re}}{3} \sin \theta \quad (2.12)$$

Correspondingly, by defining the Kapitza number²

$$\text{Ka} := \frac{\sigma}{\rho g^{1/3} \nu^{4/3}} \quad (2.13)$$

the Weber number can also be written in terms of Re, θ and Ka, thus

$$\text{We} = \left(\frac{3\text{Ka}^3}{\text{Re}^5 \sin \theta} \right)^{1/3} \quad (2.14)$$

Instead of choosing the *natural* triple $\{\text{Re}, \text{We}, \text{Fr}\}$ one may also chose the alternative triple $\{\text{Re}, \text{Ka}, \theta\}$ where the equations (2.12) and (2.14) are used for conversion. The first-mentioned set of parameters is suitable for purely theoretical studies that vary Re, Fr and We independently from another. However, choosing an inclination angle θ , a Kapitza number Ka (representing a fluid) and varying the Reynolds number Re mimics the situation that an experimentalist would encounter.

In the following investigations we will refer to the results presented by [Salamon *et al.* \(1994\)](#) and [Dietze \(2010\)](#). Table 2.2 summarizes their definitions of the non-dimensional numbers. The present study employs the so-called open flow condition (OFC) and the

²Some authors use the streamwise gravitational acceleration g_x instead of g . However, the given definition is very convenient since it depends on fluid properties only. For H₂O at ambient conditions one finds $\text{Ka} \approx 3000$ and roughly $\text{Ka} \approx 500$ for LiBr–H₂O.

closed flow condition (CFC), both discussed in detail at the end of Section 4.1.1. Using the CFC implies a different definition of length and velocity scale, so that Reynolds and Weber number become for the CFC

$$\text{Re}_C = \frac{\bar{u}\bar{h}}{\nu}, \quad (2.15a)$$

$$\text{We}_C = \frac{\sigma}{\rho\bar{h}\bar{u}^2} \quad (2.15b)$$

with the later introduced averaged thickness of the wavy film \bar{h} and the corresponding averaged velocity \bar{u} .

Table 2.2.: Conversion of the non-dimensional parameters used in the literature given in the first row. The subscripts S and D refer to the corresponding author, the subscript C indicates the reference to the closed flow condition (CFC).

	present study		Salamon <i>et al.</i> (1994)	Dietze (2010)
	OFC	CFC		
Kapitza number	Ka	Ka	–	$\text{Ka}_D = \text{Ka}/(\sin\theta)^{1/3}$
Reynolds number	Re	Re_C	$\text{Re}_S = 3\text{Re}_C/2$	Re
Weber number	We	We_C	$\text{We}_S = 3\text{We}_C/\text{Re}_C$	We
inclination	θ	θ	$\theta = \pi/2$	θ

2.4. Boundary layer equations

Since the boundary layer (BL) equations are the model equations of choice for the present problem we shall briefly comment on our decision to employ Navier–Stokes simulations. Basically, the derivation of the BL equations includes two important steps.

1. Long wave assumption: introduction of a perturbation parameter $\varepsilon \ll 1$
2. Boundary layer approximation: elimination of the pressure by integrating the cross-stream momentum equation

For the long wave assumption one introduces $\varepsilon = h_{\text{Nu}}/x_0 \ll 1$ with some characteristic length scale in streamwise direction x_0 . Following Kalliadasis *et al.* (2012), ε shall be understood as an ordering parameter since the streamwise length scale x_0 is a priori unknown. All variables are then expanded as usual in powers of ε and terms of $O(\varepsilon^3)$ and higher are neglected. Since the cross stream inertia terms turn out to be of second order, the terms are also neglected so that the cross stream momentum equation can be

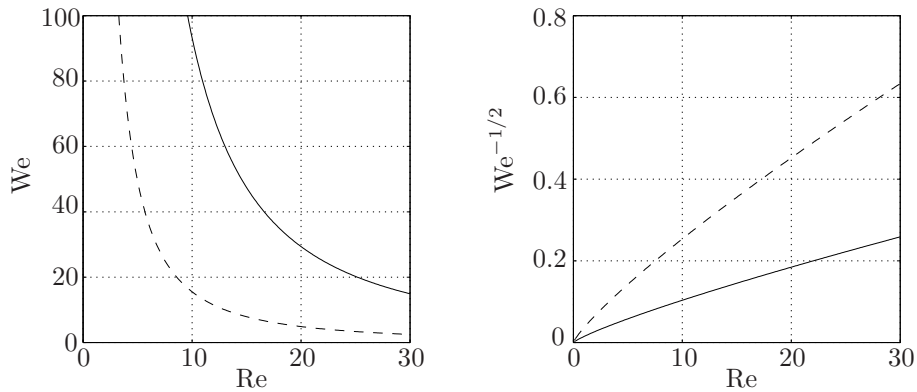


Figure 2.3.: Left: Weber number We vs. Reynolds number Re for const. Kapitza number $Ka = 3000$ (full), $Ka = 500$ (dashed) and $\theta = \pi/2$. Right: Plot of $We^{-1/2} \sim \varepsilon$ vs. Re for the given Kapitza numbers.

integrated across the film to eliminate the pressure, as in Prandtl's boundary layer theory. Finally, surface tension effects contribute to the pressure at $O(1)$ only if one assumes

$$\varepsilon^2 We = O(1) \quad (2.16)$$

which is known as the strong surface tension limit which *becomes the cornerstone of the long wave assumption for the boundary layer approximation* (Kalliadasis *et al.*, 2012). The result are the second-order boundary layer equations including the perturbation parameter ε (up to ε^2) and the non-dimensional triple $\{Re, We, \theta\}$. In a subsequent step the BL-equations are again rescaled by using the Shkadov scale $\propto We^{1/3}$ leading to a corresponding triple of reduced BL-parameters, the reduced Reynolds number, the viscous dispersion number and the reduced inclination number.

Figure 2.3 shows the relation between Re and We for $Ka = 500$ (LiBr–H₂O), $Ka = 3000$ (H₂O) and $\theta = \pi/2$. It becomes evident that the relation dictated by the strong surface tension limit $\varepsilon \sim We^{-1/2}$ together with the long wave assumption $\varepsilon \ll 1$ can only be satisfied for very small Reynolds numbers. It is, therefore, questionable whether the BL-equations are the adequate choice for investigations focusing on LiBr–H₂O. From this result we decide to solve the Navier–Stokes equations.

2.5. Stability

The stability of the falling film has attracted enormous interest of many investigators since decades. The first important theoretical contributions to the stability problem were due to Yih (1955) and Benjamin (1957) analyzing the stability of the flat film by using the

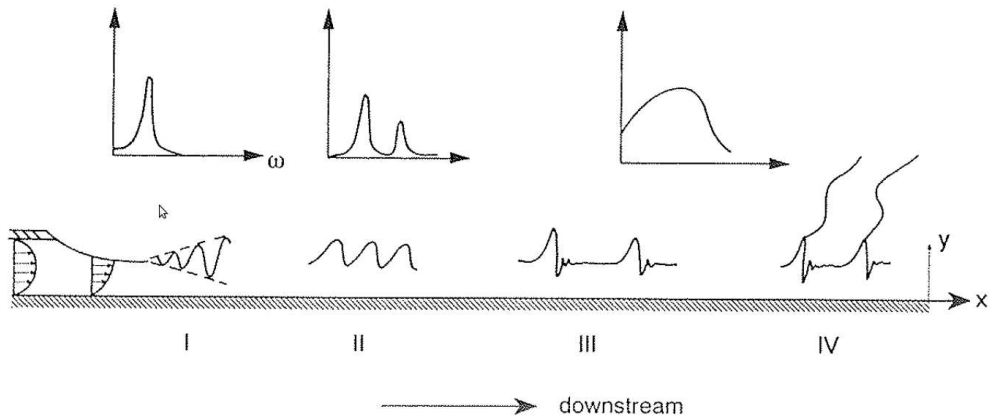


Figure 2.4.: Schematic representation of the four wave regions I-IV. The localized wave spectra, with ω being the wave frequency, is also shown. The image is taken from [Chang \(1994\)](#).

Orr-Sommerfeld equation. As the most interesting result [Benjamin \(1957\)](#) has shown that film flow down the vertical plate ($\theta = \pi/2$) is unstable for all Reynolds numbers. This first transition where the flat film becomes unstable is known as the primary (linear) instability. As a result of the instability waves grow on the interface.

The spatial evolution of film flows is typically divided into several stages or regions called in the following. It is further important to distinguish whether the waves evolve from an *unperturbed* inlet, i.e. just from the presence of natural/artificial noise, or from a perturbed inlet where a monochromatic excitation is added to the incoming flow. Finally, forcing frequency and forcing amplitude are also important parameters for the evolution of the film. The spatial evolution of the liquid film flow is explained by [Chang \(1994\)](#), [Chang et al. \(1994\)](#) and [Kalliadasis et al. \(2012\)](#), summarized below. The schematic representation given by [Chang \(1994\)](#) is shown in Figure 2.4.

1. **Region I:** The primary instability leads to an amplification of inlet perturbations which are growing downstream (convective instability). Depending on the type of the perturbations at the inlet one finds the following scenarios.
 - infinitesimal, broadband natural (or artificial) noise: a linear filtering process selects a unique frequency,
 - infinitesimal, monochromatic perturbation: the forcing frequency is inherited to the flow,
 - finite, monochromatic excitation: the first waves that appear are those of region III with a wave frequency close to the forcing frequency.

2. **Region II:** The exponential growth of the monochromatic wave of region I is arrested by non-linear effects. A subsequent non-linear interaction leads to a nearly monochromatic wave which persists a few wavelengths before it becomes subject to another transition, which strongly depends on the forcing frequency.
 - periodic forcing with low frequencies \implies region III, i.e. evolution into two-dimensional solitary waves,
 - periodic forcing with high frequencies \implies region IV, i.e. evolution into three-dimensional waves.

3. **Region III:** For low forcing frequencies, the saturated waves of region II undergo a secondary instability and form two-dimensional solitary waves. The instability mechanisms behind this secondary transition are the subharmonic and the sideband instability, leading to spatio-temporal chaos, see [Liu & Gollub \(1993\)](#). As already mentioned, the solitary waves can also be formed *directly* by large monochromatic excitations which circumvent region I and region II.

4. **Region IV:** [Kalliadasis *et al.* \(2012\)](#) collect three different three-dimensional states within this region. For large forcing frequencies the saturated waves of region II are subject to two different transitions, called the synchronous instability and the herringbone pattern instability. The third state applies to the solitary waves of region III which are in general unstable to spanwise perturbations and, therefore, become three-dimensional.

The present investigation will focus on the solitary waves out of region III.

2.6. Nusselt and Sherwood number

Discussions in the literature on absorbing falling films are rather ambiguous regarding the definition of the transfer coefficients and the driving potentials, respectively. For the driving potentials several definitions are possible and almost all combinations can be found. Therefore, we shall introduce the common definitions that account for the characterization of heat and mass transfer and discuss some difficulties arising in the present system.

2.6.1. Basic setup

By neglecting the gas phase, the present system consists of the coupled temperature fields of the absorbing falling film $T(x, y)$ and the temperature field of the liquid coolant $\Theta(x, y)$, as sketched in [Figure 2.5](#).

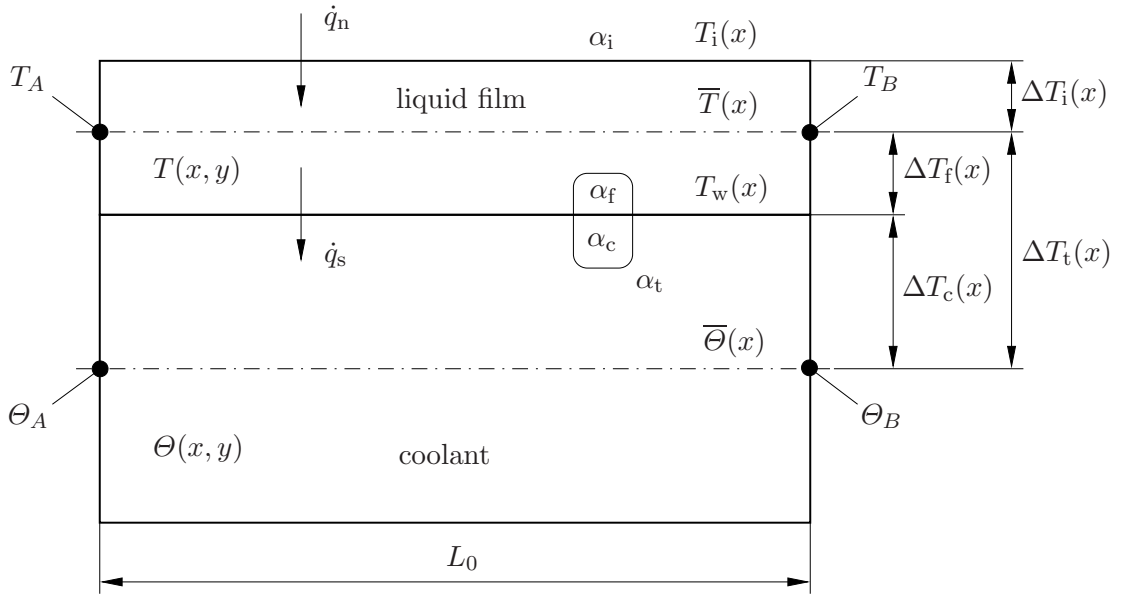


Figure 2.5.: Meridional cut of a film absorber to illustrate the thermal conditions.

The dash-dotted lines in the center of the domains symbolize the respective mixing temperatures

$$\bar{S}(x) = \frac{1}{A\bar{u}} \int_A uS \, dA \quad , \quad \bar{S} = \bar{T}, \bar{\Theta}, \quad (2.17)$$

with the averaged velocity \bar{u} and the flow cross section A . Further, we have indicated the wall temperature $T_w(x)$ and the temperature at the free surface of the liquid film $T_i(x)$. The heat flux density due to absorption is \dot{q}_n and the heat flux density to the coolant \dot{q}_s . The boundary values represent the mixing temperatures at the in- and outlets, thus

$$\begin{aligned} T_A &:= \bar{T}|_{x=0} \quad , \quad T_B := \bar{T}|_{x=L_0}, \\ \Theta_A &:= \bar{\Theta}|_{x=0} \quad , \quad \Theta_B := \bar{\Theta}|_{x=L_0}. \end{aligned}$$

2.6.2. Nusselt number

As it is most common, we define the local (boundary) heat flux density \dot{q} in y -direction as

$$\dot{q} := \alpha \Delta T_x \quad (2.18)$$

with the local heat transfer coefficient α and a (in general local) driving potential ΔT_x .

The heat flux \dot{Q} , corresponding to L_0 , or the length-averaged³ heat flux density \bar{q} reads

$$\bar{q} = \frac{\dot{Q}}{L_0} = \frac{1}{L_0} \int_0^{L_0} \dot{q} dx. \quad (2.19)$$

In addition we define the (length-)averaged heat transfer coefficient $\bar{\alpha}$, i.e.

$$\bar{\alpha} := \frac{1}{L_0} \int_0^{L_0} \alpha dx = \frac{1}{L_0} \int_0^{L_0} \frac{\dot{q}}{\Delta T_x} dx. \quad (2.20)$$

Furthermore, we introduce the local Nusselt number Nu by choosing a characteristic length scale d and we define the corresponding (length-)averaged Nusselt number $\overline{\text{Nu}}$, thus

$$\text{Nu} := \frac{\alpha d}{\lambda} = \frac{\dot{q} d}{\lambda \Delta T_x}, \quad (2.21a)$$

$$\overline{\text{Nu}} := \frac{\bar{\alpha} d}{\lambda} = \frac{1}{L_0} \int_0^{L_0} \text{Nu} dx. \quad (2.21b)$$

with the thermal conductivity λ .

Absorber From the thermal conditions sketched in Figure 2.5 we can define three local heat transfer coefficients: α_i for the free surface, α_f for the wall/film interface and α_c for the wall/coolant interface, which are related to the respective heat flux densities as

$$\dot{q}_n = \alpha_i \Delta T_i = \alpha_i (T_i - \bar{T}), \quad (2.22a)$$

$$\dot{q}_s = \alpha_f \Delta T_f = \alpha_f (\bar{T} - T_w), \quad (2.22b)$$

$$\dot{q}_s = \alpha_c \Delta T_c = \alpha_c (T_w - \bar{\Theta}), \quad (2.22c)$$

where we have introduced appropriate local temperature differences (driving potentials) for every single heat flux density. Furthermore, one may eliminate the wall temperature T_w to express a heat transfer coefficient α_t with respect to the driving potential ΔT_t , i.e.

$$\dot{q}_s = \alpha_t \Delta T_t = \alpha_t (\bar{T} - \bar{\Theta}). \quad (2.23)$$

By accounting for the additional resistance of the plate between coolant and liquid film the heat transfer coefficient α_t becomes

$$\alpha_t = \left(\frac{1}{\alpha_f} + \frac{d_p}{\lambda_p} + \frac{1}{\alpha_c} \right)^{-1}, \quad (2.24)$$

where d_p and λ_p represent thickness and thermal conductivity of the plate, respectively.

³Since the problem is two-dimensional, (length-)averaged stands for streamwise-averaged.

Film flow The Nusselt numbers regarding the liquid film are commonly defined with the Nusselt film thickness h_{Nu} as the length scale, hence

$$Nu_i := \frac{\alpha_i h_{Nu}}{\lambda}, \quad (2.25a)$$

$$Nu_f := \frac{\alpha_f h_{Nu}}{\lambda} \quad (2.25b)$$

where the subscripts account for the respective interface, corresponding to the transfer coefficients (2.22a) and (2.22b). For the laminar, fully developed, non-absorbing flat film, Dietze (2010) summarizes four scenarios where either the wall or the free surface is assumed to be diabatic or adiabatic and where the diabatic boundary is either represented by a Dirichlet or a Neumann boundary condition (bc). The results for Nu_f and Nu_i are given in Table 2.3.

Table 2.3.: Nusselt numbers for the laminar, fully developed, non-absorbing flat film for different scenarios. Taken from Dietze (2010) (his Table 2.7).

wall / free surface	Dirichlet bc	Neumann bc
adiabatic / diabatic	$Nu_i = 3.41$	$Nu_i = 140/33 \approx 4.24$
diabatic / adiabatic	$Nu_f = 1.88$	$Nu_f = 35/17 \approx 2.06$

For the absorbing flat film, Grossman (1983) derived numerically the asymptotic values for the Nusselt numbers⁴ which are given in Table 2.4 for two different wall boundary conditions. The non-absorbing case with the adiabatic wall and the diabatic free surface with Neumann bc shows almost the same value for Nu_i even if the bc at the absorbing free surface is a Robin bc rather than a Neumann bc.

Table 2.4.: Nusselt numbers for the laminar, fully developed absorbing flat film (Grossman, 1983).

	free surface	wall/film interface
adiabatic wall	$Nu_i = 4.23$	$Nu_f = 0$
isothermal wall	$Nu_i = 2.65$	$Nu_f = 1.60$

Coolant flow We assume the coolant flow as a duct flow with a corresponding hydraulic diameter of d_c . The coolant Reynolds number Re_c and the coolant Nusselt number Nu_c

⁴Contrary to the commonly used mixing temperatures, Grossman (1983) employed the bulk temperature in his definitions of the Nusselt numbers, which is the temperature at the half width of the liquid film.

are then defined by

$$\text{Re}_c := \frac{\bar{u}_c d_c}{\nu_c}, \quad (2.26a)$$

$$\text{Nu}_c := \frac{\alpha_c d_c}{\lambda_c}, \quad (2.26b)$$

with the kinematic viscosity and thermal conductivity of the coolant ν_c and λ_c , respectively. Literature provides numerous correlations for the Nusselt number which depend on the thermal wall boundary condition, on whether the streamwise position lies within the thermal entrance length or within the fully developed region and on whether the flow is laminar or turbulent. For a laminar, fully developed plane channel flow, for instance, where the lower boundary is adiabatic, [Shah & London \(1978\)](#) present $\text{Nu}_c = 4.861$ (their Table 43) for an isothermal (upper) boundary and $\text{Nu}_c = 5.385$ (their Table 44) for a boundary with a constant heat flux density. Furthermore, the VDI Heat Atlas ([VDI-GVC, 2010](#)) provides several relations to derive the Nusselt number for fully developed turbulent flow ($\text{Re}_c > 10^4$) and transient flow ($2300 < \text{Re}_c < 10^4$).

2.6.3. Sherwood number

In accordance to the local heat flux density, one introduces the local mass flux density as

$$\dot{m} := \rho \beta \Delta C_x \quad (2.27)$$

with the mass transfer coefficient β and a (in general local) driving potential for mass transfer ΔC_x . Additionally, one defines the length-averaged mass transfer coefficient

$$\bar{\beta} := \frac{1}{L_0} \int_0^{L_0} \beta \, dx = \frac{1}{L_0} \int_0^{L_0} \frac{\dot{m}}{\rho \Delta C_x} \, dx. \quad (2.28)$$

The corresponding local Sherwood number Sh and the (length-)averaged Sherwood number $\bar{\text{Sh}}$ then read

$$\text{Sh} := \frac{\beta d}{D} = \frac{\dot{m} d}{\rho D \Delta C_x}, \quad (2.29a)$$

$$\bar{\text{Sh}} := \frac{\bar{\beta} d}{D} = \frac{1}{L_0} \int_0^{L_0} \text{Sh} \, dx, \quad (2.29b)$$

again with a characteristic length d and the binary diffusion coefficient D .

2.6.4. Non-dimensional fluxes

For the case of a constant driving potential ($\Delta T = \text{const.}$) the equations (2.19) and (2.20) lead us to $\bar{q} = \bar{\alpha}\Delta T$ in accordance to the definition of the local quantity $\dot{q} = \alpha\Delta T$. Therefore, it seems to be obvious to again define

$$\bar{q} := \bar{\alpha}\overline{\Delta T}, \quad (2.30)$$

where $\overline{\Delta T}$ represents a compatible averaged driving potential. At this point we shall mention the important result for the laminar flow in a duct, as sketched in Figure 2.5, with the local driving potential $\Delta T = T_w - \bar{\Theta}$ and a const. wall temperature $T_w = \text{const.}$ For this case the averaged driving potential $\overline{\Delta T}$ is the well known logarithmic mean temperature difference (LMTD⁵) (Shah & London, 1978)

$$\overline{\Delta T} = \Delta T_{\text{lm}} = \frac{\Delta T_0 - \Delta T_X}{\ln \frac{\Delta T_0}{\Delta T_X}} \quad (2.31)$$

with $\Delta T_0 = T_w - \bar{\Theta}_0$, $\Delta T_X = T_w - \bar{\Theta}_X$, the inlet temperature $\bar{\Theta}_0$ and the mixing temperature at X , thus $\bar{\Theta}_X = \bar{\Theta}(X)$. Again, this holds true only for the isothermal wall, other wall boundary conditions need a thorough discussion of $\overline{\Delta T}$. Altogether, for cases where the driving potential is a local quantity which is in addition itself part of the solution, definition (2.30) bears the difficulty that the calculation of the averaged heat flux density \bar{q} from $\bar{\alpha}$ is only possible by also knowing $\overline{\Delta T}$. This leads to the situation that (2.30) generates two quantities for the determination of \bar{q} , where $\overline{\Delta T}$ is in general a non-trivial quantity which is most likely not accessible in an experiment. For practical reasons it is therefore more advantageous to introduce a transfer modulus based on a characteristic outer potential difference. Guided by the definition of the Nusselt and Sherwood numbers we define the non-dimensional heat flux density ϕ_q and the non-dimensional mass flux density ϕ_m , thus

$$\phi_q := \frac{\dot{q}d}{\lambda\Delta T}, \quad (2.32a)$$

⁵ The LMTD is also an important value for designing heat exchangers. By assuming an adiabatic free surface ($\dot{q}_n \equiv 0$), the film-coolant arrangement of Figure 2.5 is equivalent to an ordinary heat exchanger. The averaged heat flux density exchanged by the fluids is given for $\alpha_t = \text{const.}$ by $\bar{q}_s = \alpha_t\Delta T_{\text{lm}}$ again with the LMTD

$$\Delta T_{\text{lm}} = \frac{\Delta T_B - \Delta T_A}{\ln \frac{\Delta T_B}{\Delta T_A}},$$

with the temperature differences at both ends, thus $\Delta T_A = \Theta_A - T_A$ and $\Delta T_B = \Theta_B - T_B$. It is important to note that the present LMTD results by assuming a constant heat transfer coefficient $\alpha_t = \text{const.}$ in contrast to the LMTD in the duct (2.31) following from a constant wall temperature.

$$\phi_m := \frac{\dot{m}d}{\rho D \Delta C}. \quad (2.32b)$$

It is essential that the employed driving potentials represent some outer (characteristic), constant temperature or concentration difference. These definitions allow an easy conversion between non-dimensional and dimensional flux densities. However, the non-dimensional flux densities (2.32) are to distinguish from Nu and Sh representing non-dimensional transfer coefficients, i.e. (2.32) do no longer represent a conductance for the respective flux densities (Shah & London, 1978). From the given definitions we find the non-dimensional relations

$$\phi_q = \text{Nu} \Delta T_x, \quad (2.33a)$$

$$\phi_m = \text{Sh} \Delta C_x. \quad (2.33b)$$

2.6.5. Thermal entrance length

A quantity that is used further below is the non-dimensional thermal entrance length L_{th} , which is commonly defined as the length where the local Nusselt number Nu reaches 1.05 times the Nusselt number of the fully developed state. Values for L_{th} can be found in Shah & London (1978) for several laminar flow configurations in ducts and are given in terms of the hydraulic diameter d^* and the Péclet number Pe, i.e.

$$L_{\text{th}} = \frac{1}{\text{Pe}} \frac{L_{\text{th}}^*}{d^*}. \quad (2.34)$$

For the hydrodynamically developed plane channel flow Shah & London (1978) present the thermal entrance length as $L_{\text{th}} \approx 0.008 \dots 0.01$ depending on the boundary condition.

3. Governing equations

This chapter presents a detailed derivation of the governing equations and boundary conditions for momentum, heat and species transport, an extensive discussion of the most important physical effects and their relevance in the considered system. We further present a discussion of several coupling effects to justify a one-way coupled formulation of the problem. One-way coupled means that the scalar quantities (temperature and concentration) do not influence the flow field but the flow field influences the scalar transport by convection.

3.1. Bulk equations

3.1.1. Momentum equations

Since we have concluded that the BL-equations might not be a good choice for our purpose, we employ the (two-dimensional) incompressible Navier–Stokes-equations

$$\rho(\partial_t + \mathbf{u} \cdot \nabla)\mathbf{u} = \nabla \cdot \mathbf{S} + \rho\mathbf{g}, \quad (3.1a)$$

$$\nabla \cdot \mathbf{u} = 0 \quad (3.1b)$$

with the fluid velocity $\mathbf{u} = ue_x + ve_y$, the fluid density ρ , the gravitational acceleration \mathbf{g} and the stress tensor

$$\mathbf{S} = -P\mathbf{1} + \boldsymbol{\tau} = -P\mathbf{1} + \bar{\eta}(\nabla\mathbf{u} + (\nabla\mathbf{u})^T) \quad (3.2)$$

that holds true for an incompressible flow of a Newtonian fluid. Here, P stands for the pressure, $\mathbf{1}$ for the unity matrix, $\boldsymbol{\tau}$ for the viscous part of the stress tensor and $\bar{\eta}$ for the dynamic viscosity.

For the present non-isothermal flow, we may investigate the relevance of the Boussinesq approximation. We therefore assume thermally and solutally induced density variations by including the first order terms of the Taylor series approximation

$$\rho(T, P_0, C) \approx \rho_0[1 - \beta_T(T - T_0) - \beta_C(C - C_0)] \quad (3.3)$$

into the Navier–Stokes equations. Here we have introduced a reference state (T_0, P_0, C_0) ,

the corresponding reference density $\rho_0 := \rho(T_0, P_0, C_0)$ and the thermal and solutal expansion coefficients

$$\beta_T := -\frac{1}{\rho} \left(\frac{\partial \rho}{\partial T} \right)_{P,C}, \quad (3.4a)$$

$$\beta_C := -\frac{1}{\rho} \left(\frac{\partial \rho}{\partial C} \right)_{T,P}. \quad (3.4b)$$

Comparing the Boussinesq terms with the convective term yields

$$\frac{g_x \beta_S \Delta S y_0}{u_0^2} = \frac{g_x \beta_S \Delta S y_0^3}{\nu^2} \frac{1}{\text{Re}^2} = \frac{\text{Gr}_S}{\text{Re}^2} \quad (3.5)$$

with the Grashof numbers Gr_S . For convenience we have introduced the subscript S , standing for T and C , respectively. By employing the Nusselt film thickness $y_0^3 = 3\text{Re} \nu^2 / g_x$ one finds $\text{Gr}_S = 3\text{Re} \beta_S \Delta S$. Below we will introduce the concentration coefficient γ connecting the scales as $\Delta C = \gamma \Delta T$ so that (3.5) becomes

$$\frac{\text{Gr}_T}{\text{Re}^2} \propto \beta_T \frac{\Delta T}{\text{Re}} \quad , \quad \frac{\text{Gr}_C}{\text{Re}^2} \propto \gamma \beta_C \frac{\Delta T}{\text{Re}}. \quad (3.6)$$

The values for β_S and γ can be extracted numerically from the Gibbs energy equation of state and are shown in Appendix A.2 to be $\beta_T \approx 4 \times 10^{-4} \text{K}^{-1}$, $\beta_C \approx -1$ and $\gamma \approx 5 \times 10^{-3} \text{K}^{-1}$. Therefrom, we conclude that the solutally induced body force is one order of magnitude larger than its thermal counterpart. However, as long as $\Delta T / \text{Re}$ is sufficiently small, we may safely conclude that buoyancy has no relevance for the present system.

3.1.2. Species and energy transport in a binary mixture

Since there are many ways to define a concentration measure, we shall firstly present a detailed derivation of the species transport equation to introduce all important termini. In a certain volume of the binary mixture (solution) V one finds the mass m of the solution and the mass m_α of its components (constituents) $\alpha = 1, 2$. The mass concentration is then defined as $\rho_\alpha := m_\alpha / V$ and the mass conservation for every component reads

$$\partial_t \rho_\alpha + \nabla \cdot (\rho_\alpha \mathbf{u}_\alpha) = 0 \quad , \quad \alpha = 1, 2 \quad (3.7)$$

where \mathbf{u}_α is the velocity field of the corresponding constituent. The density of the solution trivially derives as $\rho = \rho_1 + \rho_2$ and the (barycentric) fluid velocity of the solution \mathbf{u} derives from $\rho \mathbf{u} = \rho_1 \mathbf{u}_1 + \rho_2 \mathbf{u}_2$. The total mass balance, the sum of (3.7) over α , certainly brings us to the continuity equation of the solution $\partial_t \rho + \nabla \cdot (\rho \mathbf{u}) = 0$.

The mass fraction is defined as

$$C_\alpha := \frac{\rho_\alpha}{\rho} = \frac{m_\alpha}{m} \quad , \quad [C_\alpha] = 1 = 100 \text{ wt\%} \quad (3.8)$$

and frequently labeled with the unit wt% (percentage by weight). With $\rho_\alpha = \rho C_\alpha$ and the fluid velocity \mathbf{u} we rewrite (3.7) to

$$\partial_t(\rho C_\alpha) + \nabla \cdot (\rho C_\alpha \mathbf{u}) = -\nabla \cdot (\rho_\alpha (\mathbf{u}_\alpha - \mathbf{u})) = -\nabla \cdot \mathbf{i}_\alpha. \quad (3.9)$$

The term $\mathbf{i}_\alpha = \rho_\alpha (\mathbf{u}_\alpha - \mathbf{u})$ represents the diffusive species flux density. With the continuity equation of the solution, the material derivative $D/Dt := D_t = \partial_t + \mathbf{u} \cdot \nabla$ and by defining $C := C_1$ and $\mathbf{i} := \mathbf{i}_1$ the species transport equation becomes

$$\rho \frac{DC}{Dt} = -\nabla \cdot \mathbf{i}. \quad (3.10)$$

For the discussion of the energy transport in a binary mixture we start from the first law of thermodynamics

$$\rho \left(\frac{De}{Dt} - \frac{P}{\rho^2} \frac{D\rho}{Dt} \right) = \Phi - \nabla \cdot \dot{\mathbf{q}} \quad (3.11)$$

with the specific internal energy e , the pressure P , the dissipation function $\Phi = \tau_{ij} \partial_i u_j$ and the heat flux density $\dot{\mathbf{q}}$. The following demonstration is strongly orientated to the derivation shown in [Landau & Lifshitz \(1987\)](#).

We use the fundamental thermodynamic relation $dE = TdS - PdV + \sum_\alpha \mu_\alpha dN_\alpha$ with the internal energy E , the entropy S , the volume V , the chemical potential μ_α and the number of particles N_α . Dividing by the mass of the solution m yields the relation for the specific values, thus

$$de = Tds + \frac{P}{\rho^2} d\rho + N_A \sum_\alpha \frac{\mu_\alpha}{M_\alpha} dC_\alpha \quad (3.12)$$

where we have introduced the molar mass M_α , the Avogadro constant N_A and made use of

$$m_\alpha = M_\alpha n_\alpha = M_\alpha \frac{N_\alpha}{N_A} = m C_\alpha \quad \implies \quad \frac{dN_\alpha}{m} = \frac{N_A}{M_\alpha} dC_\alpha$$

introducing the amount of constituent n_α . Since we assume a binary mixture we employ $C_2 = 1 - C_1$ and define the chemical potential of the solution μ again with $C := C_1$, thus

$$N_A \sum_{\alpha=1}^2 \frac{\mu_\alpha}{M_\alpha} dC_\alpha = N_A \left(\frac{\mu_1}{M_1} - \frac{\mu_2}{M_2} \right) dC_1 := \mu dC. \quad (3.13)$$

We now rewrite the first law of thermodynamics (3.11) as $\rho(TD_t s + \mu D_t C) = \Phi - \nabla \cdot \dot{\mathbf{q}}$, replace the material derivative of the mass fraction $\rho D_t C$ by using (3.10) and find

$$\rho T \frac{Ds}{Dt} = \Phi - \nabla \cdot \dot{\mathbf{q}} + \mu \nabla \cdot \mathbf{i}. \quad (3.14)$$

The diffusive flux densities are presented by Landau & Lifshitz (1987) as

$$\mathbf{i} = -\rho D \left[\nabla C + \frac{k_T}{T} \nabla T + \frac{k_P}{P} \nabla P \right], \quad (3.15a)$$

$$\dot{\mathbf{q}} = -\lambda \nabla T + \left[k_T \left(\frac{\partial \mu}{\partial C} \right)_{T,P} \right] \mathbf{i} + \left[\mu - T \left(\frac{\partial \mu}{\partial T} \right)_{P,C} \right] \mathbf{i}. \quad (3.15b)$$

The fraction of the species flux density \mathbf{i} which is driven by the concentration gradient represents *ordinary diffusion*, while those parts that are driven by the temperature and pressure gradients are called thermodiffusion and barodiffusion, respectively. Thermodiffusion is also known as the Soret effect. The associated non-dimensional coefficients are the thermal diffusion ratio (Soret coefficient) k_T and the ratio for barodiffusion k_P . As mentioned in Landau & Lifshitz (1987), barodiffusion is only of relevance for systems with large pressure gradients and can be dropped for the present problem.

The heat flux density $\dot{\mathbf{q}}$ is also composed by three parts and the first term is easily identified as thermal conduction. The second term refers to inverse thermodiffusion, also known as the Dufour effect. The third part accounts for the energy transport induced by species diffusion and is referred to as interdiffusion by Grossman (1987). We shall rewrite the interdiffusion term by defining the specific enthalpy of the solution $h_s := H_s/m$ and insert the relation for the Gibbs energy $G = \sum_{\alpha} \mu_{\alpha} N_{\alpha}$ into the Gibbs–Helmholtz equation $H_s = G - T(\partial G/\partial T)_{P,C}$, thus

$$h_s := \frac{H_s}{m} = \sum_{\alpha} \frac{N_{\alpha}}{m} \left[\mu_{\alpha} - T \left(\frac{\partial \mu_{\alpha}}{\partial T} \right)_{P,C} \right]. \quad (3.16)$$

By using $h_s = \sum_{\alpha} C_{\alpha} h_{\alpha}$, with the specific enthalpy of the constituents $h_{\alpha} = H_{\alpha}/m_{\alpha}$, we can easily identify h_{α} from (3.16) as

$$h_{\alpha} = \frac{N_{\alpha}}{M_{\alpha}} \left[\mu_{\alpha} - T \left(\frac{\partial \mu_{\alpha}}{\partial T} \right)_{P,C} \right]. \quad (3.17)$$

By using the definition (3.13) for μ and (3.17), the interdiffusion term finally becomes

$$\left[\mu - T \left(\frac{\partial \mu}{\partial T} \right)_{P,C} \right] \mathbf{i} = \sum_{\alpha=1}^2 \frac{N_{\alpha}}{M_{\alpha}} \left[\mu_{\alpha} - T \left(\frac{\partial \mu_{\alpha}}{\partial T} \right)_{P,C} \right] \mathbf{i}_{\alpha} = \sum_{\alpha=1}^2 h_{\alpha} \mathbf{i}_{\alpha}. \quad (3.18)$$

From there it is obvious that the interdiffusion term (3.18) represents the enthalpy flux which is caused by the species flux, thus $(h_1 - h_2)\mathbf{i}$, so that

$$\left[\mu - T \left(\frac{\partial \mu}{\partial T} \right)_{P,C} \right] = h_1 - h_2. \quad (3.19)$$

To reorder the energy equation further we expand the specific entropy

$$ds = \left(\frac{\partial s}{\partial T} \right)_{P,C} dT + \left(\frac{\partial s}{\partial P} \right)_{T,C} dP + \left(\frac{\partial s}{\partial C} \right)_{T,P} dC$$

and employ the relations

$$\begin{aligned} \left(\frac{\partial s}{\partial T} \right)_{P,C} &= \frac{c_p}{T}, \\ \left(\frac{\partial s}{\partial P} \right)_{T,C} &= - \left(\frac{\partial \rho^{-1}}{\partial T} \right)_{P,C} = \frac{1}{\rho^2} \left(\frac{\partial \rho}{\partial T} \right)_{P,C} = -\frac{1}{\rho} \beta_T, \\ \left(\frac{\partial s}{\partial C} \right)_{T,P} &= - \left(\frac{\partial \mu}{\partial T} \right)_{P,C}, \end{aligned}$$

with the thermal expansion coefficient β_T from (3.4a). The substitution of all terms yields

$$\rho T \frac{Ds}{Dt} = \rho c_p \frac{DT}{Dt} - \beta_T T \frac{DP}{Dt} + (\nabla \cdot \mathbf{i}) T \left(\frac{\partial \mu}{\partial T} \right)_{P,C}. \quad (3.20)$$

We now use (3.20) and (3.15) in (3.14) and obtain

$$\rho c_p \frac{DT}{Dt} - \beta_T T \frac{DP}{Dt} = \Phi + \nabla \cdot (\lambda \nabla T) - \nabla \cdot \left[k_T \left(\frac{\partial \mu}{\partial C} \right)_{T,P} \mathbf{i} \right] - \mathbf{i} \cdot \nabla (h_1 - h_2). \quad (3.21)$$

So far, almost no simplifications have been made and we shall now identify those terms showing only negligible effects. Firstly, we presume that T and C vary only little within the domain, such that we can understand λ and D to be constant. The assumed small impact of varying thermophysical properties is strongly supported by the findings of Mittermaier *et al.* (2014).

The comparison of the viscous dissipation term Φ with the diffusion term $\lambda \nabla^2 T$ returns the Brinkmann number $\text{Br} = \bar{\eta} u_0^2 / (\lambda \Delta T)$ which is very small, so that dissipation can be dropped as expected.

By using the pressure scale $\Delta P = \rho u_0^2$ and by approximating T with a characteristic mean temperature T_0 , thus $T \approx T_0$, the ratio of the material derivative terms becomes proportional to $\beta_T T_0 \text{Ec}$. Here we have introduced the Eckert number $\text{Ec} = u_0^2 / (c_p \Delta T)$ which is related to the Brinkmann number by the Prandtl number $\text{Pr} = \nu / a$, with a being

the thermal diffusivity $a = \lambda/(\rho c_p)$, as $Ec = Br/Pr$. Since $Ec < Br \ll 1$ and $\beta_T T_0 \ll 1$ we conclude that the pressure transport term can be neglected without concern.

The last term in (3.21) accounts for interdiffusion and its significance in film absorption was discussed by Grossman (1987). Even if his approximation $h_s \approx c_p(T - T_0)$ results in a relatively large error for LiBr–H₂O (see Figure A.1 in Appendix A.2) we follow his arguments, assume $\mathbf{i} = -\rho D \nabla C$ for a moment, employ $h_s = C h_1 + (1 - C) h_2$ to approximate $\partial h_s / \partial C \approx h_1 - h_2$ and find

$$-\mathbf{i} \cdot \nabla (h_1 - h_2) \approx \rho D (\nabla C) \cdot (\nabla T) \left(\frac{\partial c_p}{\partial C} \right)_{T,P}. \quad (3.22)$$

By employing the scales for length, temperature and concentration x_0 , ΔT and ΔC , the non-dimensionalized diffusion terms become

$$\frac{a \Delta T}{x_0^2} \left[\nabla^2 T + \frac{Z}{Le} (\nabla C) \cdot (\nabla T) \right] \quad (3.23)$$

where we have introduced the Lewis number $Le = a/D$ and the interdiffusion parameter

$$Z = \frac{\Delta C}{c_p} \left(\frac{\partial c_p}{\partial C} \right)_{T,P}. \quad (3.24)$$

Again, by exploiting the Gibbs equation of state for LiBr–H₂O, we can easily evaluate the interdiffusion parameter and find $Z \approx -2\Delta C$, as shown in Figure A.1. From there, with $\Delta C < 1$, the interdiffusion term becomes negligible compared to thermal diffusion since the terms are related by Le^{-1} where the Lewis number for LiBr–H₂O is typically $Le \approx 10^2$.

Finally, only the terms accounting for Soret and Dufour effect remain. Generally, for small concentrations one finds that $k_T \rightarrow 0$ and both effects can be neglected. However, for the present problem this is in general not true, since the mass fraction of LiBr in H₂O is typically $C \approx 50$ wt%. Even if we do not have any knowledge about the Soret coefficient for LiBr–H₂O, Elperin & Fominykh (2008) gives us the hint that the error in the absorbed mass flux made by neglecting thermodiffusion is 0.1% for LiBr–H₂O. We finally assume that the Dufour effect is again smaller than the Soret effect and dropping both seems to be a defensible assumption. Finally, since most physical effects turned out to be of no relevance for the present problem, we end up at the well established equations for heat and species transport

$$\rho c_p \frac{DT}{Dt} = \lambda \nabla^2 T, \quad (3.25a)$$

$$\rho \frac{DC}{Dt} = \rho D \nabla^2 C. \quad (3.25b)$$

3.1.3. Standard transport equation

The considerations above allow us to present the dimensional governing equations in form of the standard transport equation for the quantity ψ

$$\frac{d}{dt} \int_V \rho \psi \, dV + \oint_O \rho \phi \psi \, dO = - \oint_O \hat{\mathbf{n}} \cdot \mathbf{j} \, dO + \int_V \rho q \, dV \quad (3.26)$$

with the control volume V and its boundary $O = \partial V$, the fluid density ρ , the relative volume flux density ϕ , the diffusive flux density \mathbf{j} and the source density q that are associated with the transport quantity ψ . Further, we have introduced the unit normal vector $\hat{\mathbf{n}}$ (the hat indicates normalization) on O , thus

$$\hat{\mathbf{n}} = \frac{1}{n} \begin{pmatrix} -\partial_x h \\ 1 \end{pmatrix} \quad \text{with} \quad n := \sqrt{1 + (\partial_x h)^2}. \quad (3.27)$$

The integral version of the transport equation is necessary since we are dealing with a free-surface flow where the control volume V or its boundary O moves itself. Therefrom, one has to account for the volume flux created by the movement of O by employing the relative volume flux density

$$\phi = \hat{\mathbf{n}} \cdot (\mathbf{u} - \mathbf{w}) \quad (3.28)$$

with the fluid velocity \mathbf{u} and the boundary velocity \mathbf{w} . The (volume) flux that is generated through the boundary velocity \mathbf{w} is related to the temporal change of the control volume by the space conservation law (Ferziger & Perić, 2002)

$$\frac{d}{dt} \int dV = \oint \hat{\mathbf{n}} \cdot \mathbf{w} \, dO. \quad (3.29)$$

In case of the liquid film, the boundary velocity \mathbf{w} is simply the temporal change of the free-surface position $h = h(x, t)$, thus

$$\mathbf{w} = \partial_t h \mathbf{e}_y := \dot{h} \mathbf{e}_y \quad (3.30)$$

being consistent with the space conservation law (3.29) since one can easily verify that

$$\frac{d}{dt} \int dV = \int \dot{h} \, dx. \quad (3.31)$$

All quantities needed for the present model are deduced from (3.1) and (3.25), summarized in Table 3.1.

Table 3.1.: Transport quantity ψ with associated diffusive flux density \mathbf{j} and source density q that are used in the standard transport equation (3.26) to formulate the conservation laws.

	ψ	\mathbf{j}	q
mass	1	$\mathbf{0}$	0
momentum	\mathbf{u}	$-\mathbf{S}$	\mathbf{g}
energy	$c_p T$	$-\lambda \nabla T$	0
species	C	$-\rho D \nabla C$	0

The final bulk equations are obtained by using the standard transport equation (3.26) with the quantities from Table 3.1, hence

$$\frac{d}{dt} \int \mathbf{u} dV + \oint \hat{\mathbf{n}} \cdot (\mathbf{u} - \mathbf{w}) \mathbf{u} dO = -\frac{1}{\rho} \oint \hat{\mathbf{n}} P dO + \nu \oint \hat{\mathbf{n}} \cdot \nabla \mathbf{u} dO + \int \mathbf{g} dV \quad (3.32a)$$

$$\oint \hat{\mathbf{n}} \cdot \mathbf{u} dO = 0 \quad (3.32b)$$

$$\frac{d}{dt} \int T dV + \oint \hat{\mathbf{n}} \cdot (\mathbf{u} - \mathbf{w}) T dO = a \oint \hat{\mathbf{n}} \cdot \nabla T dO \quad (3.32c)$$

$$\frac{d}{dt} \int C dV + \oint \hat{\mathbf{n}} \cdot (\mathbf{u} - \mathbf{w}) C dO = D \oint \hat{\mathbf{n}} \cdot \nabla C dO \quad (3.32d)$$

where dividing by ρ and ρc_p , respectively, results in the kinematic viscosity $\nu = \bar{\eta}/\rho$ and the thermal diffusivity a . The *original* continuity equation

$$\frac{d}{dt} \int dV + \oint \hat{\mathbf{n}} \cdot (\mathbf{u} - \mathbf{w}) dO = 0 \quad (3.33)$$

was reduced by using the space conservation law (3.29) to become (3.32b).

3.2. Boundary conditions

From the standard transport equation one can derive a very powerful formulation to deduce the corresponding boundary conditions. The jump condition, also known as Katchine's theorem (Truesdell & Toupin, 1960), reads

$$\hat{\mathbf{n}} \cdot \llbracket -\mathbf{j} \rrbracket = \llbracket \phi \rho \psi \rrbracket. \quad (3.34)$$

As convention for the jump at the free-surface we define $\llbracket X \rrbracket := X' - X''$ where the prime refers to the liquid phase and the double prime to the gaseous phase.

3.2.1. Mass flux jump

Applying the quantities from Table 3.1 regarding mass conservation to the jump condition (3.34) yields at the free-surface $[[\phi\rho]] = \phi'\rho' - \phi''\rho''$ and by inserting (3.28)

$$\dot{m} := \hat{\mathbf{n}} \cdot (\mathbf{u}' - \mathbf{w})\rho' = \hat{\mathbf{n}} \cdot (\mathbf{u}'' - \mathbf{w})\rho'' \quad (3.35)$$

with the mass flux density due to absorption \dot{m} . Since the mass flux jump must vanish, thus $[[\phi\rho]] = [[\dot{m}]] = 0$, the general jump condition (3.34) can be rewritten as

$$\hat{\mathbf{n}} \cdot [[-\mathbf{j}]] = \dot{m}[[\psi]]. \quad (3.36)$$

By introducing the relative normal velocity $u_{r,n} := \hat{\mathbf{n}} \cdot (\mathbf{u} - \mathbf{w})$ we conclude from (3.35)

$$\frac{u'_{r,n}}{u''_{r,n}} = \frac{\rho''}{\rho'} := \varrho \ll 1. \quad (3.37)$$

For a system pressure of $P_0 \approx 1$ kPa one finds $\rho'' \approx 10^{-2}$ kg/m³ for H₂O and $\rho' \approx 10^3$ kg/m³ for LiBr–H₂O giving a typical density ratio of $\varrho \approx 10^{-5}$.

Kinematic condition The kinematic boundary condition is deduced from (3.35) and by using the boundary velocity $\mathbf{w} = \dot{h}\mathbf{e}_y$, thus

$$\dot{m} = \frac{\rho'}{n} \begin{pmatrix} -\partial_x h \\ 1 \end{pmatrix} \cdot \begin{pmatrix} u' \\ v' - \dot{h} \end{pmatrix}$$

so that the kinematic condition becomes

$$-\frac{\dot{m}n}{\rho'} = \dot{h} + u'\partial_x h - v'. \quad (3.38)$$

3.2.2. Momentum jump

The dynamic boundary conditions at the free-surface derive from the jump condition (3.36) for momentum (see Table 3.1), hence $\hat{\mathbf{n}} \cdot [[-P\mathbf{1} + \boldsymbol{\tau}]] = \dot{m}[[\mathbf{u}]]$. In addition one has to account for the Laplace-pressure $\sigma\kappa\hat{\mathbf{n}}$ with the surface tension σ and the curvature of the free-surface

$$\kappa = -\nabla \cdot \hat{\mathbf{n}} = \frac{\partial_{xx}h}{(1 + (\partial_x h)^2)^{3/2}} = \frac{\partial_{xx}h}{n^3}. \quad (3.39)$$

As the surface tension depends in general on temperature and concentration, $\sigma = \sigma(T, C)$, there is also the term resulting from the Marangoni-force $\nabla_s \sigma$ with the tangential deriva-

tive at the free-surface $\nabla_s = (\mathbf{1} - \hat{\mathbf{n}}\hat{\mathbf{n}}) \cdot \nabla$. This leads to the complete stress balance

$$\hat{\mathbf{n}} \cdot \llbracket -P\mathbf{1} + \boldsymbol{\tau} \rrbracket = \dot{m} \llbracket \mathbf{u} \rrbracket + \sigma \kappa \hat{\mathbf{n}} + \nabla_s \sigma. \quad (3.40)$$

As we assume no-slip at the free-surface, the velocity jump affects the normal velocity component only such that $\llbracket \mathbf{u} \rrbracket = \hat{\mathbf{n}} \cdot \llbracket \mathbf{u} \rrbracket \hat{\mathbf{n}}$. Since the inclusion of the boundary velocity \mathbf{w} does not affect the jump condition, i.e. $\llbracket \mathbf{u} \rrbracket = \llbracket \mathbf{u} - \mathbf{w} \rrbracket$ we find $\llbracket \mathbf{u} \rrbracket = \hat{\mathbf{n}} \cdot \llbracket \mathbf{u} - \mathbf{w} \rrbracket \hat{\mathbf{n}} = (u'_{r,n} - u''_{r,n}) \hat{\mathbf{n}}$ and, therefore,

$$\dot{m} \llbracket \mathbf{u} \rrbracket = \dot{m} (u'_{r,n} - u''_{r,n}) \hat{\mathbf{n}} = -\dot{m} u''_{r,n} (1 - \varrho) \hat{\mathbf{n}} \approx -\frac{\dot{m}^2}{\rho''} \hat{\mathbf{n}} \quad (3.41)$$

where we have exploited $\varrho \ll 1$ and (3.35). This pressure, which is induced by the phase change, is known as the vapor thrust (Oron *et al.*, 1997).

Dynamic conditions As long as the system pressure P_0 is low, we can neglect the shear stress from the ambient gas and assume a constant gas pressure P_0 . The normal and tangential stress balances are obtained from a projection of (3.40) onto the unit normal vector $\hat{\mathbf{n}}$ and the unit tangential vector $\hat{\mathbf{t}} = n^{-1}(1, \partial_x h)^\top$, thus

$$P_0 - P + \hat{\mathbf{n}} \cdot \boldsymbol{\tau} \cdot \hat{\mathbf{n}} = -\frac{\dot{m}^2}{\rho''} + \sigma \kappa, \quad (3.42a)$$

$$\hat{\mathbf{n}} \cdot \boldsymbol{\tau} \cdot \hat{\mathbf{t}} = \hat{\mathbf{t}} \cdot \nabla \sigma. \quad (3.42b)$$

3.2.3. Scalar fields – Jump conditions

From the Navier–Stokes equations we have already deduced that $\llbracket \dot{m} \rrbracket = 0$. For all species we need in addition $\llbracket \dot{m}_\alpha \rrbracket = 0$. Since the absorbent ($\alpha = 1$) is non-volatile and the gas ($\alpha = 3$) non-absorbable, we find $\dot{m}_1 = \dot{m}_3 = 0$ and therefore $\dot{m} = \dot{m}_2$, stating that the mass flux through the free-surface consists of the refrigerant only.

Species flux The absorbed mass flux density \dot{m} can be readily found from the species jump conditions $\hat{\mathbf{n}} \cdot \llbracket -\mathbf{i}_\alpha \rrbracket = \llbracket -i_\alpha \rrbracket = \dot{m} \llbracket C_\alpha \rrbracket$ by using in addition the species flux densities of the binary liquid mixture $i'_1 + i'_2 = 0$, the species flux densities of the binary gaseous mixture $i''_2 + i''_3 = 0$ and the relations from Table 2.1, thus

$$\begin{aligned} \dot{m} &= -\frac{\llbracket i_1 \rrbracket}{\llbracket C_1 \rrbracket} = -\frac{i'_1}{C'_1} = \frac{i'_2}{1 - C'_2} \\ \dot{m} &= -\frac{\llbracket i_3 \rrbracket}{\llbracket C_3 \rrbracket} = -\frac{i''_3}{C''_3} = \frac{i''_2}{1 - C''_2} \end{aligned}$$

We identify $i_2 = -\rho D \partial_n C_2$ and find the Eckert–Schneider condition for unidirectional (single-sided) diffusion (Schlichting & Gersten, 1997)

$$\dot{m} = -\frac{(\rho D \partial_n C_2)'}{1 - C_2'} = -\frac{(\rho D \partial_n C_2)''}{1 - C_2''}. \quad (3.43)$$

Heat flux From a straightforward use of (3.36) together with the corresponding quantities of Table 3.1 the heat flux balance at the free-surface becomes $[[\lambda \partial_n T]] = \dot{m} [[c_p T]]$. This is not true since the phase change also contributes to the balance by the release of the enthalpy of evaporation. To account for the phase change we rewrite

$$[[c_p T]] \rightarrow h' - h'' := -\Delta h \quad (3.44)$$

where we have introduced the enthalpy of absorption Δh . Together with the mass flux density from (3.43) the heat flux condition finally reads

$$(\lambda \partial_n T)' - (\lambda \partial_n T)'' = -\Delta h \dot{m} = \Delta h \frac{(\rho D \partial_n C_2)'}{1 - C_2'}. \quad (3.45)$$

3.2.4. Scalar fields – Equilibrium conditions

Thermal equilibrium The local thermodynamic equilibrium condition requires a vanishing jump in the temperature, thus $[[T]] = 0$ and therefore

$$T' = T''. \quad (3.46)$$

Vapor pressure equilibrium For local thermodynamic equilibrium we assume that the partial pressure of the vapor within the gas phase P_2'' equals its vapor pressure within the liquid mixture P_2' , hence

$$P_2' = P_2''. \quad (3.47)$$

The refrigerant’s vapor pressure within the mixture P_2' is in general a function of the mixture temperature T' and the refrigerant concentration C_2' and must be given with the particular working pair.

We now deduce the relation between the partial pressure of the vapor P_2'' and its concentration within the gas phase C_2'' . We therefore use the definition of the mass fraction (concentration) for the vapor within the gaseous phase, thus

$$C_2'' = \frac{\rho_2''}{\rho_2'' + \rho_3''} \quad , \quad [C_2''] = \frac{\text{kg refrigerant}}{\text{kg gaseous phase}}.$$

As we assume both to be ideal gases, we use $PV = nRT$, $m = nM = \rho V$ with the amount of substance n , the gas constant R and therefrom $\rho_x RT = M_x P_x$ such that the densities satisfy

$$\rho_2'' = M_2 \frac{P_2''}{RT} \quad , \quad \rho_3'' = M_3 \frac{P_3''}{RT} = M_3 \frac{P_0 - P_2''}{RT}$$

where we have included the constant system pressure P_0 which is the sum of the partial pressure of the vapor P_2'' and the partial pressure of the gas P_3'' , thus $P_0 = P_2'' + P_3''$. The refrigerant concentration within the gas phase C_2'' finally becomes

$$C_2'' = \frac{\alpha_m P_2'}{P_0 - (1 - \alpha_m) P_2'} \quad \text{with} \quad P_2' = P_2'(T', C_2') \quad (3.48)$$

where we have introduced the molar mass ratio $\alpha_m := M_2/M_3$.¹

3.2.5. Coupling effects and summary for the free-surface

Even if the coupling effects within the bulk turned out to be of minor importance for the present system, the impact of the coupling effects at the free-surface is more delicate. The Marangoni effects influence the fluid dynamics already for the non-absorbing case whereas the absorption process gives rise to the source term in the kinematic condition and the vapor thrust in the dynamic condition. The source term $\propto \dot{m}$ in (3.38) accounts for the increase of the film thickness and since we assume only small absorption rates we can also expect that neglecting the increase of the film thickness is a reasonable approximation. The same argument applies to the vapor thrust which will be also neglected.

The remaining Marangoni effects do have a significant influence to the stability of the film (Kalliadasis *et al.*, 2012). However, it is worthwhile to aim for an one-way coupled formulation since it reduces the numerical effort drastically and, even more important, it opens the possibility to alternative approaches to solve the problem.

Therefore, we neglect all mentioned boundary coupling effects so that the free-surface boundary conditions for the Navier–Stokes equations, given by (3.38) and (3.42), finally reduce to

$$\dot{h} + u \partial_x h - v = 0, \quad (3.49a)$$

$$P - P_0 = \hat{\mathbf{n}} \cdot \boldsymbol{\tau} \cdot \hat{\mathbf{n}} - \sigma \kappa, \quad (3.49b)$$

$$\hat{\mathbf{n}} \cdot \boldsymbol{\tau} \cdot \hat{\mathbf{t}} = 0. \quad (3.49c)$$

¹For humid air, for instance, one finds the well known value $\alpha_m = 18.02/28.95 \approx 0.6225$.

For the coupled heat and mass transfer the set of boundary conditions is composed of the two equilibrium conditions (3.46), (3.48) and the two flux conditions (3.43), (3.45), hence

$$T' = T'', \quad (3.50a)$$

$$C_2'' = \frac{\alpha_m P_2'}{P_0 - (1 - \alpha_m) P_2'} \quad \text{with} \quad P_2' = P_2'(T', C_2'), \quad (3.50b)$$

$$\frac{(\rho D \partial_n C_2)'}{1 - C_2'} = \frac{(\rho D \partial_n C_2)''}{1 - C_2''}, \quad (3.50c)$$

$$(\lambda \partial_n T)' - (\lambda \partial_n T)'' = \Delta h \frac{(\rho D \partial_n C_2)'}{1 - C_2'}. \quad (3.50d)$$

The relation for the vapor pressure $P_2' = P_2'(T', C_2')$ must be given with the particular working pair. The inlet, outlet and wall boundary conditions need further attention and will be discussed below since they are subject to the solution strategy.

Literature does not fully agree with the presented boundary conditions for the coupled heat and mass transfer which is briefly demonstrated in the following.

1. As already mentioned by Killion & Garimella (2001), some authors ignore the Eckert–Schneider condition for unidirectional diffusion, see for instance (Bo *et al.*, 2010; Kim & Ferreira, 2009; Yang & Jou, 1998; Yoon *et al.*, 2005).
2. Most authors employ vapor pressure equilibrium but do not provide an explicit relation for the vapor pressure.
3. Dai & Zhang (2004) include additional (differential) terms in their flux conditions which are not explained in their paper.
4. Besides ignoring unidirectional diffusion, Yang & Jou (1998) also ignore ρD in their species flux condition.

4. The isothermal wavy film

From the dimensional equations, the given scaling (2.10) including the scales from the Nusselt film (2.7) we are now able to formulate the non-dimensional set of governing equations for the fluid dynamical problem

$$\frac{d}{dt} \int \mathbf{u} dV + \oint \hat{\mathbf{n}} \cdot (\mathbf{u} - \mathbf{w}) \mathbf{u} dO = - \oint \hat{\mathbf{n}} P dO + \frac{1}{\text{Re}} \oint \hat{\mathbf{n}} \cdot \nabla \mathbf{u} dO + \frac{3G}{\text{Re}} \int dV \quad (4.1a)$$

$$\oint \hat{\mathbf{n}} \cdot \mathbf{u} dO = 0 \quad (4.1b)$$

$$\dot{h} + u \partial_x h - v = 0 \quad (4.1c)$$

$$P - P_0 = \text{Re}^{-1} \hat{\mathbf{n}} \cdot \boldsymbol{\tau} \cdot \hat{\mathbf{n}} - \text{We} \kappa \quad (4.1d)$$

$$\hat{\mathbf{n}} \cdot \boldsymbol{\tau} \cdot \hat{\mathbf{t}} = 0 \quad (4.1e)$$

which are the incompressible Navier–Stokes equations (neglecting buoyancy), the kinematic boundary condition (neglecting the mass flux density due to absorption), the normal stress balance at the free-surface (neglecting the vapor thrust) and the tangential stress balance at the free-surface (neglecting Marangoni effects). In the momentum equations we have introduced the modified gravity vector

$$\mathbf{G} := \frac{\hat{\mathbf{g}}}{\sin \theta} = \mathbf{e}_x - \cot \theta \mathbf{e}_y. \quad (4.2)$$

The boundary velocity \mathbf{w} is discussed in the next section. By introducing the aspect ratio of the domain

$$\varepsilon_0 = \frac{h_{\text{Nu}}}{L_0} \quad (4.3)$$

the present fluid mechanical problem is defined by the four non-dimensional parameters

$$\varepsilon_0, \quad \text{Re}, \quad \text{Ka}, \quad \theta \quad (4.4)$$

where We and Ka are related in (2.14). To reduce the number of free parameters, we restrict ourselves to the vertical plate, i.e. $\theta = \pi/2$ and to a certain Kapitza number representing a particular fluid. With this given set of non-dimensional equations one may think of two strategies to solve the problem.

1. **Laboratory frame:** Solving the equations (4.1) as they are, representing a time-dependent problem within the laboratory frame. All transient phenomena are captured, including spatio-temporal chaos (Liu & Gollub, 1993). However, the free-surface flow calls for elaborate numerical techniques and we want to briefly recapitulate two of the most important ones. We also present qualitative results which had been found by using the open source CFD-toolbox OpenFOAM.

a) **VOF – Volume of fluid method:** This method is very common for two-phase flows, fairly easy to implement and relatively robust. The method operates on an Eulerian grid, which appears to be its major advantage. Since only one Navier–Stokes equation must be solved (one-fluid-approach) it is unavoidable to simulate also some fraction of the secondary (gas) phase. The location of the interface is determined from an advected color function with the drawback of a smeared interface. However, another important advantage of the method is its ability to treat topology changes. Even though VOF works for a wide range of gas-to-fluid density ratios certain limits exist. For the coupled heat and mass transfer one would also have to reformulate the free-surface boundary conditions into bulk terms, as done for the Laplace pressure in the Navier–Stokes equations by Brackbill *et al.* (1992). Figure 4.1 shows a naturally excited isothermal liquid film as a result of a VOF-simulation with the OpenFOAM-solver `interMixingFoam`. The fuzziness of the interface is clearly visible due to the relatively coarse grid. To reduce the thickness of the numerically smeared interface an adaptive mesh refinement would be desirable.

For the present problem we are neither interested in the dynamics of the gas phase nor in topology changes. With our extremely low gas density it is further likely to reach the limitation of the gas-to-fluid density ratio. The large Lewis number also indicates the appearance of a thin concentration boundary layer at the free-surface and a large number of computational cells seem to be necessary to resolve the physics of absorption accurately. Altogether, it is questionable whether the application of the VOF-method is the appropriate choice for the present task.

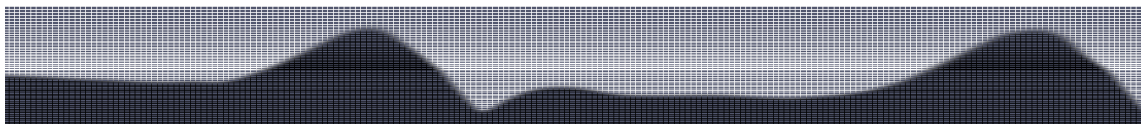


Figure 4.1.: Exemplary result of an isothermal VOF-simulation with `interMixingFoam` from OpenFOAM. Crosswise coordinate is scaled by 5.

c) **ALE – Arbitrary Lagrangian Eulerian method:** This method operates on a mesh, that is continuously adjusted to the boundaries. One can further distinguish between problems with a forced boundary movement and problems with an a priori unknown boundary movement. The latter case is found for almost all free-surface flows and fluid-structure-interaction (FSI) problems. Needless to say, most difficult are those problems where the location of the boundaries are not defined a priori (at the new time step). In transient flows the moving boundaries generate additional fluxes ($\hat{\mathbf{n}} \cdot \mathbf{w}$) that enter into the Navier–Stokes equations, giving a tight coupling between the mesh and the fluid flow. For the present case, the boundary velocity is $\mathbf{w} = \dot{h}\mathbf{e}_y$. Given a structured mesh where the vertical grid lines (normal to the wall) are fixed, the velocity of the horizontal grid lines may be distributed linearly, so that

$$\mathbf{w} \rightarrow \frac{y}{h}\dot{h}\mathbf{e}_y. \quad (4.5)$$

The OpenFOAM extended project provides the ALE-solver `interTrackFoam` (see e.g. [Jasak & Rusche \(2009\)](#)). A particular C++ class to move the structured mesh of the liquid film was provided by [Tuković \(2011\)](#). Figure 4.2 shows the result for an isothermal liquid film where the inlet velocity was perturbed sinusoidally.



Figure 4.2.: Exemplary result of an isothermal ALE-simulation with `interTrackFoam` from OpenFOAM. Crosswise coordinate is scaled by 5, the grayscale indicates the pressure P . The parameters are different from the ones in Figure 4.1.

2. **Moving frame:** For a more systematic investigation it seems to be advantageous to restrict ourselves to traveling wave solutions. This limitation allows us to transform the system into a moving frame of reference where only the stationary equations for one single wavelength have to be solved. This results in an enormous reduction of computational costs.

4.1. Moving frame

Since we are interested in traveling wave solutions only, we assume a moving frame of reference (related quantities are primed if necessary) where the flow is steady. The transformation velocity is the wave celerity $\mathbf{c} = c\mathbf{e}_x$.

4.1.1. Transformation to the moving frame

The transformation to the moving frame is done in the following steps.

1. We account for the control volume moving with \mathbf{c} .
2. Transformation to the moving coordinates $\mathbf{x} = \mathbf{x}' + \mathbf{c}t$.
3. Transformation to the velocities within the moving frame, thus $\mathbf{u} = \mathbf{u}' + \mathbf{c}$.
4. Introduction of additional constraints arising due to the transformation.

Moving control volume Firstly, we account for the moving control volume. We use Reynolds' transport theorem to rewrite the volume integral for any quantity $\psi = \psi(\mathbf{x}, t)$

$$\frac{d}{dt} \int \psi \, dV \equiv \int \partial_t \psi \, dV + \oint \hat{\mathbf{n}} \cdot \mathbf{w} \psi \, dO.$$

The lhs of the transport equation (3.26) can then be rewritten into the equivalent form

$$\frac{d}{dt} \int \psi \, dV + \oint \phi \psi \, dO = \int \partial_t \psi \, dV + \oint \hat{\mathbf{n}} \cdot \mathbf{u} \psi \, dO \quad (4.6)$$

where we have used the relative volume flux density $\phi = \hat{\mathbf{n}} \cdot (\mathbf{u} - \mathbf{w})$. It is important to note that all quantities are given in the coordinate system where \mathbf{w} is measured, i.e. (4.6) holds in the laboratory frame. For a transient flow the discretization of the time derivative, given in the rhs of (4.6), may not be possible since it is not necessarily defined in the vicinity of the moving boundary.

Moving coordinates From the coordinates transform $\mathbf{x} = \mathbf{x}' + \mathbf{c}t$ we obtain the transformation rule for the time derivative $\partial_t \rightarrow \partial_t - \mathbf{c} \cdot \nabla$. Equation (4.6) then becomes, in the moving frame of reference,

$$\begin{aligned} \int \partial_t \psi \, dV + \oint \hat{\mathbf{n}} \cdot \mathbf{u} \psi \, dO &\rightarrow \int \partial_t \psi \, dV - \int \mathbf{c} \cdot \nabla \psi \, dV + \oint \hat{\mathbf{n}} \cdot \mathbf{u} \psi \, dO = \\ &= \int \partial_t \psi \, dV + \oint \hat{\mathbf{n}} \cdot (\mathbf{u} - \mathbf{c}) \psi \, dO \end{aligned} \quad (4.7)$$

where we have used $\mathbf{c} \cdot \nabla \psi = \nabla \cdot (\mathbf{c}\psi)$ due to $\mathbf{c} = \text{const}$.

Velocities in the moving frame The fluid velocity transforms as $\mathbf{u} = \mathbf{u}' + \mathbf{c}$, such that the continuity equation becomes

$$\oint \hat{\mathbf{n}} \cdot \mathbf{u} \, dO = \oint \hat{\mathbf{n}} \cdot (\mathbf{u}' + \mathbf{c}) \, dO = \oint \hat{\mathbf{n}} \cdot \mathbf{u}' \, dO + \oint \hat{\mathbf{n}} \cdot \mathbf{c} \, dO = 0.$$

As one can simply verify, the flux generated by the constant velocity \mathbf{c} vanishes, such that the continuity equation simplifies to

$$\oint \hat{\mathbf{n}} \cdot \mathbf{u}' \, dO = 0. \quad (4.8)$$

By using $\psi = \mathbf{u}$ in (4.7) we get for the lhs of the momentum equation

$$\begin{aligned} \int \partial_t \mathbf{u} \, dV + \oint \hat{\mathbf{n}} \cdot \underbrace{(\mathbf{u} - \mathbf{c})}_{\mathbf{u}'} \mathbf{u} \, dO &= \int \underbrace{\partial_t (\mathbf{u}' + \mathbf{c})}_{:=0} \, dV + \oint \hat{\mathbf{n}} \cdot \mathbf{u}' (\mathbf{u}' + \mathbf{c}) \, dO = \\ &= \oint \hat{\mathbf{n}} \cdot \mathbf{u}' \mathbf{u}' \, dO + \mathbf{c} \underbrace{\oint \hat{\mathbf{n}} \cdot \mathbf{u}' \, dO}_{=0} = \\ &= \oint \hat{\mathbf{n}} \cdot \mathbf{u}' \mathbf{u}' \, dO. \end{aligned} \quad (4.9)$$

Here we have used that the transient term has to vanish¹ within the moving frame and we have used the continuity equation (4.8).

Phase constraint The above transformation is done with the a priori unknown wave celerity c so that the determination of c calls for an additional equation for closure. This additional equation was introduced by [Salamon *et al.* \(1994\)](#) by defining the phase of the interface deflection. To derive the constraint, the interface deflection $h = h(x')$ is firstly expanded into the Fourier series

$$h(x') = a_0 + a_1 \sin(k_1 x' + \varphi_1) + \sum_{n=2}^{\infty} [a_n \cos(k_n x') + b_n \sin(k_n x')] \quad , \quad k_n = \frac{2\pi}{L} n.$$

To then uniquely pinpoint the solution within our periodic window, one defines $\varphi_1 := 0$. This can be achieved by taking advantage of orthogonality, thus

$$\int_0^L \left(\frac{\partial h}{\partial x'} \right) \sin(k_1 x') \, dx' = 0. \quad (4.10)$$

The equation is called phase constraint² in the following.

¹By definition, since we restrict ourselves to flows which are steady in the moving frame.

²We shall point out that the equation does not explicitly return c , but it is needed for closure due to the additional unknown c that stems from the transformation into the moving frame of reference.

Ambient pressure Due to the periodic boundary conditions we are dealing with a quasi-closed system and it is therefore necessary to define a reference pressure somewhere in the domain. However, by defining an internal reference pressure, the ambient gas pressure P_0 is no longer determined and another constraint is needed, called volume constraint in the following. Literature distinguishes between two different conditions which we shall call, according to [Kalliadasis *et al.* \(2012\)](#), open flow condition and closed flow condition, where both conditions define a value for the averaged film thickness \bar{h} within the moving frame, where

$$\bar{h} = \frac{1}{L} \int_0^L h \, dx'. \quad (4.11)$$

Volume constraint A – Open flow condition For the discussion of the volume constraint it is advantageous to firstly deduce the open flow condition. We start with the continuity equation within the laboratory frame (3.33), hence

$$\frac{d}{dt} \int_V dV = \int_0^{h_0} u_0 \, dy - \int_0^{h_A} u_A \, dy = \Gamma_0(t) - \Gamma_A(t) \quad (4.12)$$

where $u_0 = u(0, y, t)$ is the inlet velocity distribution, h_0 the height of the inlet and the corresponding quantities at the position $x = A$, thus $u_A = u(A, y, t)$ and the film thickness $h_A = h(A, t)$. Most experiments and many (unsteady) numerical simulations prescribe a sinusoidal flux at the inlet to enforce the growth of waves since slow growth rates result in a long entrance region just covered by the flat film. The perturbation is defined by the forcing frequency f_f and the perturbation amplitude a_f , so that the inlet flux typically reads

$$\Gamma_0(t) = \bar{\Gamma}_0 [1 + a_f \sin(2\pi f_f t)]. \quad (4.13)$$

Since the time-periodic inlet flow induces rapidly developing traveling waves, we may assume that the entire flow is time-periodic. Averaging (4.12) over one period of time $\tau_f = 1/f_f$ by applying $\tau_f^{-1} \int dt$ yields

$$\tau_f^{-1} \underbrace{(V(\tau_f) - V(0))}_{:=0} = \bar{\Gamma}_0 - \bar{\Gamma}_A \quad (4.14)$$

where the lhs vanishes due to the assumed time-periodicity of the flow, stating that the total flow entering the domain is also leaving the domain within one period τ_f . To get a relation for $\bar{\Gamma}_A = \bar{\Gamma}_0$ we change into the moving frame, thus

$$\Gamma'(x') = \int_0^h u'(x', y) \, dy = \int_0^h u(x, y, t) \, dy - ch(x, t) \quad (4.15)$$

where continuity imposes $\Gamma'(x') = \text{const}$. We now additionally assume that the forcing frequency is inherited to the flow so that the average over one wavelength $L = 2\pi/k$ within the moving frame is equivalent to the time average within the laboratory frame, i.e. $L^{-1} \int dx' = \tau_f^{-1} \int dt$ and averaging (4.15) yields

$$\Gamma' = \bar{\Gamma}_0 - c\bar{h} \quad (4.16)$$

with the x' -averaged film thickness \bar{h} defined by (4.11). With the imposed t -averaged (inlet) volume flux $\bar{\Gamma}_0 \equiv 1$ we obtain the open flow condition

$$\bar{h} = \frac{1 - \Gamma'}{c}. \quad (4.17)$$

The assumptions for the derivation of the open flow condition were an entirely time periodic flow and that the forcing frequency is inherited to the flow. From (4.17) one may guess that the averaged film thickness \bar{h} is not equal to the Nusselt film thickness, i.e. $\bar{h} \neq 1$. We will show later that the averaged film thickness is in general lower than one, i.e. $\bar{h} < 1$.

Volume constraint B – Closed flow condition In contrast, [Salamon *et al.* \(1994\)](#) employ the closed flow condition in their investigation, thus

$$\bar{h} := 1. \quad (4.18)$$

Using this condition implies that \bar{h} serves as length scale instead of h_{Nu} . This leads to the situation that the Reynolds number of the closed flow condition is defined differently from the one related to the closed flow condition, see (2.15). To indicate the solutions that are found by using the closed flow condition we add the subscript C to the relevant non-dimensional parameters, i.e. Re_C and We_C .

Redefinition From now on all considerations are within the moving frame of reference and we will therefore omit the prime.

4.1.2. Transformation to the computational domain

Within the moving frame of reference it is apparent to replace the Cartesian coordinates (x, y) by the surface-fitted coordinates (ξ, η) . This is done by mapping the free-surface $h(x)$ to $\eta = 1$ and for reasons dictated by the later introduced *arclength continuation* we additionally map the end of the domain $x = L$ to $\xi = 1$, thus

$$\xi = \frac{x}{L} \quad , \quad \eta = \frac{y}{h(x)}. \quad (4.19)$$

The resulting computational domain is a square with a side length of 1. We shall note that the length of the domain L is not to confuse with the total length of the plate L_0 . A sketch of the resulting coordinate lines within the (x, y) space is shown in Figure 4.3. The vertical lines represent $x = \text{const.}$ or $\xi = \text{const.}$ The free-surface is indicated by $\eta = 1$ and all curvilinear levels below correspond to $\eta = \text{const.}$

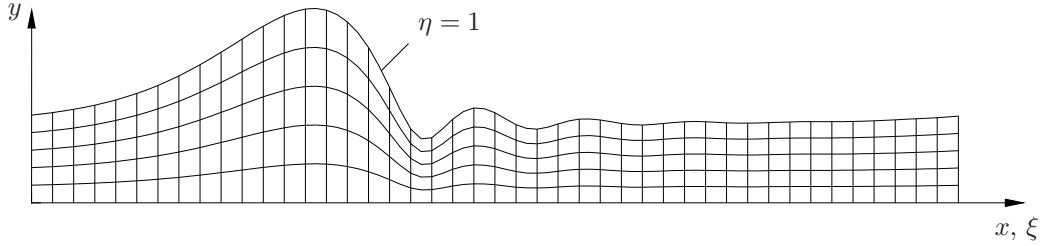


Figure 4.3.: Curvilinear coordinate levels (ξ, η) within the physical moving frame (x, y) .

The transformation rules for the derivatives become

$$\frac{\partial}{\partial x} = \frac{\partial \xi}{\partial x} \frac{\partial}{\partial \xi} + \frac{\partial \eta}{\partial x} \frac{\partial}{\partial \eta}$$

$$\frac{\partial}{\partial y} = \frac{\partial \xi}{\partial y} \frac{\partial}{\partial \xi} + \frac{\partial \eta}{\partial y} \frac{\partial}{\partial \eta}$$

so that the operators read in the new coordinates

$$\partial_x = \frac{1}{L} \left(\partial_\xi - \frac{\eta h'}{h} \partial_\eta \right) \quad (4.20a)$$

$$\partial_y = \frac{1}{h} \partial_\eta \quad (4.20b)$$

where we will use from now on $h' := \partial_\xi h$ and also $h'' := \partial_{\xi\xi} h$.

4.1.3. Governing equations on the computational domain

The final non-dimensional momentum and continuity equations within the moving frame of reference on the computational domain (ξ, η) are

$$\oint \phi u \, dO = - \oint \hat{n}_x P \, dO + \frac{1}{\text{Re}} \oint \mathcal{D}u \, dO + \frac{3}{\text{Re}} \int dV \quad (4.21a)$$

$$\oint \phi v \, dO = - \oint \hat{n}_y P \, dO + \frac{1}{\text{Re}} \oint \mathcal{D}v \, dO - \frac{3}{\text{Re}} \int \cot \theta \, dV \quad (4.21b)$$

$$\oint \phi \, dO = 0 \quad (4.21c)$$

with the volume flux density ϕ , the (bulk) normal derivative operator \mathcal{D} and the differential volume element dV

$$\phi = \hat{\mathbf{n}} \cdot \mathbf{u} = \hat{n}_x u + \hat{n}_y v \quad (4.22a)$$

$$\mathcal{D} = \hat{\mathbf{n}} \cdot \nabla = \frac{\hat{n}_x}{L} \partial_\xi - \left(\frac{\hat{n}_x \eta h'}{Lh} - \frac{\hat{n}_y}{h} \right) \partial_\eta \quad (4.22b)$$

$$dV = dx dy = Lh d\xi d\eta \quad (4.22c)$$

where the unit normal vector $\hat{\mathbf{n}}$ will be given below with the discretization. The normal and tangential stress balances at the free surface become

$$P - P_0 = \frac{2h'}{\text{Re} L(L^2 + h'^2)} (h' \partial_\xi u - L \partial_\xi v) - \frac{2}{\text{Re} Lh} (h' \partial_\eta u - L \partial_\eta v) - \frac{\text{We} Lh''}{(L^2 + h'^2)^{3/2}} \quad (4.23a)$$

$$-2h' \partial_\xi u + \frac{L^2 - h'^2}{L} \partial_\xi v + \frac{L^2 + h'^2}{h} \partial_\eta u + \frac{h'(L^2 + h'^2)}{Lh} \partial_\eta v = 0. \quad (4.23b)$$

The remaining boundary conditions

$$\{h, \mathbf{u}, P\}|_{\xi=0} = \{h, \mathbf{u}, P\}|_{\xi=1} \quad (4.24a)$$

$$\mathbf{u}|_{\eta=0} = -\mathbf{c} \quad (4.24b)$$

$$(uh' - Lv)|_{\eta=1} = 0 \quad (4.24c)$$

imply periodicity, no-slip at the wall and the kinematic boundary condition. The phase constraint reads

$$\int_0^1 h' \sin(2\pi\xi) d\xi = 0. \quad (4.25)$$

As volume constraint either the closed flow condition

$$\int_0^1 h d\xi = 1 \quad (4.26)$$

or the open flow condition

$$h|_{\xi_0} \int_0^1 u|_{\xi_0} d\eta + c \int_0^1 h d\xi = 1 \quad (4.27)$$

is used. The open flow condition (4.27) is evaluated at some arbitrary position ξ_0 . We will employ the closed flow condition (4.26) for the verification of our code with the data given by [Salamon *et al.* \(1994\)](#) whereas the open flow condition (4.27) will be used for further

investigations. Since this is common sense in the relevant literature we will replace the length of the domain L by the corresponding wave vector k , thus

$$k = \frac{2\pi}{L}. \quad (4.28)$$

4.2. Numerics

The following section gives a detailed overview of the numerical treatment of the system (4.21 – 4.27). Basically the present solver is a monolithic implementation of the Finite Volume formulation using Newton’s method including an arclength continuation in the directions of k and Re . The flow field variables are arranged in a staggered manner and the discretization is done by using central schemes and linear interpolation, leading to a method of second order accuracy. The solver was developed by the author in MATLAB for the present monograph. The basic strategy for the implementation of the solver into MATLAB is adopted from [Wesseling \(2001\)](#) and some further details are taken from [Lanzerstorfer \(2012\)](#).

4.2.1. Mesh

The coordinate transformation (4.19) already implies a structured grid, which seems to be the *natural choice* to mesh the present problem. The expected geometry of the film interface calls for a local mesh refinement in order to save computational costs. However, to limit the complexity of the solver to a certain level we distribute the cells equidistantly in both directions. With the number of cells in streamwise direction N_ξ and in crosswise direction N_η the cell lengths are $\Delta_\xi = 1/N_\xi$ and $\Delta_\eta = 1/N_\eta$. Instead of defining the number of cells in streamwise direction N_ξ we introduce the cell aspect ratio

$$R = \frac{\Delta_\xi L}{\Delta_\eta} = \frac{N_\eta L}{N_\xi} \quad (4.29)$$

so that $N_\xi = \lceil LN_\eta/R \rceil$ where the brackets represent the ceiling function. With the given meshing strategy, every cell in physical space is a trapezoid as shown in Figure 4.4(a). The notation n, e, s, w for the four cell faces and c for the cell center is indicated. Also, the unit normal vectors $\hat{\mathbf{n}}_i$ are shown, which read in Cartesian coordinates

$$\hat{\mathbf{n}}_{e/w} = \pm \begin{pmatrix} 1 \\ 0 \end{pmatrix}, \quad \hat{\mathbf{n}}_{n/s} = \pm \frac{\Delta_\xi}{\Delta_{n/s}} \begin{pmatrix} -h'_c \eta_{n/s} \\ L \end{pmatrix} \quad (4.30)$$

with $\Delta_{n/s}$ standing for the respective face area.

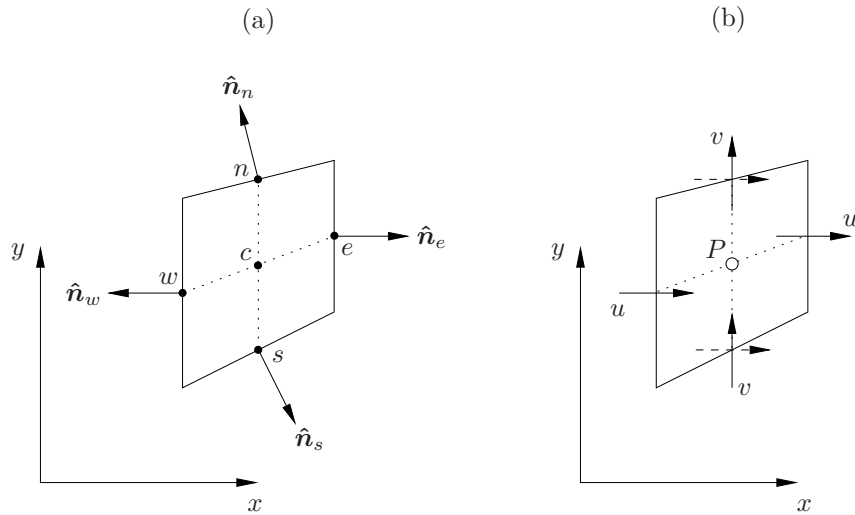


Figure 4.4.: (a) Sketch of a single trapezoidal cell (see Figure 4.3) showing the face notation and the face normal vectors. (b) Staggered variable arrangement of the Cartesian velocity components u , v and the pressure P . The cross fluxes are indicated by the dashed arrows.

4.2.2. Variable arrangement

As it is also done in the MATLAB examples of [Wesseling \(2001\)](#), we employ the staggered variable arrangement to circumvent the well known problems of pressure checker-boarding. The staggered variable arrangement is shown in Figure 4.4 (b), where the pressure P is located at the cell center (c), the streamwise velocity component u at the center of the vertical faces (w, e) and the crosswise (Cartesian) velocity component v is located at the center of the upper and lower faces (n, s). The choice of the Cartesian velocity components is desirable to keep the momentum equations in their conservative form. The drawback of using Cartesian instead of grid-oriented velocity components (covariant, contravariant), which would be orthogonal to the (ξ, η) grid lines, is the appearance of cross fluxes $\sim u$ at the northern and southern boundaries. Since the velocities for these cross fluxes u_s and u_n , indicated by the dashed arrows in Figure 4.4 (b), are not available at the positions needed, we interpolate them by using the arithmetic mean of the nearest neighbor values. Nonetheless, [Ferziger & Perić \(2002\)](#) do not recommend a staggered arrangement on a non-orthogonal grid and declare the combination as inapplicable for cases where the grid lines change their direction significantly. However, since we do not expect such a behavior (see Figure 8.5 of [Ferziger & Perić \(2002\)](#)) for the present problem, their argument is less stringent.

Figure 4.5 illustrates, for convenience on an orthogonal grid, the control volumes for the conservation equations which are indicated by shaded boxes. The control volumes

for continuity, streamwise momentum and crosswise momentum equation are chosen such that the pressure P , the streamwise velocity u and the crosswise velocity v lie in center of the respective control volume.

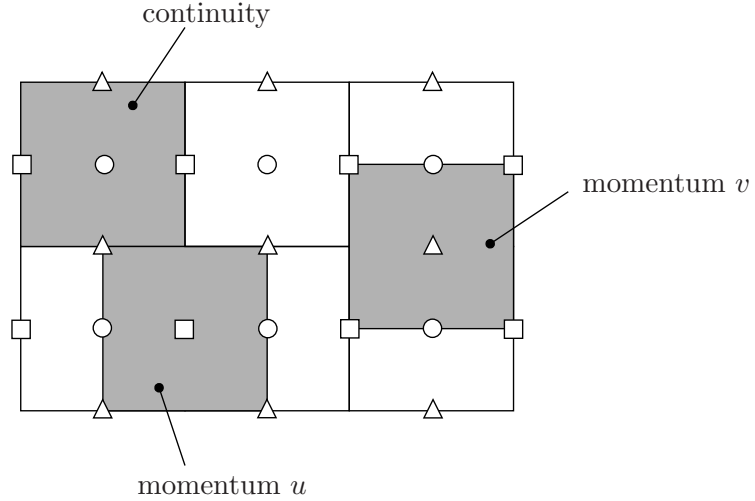


Figure 4.5.: Location of the control volumes (shaded) for the respective conservation equation. The squares indicate the location of u , the triangles the location of v and the circles the location of P .

The free-surface is treated differently since the respective boundary conditions (4.23) and (4.24c) require the introduction of all variables as shown in Figure 4.6. The free-surface is allocated by h , u , v and P so that four equations are needed. Three of them are the already mentioned dynamic and kinematic conditions and the fourth equation is found as the crosswise momentum balance over the upper half cell, which has not been used for the bulk equations. The respective control volume is indicated as shaded box in Figure 4.6.

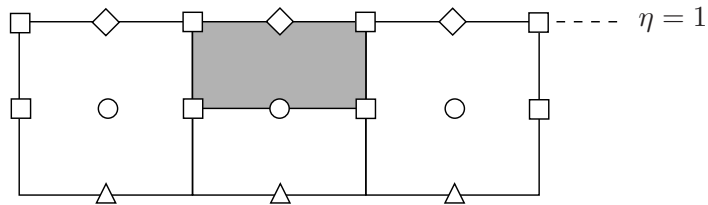


Figure 4.6.: Sketch of the variable arrangement at the free-surface. The diamond \diamond at the free-surface indicates the joint location of h , v and P . As for the bulk, the square at the free-surface indicates the location of u .

4.2.3. Discretization

Continuity equation The continuity equation is discretized in terms of the fluxes across the cell faces, i.e.

$$\oint \phi \, dO = \oint (\hat{n}_x u + \hat{n}_y v) \, dO = 0 \quad \rightarrow \quad \sum_{i=1}^4 \phi_i \Delta_i = 0 \quad (4.31)$$

with the volume flux $\phi_i \Delta_i$ across the cell face i and the respective face area Δ_i . With the face unit normal vectors (4.30) the fluxes are

$$\phi_e \Delta_e = u_e h_e \Delta_\eta \quad (4.32a)$$

$$\phi_w \Delta_w = -u_w h_w \Delta_\eta \quad (4.32b)$$

$$\phi_n \Delta_n = (L v_n - h'_c \xi_n u_n) \Delta_\xi \quad (4.32c)$$

$$\phi_s \Delta_s = -(L v_s - h'_c \xi_s u_s) \Delta_\xi \quad (4.32d)$$

Convective terms The convective terms of the momentum equations are again discretized by using the fluxes, hence

$$\oint \phi u_j \, dO \quad \rightarrow \quad \sum_{i=1}^4 (\phi_i \Delta_i) u_{j,i} \quad (4.33)$$

where u_j means $u_j = u, v$.

Pressure gradient The pressure forces become

$$\oint \hat{n}_x P \, dO \quad \rightarrow \quad \Delta_\eta (h_e P_e - h_w P_w) - h'_c \Delta_\xi (\eta_n P_n - \eta_s P_s) \quad (4.34a)$$

$$\oint \hat{n}_y P \, dO \quad \rightarrow \quad L \Delta_\xi (P_n - P_s) \quad (4.34b)$$

Gravity term The gravity force trivially derives from (4.22c) as

$$\int dV \quad \rightarrow \quad L h_c \Delta_\xi \Delta_\eta \quad (4.35)$$

Diffusive terms With the bulk normal derivative operator \mathcal{D} given in (4.22b) the diffusive term reads for $u_j = u, v$

$$\oint \mathcal{D} u_j \, dO = \oint \left[\frac{\hat{n}_x}{L} \partial_\xi - \left(\frac{\hat{n}_x \eta h'}{L h} - \frac{\hat{n}_y}{h} \right) \partial_\eta \right] u_j \, dO$$

Discretization and collection of all terms yields

$$\begin{aligned}
\oint \mathcal{D}u_j \, dO &\rightarrow \frac{\Delta\eta}{L} [h_e(\partial_\xi u_j)_e - h_w(\partial_\xi u_j)_w] - \frac{h'_c \Delta\xi}{L} [\eta_m(\partial_\xi u_j)_n - \eta_s(\partial_\xi u_j)_s] - \\
&\quad - \frac{\eta_c \Delta\eta}{L} [h'_e(\partial_\eta u_j)_e - h'_w(\partial_\eta u_j)_w] + \\
&\quad + \frac{L\Delta\xi}{h_c} \left(1 + \frac{h'_c{}^2 \eta_n^2}{L^2}\right) (\partial_\eta u_j)_n - \frac{L\Delta\xi}{h_c} \left(1 + \frac{h'_c{}^2 \eta_s^2}{L^2}\right) (\partial_\eta u_j)_s \quad (4.36)
\end{aligned}$$

Bulk derivatives All derivatives in (4.32) - (4.36) are discretized by the central finite differencing scheme of second order accuracy and intermediate values are found by linear interpolation. The overall order of accuracy will be verified below.

Normal stress balance The centers for discretization of (4.23a) are the cell centers i (diamonds in Figure 4.6), so that the ξ -derivatives become

$$h' \rightarrow \frac{h_{i+1} - h_{i-1}}{2\Delta\xi}, \quad (4.37a)$$

$$h'' \rightarrow \frac{h_{i+1} - 2h_i + h_{i-1}}{\Delta\xi^2}, \quad (4.37b)$$

$$\partial_\xi u \rightarrow \frac{u_e - u_w}{\Delta\xi}, \quad (4.37c)$$

$$\partial_\xi v \rightarrow \frac{v_{i+1} - v_{i-1}}{2\Delta\xi}, \quad (4.37d)$$

with the interfacial streamwise velocities u_w and u_e at the western and eastern cell face (squares in Figure 4.6), respectively. For the η -derivatives, one-sided three-point schemes are employed, thus

$$\partial_\eta u \rightarrow a_u u_{f,i} + b_u u_{f-1,i} + c_u u_{f-2,i}, \quad (4.38a)$$

$$\partial_\eta v \rightarrow a_v v_{f,i} + b_v v_{f-1,i} + c_v v_{f-2,i}, \quad (4.38b)$$

with the subscript f indicating the location at the free surface, the coefficients

$$a_u = \frac{8}{3\Delta\eta}, \quad b_u = -\frac{3}{\Delta\eta}, \quad c_u = \frac{1}{3\Delta\eta}, \quad (4.39a)$$

$$a_v = \frac{7}{6\Delta\eta}, \quad b_v = -\frac{4}{3\Delta\eta}, \quad c_v = \frac{1}{6\Delta\eta}, \quad (4.39b)$$

and with $u_{k,i}$ being the streamwise velocity at the cell center i , derived as the arithmetic mean of u_w and u_e .

Tangential stress balance The discretization of (4.23b) is done in full accordance to the discretization of (4.23a) before, but the centers of discretization are the cell faces (squares in Figure 4.6).

Kinematic boundary condition The discretization of (4.24c) is done at the cell centers i (diamonds in Figure 4.6) and reads

$$\frac{u_w + u_e}{2} \frac{h_{i+1} - h_{i-1}}{2\Delta_\xi} - Lv_i = 0. \quad (4.40)$$

Phase constraint, Volume constraint CFC For discretization of (4.25) and (4.26), the values at the cell centers i are employed (diamonds in Figure 4.6), thus

$$\sum_{i=1}^{N_\xi} \frac{h_{i+1} - h_{i-1}}{2\Delta_\xi} \sin(2\pi\xi_i) \Delta_\xi = 0, \quad (4.41a)$$

$$\sum_{i=1}^{N_\xi} h_i \Delta_\xi = 1. \quad (4.41b)$$

Volume constraint OFC To discretize the volume constraint for the open flow condition (4.27), the location ξ_0 is defined at Δ_ξ , i.e. on the eastern border of the first cell (second square in Figure 4.6), yielding

$$\frac{h_1 + h_2}{2} \sum_{k=1}^{N_\eta} u_{k,2} \Delta_\eta + c \sum_{i=1}^{N_\xi} h_i \Delta_\xi = 1. \quad (4.42)$$

4.2.4. Full set of equations

Continuous We collect all equations (4.21) - (4.25) including (4.26) or (4.27) and write them as $\mathbf{F}[\mathbf{X}] = \mathbf{0}$. Here, $\mathbf{F}[\mathbf{X}]$ is the vector valued non-linear functional with the solution vector \mathbf{X} representing the set of unknown functions and unknown scalars, thus

$$\mathbf{X} = \begin{pmatrix} X_1 \\ X_2 \\ X_3 \\ X_4 \\ X_5 \\ X_6 \end{pmatrix} = \begin{pmatrix} h(\xi) \\ u(\xi, \eta) \\ v(\xi, \eta) \\ P(\xi, \eta) \\ c \\ P_0 \end{pmatrix}. \quad (4.43)$$

Discretized By discretizing $\mathbf{F}[\mathbf{X}] = \mathbf{0}$ one finds the discrete equivalent $\mathbf{f}(\mathbf{x}) = \mathbf{0}$ which can be linearized and written as $\mathbf{A} \cdot \mathbf{x} = \mathbf{b}$ with the Picard matrix \mathbf{A} . Since we are dealing

with a non-linear problem, it is clear that \mathbf{x} also enters in the Picard matrix and \mathbf{x} has to be found iteratively, i.e.

$$\mathbf{A}(\mathbf{x}^n) \cdot \mathbf{x}^{n+1} = \mathbf{b}^n. \quad (4.44)$$

For the convergence measure we introduce the residual vector

$$\mathbf{f}^n := \mathbf{A}(\mathbf{x}^n) \cdot \mathbf{x}^n - \mathbf{b}^n \quad (4.45)$$

and define the residual r^n (at iteration step n) as the Euclidean norm $\|\cdot\|_2$ of the residual vector \mathbf{f}^n weighted by the number of elements N , thus

$$r^n := \frac{\sqrt{\sum_{i=1}^N (f_i^n)^2}}{N} = \frac{\|\mathbf{f}^n\|_2}{N}. \quad (4.46)$$

The solution of the discretized system $\mathbf{f}(\mathbf{x}) = \mathbf{0}$ is assumed to be converged if the residual r^n is below a certain tolerance ε_t , thus $r^n < \varepsilon_t$. As expected, the simple Picard iteration cannot be applied to the present problem, since convergence is in general not achievable.

4.2.5. Newton's method

The given problem contains a large number of non-linear terms, since the unknown location of the interface h determines the metric terms of the coordinate transformation entering everywhere in the equations. The first choice for such a problem is Newton's method which becomes inevitable anyway for the arclength continuation introduced later. Nonetheless, Newton-like techniques are rarely used in CFD (Ferziger & Perić, 2002). This is mainly because of the costs for the (numerical) generation of the Jacobian and the costs for solving the system of linear equations. We have circumvented the first restriction with a hard-coded implementation of the Jacobian by exploiting the structured mesh and by using the highly efficient sparse commands of MATLAB. Finally, the costs for the Jacobian-setup becomes negligible compared to the costs for solving the system of linear equations. However, the remaining drawback of the method is the enormous demand of memory so that the scalability is limited by the available memory.

Fréchet derivative For the construction of a Newton iteration we employ the Taylor series expansion of the functional $F[\mathbf{X}]$ around \mathbf{X}^0 , hence

$$F_i[\mathbf{X}] = F_i[\mathbf{X}^0 + \delta\mathbf{X}] = F_i[\mathbf{X}^0] + \delta F_i = F_i[\mathbf{X}^0] + \int F'_{ij}[\mathbf{X}^0] \delta X_j dx' + \dots \quad (4.47)$$

with $\delta X_j = \delta X_j(x')$, $x' = (\xi, \eta)$ and the Fréchet derivative evaluated at \mathbf{X}^0 , thus

$$F'_{ij}[\mathbf{X}^0] = \left. \frac{\delta F_i}{\delta X_j} \right|_{\mathbf{X}^0}. \quad (4.48)$$

For convenience we write the first variation δF_i in terms of the linear, in general partial differential, operator $T_{ij}[\mathbf{X}^0]$

$$\delta F_i = \int F'_{ij}[\mathbf{X}^0] \delta X_j \, dx' := T_{ij}[\mathbf{X}^0] \delta X_j. \quad (4.49)$$

Note that $F'_{ij}[\mathbf{X}^0]$ and $T_{ij}[\mathbf{X}^0]$ may be used interchangeably (Thurston, 1980). The solution to the problem $\mathbf{F}[\mathbf{X}] = \mathbf{0}$ is determined by the iterative procedure $0 = F_i[\mathbf{X}^n] + T_{ij}[\mathbf{X}^n] \delta X_j$ and by solving the system of linear differential equations

$$T_{ij}[\mathbf{X}^n] \delta X_j = -F_i[\mathbf{X}^n] \quad (4.50)$$

for the correction δX_j yielding the solution at iteration step $(n + 1)$ as

$$\mathbf{X}^{n+1} = \mathbf{X}^n + \delta \mathbf{X}. \quad (4.51)$$

Evaluation of the Fréchet derivative The implementation of the given formulation shall be briefly demonstrated on the curvature term of the dynamic boundary condition (4.23). We therefore define the functional

$$G[h] := \frac{h''}{(L^2 + h'^2)^{3/2}}.$$

The Fréchet derivative derives (by using a computer algebra system like Mathematica) as

$$G'[h(x)] := \frac{\delta G[h(x)]}{\delta h(x')} = \left[-\frac{3h'h''}{(L^2 + h'^2)^{5/2}} \frac{d}{dx} + \frac{1}{(L^2 + h'^2)^{3/2}} \frac{d^2}{dx^2} \right] \delta_D(x - x')$$

with the Dirac-delta distribution δ_D so that the first variation becomes

$$\int G'[h(x)] \delta h(x') \, dx' = \left[-\frac{3h'h''}{(L^2 + h'^2)^{5/2}} \frac{d}{dx} + \frac{1}{(L^2 + h'^2)^{3/2}} \frac{d^2}{dx^2} \right] \delta h$$

where the spatial derivatives are passed to δh through an integration by parts.

Discretization The discretized version of (4.50) corresponds to a system of linear algebraic equations where the discretized differential operator $T_{ij}[\mathbf{X}^n]$ becomes the Jacobian

matrix $\mathbf{J}(\mathbf{x}^n)$ leading finally to the Newton–Raphson method

$$\mathbf{J}(\mathbf{x}^n) \cdot (\mathbf{x}^{n+1} - \mathbf{x}^n) = -\mathbf{f}(\mathbf{x}^n). \quad (4.52)$$

Linear equation solver Any system of linear algebraic equations is solved by using the internal MATLAB-routine `mldivide` (backslash operator). Basically the algorithm chooses a proper routine out of the Linear Algebra Package (LAPACK) depending on the structure of the matrix whereas for sparse matrices specific packages are incorporated ([MATLAB, 2010](#)).

4.2.6. Arclength continuation

For the continuation of the solution branches it is inevitable to implement an arclength continuation method ([Keller, 1977](#)). We therefore introduce the parameter χ indicating the direction of continuation. For the present case, the wave vector k and the Reynolds number Re had been implemented as continuation directions, thus $\chi \in \{k, \text{Re}\}$. With the new variable χ the solution vector \mathbf{x} is extended to the new solution vector $\hat{\mathbf{x}} = (\mathbf{x}, \chi)^\top$. We introduce the arclength Δs measuring the distance between two consecutive solutions in the Euclidian norm, thus

$$\Delta s^2 = \|\hat{\mathbf{x}} - \hat{\mathbf{x}}^*\|_2^2 = \|\mathbf{x} - \mathbf{x}^*\|_2^2 + (\chi - \chi^*)^2$$

where $\hat{\mathbf{x}} = (\mathbf{x}, \chi)^\top$ represents the new (unknown) solution on the solution branch, whereas $\hat{\mathbf{x}}^* = (\mathbf{x}^*, \chi^*)^\top$ stands for the recent (known) solution. We shall point out that one may not confuse the *recent solution* of the arclength continuation $\hat{\mathbf{x}}^*$ with the *recent result* of the Newton iteration $\hat{\mathbf{x}}^n$. The arclength constraint is defined as

$$g(\hat{\mathbf{x}}) := \|\mathbf{x} - \mathbf{x}^*\|_2^2 + (\chi - \chi^*)^2 - \Delta s^2 = 0. \quad (4.53)$$

Including this constraint yields the extended functional $\hat{\mathbf{f}}(\hat{\mathbf{x}}) := (\mathbf{f}, g)^\top$, the extended Jacobian

$$\hat{\mathbf{J}}(\hat{\mathbf{x}}^n) := \left. \frac{\partial \hat{\mathbf{f}}_i}{\partial \hat{\mathbf{x}}_j} \right|_{\hat{\mathbf{x}}^n}, \quad (4.54)$$

and finally the corresponding extended system of linear equations

$$\hat{\mathbf{J}}(\hat{\mathbf{x}}^n) \cdot (\hat{\mathbf{x}}^{n+1} - \hat{\mathbf{x}}^n) = -\hat{\mathbf{f}}(\hat{\mathbf{x}}^n). \quad (4.55)$$

For further use it is convenient to denote (4.55) in the *bordered* form

$$\begin{pmatrix} \mathbf{J} & \mathbf{l} \\ \mathbf{m}^\top & o \end{pmatrix}_{\hat{\mathbf{x}}^n} \cdot \begin{pmatrix} -\Delta\mathbf{x} \\ -\Delta\chi \end{pmatrix} = \begin{pmatrix} \mathbf{f} \\ g \end{pmatrix}_{\hat{\mathbf{x}}^n} \quad (4.56)$$

with the difference between two consecutive iterations

$$\Delta\mathbf{x} = \mathbf{x}^{n+1} - \mathbf{x}^n, \quad (4.57a)$$

$$\Delta\chi = \chi^{n+1} - \chi^n, \quad (4.57b)$$

and the blocks of the extended Jacobian

$$\mathbf{J} = \frac{\partial f_i}{\partial x_j}, \quad \mathbf{l} = \frac{\partial f_i}{\partial \chi}, \quad \mathbf{m} = \frac{\partial g}{\partial x_j}, \quad o = \frac{\partial g}{\partial \chi}. \quad (4.58)$$

Predictor step A new step along the solution branch is initialized by a predictor step. We therefore derive the tangential vector $\hat{\mathbf{T}}$ of the functional \mathbf{f} at the recent solution $\hat{\mathbf{x}}^*$ from the condition for the directional derivative

$$(\hat{\mathbf{T}} \cdot \hat{\nabla})\mathbf{f}(\hat{\mathbf{x}}^*) = \mathbf{0}. \quad (4.59)$$

Rearranging yields $\hat{T}_j \hat{\partial}_j f_i = (\hat{\partial}_j f_i) \hat{T}_j := M_{ij} \hat{T}_j = 0$ where the matrix M_{ij} is represented by the upper two blocks \mathbf{J} and \mathbf{l} of the extended Jacobian evaluated at $\hat{\mathbf{x}}^*$. A unique solution is found by additionally defining the length of the tangential vector and as long as the vector is subject to normalization, one may define any component to an arbitrary value, say $\hat{T}_1 := 1$, leading to

$$\begin{pmatrix} \mathbf{J} & \mathbf{l} \\ \mathbf{e}_1^\top & 0 \end{pmatrix}_{\hat{\mathbf{x}}^*} \cdot \hat{\mathbf{T}} = \begin{pmatrix} \mathbf{0} \\ 1 \end{pmatrix} \quad (4.60)$$

with $\mathbf{e}_1^\top = (1, 0, \dots, 0)$. Finally, we have to deduce the peripheral direction of the continuation process corresponding to the sign of Δs . Figure 4.7 shows that the recent continuation direction \mathbf{t}^* is set by the two latter solutions $\hat{\mathbf{x}}^*$ and $\hat{\mathbf{y}}^*$. The tangent vector at $\hat{\mathbf{x}}^*$ within the ck -plane reads $\mathbf{t}^0 = (\hat{T}_c, \hat{T}_k)^\top$ so that the sign for Δs is found from $\text{sgn}(\mathbf{t}^* \cdot \mathbf{t}^0)$. The initial state for the Newton iteration (predictor step) then reads

$$\hat{\mathbf{x}}^0 = \hat{\mathbf{x}}^* + \frac{\hat{\mathbf{T}}}{\|\hat{\mathbf{T}}\|_2} \text{sgn}(\mathbf{t}^* \cdot \mathbf{t}^0) \Delta s. \quad (4.61)$$

Simple strategies for the control of Δs can be found in Seydel (1994).

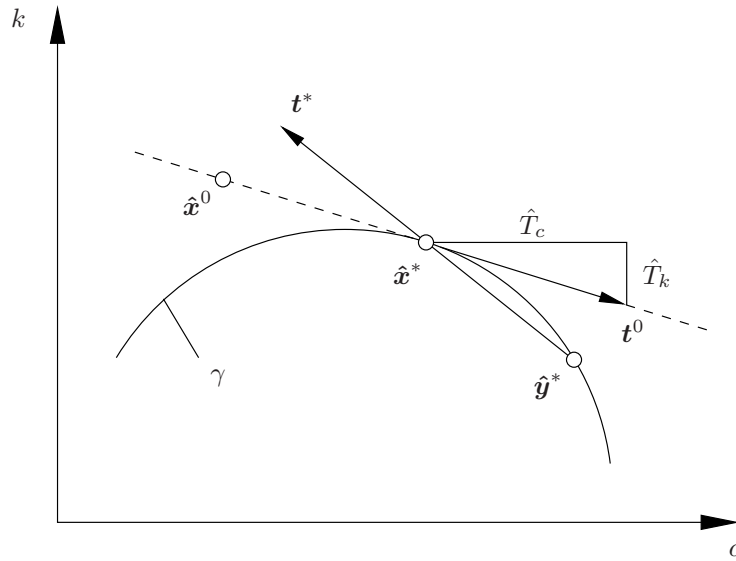


Figure 4.7.: Sketch of a predictor process with solution branch γ , already converged solutions $\hat{\mathbf{x}}^*$ and $\hat{\mathbf{y}}^*$, tangent vector at the recent solution $\mathbf{t}^0 = (\hat{T}_c, \hat{T}_k)^T$ and predicted initial guess $\hat{\mathbf{x}}^0$.

4.2.7. Bordering algorithm

Figure 4.8 shows the structure of the extended Jacobian (4.56). The discretized equations (rows) and the unknowns (columns) are also indicated. The additional blocks arising with the arclength continuation (\mathbf{l} , \mathbf{m} , o) lead to an unfavorable matrix allocation resulting in an enormous increase of computational costs for solving the linear system. This increase can be substantially reduced by using the bordering algorithm (Keller, 1986). Instead of solving the system (4.56) directly, we introduce the auxiliary vectors \mathbf{y} and \mathbf{z} and solve

$$\mathbf{J} \cdot \mathbf{y} = \mathbf{l}, \quad (4.62a)$$

$$\mathbf{J} \cdot \mathbf{z} = \mathbf{f}. \quad (4.62b)$$

The solution of (4.56) then becomes

$$-\Delta\chi = \frac{g - \mathbf{m} \cdot \mathbf{z}}{o - \mathbf{m} \cdot \mathbf{y}}, \quad (4.63a)$$

$$-\Delta\mathbf{x} = \mathbf{z} - (-\Delta\chi)\mathbf{y}. \quad (4.63b)$$

By means of efficiency it is indispensable to implement the bordering algorithm, since (4.62) making use of \mathbf{J} twice is considerably less expensive to solve than (4.56) including $\hat{\mathbf{J}}$ just once.

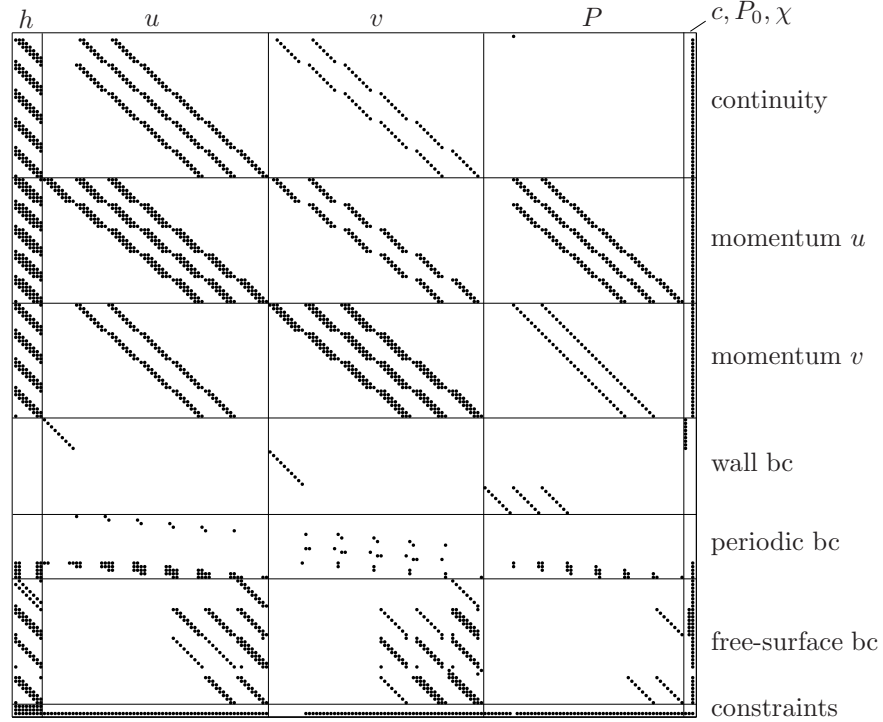


Figure 4.8.: Data allocation of the extended Jacobian $\hat{\mathcal{J}}$. The horizontal ledger lines separate the discretized equations and the vertical ledger lines separate the discretized field variables from another.

4.2.8. Tests

Verification of the Jacobian For a verification of the Jacobian matrix we employ the strategy proposed by [Squire & Trapp \(1998\)](#). We, therefore, create the Jacobian numerically column by column where the n -th column \mathbf{j}_n derives from

$$\mathbf{j}_n = \frac{\Im \hat{\mathbf{f}}(\hat{\mathbf{x}}^0 + i b \hat{\mathbf{e}}_n)}{b} \quad (4.64)$$

with the imaginary unit i and a small increment $b \hat{\mathbf{e}}_n$ in the direction of the n -th unit vector $\hat{\mathbf{e}}_n$ where b is (numerically) small, say $b = 10^{-14}$. For the evaluation of $\hat{\mathbf{f}}$ we employ the Picard matrix, thus $\hat{\mathbf{f}} = \hat{\mathbf{A}} \cdot \hat{\mathbf{x}} - \hat{\mathbf{b}}$. The resulting Jacobian

$$\hat{\mathcal{J}}(\hat{\mathbf{x}}^0) = [\dots, \mathbf{j}_n, \dots] \quad (4.65)$$

is then compared to its hard-coded equivalent. From a positive test result we can conclude that the hard-coded Jacobian fits to $\hat{\mathbf{f}}$ and to the Picard matrix $\hat{\mathbf{A}}$, respectively. However, $\hat{\mathbf{A}}$ could still be incorrect, but this cannot be derived from the present test.

Basic convergence test A very basic convergence test of the solver is shown in Figure 4.9. The left image shows the residuum \hat{r}^n versus the iteration index n with $n = 0$ standing for the start residuum of the initial guess and $n = 8$ representing the residuum of the finally converged solution. We introduce the offset of the iterated state $\hat{\mathbf{x}}^n$ from the exact solution $\hat{\mathbf{x}}$, hence

$$\delta^n = \|\hat{\mathbf{x}}^n - \hat{\mathbf{x}}\|_2. \quad (4.66)$$

The right image of Figure 4.9 shows the offset δ^{n+1} versus the previous offset δ^n by approximating the unknown exact solution by the one with the highest resolution, thus $\hat{\mathbf{x}} \approx \hat{\mathbf{x}}^8$. By comparing the result with the dashed line representing $\delta^{n+1} = (\delta^n)^2$ the quadratic convergence of the Newton iteration becomes evident.

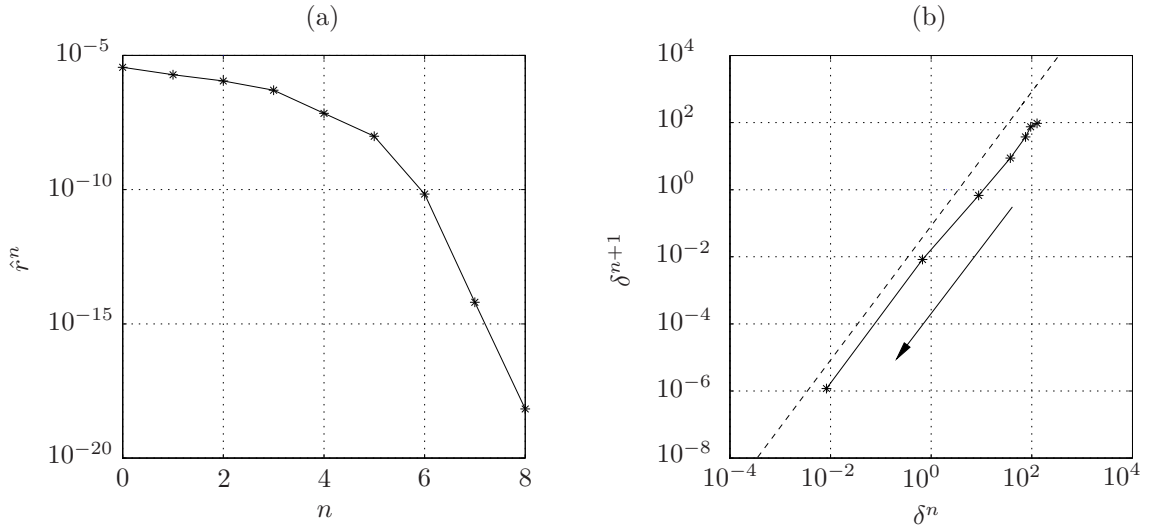


Figure 4.9.: Convergence of a Newton iteration (a) Residuum \hat{r}^n vs. iteration index n . (b) Offset δ^{n+1} vs. previous offset δ^n . The dashed line represents quadratic convergence and the arrow indicates the direction of increasing iteration index n .

Grid convergence The present paragraph provides a grid convergence check which is performed for several cell aspect ratios R and different Reynolds numbers. The wave celerity c is assumed to serve as representative quantity to measure the convergence. We introduce d^n as the deviation of wave celerity of the n -th discrete solution c^n from the exact value c , hence

$$d^n = c^n - c. \quad (4.67)$$

Again, since the exact value is unknown, c has to be approximated by the value from the solution with the highest resolution c^\dagger , so that $d^n = c^n - c^\dagger$. The images of Figure 4.10 show the offset d^n as function of the vertical resolution N_η for the cell aspect ratios $R = 1, \dots, 5$. The left image corresponds to $(\text{Re}_C, \text{We}_C) = (5, 49)$ and the right image to $(\text{Re}_C, \text{We}_C) = (20, 4.9)$, where the Weber numbers derive from $\text{Ka} = 500$. The dashed line indicates exact second order accuracy and as expected from the discretization schemes, the algorithm provides second-order accuracy. We clearly notice that the cell aspect ratio R has a negligible effect on the accuracy of the result for $\text{Re}_C = 5$ in contrast to $\text{Re}_C = 20$. This difference is mainly caused by the decrease of the Weber number indicating a reduced resistance to interface deflections by surface tension.

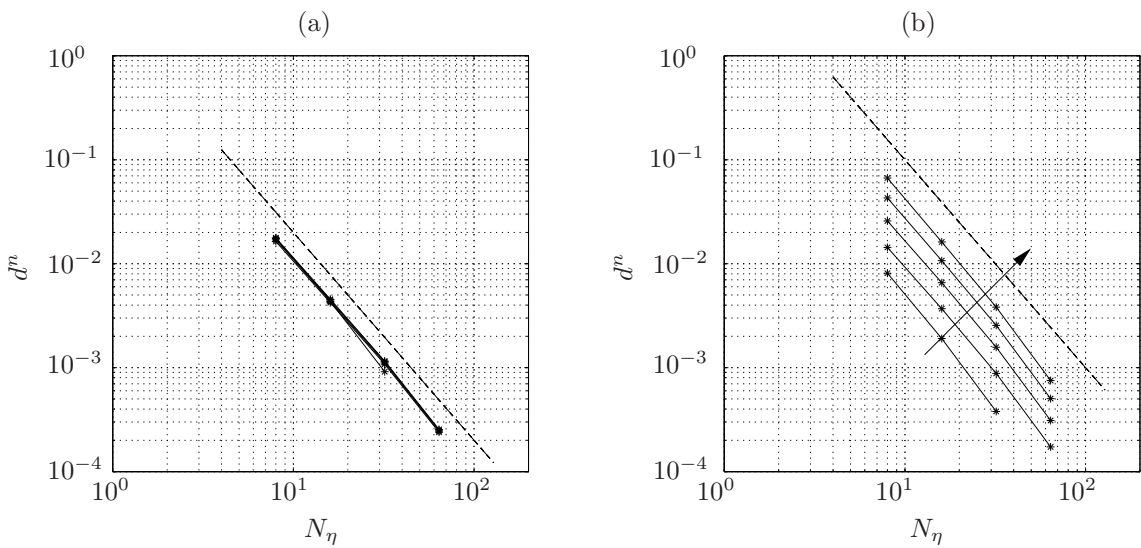


Figure 4.10.: Grid convergence check showing the offset d^n as function of the vertical grid resolution N_η for the cell aspect ratios $R = 1, \dots, 5$, $\text{Ka} = 500$, (a) $\text{Re}_C = 5$ and (b) $\text{Re}_C = 20$. The arrow indicates the direction of increasing R and the dashes lines indicate second-order accuracy.

Verification To verify the current calculation we use the data given by [Salamon *et al.* \(1994\)](#). Figure 4.11 shows the solution branches γ_1 (slow family) and γ_2 (fast family) in the ck -plane for $\text{Re}_C = 7.6(11.4)$ and $\text{We}_C = 214.7(544)$. The bracketed values are the parameters in the scales of [Salamon *et al.* \(1994\)](#), see Table 2.2. From the figure the excellent agreement becomes apparent. For $k_C \rightarrow 0$ the computational domain extends to infinity, thus $L \rightarrow \infty$, so that the continuation of the solution branch has to be terminated at a certain point for computational reasons. These points, at the lower ends of both branches, are marked by arrows indicating that the branches continue. The origin of the

slow branch γ_1 is indicated by the bullet and represents the Hopf bifurcation associated with the primary instability of the flat film. The circle at the emanation point of the fast branch γ_2 indicates a period doubling bifurcation (Salamon *et al.*, 1994).

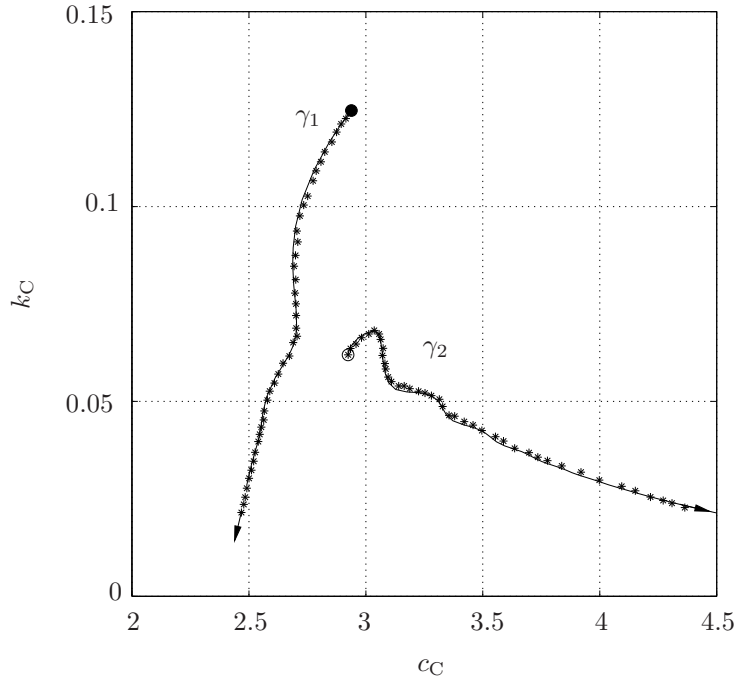


Figure 4.11.: Comparison of the result given by Salamon *et al.* (1994) for $(\text{Re}_S, \text{We}_S) = (11.4, 544)$ corresponding to our $(\text{Re}_C, \text{We}_C) = (7.6, 214.7)$. The branches composed by the asterisks represent the extracted data from Salamon *et al.* (1994), the black curves represent the current calculation. The arrows indicate that the branches continue, the bullet marks the Hopf bifurcation and the circle the period doubling bifurcation.

The left block of Table 4.1 presents the data given by Salamon *et al.* (1994) (their Table I) where they show the maximum height of the film h_{\max} and the wave celerity $c_S = c_C/1.5$ for their parameter set $(\text{Re}_S, \text{We}_S, k) = (9.1, 76.4, 0.07)$ and several FEM-resolutions with (N_x, N_y) representing the number of bi-quadratic elements in each direction. Since they use bi-quadratic basis functions for u, v and bi-linear basis functions for P , the value for their degrees of freedom may be deduced from

$$N_{\text{FEM}} = 2(2N_x + 1)(2N_y + 1) + N_x N_y + 2N_x \quad (4.68)$$

and represents the number of unknowns³. To get to a FVM-resolution that is comparable

³Their value 29922 for $(N_x, N_y) = (160, 20)$ does not fit to our given calculation yielding 29842.

Table 4.1.: Left: FEM-data taken from [Salamon *et al.* \(1994\)](#) for $(\text{Re}_S, \text{We}_S, k) = (9.1, 76.4, 0.07)$. Right: Corresponding FVM-study for $(\text{Re}_C, \text{We}_C, k_C) = (6.0\dot{6}, 37.78, 0.07)$.

(N_x, N_y)	N_{FEM}	h_{max}	c_S	(N_ξ, N_η)	N_{FVM}	$h_{C,\text{max}}$	$c_C/1.5$
(20, 5)	1 042	1.9503	2.4616	(40, 10)	1 476	1.8266	2.5013
(40, 10)	3 882	1.9112	2.4987	(80, 20)	5 346	1.8652	2.5051
(80, 20)	14 962	1.8822	2.5033	(160, 40)	20 286	1.8769	2.5036
(160, 20)	29 922	1.8815	2.5031	(320, 40)	40 446	1.8808	2.5037

Table 4.2.: Extended convergence check for $(\text{Re}_C, \text{We}_C, k_C) = (6.0\dot{6}, 37.78, 0.07)$ and a cell aspect ratio of $R = 10$.

(N_ξ, N_η)	N_{FVM}	$h_{C,\text{max}}$	$c_C/1.5$
(89, 10)	3 240	1.8724	2.5098
(179, 20)	11 880	1.8787	2.5050
(359, 40)	45 360	1.8810	2.5037
(718, 80)	176 874	1.8816	2.5034
(1436, 160)	698 382	1.8818	2.5033
(2872, 320)	2 775 318	1.8818	2.5033

to the FEM-resolution of [Salamon *et al.* \(1994\)](#) we simply employ the doubled number of bi-quadratic elements (N_x, N_y) as the number of cells (N_ξ, N_η) in our FVM-simulation. The results for the corresponding parameters $(\text{Re}_C, \text{We}_C, k_C) = (6.0\dot{6}, 37.78, 0.07)$ are given in the right block of Table 4.1 where our degrees of freedom N_{FVM} are typically larger due to a different variable arrangement. An extended convergence study is shown in Table 4.2 where we have fixed the cell aspect ratio to $R = 10$ and varied the cross-stream resolution N_η ⁴. From Table 4.1 we see that a precision of three significant digits for c_C is reached already with a resolution of $N_\eta = 40$. The side-by-side comparison in Table 4.1 shows that the accuracy of both methods is practically the same, although the FEM results seem to be slightly better.

⁴The case with the highest resolution already requires about 24 GB memory, very close to the maximum available.

4.3. Results

4.3.1. Solution branching

The analysis of the problem in the boundary layer approximation presented in literature has already indicated the rich solution structure of the present system. The principle branching behavior was given by [Chang *et al.* \(1993\)](#). By increasing the reduced Reynolds number they show that the γ_1 -branch remains qualitatively unaltered and the γ_2 -branch successively coalesces with the γ_n -branches through pinching bifurcations to form new branches, so that γ_2 and γ_3 form γ'_2 for instance. However, the pinching of the branches γ_1 and γ_2 cannot be predicted by the first order boundary layer approximation employed by [Chang *et al.* \(1993\)](#). This result was found by [Salamon *et al.* \(1994\)](#) by fixing the reduced Reynolds number δ_S and varying the viscous dispersion number ε_S , both are defined as

$$\delta_S = \frac{2\text{Re}_S}{45\text{We}_S^{1/3}}, \quad (4.69a)$$

$$\varepsilon_S = \frac{1}{15\text{We}_S^{2/3}}. \quad (4.69b)$$

All parameters are collected in [Table 4.3](#) where the first column indicates the label of [Figure 19](#) in [Salamon *et al.* \(1994\)](#). We see that decreasing ε_S by keeping $\delta_S = \text{const.}$ yields an increase of Re_C with a simultaneous increase of We_C and Ka . The path in terms of the reduced parameters $(\delta_S, \varepsilon_S)$ results in a somewhat inappropriate path in terms of the Navier–Stokes parameters $(\text{Re}_C, \text{We}_C)$. Thus, to mimic experimental conditions, we instead vary Re_C by keeping $\text{Ka} = \text{const.}$

[Figure 4.12](#) shows the solution branches for $\text{Ka} = 500$ and $\text{Re}_C = \{3, 3.5, 4, 4.5\}$. From the figure we clearly identify the pinching between γ_1 and γ_2 in qualitative agreement with the Navier–Stokes study of [Salamon *et al.* \(1994\)](#).

Table 4.3.: Path taken for $\delta_S = 0.062$ in [Salamon *et al.* \(1994\)](#) (their [Figure 19](#)) and corresponding Navier–Stokes parameters in the present scaling.

	ε_S	Re_S	We_S	Re_C	We_C	Ka
(f)	0.005	5.10	48.7	3.40	55.2	294
(e)	0.004	5.70	68.0	3.80	86.1	553
(d)	0.0035	6.09	83.1	4.06	113	806
(c)	0.0034	6.18	86.8	4.12	119	875
(b)	0.003	6.58	105	4.39	154	1251
(a)	0.001	11.4	544	7.60	1378	28 072

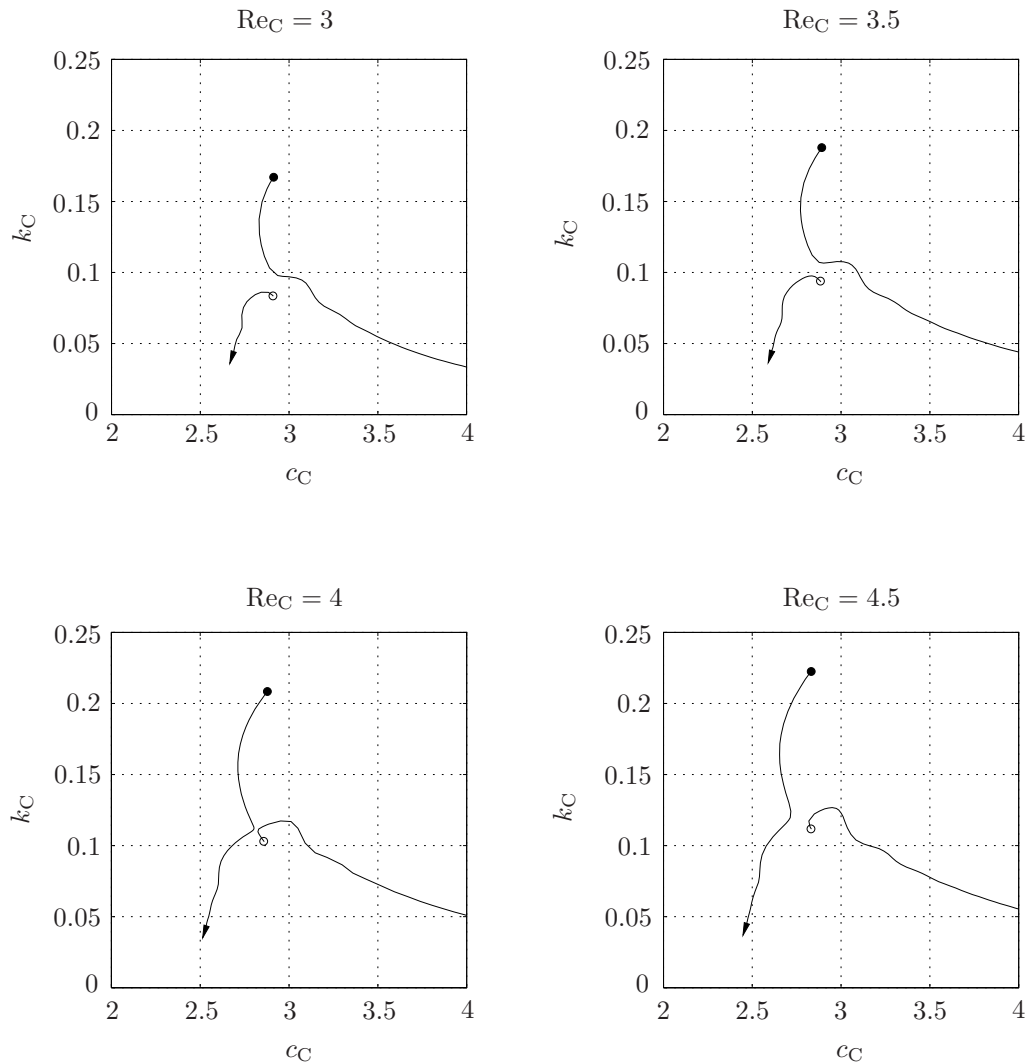


Figure 4.12.: Solution branches γ_1 and γ_2 for $Ka = 500$ and $Re_C = \{3, 3.5, 4, 4.5\}$. The arrow indicates that the branch continues, the bullet marks the Hopf bifurcation and the circle the period doubling bifurcation.

Increasing Re_C further yields another pinching, where γ'_2 is created by the coalescence of γ_2 and γ_3 . The process is shown in Figure 4.13. This agrees qualitatively well with the BL-prediction given by Chang & Demekhin (2002) and also with the investigation by Kalliadasis *et al.* (2012). Representative wave shapes are given in Figure 4.14 for $Re_C = 10$, and in Figure 4.15 for $Re_C = 12$.

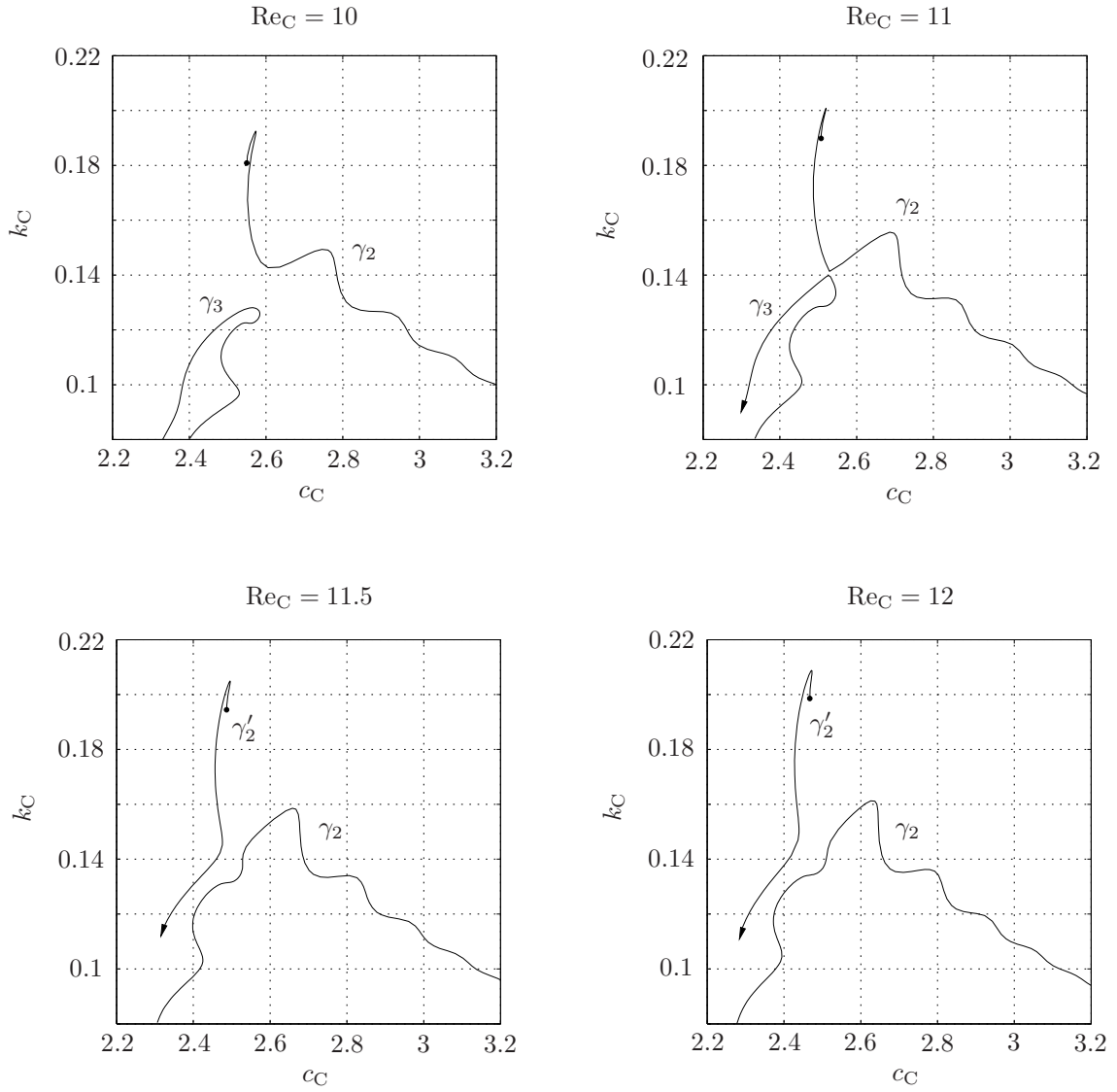


Figure 4.13.: Coalescence of γ_2 and γ_3 to form γ'_2 for $Ka = 500$ and $Re_C = \{10, 11, 11.5, 12\}$. The arrow indicates that the branch continues and the bullet marks the Hopf bifurcation.

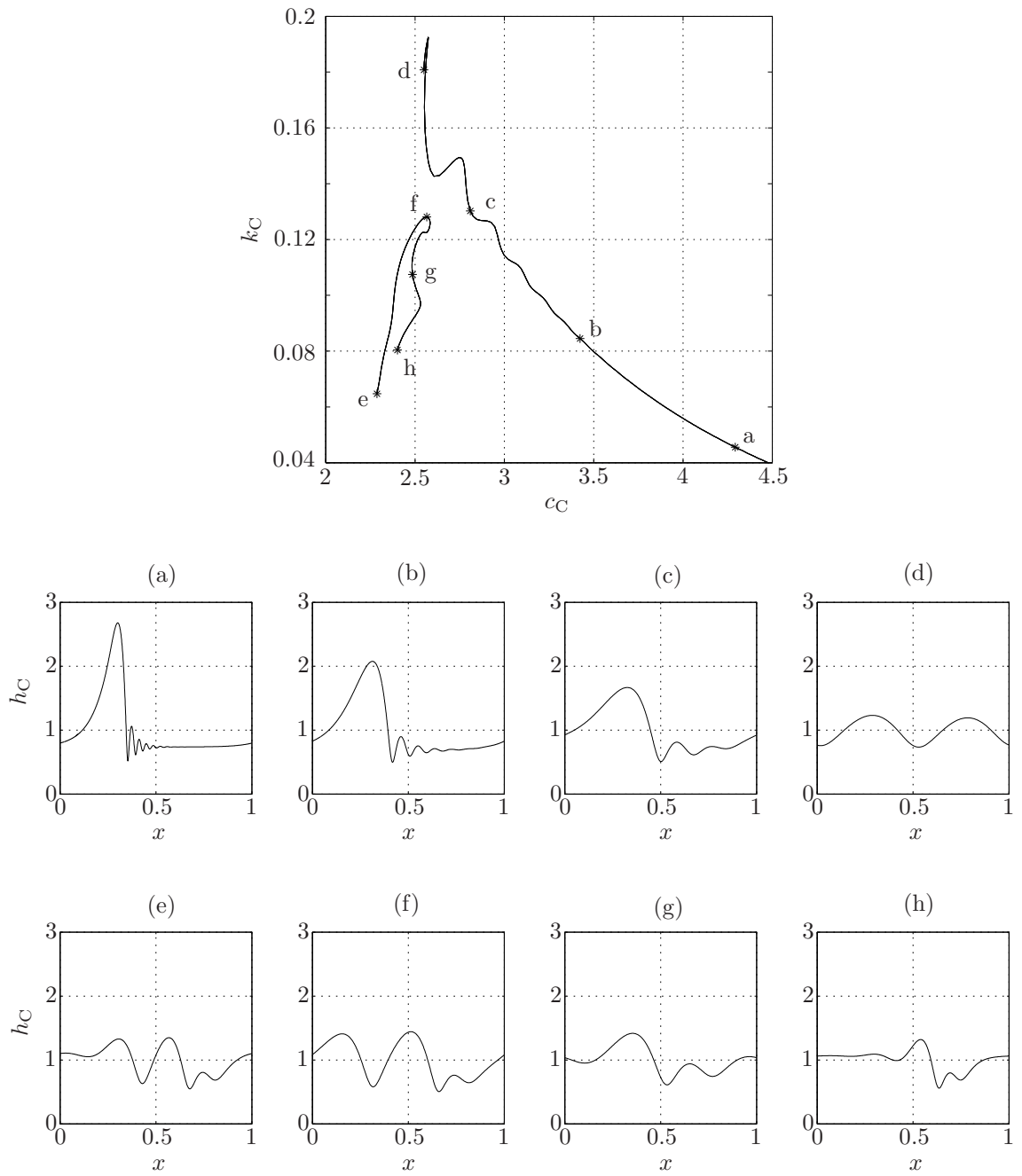


Figure 4.14.: Selected wave forms for $Ka = 500$ and $Re_C = 10$. Upper row: Solutions along branch γ_2 . Lower row: Solutions along branch γ_3 .

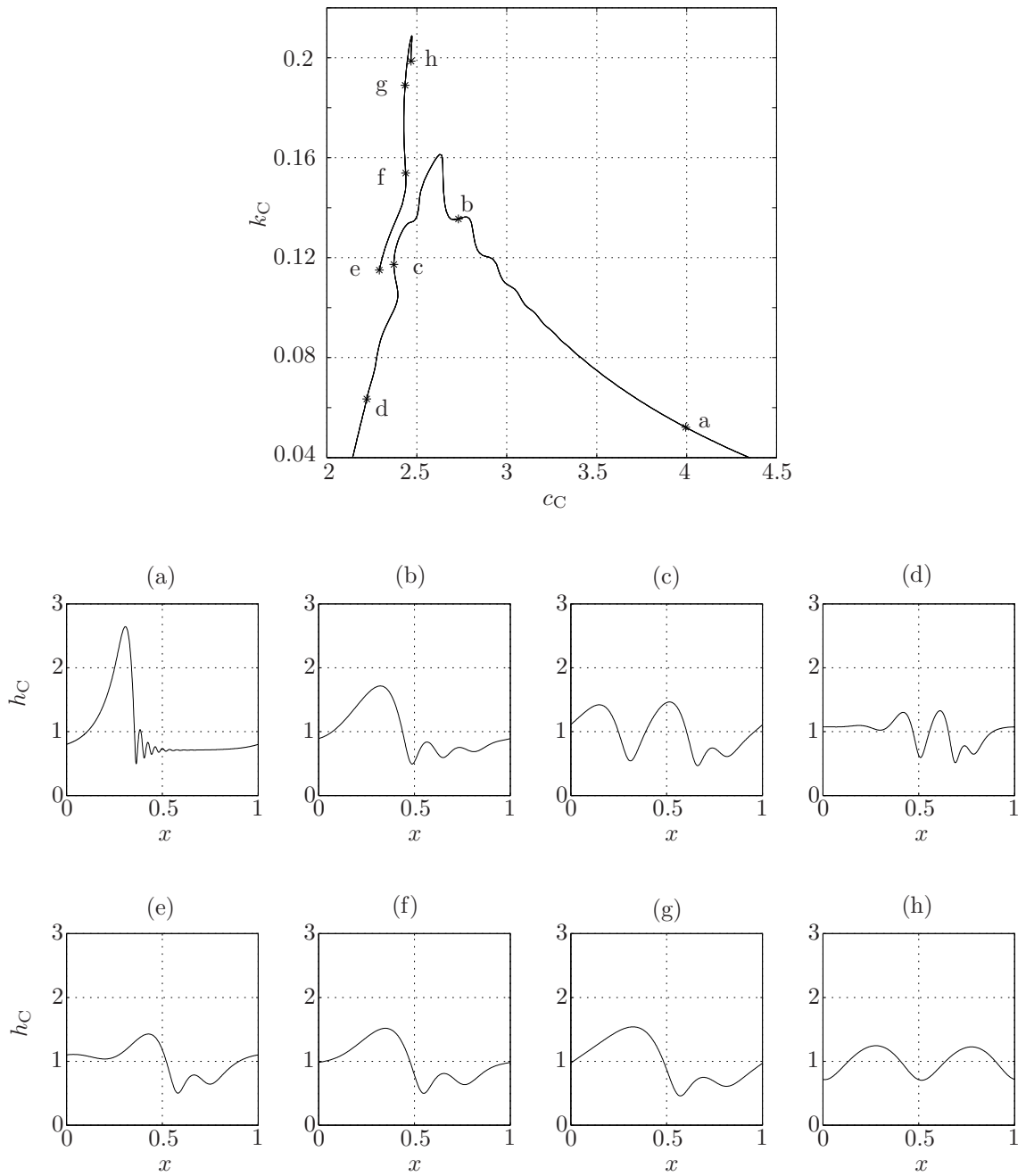


Figure 4.15.: Selected wave forms for $Ka = 500$ and $Re_C = 12$. Upper row: Solutions along branch γ_2 . Lower row: Solutions along branch γ'_2 .

4.3.2. Relation to unsteady simulations

Experiments and transient simulations typically employ a sinusoidal perturbation at the inlet corresponding to (4.13). It is known that the forcing frequency f_f is inherited to the flow if the perturbation amplitude a is sufficiently large. Due to this synchronization we equate the forcing frequency f_f with the wave frequency $f = kc/(2\pi)$, thus $f_f = f$. We shall then check whether the solutions of our steady simulations within the moving frame compare with the solutions of unsteady simulations within the laboratory frame. For a comparison we use the results presented by Dietze (2010) who employed the VOF-method to solve the non-stationary Navier–Stokes equations. As already mentioned, the closed-flow condition used by Salamon *et al.* (1994) is rather impractical, so that we switch to the open flow condition from now on. From the data given by Dietze (2010) we obtain his time scale as

$$t_0 = \frac{h_{\text{Nu}}}{\bar{u}_{\text{Nu}}} = \left(\frac{9\nu}{g_x^2 \text{Re}} \right)^{1/3}. \quad (4.70)$$

Therefrom the non-dimensional frequency is $f = f^* t_0$. Table 4.4 summarizes most of the 2D-cases defined by Dietze (2010), where block A refers to a constant Re with different forcing frequencies, block B collects different Re with constant (dimensional) forcing frequency and block C contains the inclined cases. The case numbers used by Dietze are adopted and are given in the respective column. His Kapitza number Ka_D is related to the present one by $\text{Ka}_D = \text{Ka}/(\sin \theta)^{1/3}$, so that our Kapitza number becomes $\text{Ka} = 116.1$ for the inclined cases.

Table 4.4.: Selected two dimensional cases defined by Dietze (2010).

block	case	Re	Ka_D	θ/deg	$\nu/10^{-6} \text{ m}^2 \text{ s}^{-1}$	f^*/s^{-1}	$h_{\text{Nu}}/\mu\text{m}$	$f \times 10^3$
A	6	10.7	509.5	90	2.85	16.0	298	46.73
	10	10.7	509.5	90	2.85	18.0	298	52.57
	9	10.7	509.5	90	2.85	20.0	298	58.41
B	5	8.6	509.5	90	2.85	16.0	277	50.26
	7	12.9	509.5	90	2.85	16.0	318	43.90
	8	15.0	509.5	90	2.85	16.0	334	41.75
C	4	21.4	139.8	35	5.21	11.3	677	46.39
	3	21.4	139.8	35	5.21	17.7	677	72.67
	2	21.4	139.8	35	5.21	24.0	677	98.54

Before we concentrate on the particular solutions for the cases given in Table 4.4, we construct the relevant solution branches in the ck -plane by employing the open flow condition. The results for $\text{Re} = \{8.6, 10.7, 12.9, 15\}$, $\text{Ka} = 509.5$ and $\theta = \pi/2$ are shown in

Figure 4.16 (top). Firstly, we see that the branches look qualitatively different from the ones that are constructed with the closed flow condition. Using the notation from above we find that the branches for $\text{Re} = \{8.6, 10.7\}$ are members of the γ_2 -family since the respective solution at the upper end of the branch is almost sinusoidally shaped. Between $\text{Re} = 8.6$ and $\text{Re} = 10.7$ the branches change their shape significantly. A bifurcation took place in between similar as in Figure 4.13. The branches for $\text{Re} = \{12.9, 15\}$ are therefore of γ'_2 -type. For the inclined case, the solution branches γ_2 and γ'_2 will be important later, both shown in Figure 4.16 (bottom).

A detailed analysis of the relevant solution branches is given in Figures 4.17 – 4.21 for all (Re, Ka) -combinations of Table 4.4. All figures hold four images and are structured as follows.

- Northwest: The (relevant) solution branches are presented in the ck -plane, as in Figure 4.16.
- Northeast: The ck -plane is mapped to the fc -plane. This is more intuitive, since the frequency f serves as independent variable. In addition, the forcing frequencies from Table 4.4 are given as vertical, dashed lines and the resulting intersection points are drawn as bullets.
- Southwest: The averaged height \bar{h} is presented in this image as function of f .
- Southeast: This image shows the surface length increase ΔA , which is defined as

$$\Delta A := \int_0^1 \sqrt{1 + h'^2} dx - 1. \quad (4.71)$$

In general we can conclude that the surface length increase ΔA is small for all cases so that we do not expect a relevant influence for the absorption process. In turn, the averaged height \bar{h} is reduced significantly for many cases and a more detailed analysis concerning absorption enhancement will be given in the next chapters. Regarding the intersection points we find different scenarios.

- Figure 4.17 ($\text{Re} = 8.6$) indicates a unique intersection with the solution branch γ_2 . We shall note that the chosen frequency is located in a region with a steep slope so that a small variation of f leads to a relatively large deviation of c .
- Figure 4.18 ($\text{Re} = 10.7$) shows three intersections with γ_2 for the largest frequency, indicating a non-unique solution. This is nothing outstanding since the non-uniqueness is the rule rather than the exception for the present system.
- Figure 4.19 ($\text{Re} = 12.9$) and Figure 4.20 ($\text{Re} = 15$) show the same scenario. Practically two solutions are found on γ'_2 for every case even if only one intersection point is

drawn. The second intersections are not realized on the images since we have abandoned to continue the γ_2' -branch into the region of small c . This is motivated by the comparison of Figure 4.15 (a) with 4.15 (d), showing qualitatively very different solutions at the ends of the branch.

- Figure 4.21 (Re = 21.4 inclined) shows beside all other cases that the intersection for the largest frequency is only possible with the γ_2 -branch. Intersections that are not indicated by a bullet are simply not relevant for our purpose.

Once the intersection points are found we extract the respective wave celerity c and obtain the non-dimensional wave number $k = 2\pi f/c$ with the given non-dimensional forcing frequency f . Finally, the scale h_{Nu} leads us to the dimensional wavelength $L^* = h_{Nu}2\pi/k$ which we compare with the wavelength L_D^* that has been extracted from Dietze (2010). All data are summarized in Table 4.5. We find a good agreement for most cases between the dimensional wavelength of our solution branch L^* and the wavelength from the transient simulation L_D^* . However, case 9 has a noticeable variation in L_D^* . We speculate that this is caused by the non-uniqueness. Also, case 4 shows a significant error in contrast to the remaining inclined cases.

Table 4.5.: Data at the intersection points.

block	case	Re	c	k	L^*/mm	L_D^*/mm
A	6	10.7	2.718	0.1080	17.36	17.35
	10	10.7	2.535	0.1303	14.39	14.35
	9	10.7	2.487	0.1476	12.70	11.3 ... 12.4
			2.475	0.1483	12.65	
			2.348	0.1563	12.00	
B	5	8.6	2.709	0.1166	14.95	14.75
	7	12.9	2.686	0.1027	19.43	19.40
	8	15.0	2.660	0.0986	21.28	21.13
C	4	21.4	2.533	0.1151	36.94	32.80
	3	21.4	2.154	0.2120	20.05	19.56
	2	21.4	1.922	0.3221	13.20	13.11

The Figures 4.22 – 4.24 present the qualitative comparisons for all cases showing an excellent agreement except for the cases 4 and 9. The variation of L_D^* in case 9 is also reflected in Figure 4.22 where a clear matching, which is easily possible for the other cases, is difficult to obtain. It seems obvious that the non-uniqueness of this case is responsible for this issue and we speculate that the wave train contains more than only one of the possible solutions. The excellent overall agreement is somewhat irritated by the poor comparison of case 9. However, since the remaining inclined cases compare very well, we

are able to rule out an erroneous code for inclination angles other than $\theta = \pi/2$. At the end, the reason for the deviation remains unclear.

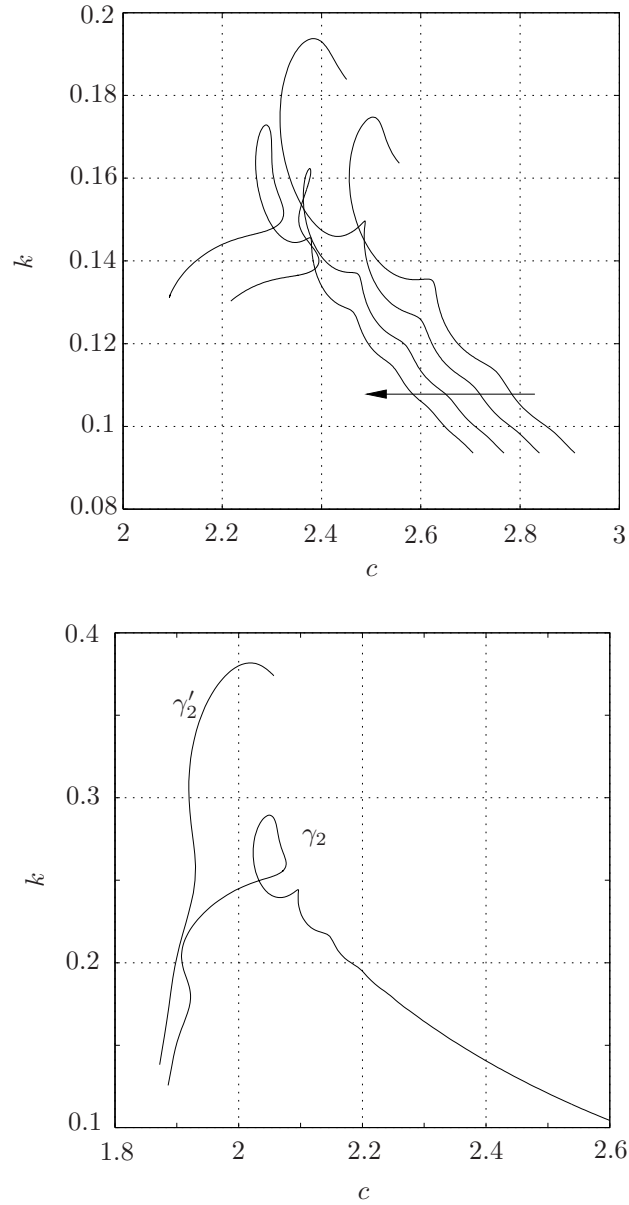


Figure 4.16.: Top: Relevant solution branches for $\text{Re} = \{8.6, 10.7, 12.9, 15\}$, $\text{Ka} = 509.5$ and $\theta = \pi/2$. The arrow indicates the direction of increasing Re . Bottom: Solution branches γ_2 and γ'_2 for $\text{Re} = 21.4$, $\text{Ka} = 116.1$ ($\text{Ka}_D = 139.8$) and $\theta = 35^\circ$.

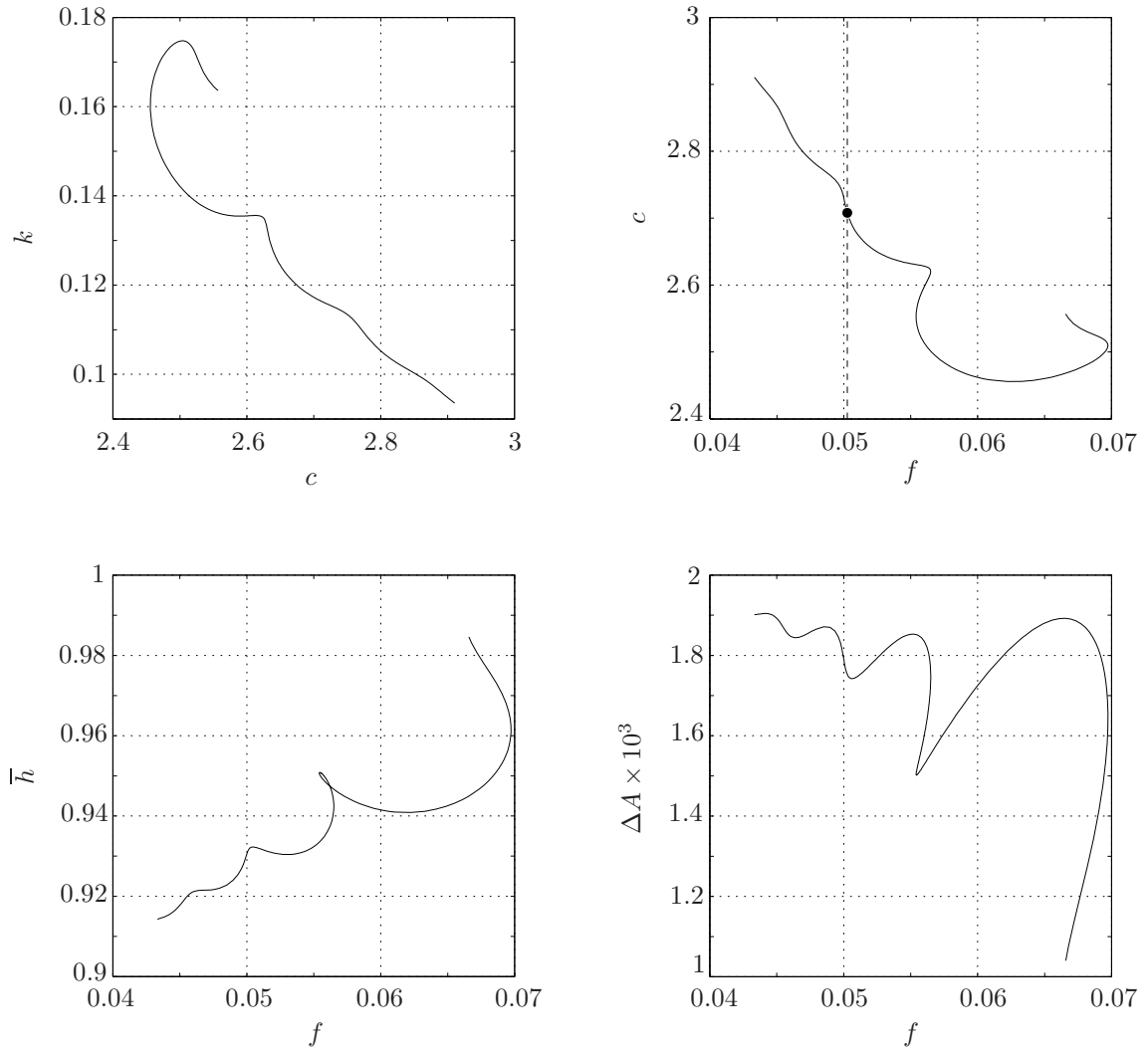


Figure 4.17.: Results for the parameter set $\text{Re} = 8.6$, $\text{Ka} = 509.5$ and $\theta = \pi/2$. (a) Solution branch γ_2 in the ck -plane and (b) in the fc -plane. The vertical line indicates the forcing frequency from Table 4.4. (c) Averaged height \bar{h} and (d) surface area increase ΔA vs. wave frequency f .

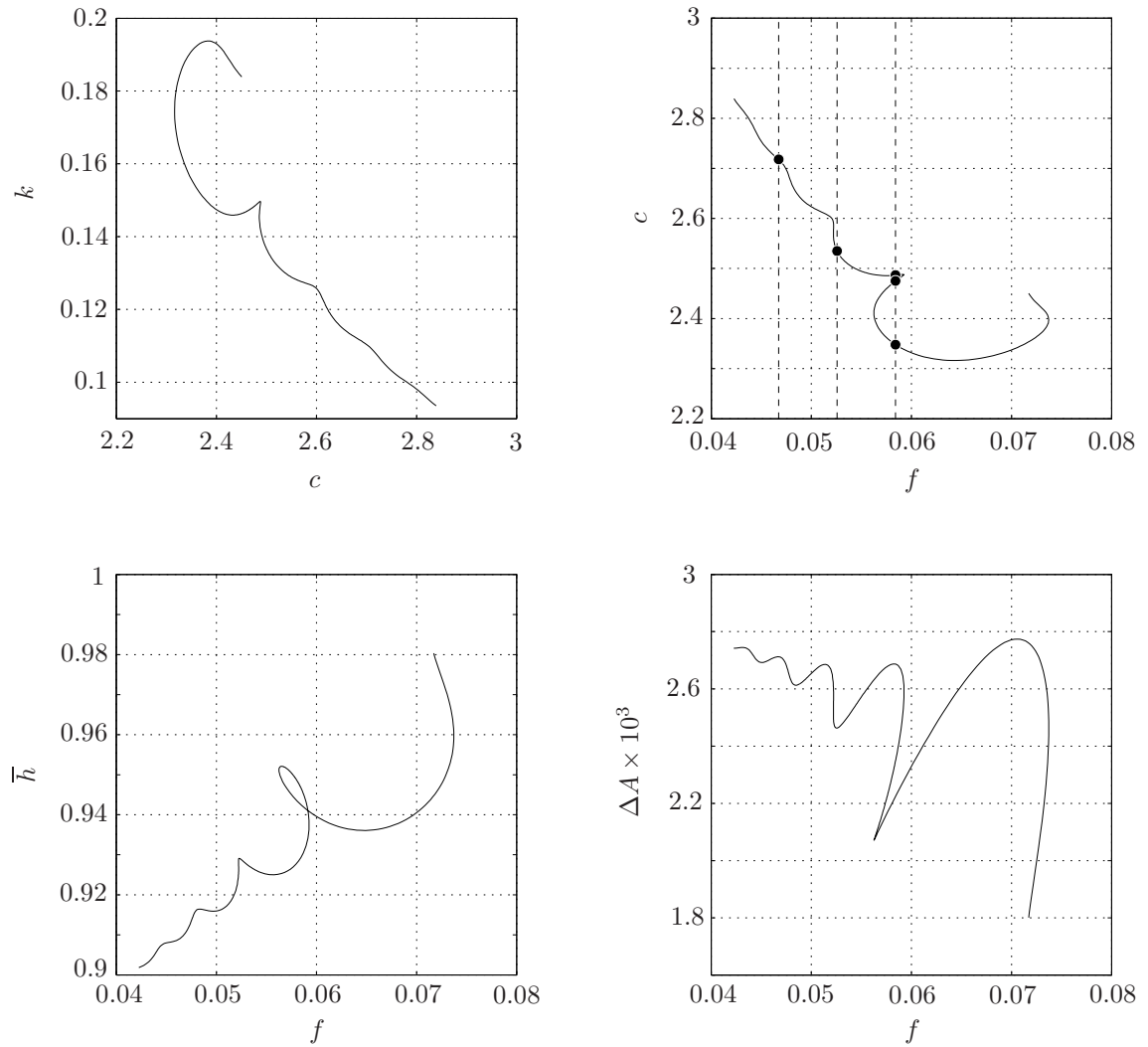


Figure 4.18.: Results for the parameter set $Re = 10.7$, $Ka = 509.5$ and $\theta = \pi/2$. (a) Solution branch γ_2 in the ck -plane and (b) in the fc -plane. The vertical lines indicate the forcing frequencies from Table 4.4. (c) Averaged height \bar{h} and (d) surface area increase ΔA vs. wave frequency f .

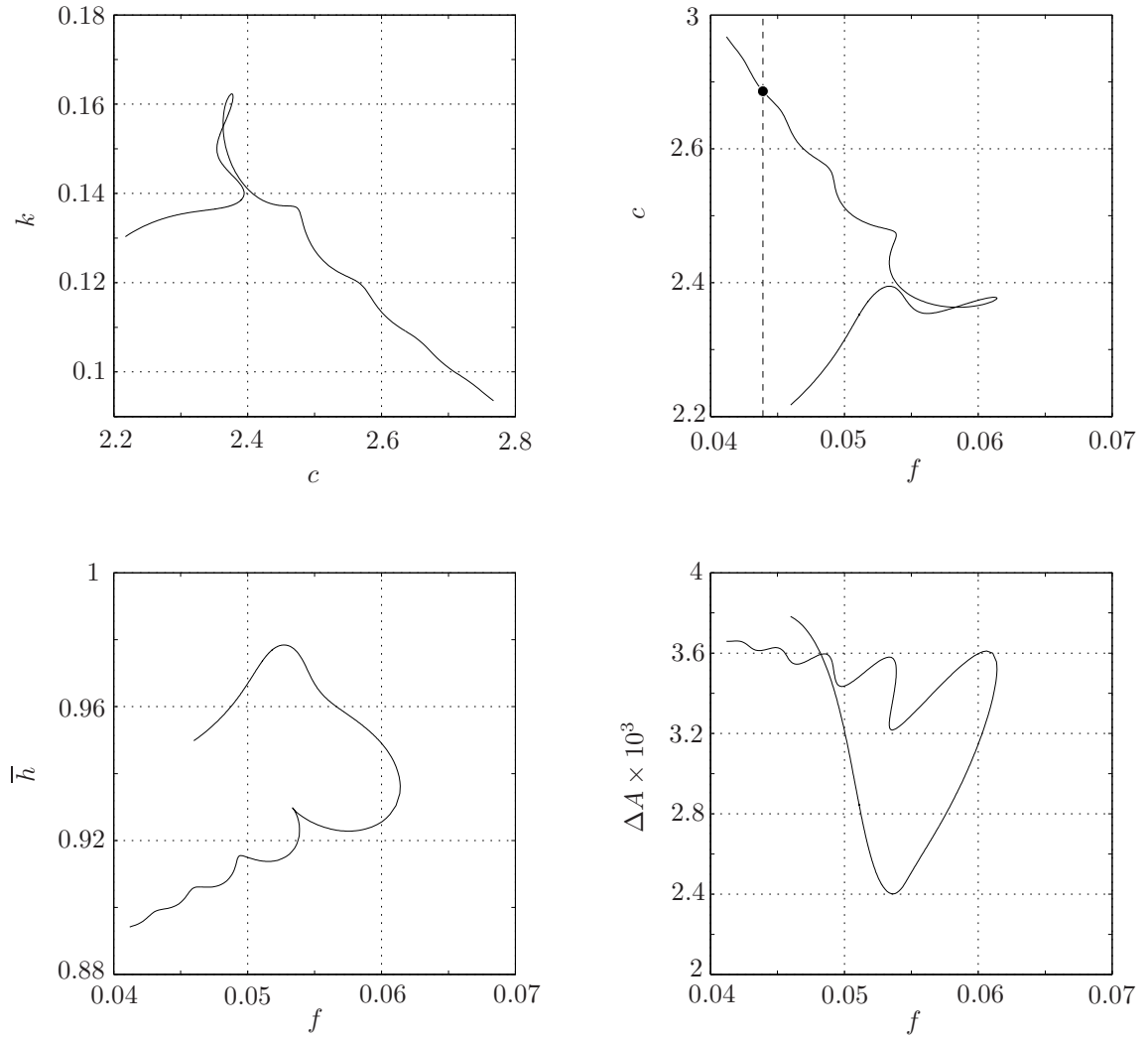


Figure 4.19.: Results for the parameter set $\text{Re} = 12.9$, $\text{Ka} = 509.5$ and $\theta = \pi/2$. (a) Solution branch γ_2 in the ck -plane and (b) in the fc -plane. The vertical line indicates the forcing frequency from Table 4.4. (c) Averaged height \bar{h} and (d) surface area increase ΔA vs. wave frequency f .

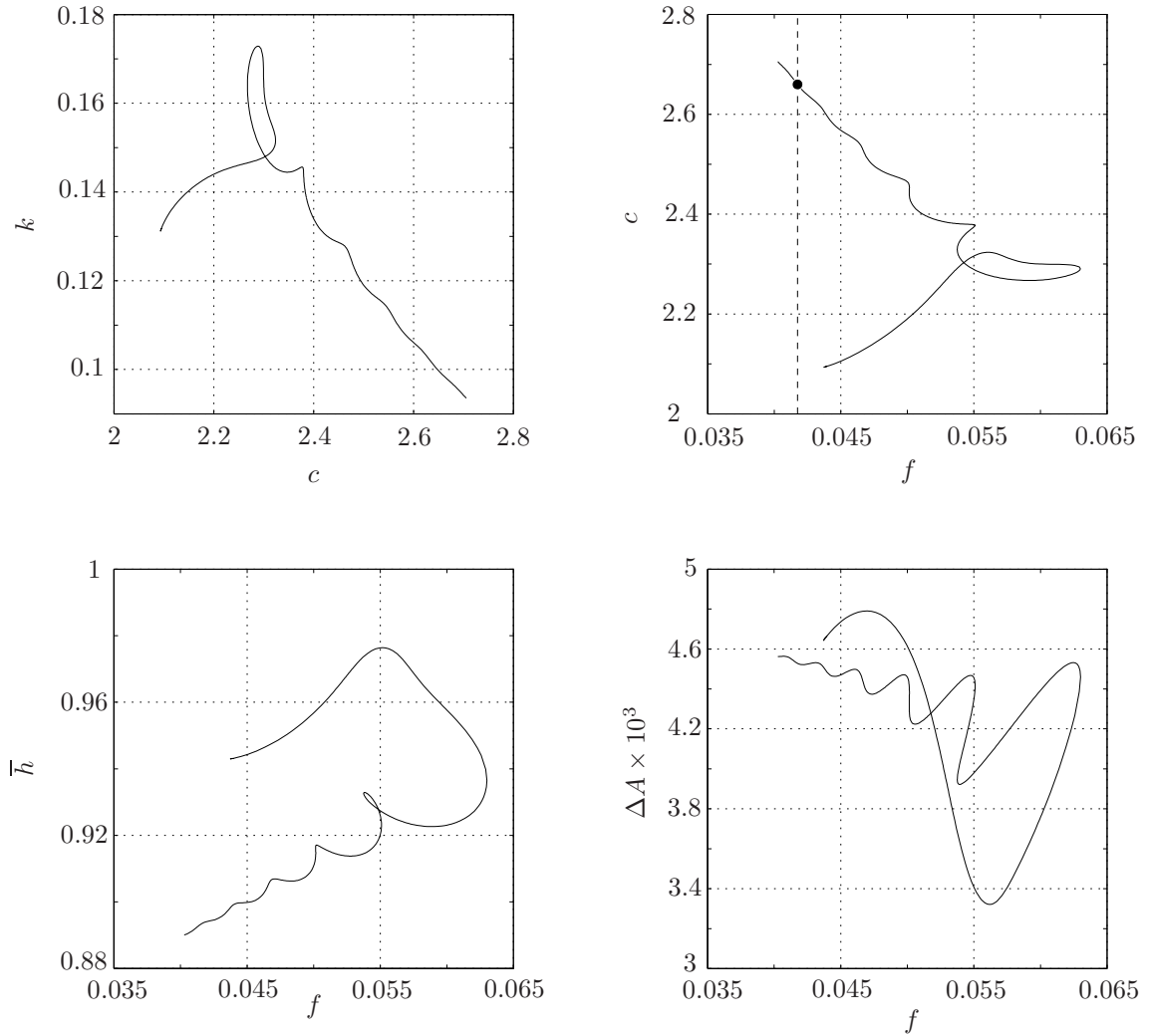


Figure 4.20.: Results for the parameter set $\text{Re} = 15$, $\text{Ka} = 509.5$ and $\theta = \pi/2$. (a) Solution branch γ_2 in the ck -plane and (b) in the fc -plane. The vertical line indicates the forcing frequency from Table 4.4. (c) Averaged height \bar{h} and (d) surface area increase ΔA vs. wave frequency f .

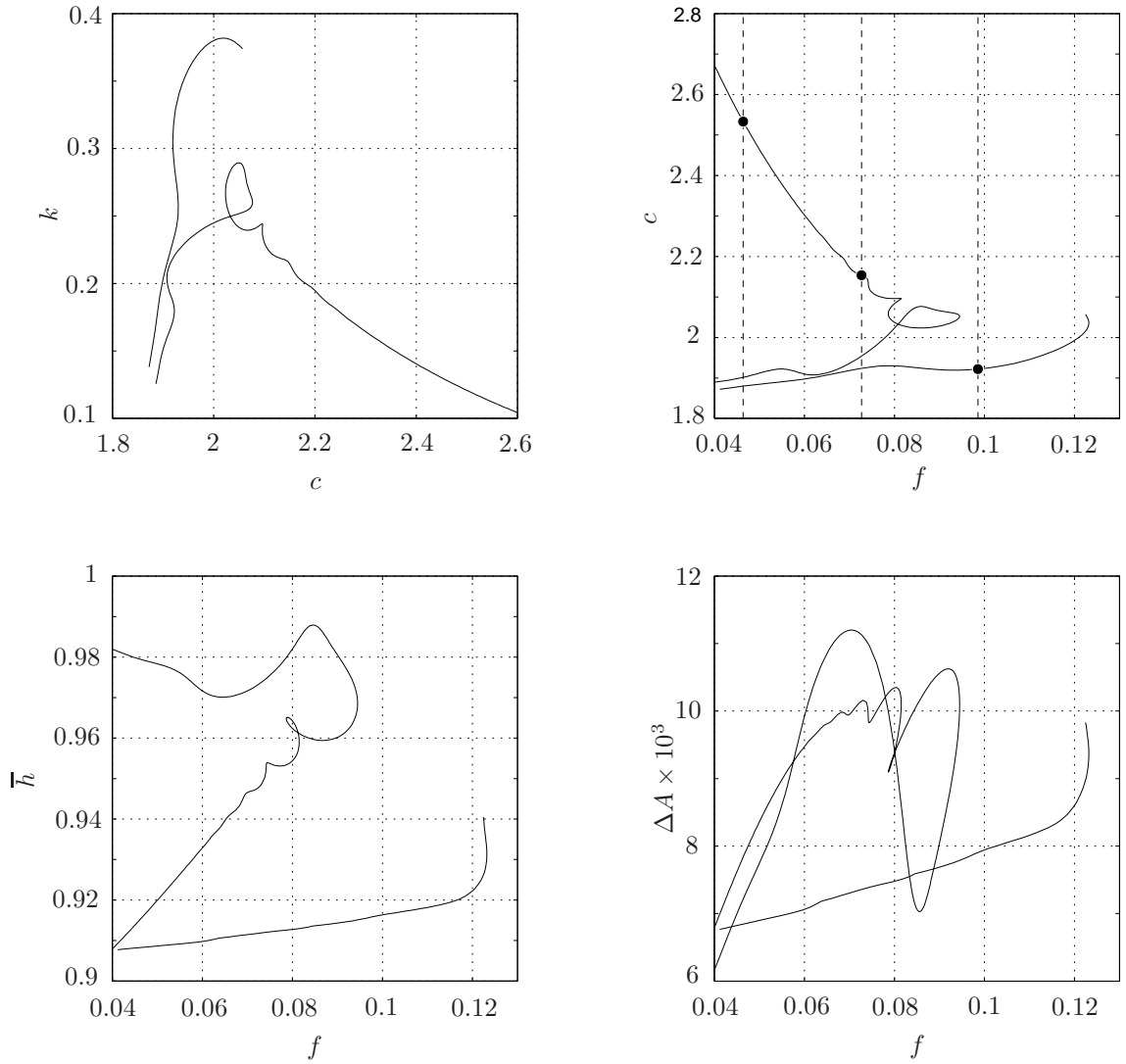


Figure 4.21.: Results for the parameter set $\text{Re} = 21.4$, $\text{Ka} = 116.1$ ($\text{Ka}_D = 139.8$) and $\theta = 35^\circ$. (a) Solution branches γ_2 and γ'_2 in the ck -plane and (b) in the fc -plane. The vertical lines indicate the forcing frequencies from Table 4.4. (c) Averaged height \bar{h} and (d) surface area increase ΔA vs. wave frequency f .

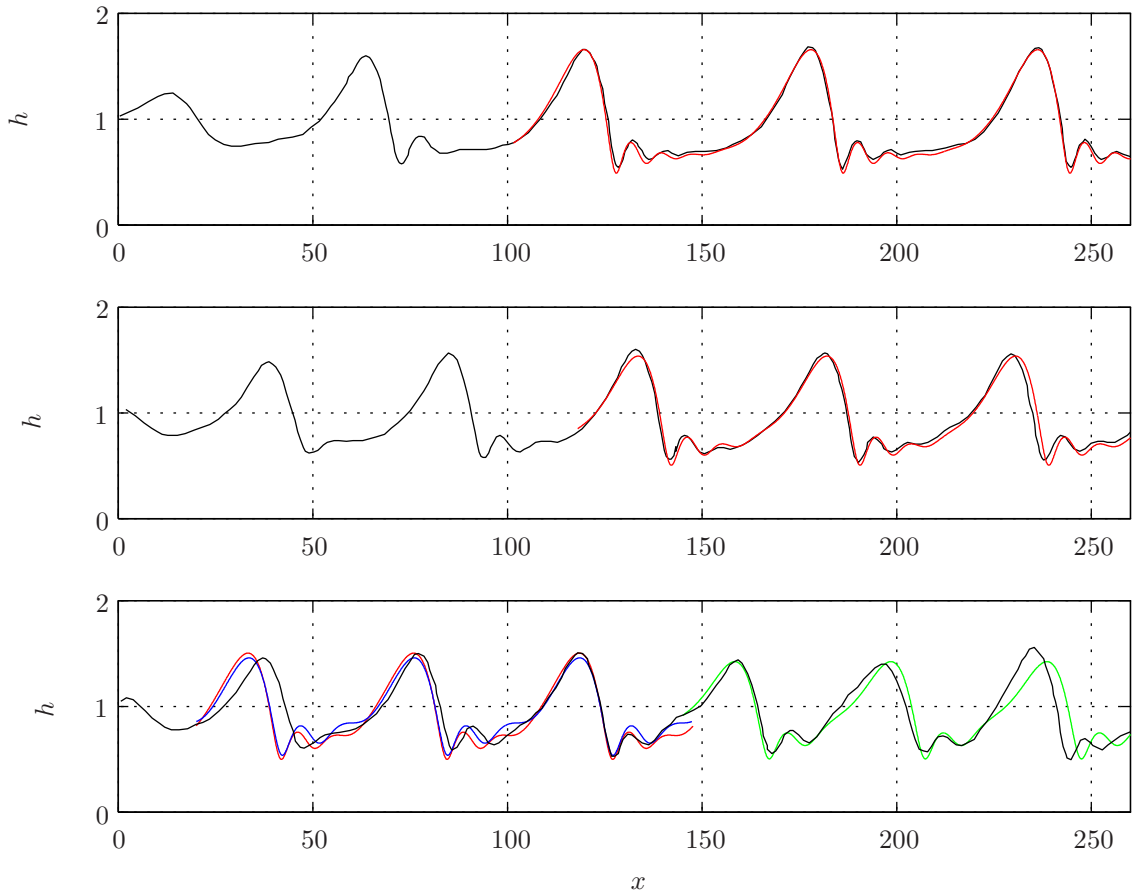


Figure 4.22.: Comparison for the cases of block A defined in Table 4.4 employing $Re = 10.7$. The red graphs represent the solutions at the corresponding intersection points and the black graphs correspond to the data extracted from Dietze (2010). Uppermost image: Case 6, $f^* = 16$ Hz, Central image: Case 10, $f^* = 18$ Hz, Lowermost image: Case 9, $f^* = 20$ Hz. The two additional solutions are given in green and blue.

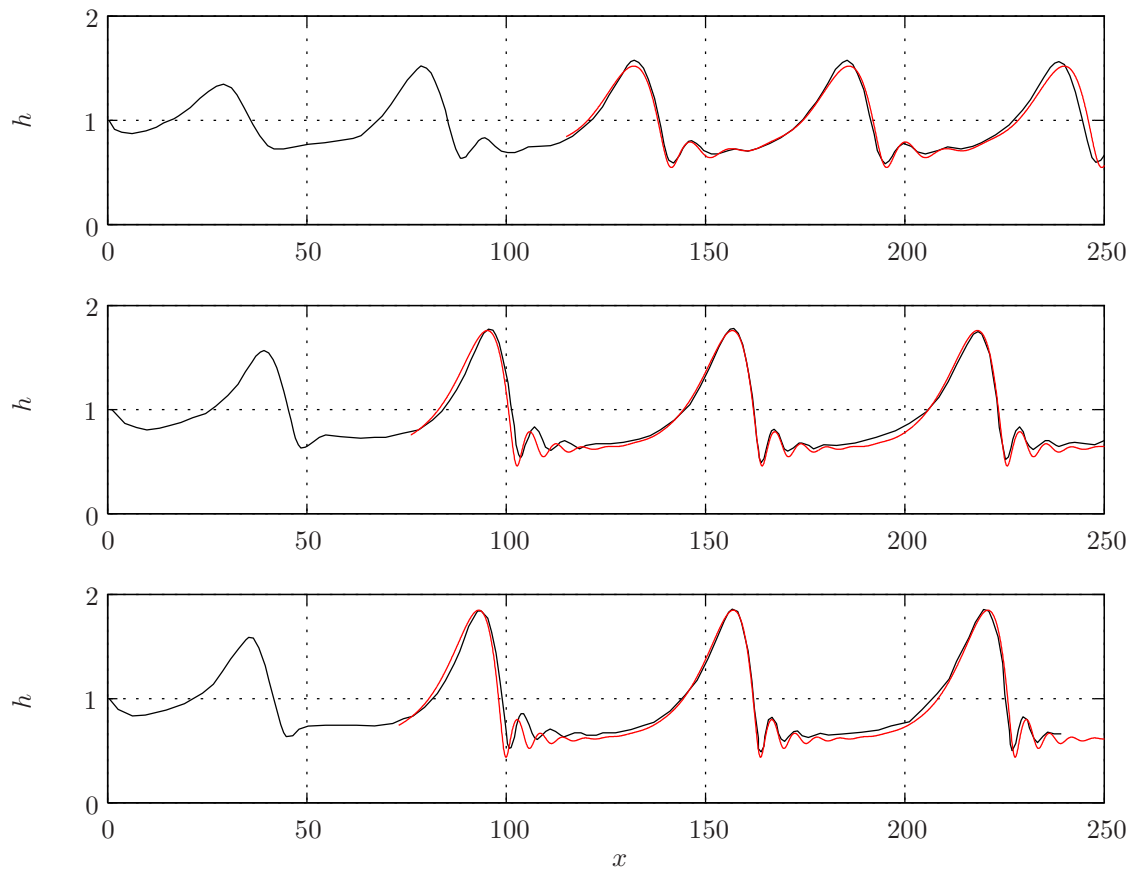


Figure 4.23.: Comparison for the cases of block B defined in Table 4.4 employing $f^* = 16$ Hz. The red graphs represent the solutions at the corresponding intersection points and the black graphs correspond to the data extracted from Dietze (2010). Uppermost image: Case 5, $\text{Re} = 8.6$, Central image: Case 7, $\text{Re} = 12.9$, Lowermost image: Case 8, $\text{Re} = 15$.

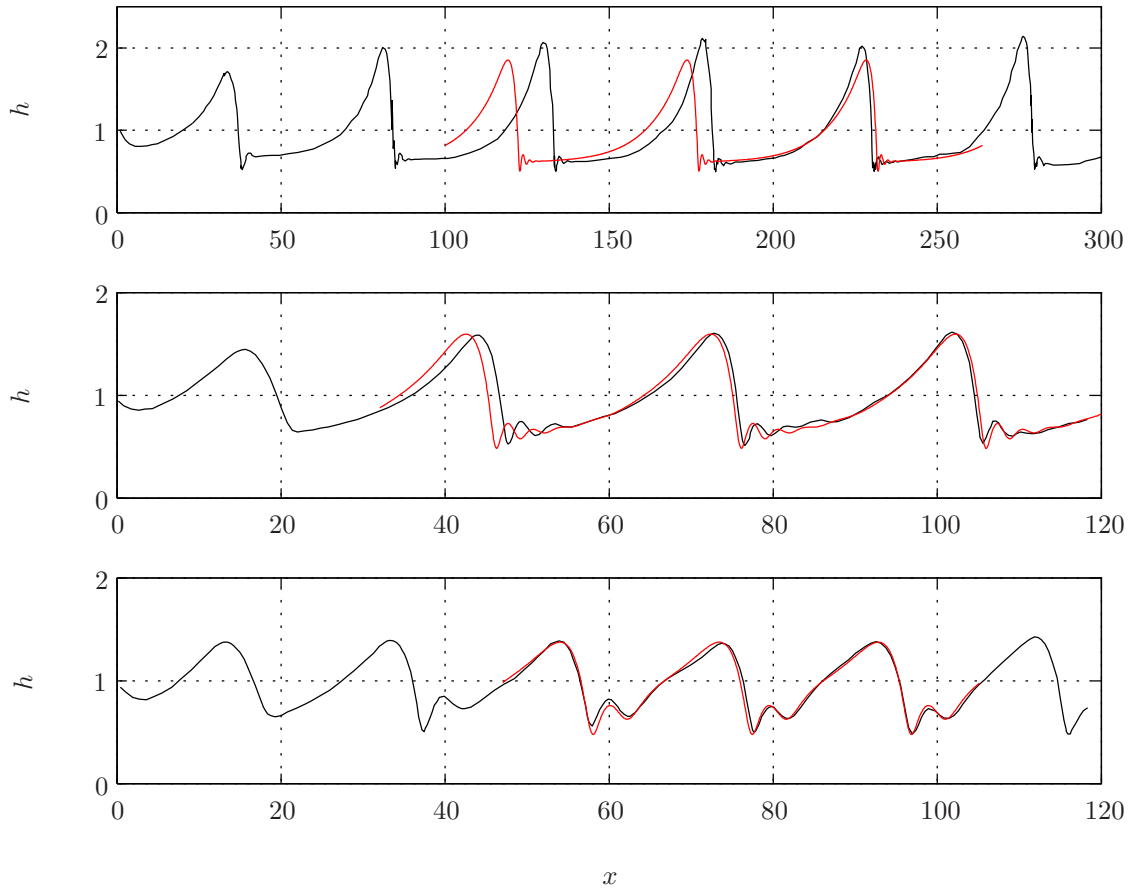


Figure 4.24.: Comparison for the cases of block C defined in Table 4.4 employing $Re = 21.4$ (inclined). The red graphs represent the solutions at the corresponding intersection points and the black graphs correspond to the data extracted from Dietze (2010). Uppermost image: Case 4, $f^* = 11.3$ Hz, Central image: Case 3, $f^* = 17.7$ Hz, Lowermost image: Case 2, $f^* = 24$ Hz.

4.3.3. Backflow phenomenon

As it was shown by [Dietze \(2010\)](#) and [Dietze *et al.* \(2008\)](#) the falling film exhibits backflow regions for certain parameter ranges. Figure 4.25 shows again all solution branches where the solutions without backflow are indicated as thick segments. From the figure it becomes evident that the majority of the solutions are those with at least one backflow region. Certainly, this statement holds true only for the given parameter set and has no general character. However, we can expect that the fraction of backflow solutions reduces in general for decreasing Re and/or increasing Ka corresponding to an increase of We .

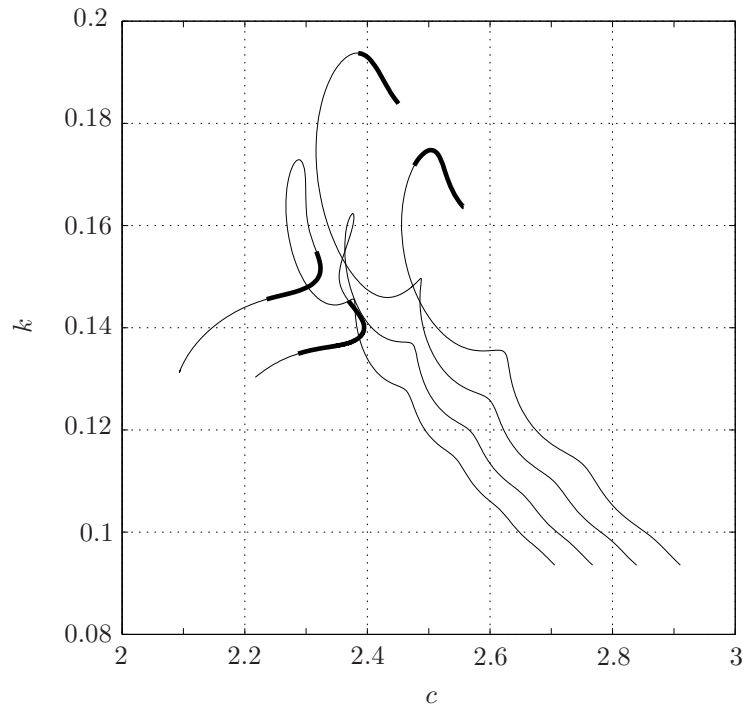


Figure 4.25.: Solution branches for $Re = \{8.6, 10.7, 12.9, 15\}$, $Ka = 509.5$ and $\theta = \pi/2$ where all solutions without backflow are indicated as thick segments.

Figure 4.26 shows the result of case 8 as an exemplary solution with two backflow regions. The bounds associated with $u = 0$ are shown in red, the upper image depicts the pressure distribution and lower image the velocity field. From the figure it is clear that the pressure (grayscale) is almost constant across the film and that the streamwise velocity seems to retain a semi-parabolic profile, at least for the regions outside the backflow. Both observations are clear indicators that the BL-approach may still be a good approximation for this parameter set. For a test we use our solution and extract $h(x)$ and $\Gamma(x) = \int_0^h u(x, y) dy$. With these data we then evaluate the self-similar velocity distribution that

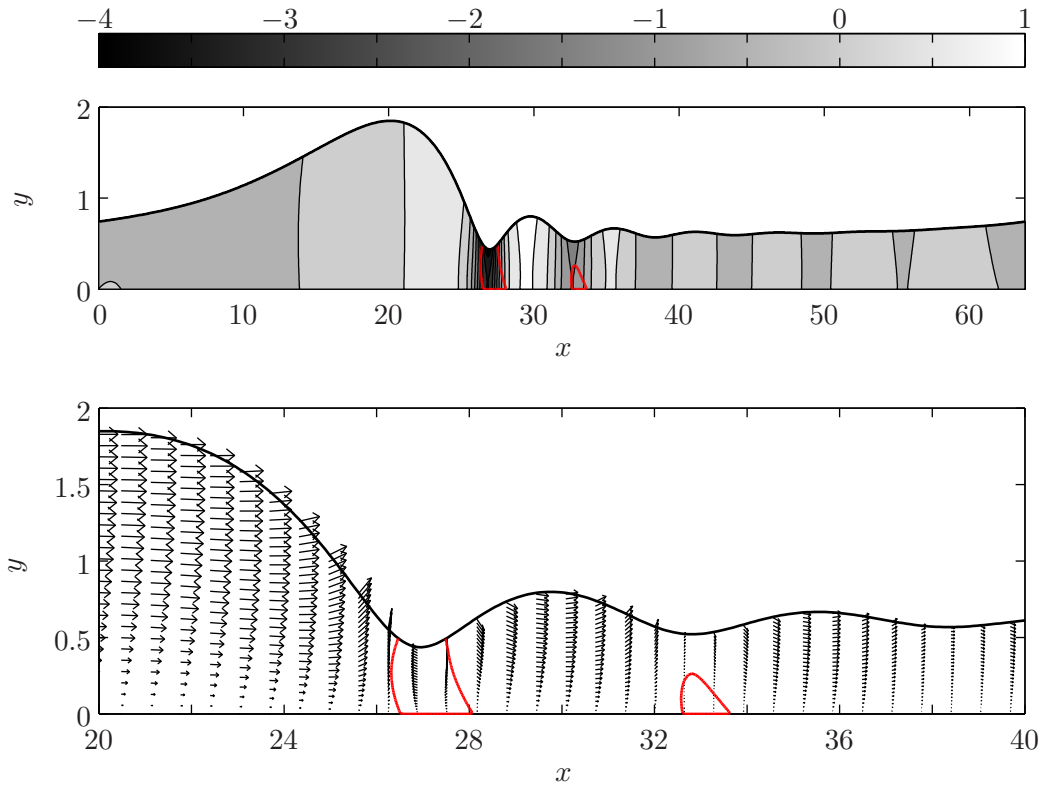


Figure 4.26.: Exemplary solution with two backflow regions for $\text{Re} = 15$, $\text{Ka} = 509.5$, $\theta = \pi/2$ and $k = 0.0986$ (case 8). Upper image: Pressure (grayscale) and bounds of the backflow regions $u = 0$ (red). Lower image: Close up with velocity field (within the laboratory frame) and again with the bounds of the backflow regions (red).

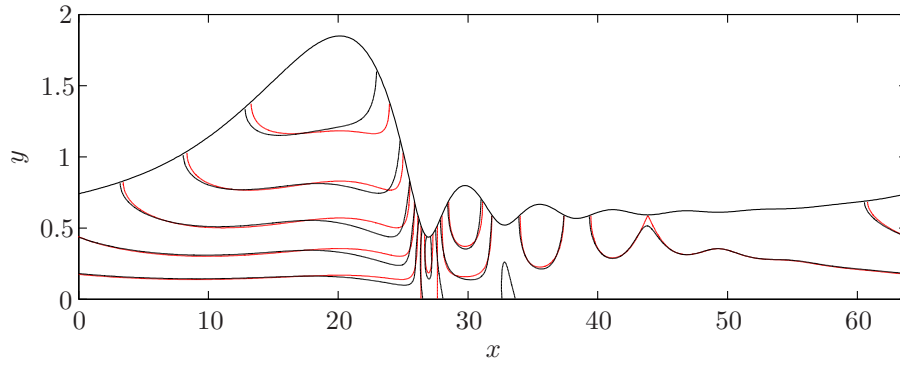


Figure 4.27.: Isolines of the streamwise velocity component $u(x, y)$ from the present simulation (case 8 - black) and from the Kapitza–Shkadov assumption $u_{\text{KS}}(x, y)$ (red).

is known as the Kapitza–Shkadov approach (Kalliadasis *et al.*, 2012)

$$u_{\text{KS}} = 3 \frac{\Gamma}{h} \left[\frac{y}{h} - \frac{1}{2} \left(\frac{y}{h} \right)^2 \right]. \quad (4.72)$$

In Figure 4.27 we compare the isolines of the streamwise velocity component $u(x, y)$ from our Navier–Stokes simulation in black with the ones of the Kapitza–Shkadov assumption $u_{\text{KS}}(x, y)$ in red. In view of the simplicity of the approach the result is very good. We shall note that we have employed $\Gamma(x)$ and $h(x)$ from the Navier–Stokes-solution so that we can just argue that (4.72) is a reasonable approximation to the Navier–Stokes-solution (for the present parameter set). The given evaluation cannot verify whether $\Gamma(x)$ and $h(x)$, resulting from a reduced order model, are in agreement with the Navier–Stokes solution.

4.3.4. Variation of the Reynolds number

We finally present the solution path within the k - c - Re -space for $\text{Ka} = 3000$ and $k = 0.0365$ by varying the Reynolds number starting from $\text{Re} = 11$ up to $\text{Re} = 100$. To that end we used the solution $\{\text{Re}, \text{Ka}, k\} = \{10.7, 509.5, 0.1\}$ as initial guess, increased $\text{Re} \rightarrow 11$ manually, used the arclength continuation to follow the path until $k = 0.0365$, increased $\text{Ka} \rightarrow 3000$ manually and used the arclength continuation again for $\text{Re} \rightarrow 100$. The evolution of the height $h(x)$ along Re is shown in Figure 4.28. The most obvious qualitative results of the image are the appearance of a maximum for h_{max} and that the wavelength of the capillary waves decrease with increasing Re . The left image of Figure 4.29 shows the variation of the maximum height h_{max} and the celerity c versus Re where we find the maximum of h_{max} at $\text{Re} \approx 45$. The right image presents the averaged height \bar{h} versus Re showing a minimum at $\text{Re} \approx 31$.

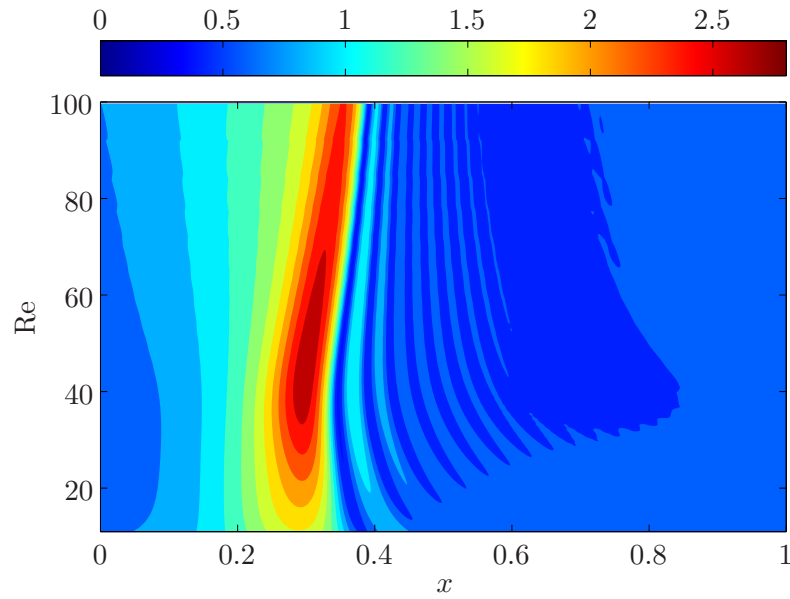


Figure 4.28.: Contours of the height $h(x)$ as function of Re and x for $\theta = \pi/2$, $Ka = 3000$ and $k = 0.0365$.

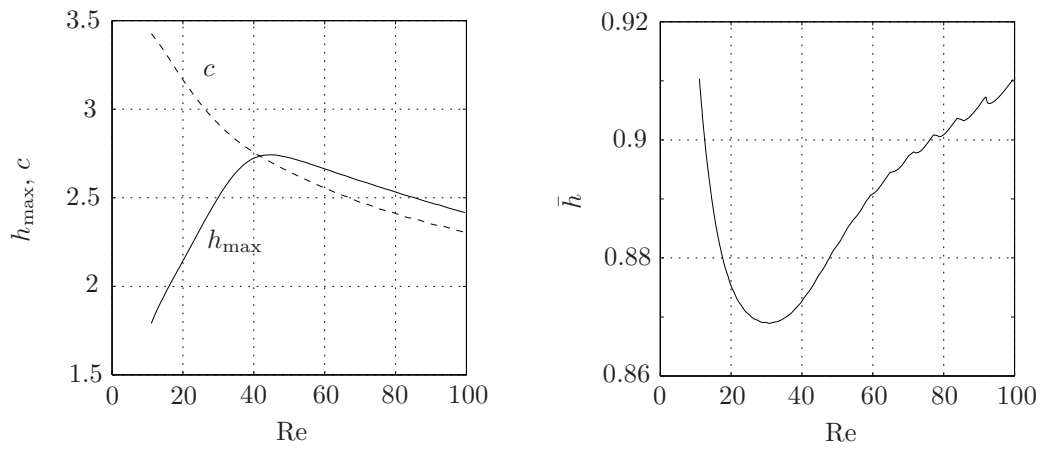


Figure 4.29.: Left: Maximum height h_{\max} (full) and celerity c (dashed) vs. Re . Right: Averaged height \bar{h} vs. Re . The remaining parameters are $\theta = \pi/2$, $Ka = 3000$ and $k = 0.0365$.

4.4. Interim summary

We briefly summarize the results of this Chapter 4.

- The implemented numerical method including the bordering algorithm works fast and the solution branches can be efficiently tracked by the arclength continuation even for relatively large Reynolds numbers.
- The comparison of our results with [Salamon *et al.* \(1994\)](#) (steady, closed flow condition) is outstanding.
- We have shown that our steady-solutions can be matched with the forced, transient solutions given by [Dietze \(2010\)](#) by using the open flow condition. Again, the agreement is excellent for almost all cases presented. The prediction of the wave form by intersecting the solution branch with the forcing frequency works also excellent. The construction of the entire solution branch(es) is tedious but it represents a rich source for experimentalist to properly choose the forcing frequencies. For instance, one could avoid/choose values leading to non-unique solutions that lie closely together.
- For Kapitza number $Ka = 509.5$ regions of backflow are the rule rather than the exception, even for small Re .
- The variation of Re for a given k leads to a continuously decreasing celerity c , a maximum for h_{\max} and a minimum for \bar{h} . Also, the wavelength of capillary waves decreases for increasing Re .

We may draw the following interim conclusions for our further analysis regarding absorption.

- The surface increase ΔA is generally small, i.e. $\Delta A < 1\%$ for the cases shown. Therefrom we can conclude that ΔA is not relevant for significant absorption enhancement.
- The averaged height of the liquid film \bar{h} is reduced significantly so that an impact on absorption enhancement is expected.
- Convective heat and mass transport due to the backflow regions may also contribute to absorption enhancement.

5. The thermal wavy film

The present chapter briefly discusses the evaporating/condensing falling film with a vanishing evaporation/condensation rate, *thermal film* called in the following. We assume one-way coupling, an isothermal wall and a free surface being in local thermodynamic equilibrium. The latter assumption yields an isothermal free surface with the evaporation temperature as temperature level. Due to the assumption of one-way coupling we are free to employ the solutions of the isothermal wavy film so that $\mathbf{u} = \mathbf{u}(x, y, t)$ and $h = h(x, t)$ are known in the thermal transport equation. Therefrom, the discussion can be done within the moving frame of reference. The numerical treatment is very simple, since we can employ the convective and diffusive terms from Chapter 4, i.e. we adapt (4.21a) by replacing the streamwise velocity u with the temperature T , yielding

$$\oint \phi T \, dO = \frac{1}{\text{Pe}} \oint \mathcal{D}T \, dO \quad (5.1)$$

with the the Péclet number $\text{Pe} = \text{RePr}$, as product of film Reynolds number Re and Prandtl number Pr , the volume flux density ϕ and the (bulk) normal derivative operator \mathcal{D} given in (4.22). The boundary conditions

$$T|_{\xi=0} = T|_{\xi=1} \quad (5.2a)$$

$$T|_{\eta=0} = 0 \quad (5.2b)$$

$$T|_{\eta=1} = 1 \quad (5.2c)$$

are the periodic boundary condition, the isothermal wall and the isothermal free surface.

5.1. Flow field

For the investigation we reproduce the results given by Miyara (1999). In this paper, the transient Navier–Stokes and energy equations are solved on a fixed grid employing the HS MAC method. The surface waves are triggered by a sinusoidal inlet perturbation. The simulations cover the domain $(x \times t) = (600 \times 700)$ in non-dimensional units, where the Nusselt film thickness h_{Nu} serves as length scale and $h_{\text{Nu}}/u_{\text{Nu,max}}$ as time scale with the surface velocity $u_{\text{Nu,max}}$. At $t = 700$ Miyara (1999) identifies, depending on the distance

from the inlet, the *developing wave*, the *semi-developed wave* and the *fully-developed wave*.

From the parameters given by Miyara (1999) (scaled by the Nusselt surface velocity), we obtain for our simulation $Re = 100/1.5 \approx 66.7$, $\theta = \pi/2$ and $Ka = 3400$. With the given celerity $c = 1.72$ (for the fully developed wave) and the frequency $f = 0.01$, the wave number becomes $k = 2\pi f/c = 0.0365$. The parameters for the mesh are chosen as $N_\eta = 80$ (crosswise resolution) and $R = 3$ (cell aspect ratio).

The streamlines within the moving frame of reference are shown in Figure 5.1 and shall represent the *fully developed wave* of Miyara (1999). Also, the backflow regions within the laboratory frame are indicated by red curves. Our maximum height is $h_{\max} = 2.67$ and compares excellent with the value one can extract from the figures given by Miyara (1999). From our simulation we find $\bar{h} = 0.90$ and $\bar{h}^{-1} = 1.35$ where the latter is very close to the value given by Miyara (1999). Also, our celerity $c = 2.48$ is very close to his rescaled value $c = 1.72 \times 1.5 = 2.58$.

Figure 5.2 presents our result (black) with his semi-developed wave (red) and his fully developed wave (blue), where the phase is adjusted such that maximum heights merge. From the figure we see that the shape of our main hump compares well with the main hump of his fully-developed wave. However, the comparisons of the capillary wave regions are poor for both development stages of the wave given by Miyara (1999). Since we compare the results of a transient simulation on fixed grid with a high-resolution steady simulation on a boundary-fitted grid, the cause for this shortcoming may be related to numerical reasons. The numerics employed by Miyara (1999) may suffer from a more pronounced numerical diffusion, damping the capillary waves due to their large curvature. This speculation is also supported by the observation, that the shape of the main hump, the celerity and the maximum height are in excellent agreement, i.e. that the effect is local and related to the large curvature.

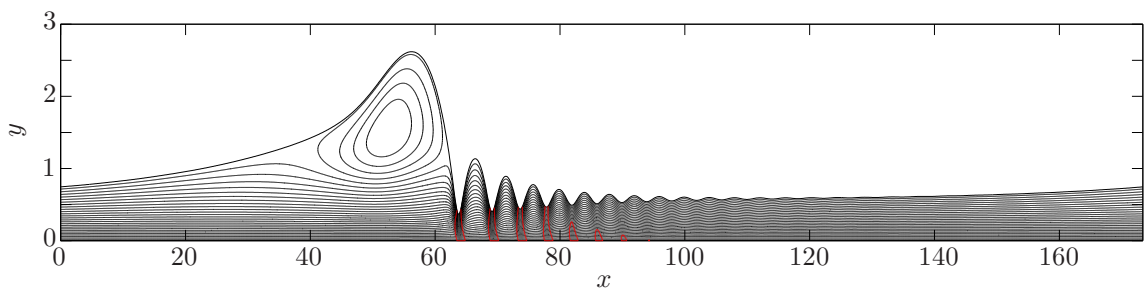


Figure 5.1.: Streamlines (within the moving frame) for $Re = 100/1.5 \approx 66.7$, $\theta = \pi/2$, $Ka = 3400$ and $k = 0.0365$. The red curves represent $u = 0$ (within the laboratory frame) to indicate the backflow regions. The celerity results as $c = 2.48$ and the average reciprocal height as $\bar{h}^{-1} = 1.35$.

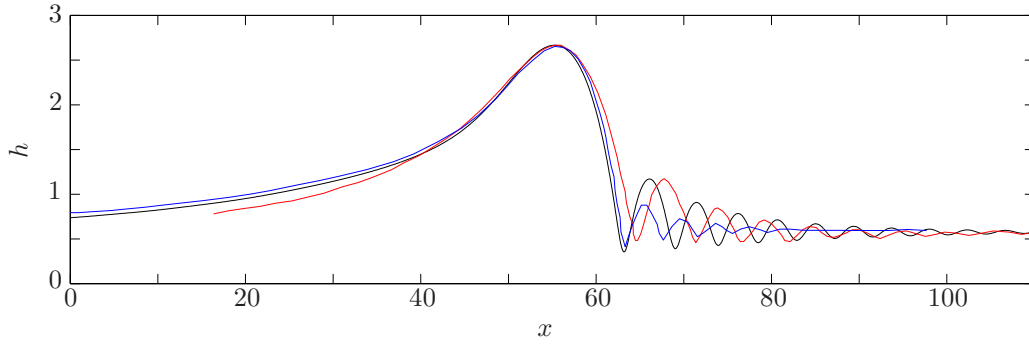


Figure 5.2.: Wave shapes for the present simulation (black), semi developed wave (red) and fully developed wave (blue) of Miyara (1999).

5.2. Nusselt numbers

We evaluate the local Nusselt numbers as defined in (2.25) by using (2.22a) and (2.22b), but with the constant temperature difference between film surface and wall¹, thus

$$\text{Nu}_f = (\partial_y T)_{y=0} = \frac{\partial_\eta T}{h} \Big|_{\eta=0}, \quad (5.3)$$

$$\text{Nu}_i = (\partial_n T)_{y=h} = \frac{n \partial_\eta T}{h} \Big|_{\eta=1} \quad (5.4)$$

where we made use of the normal derivative operator at the free surface

$$\partial_n := \hat{\mathbf{n}} \cdot \nabla = -\frac{h'}{n} \partial_\xi + \frac{n}{h} \partial_\eta. \quad (5.5)$$

The averages over the respective surfaces are

$$\overline{\text{Nu}}_f = \frac{1}{L} \int_0^L \text{Nu}_f dx, \quad (5.6)$$

$$\overline{\text{Nu}}_i = \frac{1}{L} \int_0^L \text{Nu}_i n dx \quad (5.7)$$

with the free surface increment $n dx$. It is advantageous to average both Nusselt numbers over L so that we end up at the same value due to conservation, hence

$$\overline{\text{Nu}} := \overline{\text{Nu}}_f = \overline{\text{Nu}}_i. \quad (5.8)$$

The value of $\overline{\text{Nu}}$ coincides with the asymptotic (far downstream) time average $\overline{\text{Nu}}_{\text{Miyara}}$ given by Miyara (1999). For a more systematic analysis we decompose the temperature

¹Note that the mixing temperature is no longer used in the temperature difference.

profile along η into a conductive and a convective part, thus $T(\xi, \eta) = \eta + T'(\xi, \eta)$. We obtain the (wall) Nusselt number decomposition

$$\text{Nu}_f = \frac{\partial_\eta(\eta + T')}{h} = \frac{1}{h} + \frac{\partial_\eta T'}{h} := \text{Nu}_0 + \text{Nu}' \quad (5.9)$$

where Nu_0 represents the conductive and Nu' the convective part of the heat transfer. Averaging finally yields

$$\overline{\text{Nu}} = \overline{h^{-1}} + \overline{(\partial_\eta T')h^{-1}} = \overline{\text{Nu}_0} + \overline{\text{Nu}'}. \quad (5.10)$$

The case of pure conduction ($\text{Pr} \rightarrow 0$) leads to $\overline{\text{Nu}} \rightarrow \overline{\text{Nu}_0} = \overline{h^{-1}}$. Since we can assume $\overline{h^{-1}} > 1/\bar{h}$ (even for $\bar{h} = 1$) and in general $\bar{h} < 1$ for the present system, a heat transfer enhancement is observed just by the temporal variation of the film thickness. For the present setup and by employing the temperature difference between the boundaries, the Nusselt number of the thermally developed flat film becomes $\text{Nu}_{\text{flat}} \equiv 1$. We, therefore, define the film-thinning effect as the deviation of $\overline{\text{Nu}_0}$ from unity for $\text{Pr} \rightarrow 0$.

5.3. Results

5.3.1. Benchmark case

The upper images of Figures 5.4 - 5.7 show the contours of the temperature fields for the flow discussed in 5.1 and for $\text{Pr} = \{0.1, 1, 10, 100\}$. The results compare qualitatively very well with the fully-developed cases shown by Miyara (1999). The only difference can be found for the case $\text{Pr} = 100$ where the cold area within the wave hump is not reproduced. The lower images of Figures 5.4 - 5.7 show the quantitative result regarding heat transfer, which are the film height $h(x)$ given in black, the reciprocal height h^{-1} in green, the local Nusselt number at the bottom Nu_f in blue, the local Nusselt number at the free surface Nu_i in red and the average Nusselt number $\overline{\text{Nu}}$ is shown as dashed line.

For $\text{Pr} = 0.1$ the distributions of the local Nusselt numbers Nu_j clearly correlate with the reciprocal height h^{-1} since diffusion is dominant and the temperature profile is, therefore, almost linear in y for all x . The larger the Prandtl number (or Péclet number to be more precise), the more Nu_j deviate from h^{-1} . In addition, the general trends of Nu_j with respect to h^{-1} show in the opposite directions.

The wall Nusselt number Nu_f approaches $\overline{\text{Nu}}$ for all x as $\text{Pr} \rightarrow \infty$, indicating that the wave shape is not relevant for the wall-sided heat transfer for large Pe . The local analysis shows, that the wall-sided heat transfer typically increases under the main hump as Pe is increased. This is caused by the fact that diffusion is less dominant than convection (large Pe), so that the diffusive transport across the separation streamline is not fast enough

to cool the fluid elements that are trapped in the vortex. In other words, the larger the Péclet number, the more the vortex acts as thermal insulator at the free surface, reducing Nu_i locally. In turn, the vortex compresses the thermal boundary layer near the wall, increasing Nu_f locally under the main hump. In the capillary wave region, the Nusselt number at the free surface Nu_i gets more pronounced as $Pr \rightarrow \infty$. Since $Nu_i > h^{-1}$ holds also in the residual layer, the strong increase at the wave troughs cannot be attributed to the backflow regions only. Thus, we have to declare the deviation of Nu_i from h^{-1} as result of the more pronounced convective effect.

Table 5.1 summarizes the values for the average Nusselt number \overline{Nu}_{Miyara} given by Miyara (1999) and our result \overline{Nu} with its fractions \overline{Nu}_0 and \overline{Nu}' , see (5.10), and the percentage of the convectively induced heat transfer enhancement

$$p = \frac{\overline{Nu}'}{\overline{Nu} - 1}. \quad (5.11)$$

The agreement between \overline{Nu}_{Miyara} and \overline{Nu} is good as long as Pr is small. This is due to the fact that h^{-1} is almost the same even if the wave shapes differ from another in the capillary region. The more the convective effect become significant, the more the deviation between the average Nusselt numbers becomes evident.

The case $Pr = 0.1$ is clearly dominated by the film-thinning effect so that $\overline{Nu} \approx \overline{Nu}_0$ holds true to a high degree. This is also shown by Miyara (1999). For $Pr \geq 1$ the convective effect becomes more important, visualized by the measure p . Nevertheless, for relevant values of the Prandtl number ($Pr < 100$) the heat transfer enhancement due to film-thinning stays dominant since $p \lesssim 0.25$ so that more than 75% of the enhancement is caused by film-thinning.

Table 5.1.: Average Nusselt number(s) of the present simulations compared to data given by Miyara (1999).

Pr	\overline{Nu}_{Miyara}	\overline{Nu}	\overline{Nu}_0	\overline{Nu}'	p
0.1	1.37	1.36	1.35	0.01	2.1%
1	1.41	1.39	1.35	0.04	10.0%
10	1.53	1.46	1.35	0.10	22.6%
100	1.56	1.47	1.35	0.12	25.1%

As amendment to Table 5.1, Figure 5.3 shows the average Nusselt number \overline{Nu} as function of the Prandtl number $Pr = \{0.01, \dots, 200\}$. From the graph a saturation effect becomes evident, showing that $Pr = 100$ is already an excellent approximation for the asymptotic value, i.e. for $Pr \rightarrow \infty$.

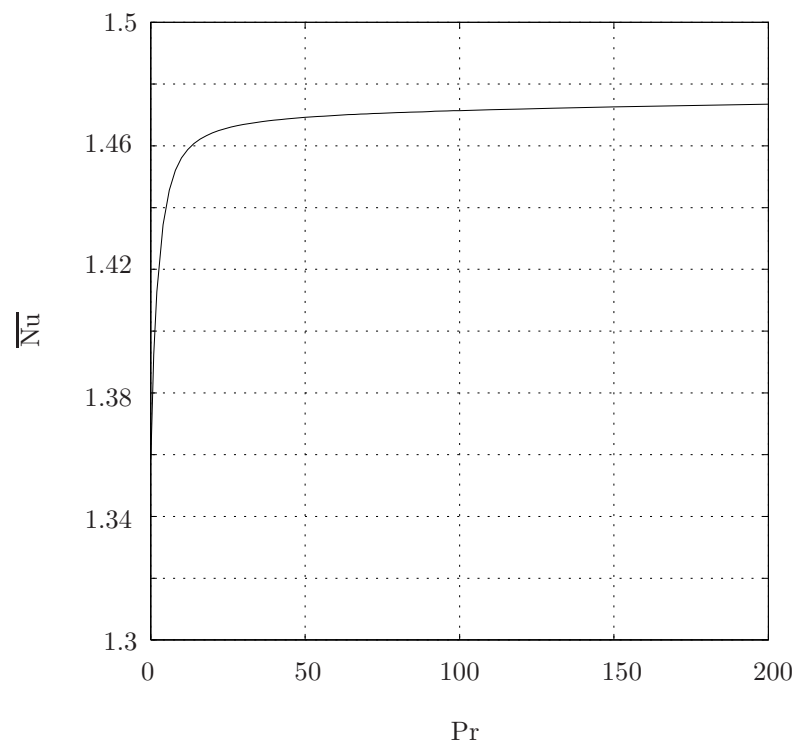


Figure 5.3.: Average Nusselt number \overline{Nu} as function of the Prandtl number Pr .

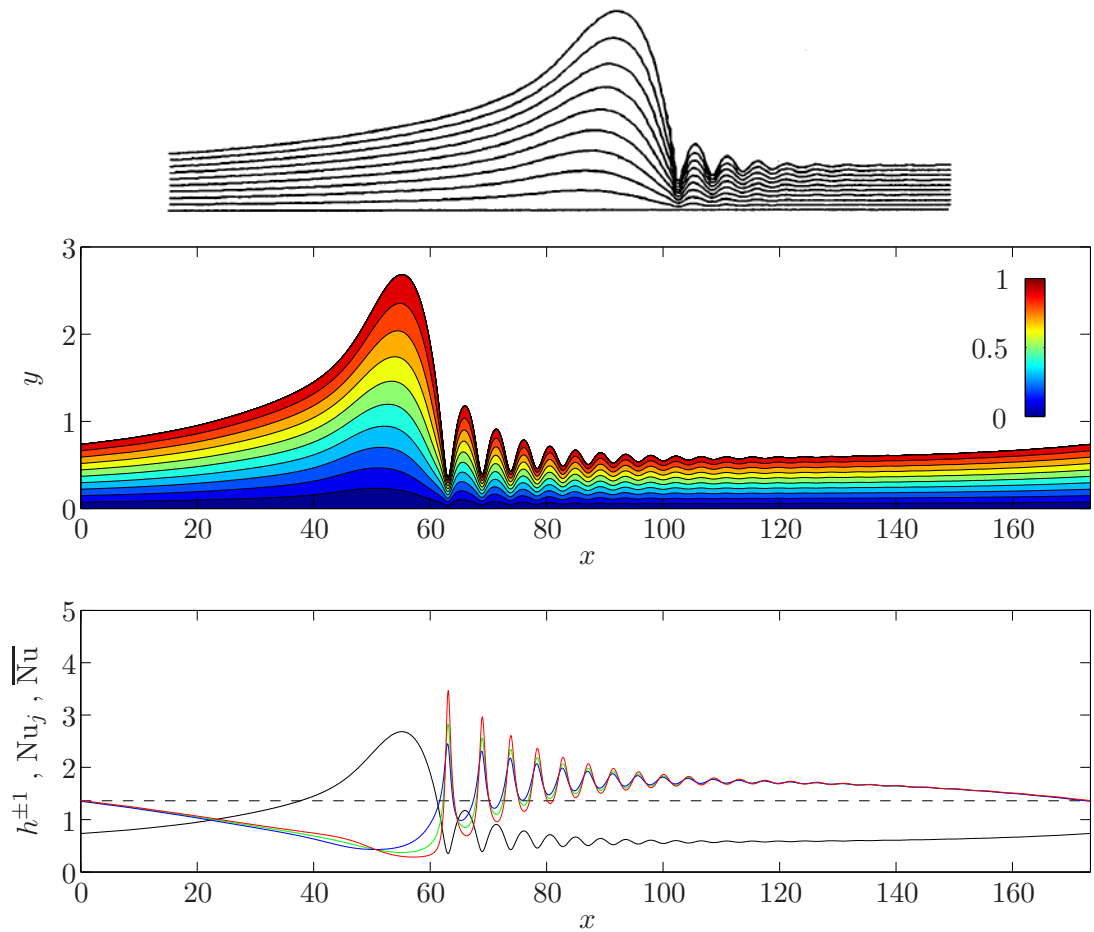


Figure 5.4.: Temperature field for the flow given by Miyara (1999) for $Pr = 0.1$. Top: Isolines of the temperature $T(x, y)$, extracted from Miyara (1999). Central: Contours of the temperature $T(x, y)$ for the present simulation. Bottom: Height h (black), reciprocal height h^{-1} (green), Nusselt number bottom Nu_b (blue), Nusselt number free surface Nu_i (red) and average Nusselt number \overline{Nu} (dashed).

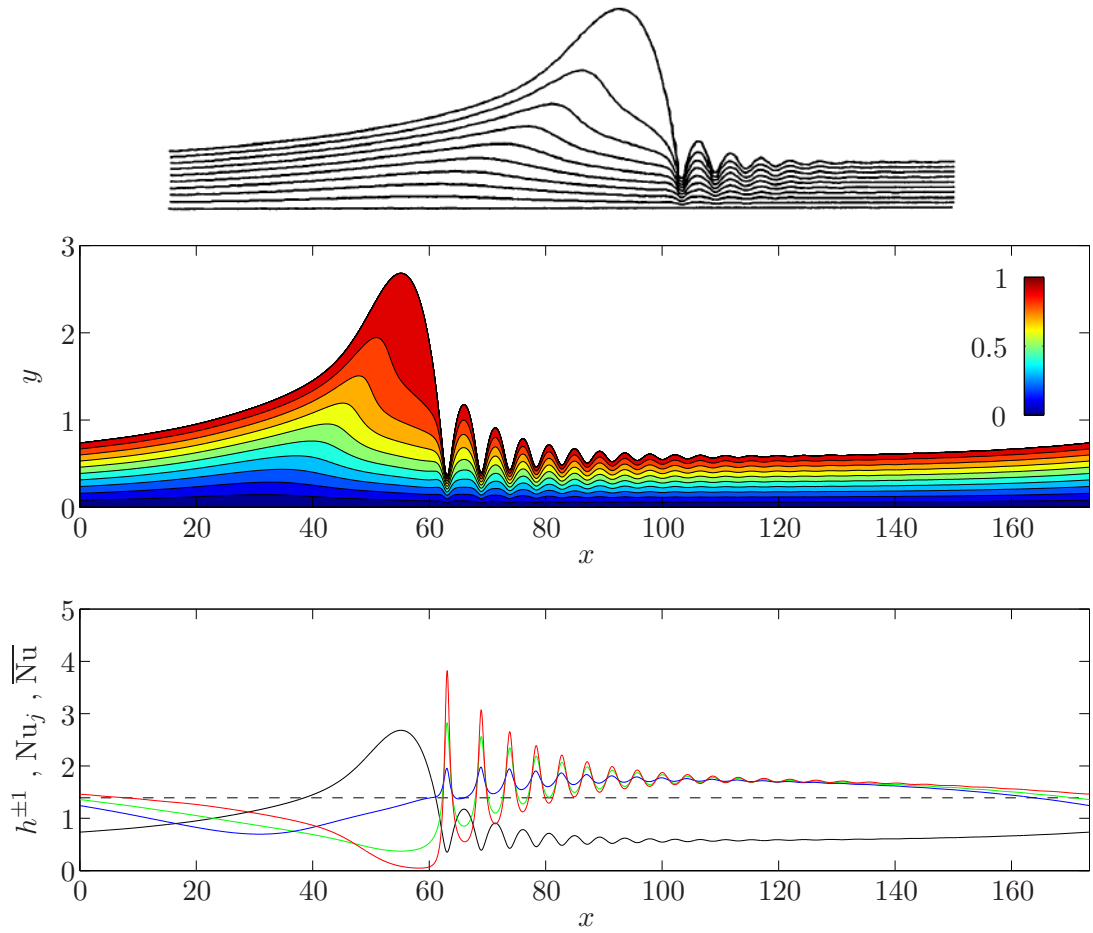


Figure 5.5.: Temperature field for the flow given by Miyara (1999) for $Pr = 1$. Top: Isolines of the temperature $T(x, y)$, extracted from Miyara (1999). Central: Contours of the temperature $T(x, y)$ for the present simulation. Bottom: Height h (black), reciprocal height h^{-1} (green), Nusselt number bottom Nu_b (blue), Nusselt number free surface Nu_i (red) and average Nusselt number \overline{Nu} (dashed).

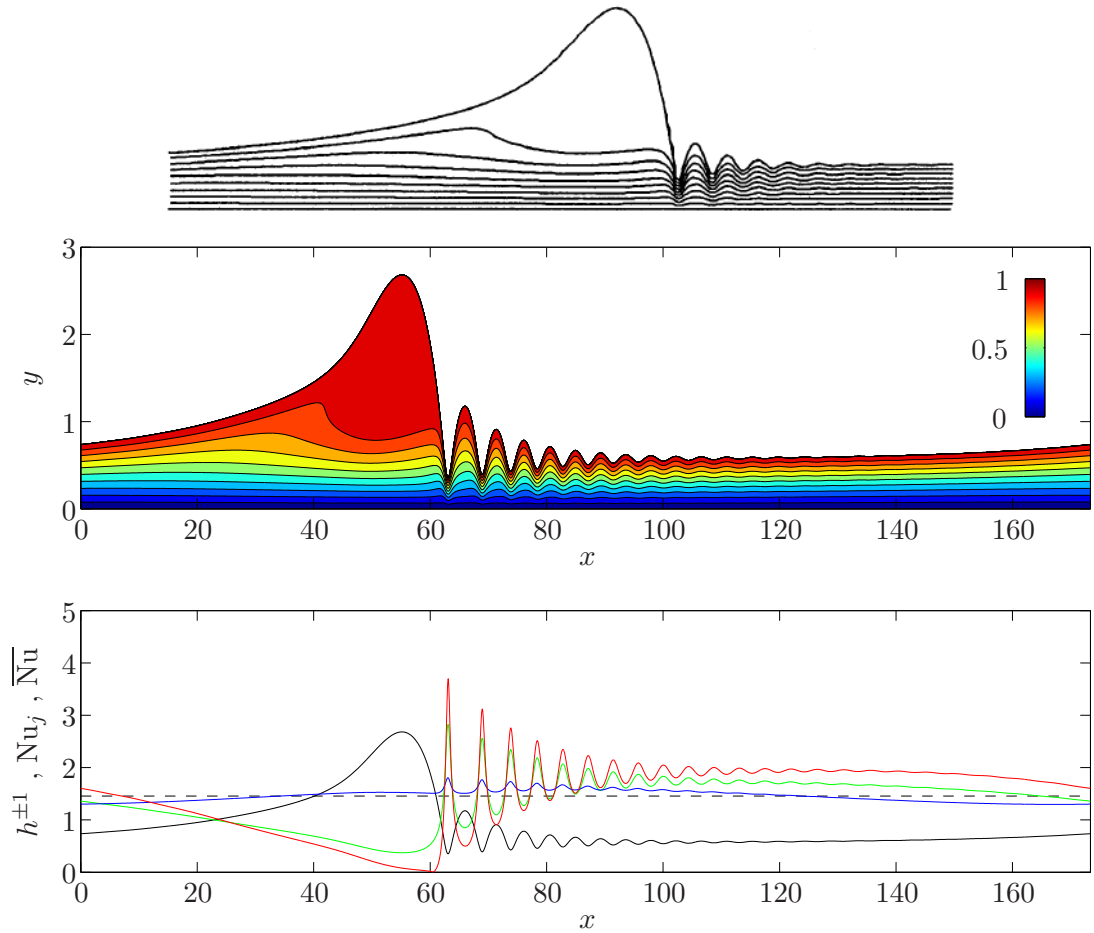


Figure 5.6.: Temperature field for the flow given by Miyara (1999) for $Pr = 10$. Top: Isolines of the temperature $T(x, y)$, extracted from Miyara (1999). Central: Contours of the temperature $T(x, y)$ for the present simulation. Bottom: Height h (black), reciprocal height h^{-1} (green), Nusselt number bottom Nu_b (blue), Nusselt number free surface Nu_i (red) and average Nusselt number \overline{Nu} (dashed).

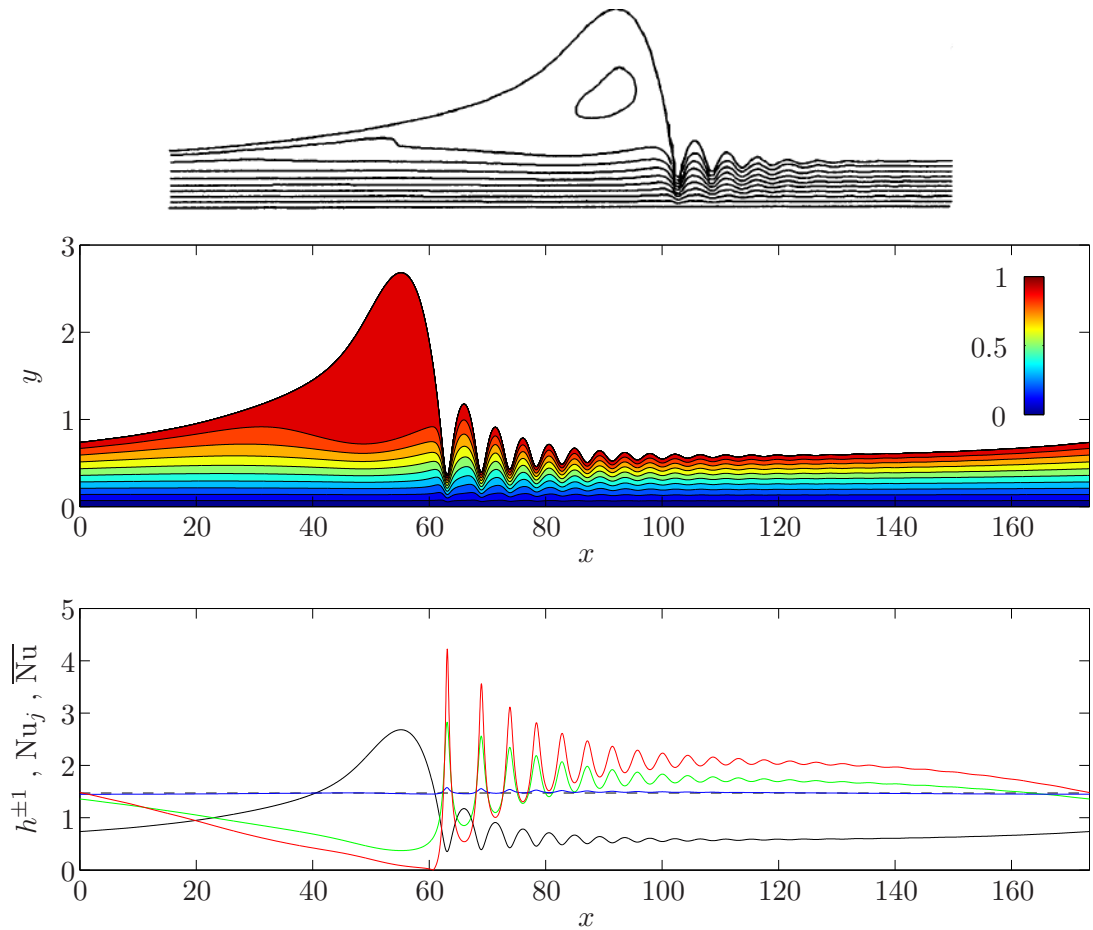


Figure 5.7.: Temperature field for the flow given by Miyara (1999) for $Pr = 100$. Top: Isolines of the temperature $T(x, y)$, extracted from Miyara (1999). Central: Contours of the temperature $T(x, y)$ for the present simulation. Bottom: Height h (black), reciprocal height h^{-1} (green), Nusselt number bottom Nu_b (blue), Nusselt number free surface Nu_i (red) and average Nusselt number \overline{Nu} (dashed).

5.3.2. Isothermal cases

To estimate the influence of convection we finally calculate the average Nusselt number $\overline{\text{Nu}}$ for all solutions along the branches presented in Chapter 4. Figure 5.8 shows the result for the solution branches given in Chapter 4, i.e. for $\text{Re} = \{8.6, 10.7, 12.9, 15\}$, $\text{Ka} = 509.5$ and $\theta = \pi/2$. The black curves show $\overline{h^{-1}}$ representing the lower bound for $\overline{\text{Nu}}$ and the red curves show the calculated average Nusselt number for $\text{Pr} = 100$ representing the upper bound. Figure 5.9 shows the maximum relative measure p , see (5.11), that results from $\text{Pr} = 100$, i.e. from the red curves of Figure 5.8.

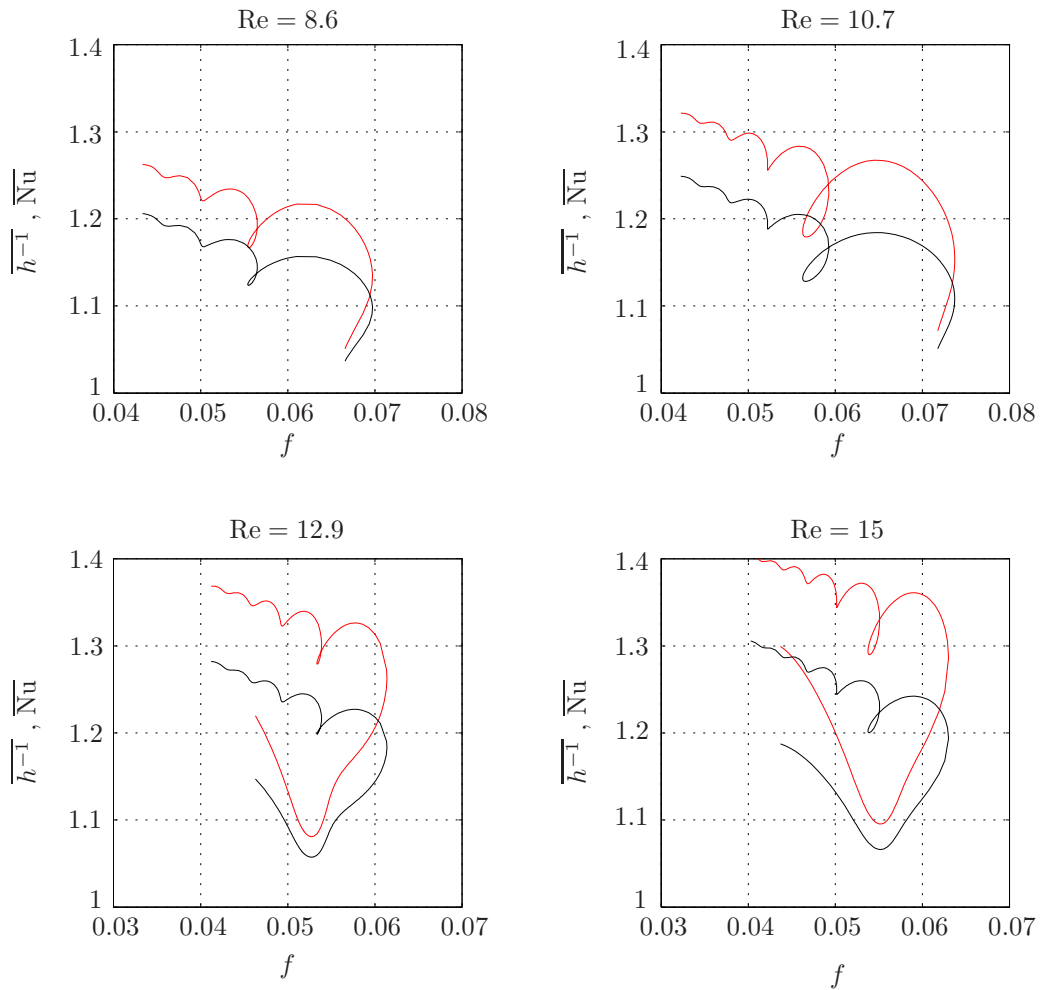


Figure 5.8.: Upper and lower bounds for $\overline{\text{Nu}}$: Average reciprocal height $\overline{h^{-1}}$ (black) and average Nusselt number $\overline{\text{Nu}}$ for $\text{Pr} = 100$ (red) as function of the wave frequency f for the solution branches given in Chapter 4, i.e. for $\text{Re} = \{8.6, 10.7, 12.9, 15\}$, $\text{Ka} = 509.5$ and $\theta = \pi/2$.

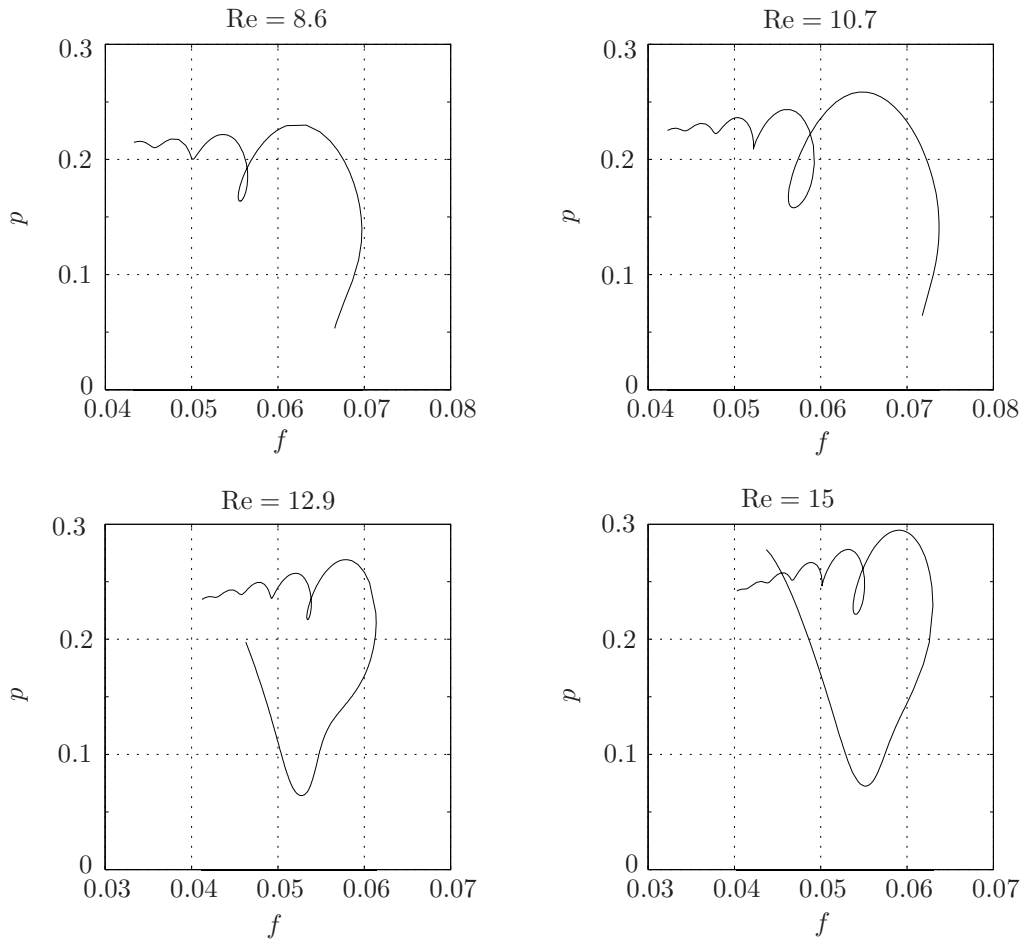


Figure 5.9.: Relative measure of the convectively induced heat transfer enhancement p for the solution branches given in Figure 5.8.

5.4. Interim summary

The major influence on the (average) Nusselt number is the film-thinning effect rather than the convective effect. This was also concluded by [Aktershev & Alekseenko \(2013\)](#) for a falling film of a condensate. Hence, $\overline{Nu} = \overline{h}^{-1}$ represents the lower bound for the (far downstream) value of the average Nusselt number. From Figure 5.8 we see that the upper and lower bounds for \overline{Nu} typically increase as Re becomes larger. Additionally, Figure 5.9 shows that the relative measure for the convectively induced heat transfer enhancement p also increases as Re is increased. This demonstrates that convection becomes more significant for larger Re and reaches almost 30% of the total heat transfer enhancement.

6. The absorbing flat film

The ideas of the following chapter are essentially published in [Hofmann & Kuhlmann \(2012\)](#). However, some modifications have been introduced and the notation has been adapted to be consistent with the present monograph.

6.1. Governing equations

We consider a typical setup of a film absorber as sketched in Figure 6.1. We assume a flat liquid film without surface waves, corresponding to the limit of infinitely large surface tension. The flat surface implies that the fluid dynamics induced by the absorption process is neglected, i.e. we do not account for the crosswise velocity and the increase of the film thickness. The binary solution (subscript s) enters the system at $x = 0$ with the inlet temperature $T|_{x=0} = T_0$ and with the inlet concentration (LiBr) $C'_1|_{x=0} = C_s$. The liquid film is cooled by a counter-current coolant flow (subscript c) entering the system with the inlet temperature $\Theta = \Theta_c$.

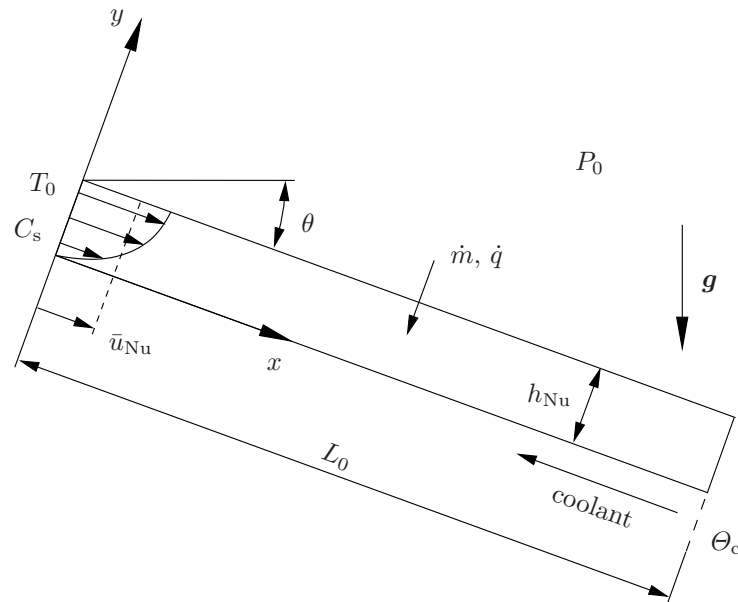


Figure 6.1.: Simplified model of an absorbing falling film device.

We presume that non-absorbable gases are not present, $C_3'' \equiv 0$, such that the gaseous phase consists of pure H_2O , i.e. $C_2'' \equiv 1$. Therefore, the system pressure P_0 coincides with the partial pressure (of H_2O in the gas phase) P_2'' and further, by assuming local thermodynamic equilibrium, with the vapor pressure (of H_2O in the liquid solution) P_2' , hence

$$P_0 = P_2' = P_2''.$$

Additionally, the system pressure P_0 shall coincide with the saturation pressure which again corresponds to the saturation temperature (dew point temperature) T_d . Figure 6.2 shows a contour plot of the vapor pressure P_2' as function of the solution temperature T in degree Celsius and the LiBr-concentration C_1' in wt% LiBr. The plot was generated from the relations given by [Kim & Ferreira \(2006\)](#). The isolines represent isobars and the numbers indicate the corresponding vapor pressure in kPa.

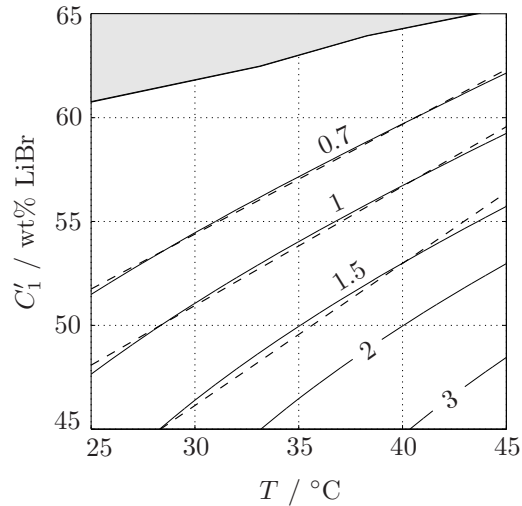


Figure 6.2.: Contour plot of the vapor pressure P_2' as function of the temperature T in degree Celsius and the LiBr-concentration C_1' in wt% LiBr. The labels indicate the vapor pressure P_2' in kPa. The least-squares linear fits of the isobars are shown as dashed lines. The shaded region, bounded by the thick curve ([Boryta, 1970](#)), indicates crystallization of LiBr.

We also presume that the heat loss to the gas phase is small since the system pressure is very low. We therefore reduce our simulation to the liquid film and do not solve for the gaseous phase. The concentration variables can be reduced to one representative and we define $C_1' := C$ since this is most common for LiBr– H_2O . Also, we are able to reduce the boundary conditions at the free-surface (3.50), firstly by dropping the temperature equilibrium condition (3.50a), and secondly by approximating the heat loss to the gas

phase $\dot{q}'' = -(\lambda\partial_n T)''$ in (3.50c). The heat loss is estimated as the sensible heat needed to elevate the mass flux temperature from the saturation temperature T_d at the point of vaporization to the free-surface temperature T , thus

$$\dot{q}'' = -(\lambda\partial_n T)'' \approx -\dot{m}c_p''(T - T_d) \approx -\dot{m}c_p''(T_0 - T_d) := -\dot{m}h_d \quad (6.1)$$

where we have again approximated the (variable) surface temperature T by the (constant) reference temperature T_0 . It is then convenient to redefine the enthalpy of absorption to $\Delta h := h'' - h' - h_d$ such that the simplified heat flux condition becomes

$$-(\lambda\partial_y T)' = \Delta h \dot{m}. \quad (6.2)$$

From now on all variables refer to the liquid phase, so that we can omit the prime and double prime, respectively.

We notice that the isobars in Figure 6.2 can be well approximated by the linear function

$$C(T, P_0) \approx C_0 + \gamma(T - T_0) \quad (6.3)$$

with the equilibrium concentration at the reference state $C_0 := C(T_0, P_0)$ and the linear concentration coefficient

$$\gamma := \left(\frac{\partial C}{\partial T} \right)_{P_0}. \quad (6.4)$$

This simple approach was already employed by Grigor'eva & Nakoryakov (1977) and seems to be justified for LiBr–H₂O, at least for low system pressures and a certain range of temperatures. After defining a system pressure P_0 (or the according saturation temperature T_d) we derive the linear concentration coefficient γ from a least-squares fit (LSQ-fit) of the isobar representing $P_0(T, C)$ within the interval $T = [25, 45]^\circ\text{C}$. Three representative linear fits are shown in Figure 6.2 as dashed lines. All resulting thermophysical properties of LiBr–H₂O are collected in Table 6.1 for three representative operating states A–C and derive from the correlations provided by the authors given in the last column.

The condition (6.3) stands for the equilibrium condition (3.50b). Finally we write the absorbed mass flux density in terms of the introduced representative concentration variable C and find

$$\dot{m} = \frac{\rho D \partial_y C}{C} \approx \frac{\rho D \partial_y C}{C_0}. \quad (6.5)$$

Here we have assumed that the interface concentration C is never too far away from the reference concentration C_0 so that the linearization is justified.

Table 6.1.: Thermophysical properties of LiBr–H₂O for the reference states A–C.

quantity	A	B	C	unit	reference/remark
T_d	1.9	7.0	13.1	°C	Magnus formula, see (A.8)
P_0	0.7	1.0	1.5	kPa	by definition
T_0	45	45	45	°C	by definition
C_0	62.3	59.6	56.4	wt% LiBr	LSQ-fit
γ	5.29	5.74	6.84	10^{-3} K^{-1}	Kim & Ferreira (2006)
ρ	1748	1691	1629	kg/m^3	Kim & Ferreira (2006)
c_p	1.84	1.91	2.00	$\text{kJ}/(\text{kg K})$	Kim & Ferreira (2006)
h''	2583	2583	2583	kJ/kg	VDI-GVC (2010)
h'	141	125	111	kJ/kg	Kim & Ferreira (2006)
h_d	82	72	61	kJ/kg	VDI-GVC (2010)
Δh	2360	2386	2411	kJ/kg	$\Delta h = h'' - h' - h_d$
λ	0.42	0.43	0.44	$\text{W}/(\text{m K})$	Patterson & Perez-Blanco (1988)
$\bar{\eta}$	7.32	5.49	3.95	10^{-3} Pa s	Patterson & Perez-Blanco (1988)
D	1.50	1.71	2.07	$10^{-9} \text{ m}^2/\text{s}$	Gierow & Jernqvist (1993)
ν	4.19	3.25	2.43	$10^{-6} \text{ m}^2/\text{s}$	$\nu = \bar{\eta}/\rho$
a	1.31	1.33	1.36	$10^{-7} \text{ m}^2/\text{s}$	$a = \lambda/(\rho c_p)$

After we have defined the system pressure P_0 , the inlet temperature T_0 and the equilibrium concentration C_0 as reference states, we shall note that the inlet concentration C_s does not necessarily need to be the equilibrium concentration, i.e. $C_s - C_0 \neq 0$. Below we will account for this deviation by introducing a non-dimensional parameter.

6.1.1. Non-dimensionalization

For a further analysis we consider the non-dimensional quantities¹

$$x = \frac{x^*}{L_0} \quad , \quad y = \frac{y^*}{h_{\text{Nu}}} \quad , \quad u = \frac{u^*}{\bar{u}_{\text{Nu}}} \quad , \quad T = \frac{T^* - T_0}{\Delta T} \quad , \quad C = \frac{C^* - C_0}{\Delta C} \quad (6.6)$$

which have been scaled using the length of the plate L_0 , the film thickness h_{Nu} , the mean velocity \bar{u}_{Nu} , the characteristic temperature difference of the system $\Delta T := T_0 - \Theta_c$ and $\Delta C := \gamma \Delta T$ corresponding to the maximum possible concentration variation within the system. The non-dimensional scalar fields T and C vary within the range $[-1, 0]$. From the given scales we obtain the non-dimensional transport equations

$$u_{\text{Nu}} \partial_x T = \frac{1}{\varepsilon_0 \text{Pe}} (\varepsilon_0^2 \partial_{xx} + \partial_{yy}) T,$$

$$u_{\text{Nu}} \partial_x C = \frac{1}{\varepsilon_0 \text{Pe} \text{Le}} (\varepsilon_0^2 \partial_{xx} + \partial_{yy}) C,$$

¹Dimensional quantities are indicated by an asterisk.

with the non-dimensional velocity profile

$$u_{\text{Nu}} = 3 \left(y - \frac{y^2}{2} \right), \quad (6.7)$$

the (thermal) Péclet number $\text{Pe} = \text{Re Pr}$ and the Lewis number $\text{Le} = a/D$. We have also introduced the aspect ratio $\varepsilon_0 = h_{\text{Nu}}/L_0$, for which one can easily verify from (2.9)

$$\varepsilon_0 = \frac{1}{L_0} \left(\frac{3\nu^2 \text{Pe}}{g_x \text{Pr}} \right)^{1/3} = \frac{1}{L_0} \left(\frac{3\nu a}{g_x} \right)^{1/3} \text{Pe}^{1/3}. \quad (6.8)$$

In a typical experimental setup, the working pair (determining ν and a), the length of the plate L_0 and the inclination angle $\theta \propto g_x$ are fixed, so that the introduction of the apparatus parameter

$$A = \frac{1}{L_0} \left(\frac{3\nu a}{g_x} \right)^{1/3} = \text{const.} \quad (6.9)$$

seems to be convenient to mimic experimental conditions. Rather than performing a pure theoretical study by varying Pe and ε_0 independently, we shall focus on the experimental reality and vary ε_0 according to

$$\varepsilon_0 = A \text{Pe}^{1/3}. \quad (6.10)$$

However, instead of eliminating ε_0 from all equations by implementing A , we keep ε_0 for readability and include the constraint (6.10) in the model. Further, the scaled equations indicate that streamwise diffusion is very small so that we may safely neglect it. We finally end up with the bulk equations

$$u_{\text{Nu}} \partial_x T = \frac{\partial_{yy} T}{\varepsilon_0 \text{Pe}}, \quad (6.11a)$$

$$u_{\text{Nu}} \partial_x C = \frac{\partial_{yy} C}{\varepsilon_0 \text{Pe Le}}. \quad (6.11b)$$

Even though we have not yet developed the thermal wall boundary condition, we shall already present the final set of non-dimensional boundary conditions following from the thoughts above and from Section 6.2 below,

$$\partial_y T = -B \partial_y C, \quad C = T, \quad (6.12a)$$

$$T = 0, \quad C = \zeta, \quad (6.12b)$$

$$\partial_y T = \text{Nu}_w (T - \bar{\Theta}), \quad \partial_y C = 0 \quad (6.12c)$$

where (6.12a) applies to the free-surface, (6.12b) to the inlet and (6.12c) to the wall. The (numerical) outlet boundary condition will be given in Section 6.3. The additional parameters

$$B = \frac{\gamma\rho D\Delta h}{\lambda C_0} \quad , \quad \zeta = \frac{C_s - C_0}{\Delta C} \quad , \quad \text{Nu}_w = \frac{\alpha_c h_{\text{Nu}}}{\lambda} \quad (6.13)$$

are the non-dimensional enthalpy of evaporation B , the non-dimensional deviation of the inlet concentration from equilibrium ζ and the wall Nusselt number Nu_w . Table 6.2 collects the non-dimensional parameters resulting from the definitions and the data given in Table 6.1. The coolant mixing temperature $\bar{\Theta}$ derives from the heat flux balance as

$$\text{Pe}_c^* \frac{d\bar{\Theta}}{dx} = \text{Nu}_c^*(T - \bar{\Theta}) \quad (6.14)$$

with the reduced coolant Péclet number Pe_c^* and the reduced coolant Nusselt number Nu_c^* (both to be defined below). The presented Nusselt numbers are related by (to be shown below)

$$\text{Nu}_w = \text{Nu}_c^* \varepsilon_0. \quad (6.15)$$

Due to the counter-current coolant flow we employ the boundary condition for the coolant

$$\bar{\Theta}(1) = -1. \quad (6.16)$$

Table 6.2.: Approximative non-dimensional parameters for the reference states A–C.

quantity	A	B	C	remark
$AL_0 \times 10^5$	5.5	5.1	4.6	vertical wall
Pr	32	24	18	
Le	87	78	65	
$1/B$	8	6.5	4.5	

6.1.2. Involved Nusselt numbers

The introduced wall Nusselt number Nu_w scales with the film thickness h_{Nu} and since we want to avoid a change of the primary coolant Nusselt number Nu_c due to a change of the film thickness, we shall rewrite the wall Nusselt number Nu_w as

$$\text{Nu}_w = \frac{\alpha_c h_{\text{Nu}}}{\lambda} = \frac{\alpha_c d_c}{\lambda_c} \frac{L_0}{d_c} \frac{\lambda_c}{\lambda} \frac{h_{\text{Nu}}}{L_0} = \frac{\text{Nu}_c \Lambda}{\varepsilon_c} \varepsilon_0 \quad (6.17)$$

where we have used the definition for the coolant Nusselt number (2.26b) and introduced the ratio of the thermal conductivities $\Lambda = \lambda_c/\lambda$ and the coolant aspect ratio $\varepsilon_c = d_c/L_0$.

As long as we consider the model from above, simplified model called in the following, neither Λ nor ε_c are explicit parameters. This is due to the reduction of the coolant flow to the one-dimensional mixing temperature $\bar{\Theta}$. It is, therefore, convenient to merge these two parameters with the coolant Nusselt Nu_c number by defining the reduced coolant Nusselt number Nu_c^* , thus

$$\text{Nu}_c^* := \frac{\text{Nu}_c \Lambda}{\varepsilon_c} = \frac{\text{Nu}_w}{\varepsilon_0}. \quad (6.18)$$

The analogous argument applies to the reduced Péclet number Pe_c^* (to be defined below).

6.2. Wall boundary condition

Since one of the driving forces for the absorption process is the cooled wall, the corresponding thermal wall boundary condition is expected to have a crucial influence. Certain limit cases, the adiabatic wall and the isothermal wall, were the first ones discussed in literature. Some recent studies (Karami & Farhanieh, 2009, 2011; Yoon *et al.*, 2005) have introduced a linear temperature variation along the wall. This choice is very convenient since it does not introduce new parameters. A more realistic thermal wall boundary was employed by Bo *et al.* (2010), using a boundary condition of mixed type with a linearly varying averaged coolant temperature (mixing temperature). Wassenaar (1996) also introduced a boundary condition of mixed type but implemented an additional equation to determine the coolant mixing temperature. In the following we construct a realistic test case and compare the results with those resulting from the simplified thermal wall boundary conditions which were employed in the studies mentioned. From the comparison we will then deduce the best model.

6.2.1. Test model

Realistic conditions at the wall can only be obtained from a thermal coupling of the film flow to the coolant flow. We therefore assume a cooling channel which is directly attached to the liquid film at $y = 0$, i.e. the separating solid wall has a negligible thermal resistance. The coolant flow is considered as plane Poiseuille flow within a channel of width $H_c^* = 2h_c^*$. In addition, we implement a transport equation for a coolant flow by employing (3.26) and the identifications

$$\mathbf{u}^* \rightarrow u_{\text{Po}}^* \mathbf{e}_x \quad , \quad \psi^* \rightarrow c_{p,c} \Theta^* \quad , \quad \mathbf{j}^* \rightarrow -\lambda_c \nabla^* \Theta^* \quad (6.19)$$

where u_{Po}^* is the plane Poiseuille profile, Θ^* the coolant temperature, $c_{p,c}$ the specific heat capacity and λ_c the thermal conductivity of the coolant. The flow is characterized by the coolant Reynolds number corresponding to (2.26a), hence

$$\text{Re}_c = \frac{\bar{u}_{\text{Po}}^* 2H_c^*}{\nu_c} = \frac{2\Gamma_c^*}{\bar{\eta}_c} \quad (6.20)$$

with the mean velocity \bar{u}_{Po}^* , the coolant mass flux Γ_c^* (per unit length in spanwise direction) and the kinematic and dynamic viscosity ν_c and $\bar{\eta}_c$, respectively. The factor 2 has its origin in using the hydraulic diameter which is $d_c^* = 2H_c^* = 4h_c^*$ for plane channel flow. Note that Re_c becomes negative for counterflow. With the scales from the liquid film, $\Theta = (\Theta^* - T_0)/\Delta T$ and by dropping streamwise diffusion we find the non-dimensional transport equation

$$u_{\text{Po}} \partial_x \Theta = \frac{\varepsilon_c}{\varepsilon_0^2} \frac{\partial_{yy} \Theta}{\text{Pe}_c} \quad (6.21)$$

with the coolant Péclet number $\text{Pe}_c = \text{Re}_c \text{Pr}_c$, the coolant Prandtl number Pr_c , the coolant aspect ratio $\varepsilon_c = 2H/L_0$ and the non-dimensional Poiseuille profile

$$u_{\text{Po}} = \frac{3}{2} \left(1 - \frac{(y + h_c)^2}{h_c^2} \right). \quad (6.22)$$

Note that h_c and y in (6.21-6.22) are scaled by h_{Nu} and the shift $(y + h_c)$ is due to the wall position at $y = 0$. The non-dimensional channel width can be expressed as $H_c = \varepsilon_c/(2\varepsilon_0)$. The non-dimensional wall boundary conditions are derived from the heat flux balance $-\lambda \partial_y^* T^* = -\lambda_c \partial_y^* \Theta^*$ and temperature matching at the wall, thus

$$\partial_y T - \Lambda \partial_y \Theta = 0 \quad , \quad T = \Theta. \quad (6.23)$$

The lower boundary is assumed to be adiabatic. By considering the solution/coolant combination LiBr–H₂O/H₂O with $\text{Pr}_c := 6$ and a plane channel flow with a critical Reynolds number of $\text{Re} \approx 4000^2$ the maximum coolant Péclet number for the present laminar consideration becomes $\text{Pe}_c \approx 24000$. The given model leaves us with the three additional parameters Pe_c , Λ and ε_c (or H). However, to keep the number of free parameters to a minimum, we define $\Lambda := 1.4$ representing LiBr–H₂O/H₂O. Figure 6.3 shows the results for the test model given by the coupled set (6.11)–(6.12) and (6.21)–(6.23) where (6.23) replaces the thermal boundary condition in (6.12c). The results correspond to all combinations given by the coolant Péclet numbers $\text{Pe}_c = \{-240, -2400, -24000\}$ and the

²Investigations regarding stability typically employ a Reynolds number based on the half channel width $h_c = H_c/2$, so that a conversion factor of four arises between their Reynolds number and the present one based on the hydraulic diameter $2H_c$.

non-dimensional channel widths $H_c = \{10, 50, 200\}$. The remaining parameters of the liquid film are $\{\text{Pe}, \text{Le}, A, B, \zeta\} = \{300, 80, 5 \times 10^{-5}, 1/8, 0\}$. The uppermost row of Figure 6.3 shows the wall temperature $T(x)$ and in addition the linear temperature variation which is indicated as dashed line. The second row shows the coolant mixing temperature

$$\bar{\Theta} = \frac{1}{H_c} \int_{-H_c}^0 u_{\text{Pc}} \Theta \, dy. \quad (6.24)$$

The third and lowermost rows show the wall Nusselt number $\text{Nu}_w = \partial_y T / (T - \bar{\Theta})$ and the resulting coolant Nusselt number $\text{Nu}_c = \text{Nu}_w \varepsilon_c / (\varepsilon_0 \Lambda)$, respectively.

From Figure 6.3 we can firstly conclude that the wall temperature is in general far from being linear. In addition, the thermal entrance length L_{th} increases as the coolant Péclet number increases and/or the channel width increases, as we have expected from (2.34). For the shortest thermal entrance length, that is for $|\text{Pe}_c| = 240$ and $H_c = 10$, the thermally developed state reaches $\text{Nu}_c \approx 5$, in agreement with the values for laminar, plane channel flow. However, the thermally fast developing configurations are likely of no practical importance, so that the assumption of a constant coolant Nusselt number seems to be invalid for real systems. Also, the presumption of a laminar coolant flow does not hold for real systems. Nonetheless, to reduce complexity we shall assume a constant (length averaged) coolant Nusselt number as reasonable approximation which can be utilized to formulate a simplified model.

6.2.2. Simplified model

As stated above, we employ a boundary condition of mixed type for the wall temperature T^* , thus

$$\dot{q}^* = -\lambda \partial_y^* T^* = -\alpha_c (T^* - \bar{\Theta}^*) \quad (6.25)$$

by assuming a constant coolant heat transfer coefficient α_c . The heat flux balance of the coolant reads

$$\dot{q}^* dx^* = -\Gamma_c c_{p,c} \frac{d\bar{\Theta}^*}{dx^*} dx^*. \quad (6.26)$$

Using the scales (6.6) and $\bar{\Theta} = (\bar{\Theta}^* - T_0) / \Delta T$ yields

$$\partial_y T = \text{Nu}_w (T - \bar{\Theta}), \quad (6.27a)$$

$$\text{Nu}_c^* (T - \bar{\Theta}) = \text{Pe}_c^* \frac{d\bar{\Theta}}{dx} \quad (6.27b)$$

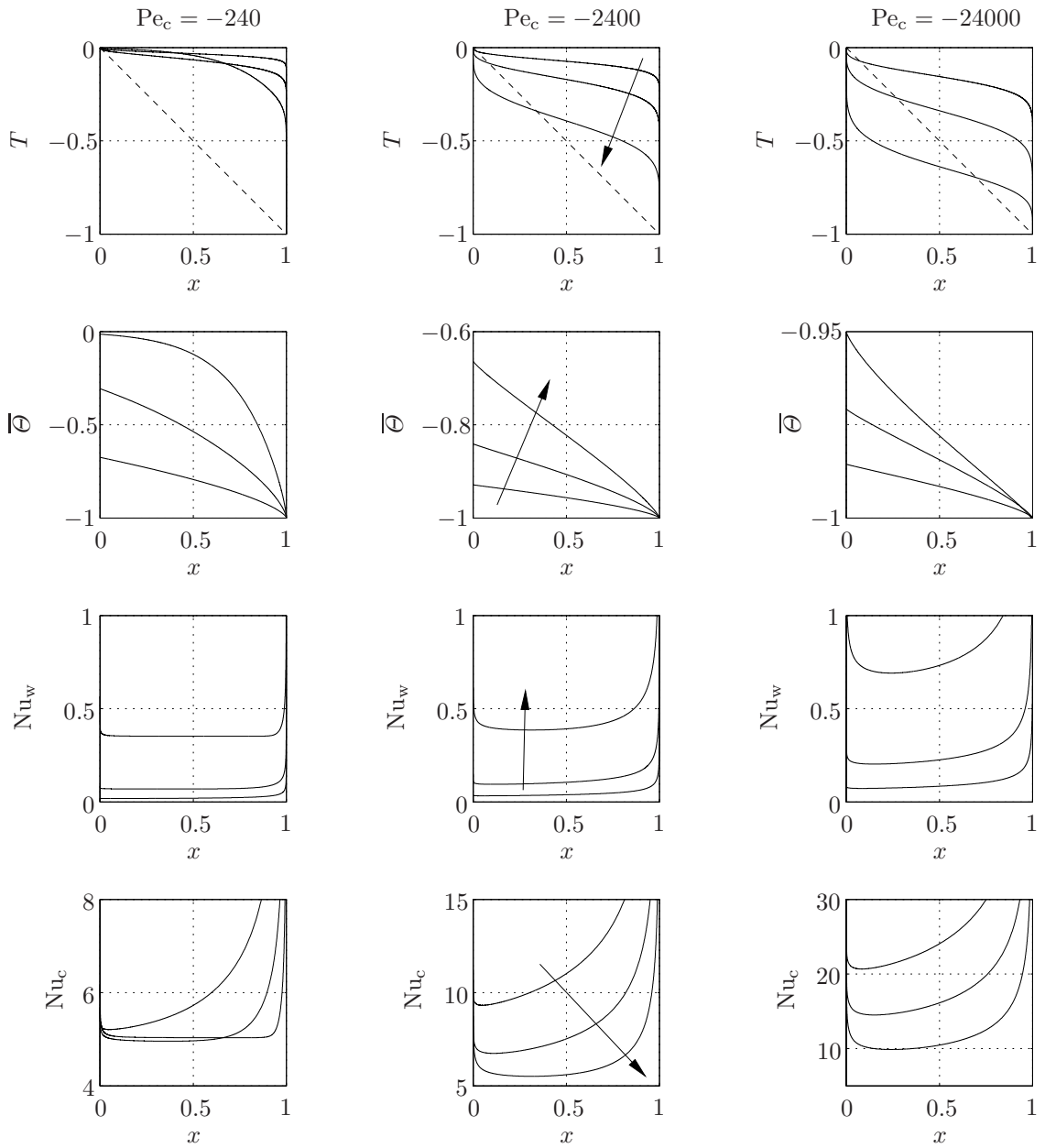


Figure 6.3.: Results for the test model as functions of the streamwise coordinate x . The coolant Péclet numbers Pe_c are stated above the figures and the arrows indicate the direction of decreasing channel width $H_c = [200, 50, 10]$. The remaining parameters are $\Lambda = 1.4$ and $\{Pe, Le, A, B, \zeta\} = \{300, 80, 5 \times 10^{-5}, 1/8, 0\}$. Uppermost row: Wall temperature T . The linear temperature variation is shown as dashed line. Second row: coolant mixing temperature $\bar{\Theta}$. Third row: wall Nusselt number Nu_w . Lowermost row: coolant Nusselt number Nu_c .

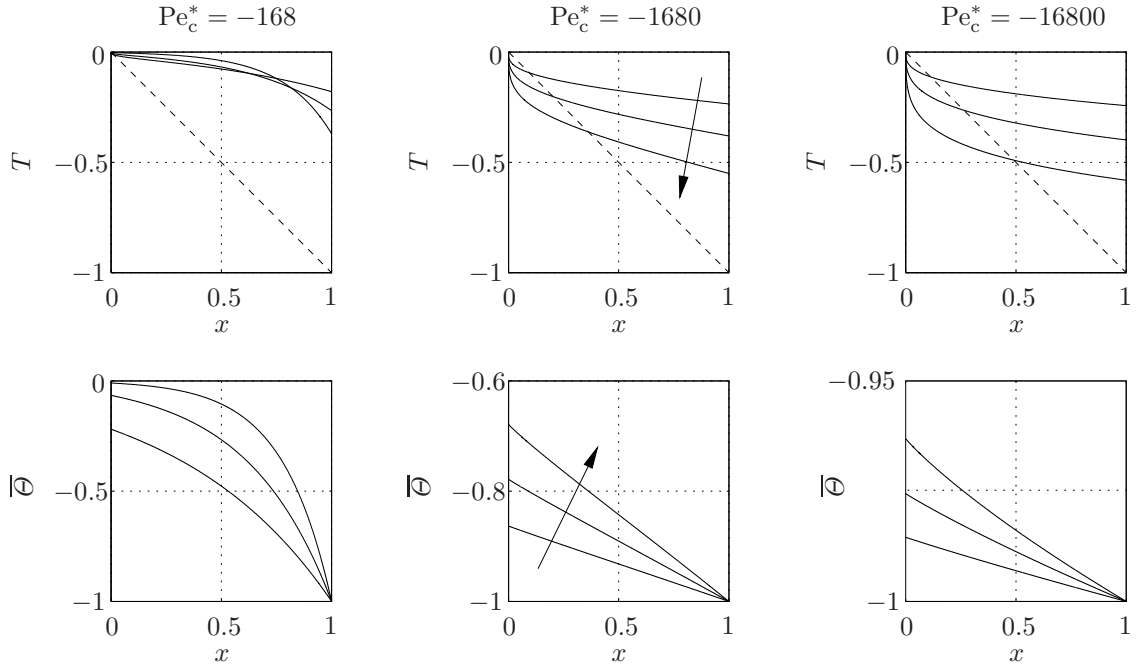


Figure 6.4.: Results for the simplified model as functions of the streamwise coordinate x . The reduced coolant Péclet numbers Pe_c^* are stated above the figures and the arrows indicate the direction of increasing reduced Nusselt number $Nu_c^* = \{300, 600, 1200\}$. The remaining parameters are $\{Pe, Le, A, B, \zeta\} = \{300, 80, 5 \times 10^{-5}, 1/8, 0\}$. Upper row: Wall temperature T . The linear temperature variation is shown as dashed line. Lower row: coolant mixing temperature $\bar{\Theta}$.

with the reduced coolant Nusselt number Nu_c^* (6.18) and the reduced coolant Péclet number

$$Pe_c^* = \frac{\Lambda}{2} Pe_c = \frac{\Lambda}{2} Re_c Pr_c = \frac{\Gamma_c c_{p,c}}{\lambda}. \quad (6.28)$$

Figure 6.4 presents results from the simplified model. Again, the upper row shows the wall temperature $T(x)$ for the reduced coolant Péclet numbers $Pe_c^* = \{-168, -1680, -16800\}$ (according to Pe_c from above and $\Lambda = 1.4$) and for the reduced coolant Nusselt numbers $Nu_c^* = \{300, 600, 1200\}$. The lower row displays the corresponding coolant mixing temperature $\bar{\Theta}(x)$. Both, the wall temperature and the coolant mixing temperature from the simplified model are, at least qualitatively, in a good agreement with those of the test model. The simplified model includes only two instead of three new parameters and it is considerably less expensive to solve, since the additional PDE for the coolant is reduced to an ODE.

We conclude that the simplified model, which corresponds practically to the approach

of [Wassenaar \(1996\)](#), represents a reasonable approximation to our realistic test case. In turn, the linear variation of the wall temperature, employed by [Karami & Farhanieh \(2009, 2011\)](#); [Yoon *et al.* \(2005\)](#), appears to be an over-simplification. On the other hand, a linear variation of the coolant mixing temperature in combination with a constant heat-transfer coefficient as it was used by [Bo *et al.* \(2010\)](#), seems to be a good approximation as long as the coolant Péclet number is not too small which is true for real applications.

6.3. Numerics

6.3.1. Method

The bulk equations (6.11) and boundary conditions (6.12) are discretized implicitly with finite differences. We use a central scheme for the bulk equations and a one-sided three-point scheme on the boundaries. Intermediate values are found by linear interpolation, leading to a method of second-order accuracy. All equations are solved simultaneously and the computation of a single parameter set typically requires only a few seconds of computational time.

The numerical implementation of the outlet boundary conditions corresponds to a linear extrapolation in streamwise direction of the (last) bulk value of any quantity S_N at the N -th grid point to the boundary at $N + 1/2$, i.e. $S_{N+1/2} = 2S_N - S_{N-1/2}$ for $S = T, C$.

The grid is homogeneous in x and y direction except near the in- and outlet. Within $x \in [0, 0.1]$ and $x \in [0.9, 1]$ the grid is refined towards the in- and outlet such that the aspect ratio of the four corner cells is less than two, i.e. $\Delta x / \Delta y \leq 2$. A grid convergence check has shown that 100 grid points in y and 1000 grid points in the central block $x \in [0.1, 0.9]$ are sufficient to resolve the absorbed mass flux density accurately.

6.3.2. Verification

To verify the code we use the semi-analytical results given by [Grossman \(1983\)](#) for the adiabatic and the isothermal wall. To mimic the equations used by Grossman we set $Pe = \varepsilon_0 = 1$, $Le = 1000$ and identify his parameter $\lambda = B$. In addition we have adjusted the inlet, free-surface and wall boundary conditions. For the numerical evaluation of the series expansion given by Grossman we have used 20 terms in the power series for the temperature and 200 terms for the concentration. The results obtained from Grossman's series expansion and from our numerical solution are compared with each other in [Figure 6.5](#) for the case of an isothermal wall. The dashed curves correspond to the solution of Grossman with his similarity solution for small x_G , shown here for $x_G < 1$, while the full curves represent the present numerical calculation. We have introduced the subscript G to distinguish between the scaling used by Grossman and the scaling we are using. The

semi-analytical solution compares very well with the numerical result. However, minor deviations close to the inlet arise due to the discontinuity in temperature and concentration at $(x_G, y) = (0, 1)$. A better comparison is obtained if the cell size close to the singular point is further decreased. More pronounced deviations are found around $x_G = 0.5$, which are most likely due to the missing matching of the two partial solutions given by Grossman.

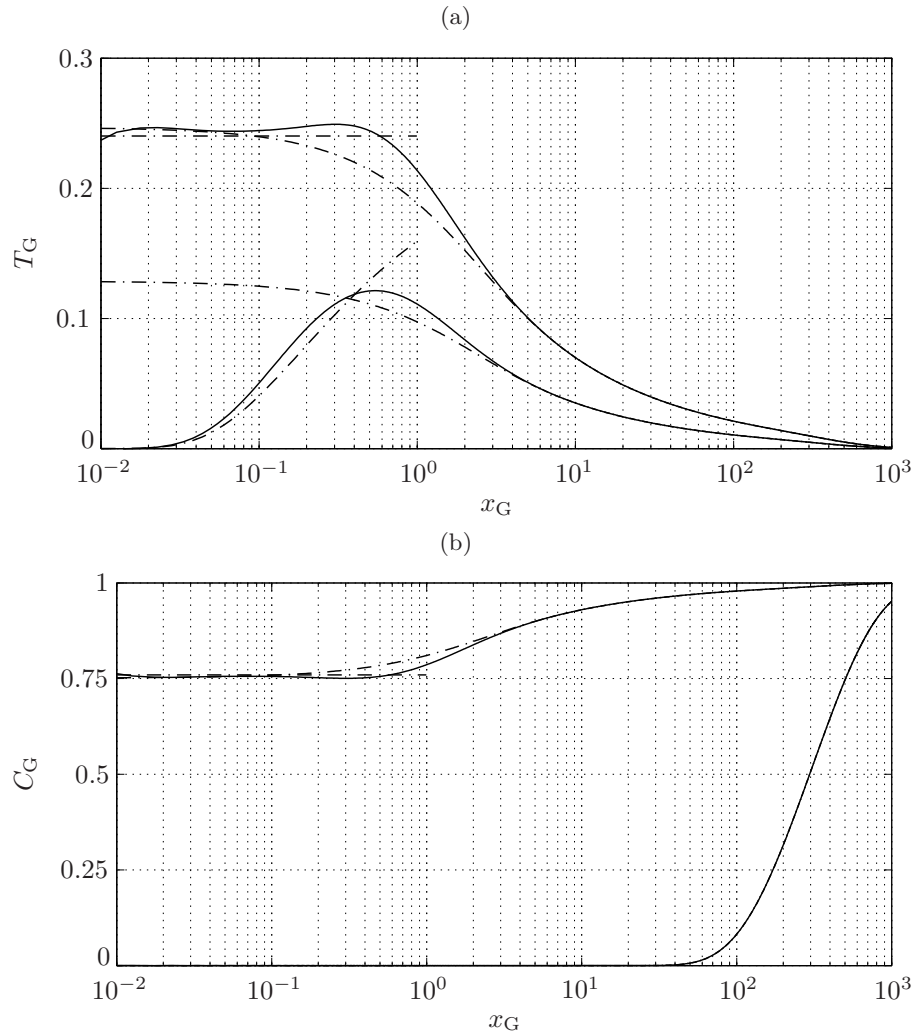


Figure 6.5.: (a) Temperature T_G and (b) concentration C_G as functions of the stream-wise coordinate x_G for the isothermal wall. The semi-analytical results by Grossman (1983) are shown as dash-dotted curves, the present numerical results by full curves. The upper curves indicate the solutions at the free-surface ($y = 1$) and the lower curves correspond to the bulk ($y = 0.5$).

6.4. Results

6.4.1. Local Nusselt and Sherwood numbers

As stated in Section 2.6.2 we evaluate the local Nusselt number for the free-surface Nu_i and for the film/wall interface Nu_f . Figure 6.6 shows the results for a certain parameter set and several Pe (see caption). Firstly we see that the asymptotic values given in Table 2.4 are almost met. We have checked that the asymptotic values are clearly captured for the isothermal wall, so that we can exclude the numerics being responsible for the small offsets. As expected, increasing Pe results in an elongation of the thermal entrance length so that Nu_i approach the asymptotic value more and more farther downstream. Additionally the local driving potentials ΔT_j , which are shown beside their corresponding Nusselt numbers Nu_j , also increase for most x with increasing Pe . Guided by (2.29a) we define for the present case

$$Sh := \frac{\partial_y C}{\Delta C_i}. \quad (6.29)$$

This is convenient but not fully consistent with the original definition, since the Eckert–Schneider condition is not included. The local Sherwood number Sh and its corresponding driving potential ΔC_i are also presented in Figure 6.6. From a practical point of view, the given evaluation is not very helpful and may be even misleading. This is due to the local driving potential which makes it impossible to decide whether large or small Pe are preferable to gain large absorption. For this question it is necessary to define a non-dimensional mass flux density as it is shown in the next section.

6.4.2. Local flux densities

We introduce the non-dimensional heat flux densities by adopting (2.33a), thus

$$\phi_{q,i} = Nu_i \Delta T_i, \quad (6.30a)$$

$$\phi_{q,f} = Nu_f \Delta T_f. \quad (6.30b)$$

For the non-dimensional mass flux density we use the exact version of (6.5) and employ (2.32b) so that

$$\phi_m := -\frac{\dot{m}^* h_{Nu}}{\rho D \Delta C} = -\frac{\partial_y C}{C_0(1 + C/\Xi)} \quad (6.31)$$

where we have introduced $\Xi = C_0/\Delta C$. For convenience we have inverted the sign of ϕ_m to get a positive value for the case of absorption. We call this evaluation linear/non-linear (linearized Eckert–Schneider condition/non-linear post processing of the mass flux

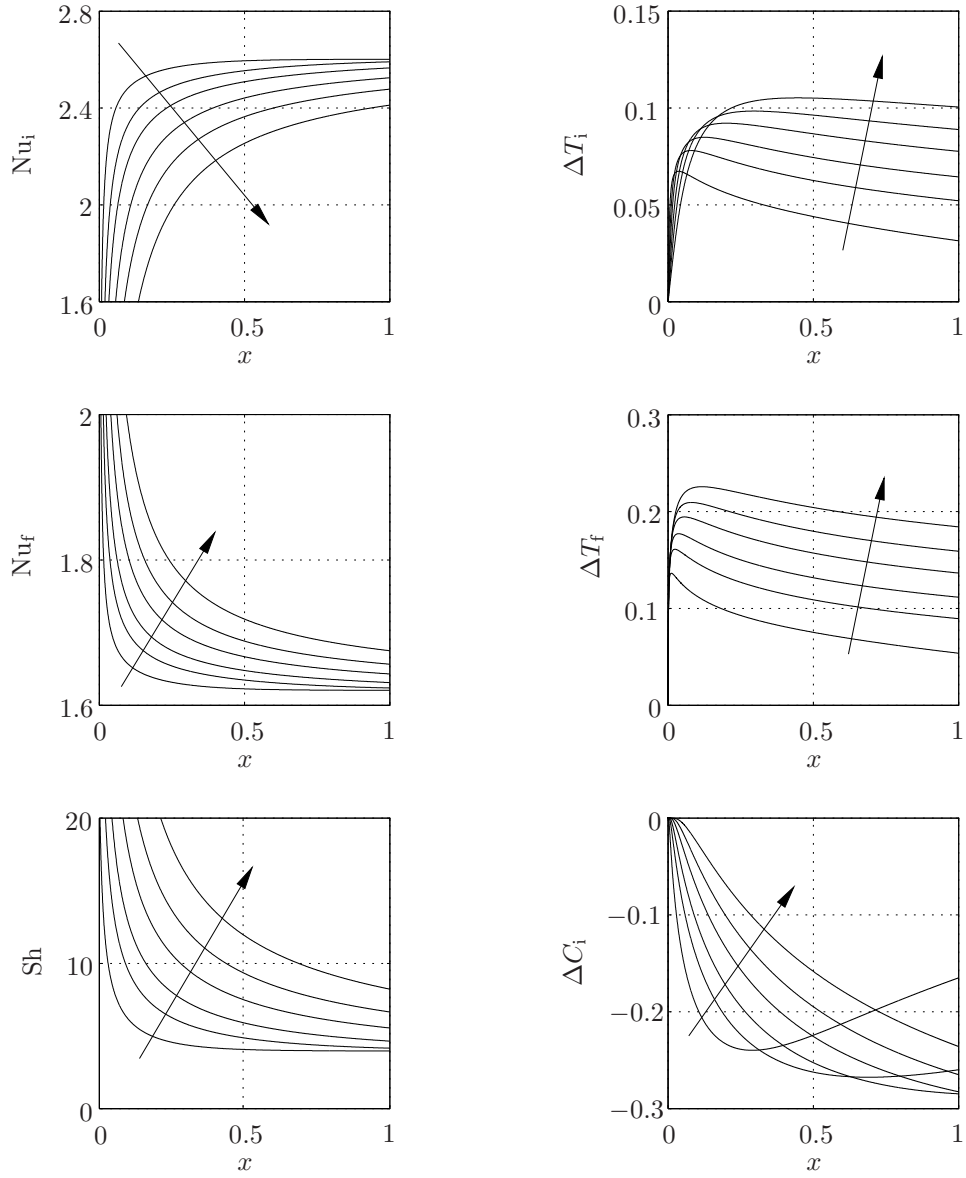


Figure 6.6.: Local Nusselt numbers and Sherwood number with their corresponding local (non-dimensional) driving potentials for $Pe = \{100, 200, 300, 450, 625, 875\}$ and the parameter set $\{Le, A, B, \zeta, Pe_c^*, Nu_c^*\} = \{80, 5 \times 10^{-5}, 1/8, 0, -15000, 1500\}$. Uppermost row: surface Nusselt number Nu_i (left) and driving potential ΔT_i (right). Centered row: film/wall Nusselt number Nu_f (left) and driving potential ΔT_f (right). Lowermost row: Sherwood number Sh (left) and driving potential ΔC_i (right). The arrows indicate the direction of increasing Pe .

density). According to our linearization of the Eckert–Schneider condition in (6.5) we shall also define the linearized mass flux density

$$\varphi_m := -\frac{\partial_y C}{C_0} = -\frac{\text{Sh}\Delta C_i}{C_0} \quad (6.32)$$

implying that $C/\varepsilon \ll 1$, called linear/linear in the following. Below we will also evaluate the mass flux density from the fully non-linear model ϕ_m^\dagger . To avoid confusion, Table 6.3 gives an overview of the introduced evaluations of the non-dimensional mass flux density.

Table 6.3.: Overview of the different evaluations of the non-dimensional mass flux density.

	Eckert–Schneider linearized	Eckert–Schneider non-linear
linear post-processing	φ_m	–
non-linear post-processing	ϕ_m	ϕ_m^\dagger

Figure 6.7 shows the results for the local flux densities for the parameter set that was used in Figure 6.6. From the figure we see that the non-dimensional (linearized) mass flux density (right image) is increasing for most x as Pe increases. Note that the product $\varphi_m C_0$ is shown for convenience. In contrast to Sh , which is diverging at the inlet, the mass flux density is actually not largest but vanishing at the inlet due to the vanishing driving potential. However, the diverging Sherwood number already indicates that increasing the driving potential at the inlet (by varying ζ) will lead to a large local absorption rate.

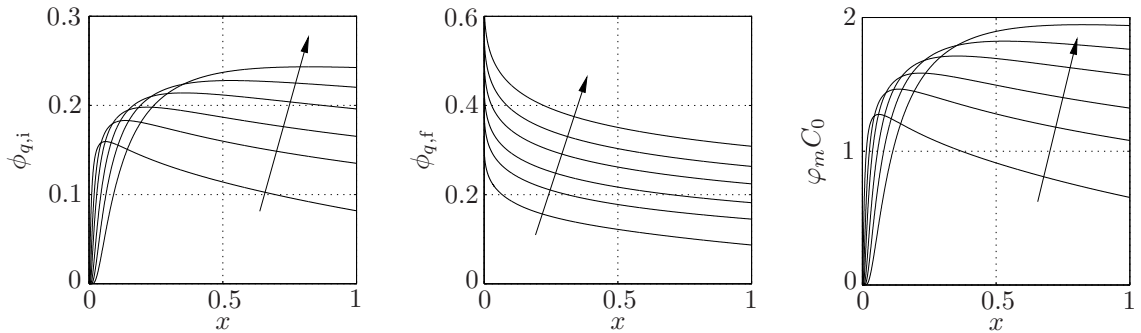


Figure 6.7.: Local flux densities as defined in (6.30) vs. the streamwise coordinate x . The parameters are those from Figure 6.6. The arrows indicate the direction of increasing Pe .

6.4.3. Modeling errors regarding unidirectional diffusion

Since some authors neglect the Eckert–Schneider condition in their works, we shall investigate the impact of this shortcoming. Ignoring the relation either means that equimolar diffusion is present at the free-surface or that one constituent is infinitely dilute. Both assumptions are clearly not met for the present case, since LiBr is non-volatile and additionally far from being infinitely dilute ($C \approx 0.5$). We shall compare two models in the following.

1. A model that employs the Nusselt film (non-varying film thickness) with equimolar diffusion at the free-surface is formulated consistently but it does not meet the physical reality of the unidirectional absorption process.
2. The present model accounts for unidirectional diffusion by using the (linearized) Eckert–Schneider condition but it neglects the effects that are induced by the absorption process (increase of film thickness, crosswise velocity) and is formulated inconsistently therefore.

Ignoring the varying film thickness In order to illustrate this inconsistency we derive the total mass balance of the non-volatile constituent, thus

$$\int_{\text{out}} \rho u^* C^* dy^* - \int_{\text{in}} \rho u^* C^* dy^* + \int_{\text{fs}} \rho \mathbf{n} \cdot \mathbf{u}^* C^* ds^* = \int_{\text{fs}} \rho D \mathbf{n} \cdot \nabla^* C^* ds^* \quad (6.33)$$

where out, in, and fs stand for the outlet, inlet and the free-surface respectively. We use the stationary version of the mass flux jump, thus $\dot{m}^* = \rho \mathbf{n} \cdot \mathbf{u}^*$, use the exact version of the Eckert–Schneider condition $\dot{m}^* C^* = -\mathbf{i} = \rho D \mathbf{n} \cdot \nabla^* C^*$ and find

$$\int_{\text{out}} \rho u^* C^* dy^* = \int_{\text{in}} \rho u^* C^* dy^* \quad (6.34)$$

since diffusion and convection equalize at the free-surface. Consistently, the mass flux of the non-volatile constituent does not change. Due to the varying film thickness we introduce the local height h_x^* , the local averaged velocity \bar{u}_x^* and the local mass flux $\Gamma_x^* = \rho \bar{u}_x^* h_x^*$ so that (6.34) reads in general $\Gamma_x^* \bar{C}_x^* = \text{const}$. Using the scales from above yields the condition

$$\Gamma_x \bar{C}_x = \Xi(1 - \Gamma_x) \quad (6.35)$$

where we have exploited $\bar{C}_{\text{in}} = 0$ and $\Gamma_{\text{in}} = 1$. Our present model employs the flat film, so that $\Gamma_x = 1$ holds for all x which clearly violates (6.35) since $\bar{C}_x \neq 0$ apart from the inlet, illustrating the mentioned inconsistency in our present model.

However, in a post-processing step we shall deduce the non-dimensional local mass flux

$$\Gamma_x = 1 - \frac{1}{\varepsilon_0 \text{PeLe}} \int_0^x \frac{\partial_y C}{C + \Xi} dx' \quad (6.36)$$

that results for a concentration field C which is deduced from our model. We then define the absolute deviation a of the constraint (6.35), thus

$$a := \Gamma_x \overline{C}_x - \Xi(1 - \Gamma_x) \quad (6.37)$$

Figure 6.8 shows the result of (6.37) vs. the streamwise coordinate x for different values of Pe . The absolute error remains acceptable small for the chosen parameter sets. This implies that the condition (6.35) is fulfilled to a high degree. Therefrom, we conclude that the simplifications of the present model are justified and we are thus confident that our results are close to the results of the full model. In addition, Figure 6.9 shows the actual film height $h(x)$ which is deduced from the local mass flux (6.36) as $h = \Gamma_x^{1/3}$. The decreasing film thickness with increasing Pe does not contradict the result that the absorbed mass flux typically increases for increasing Pe . This can be explained with the apparatus parameter A , which is kept const. so that an increase of Pe practically means an increase of Re and therefore an increase of the film thickness. From there it is clear that a larger Pe implies a larger film thickness leading to a smaller relative increase of the film thickness.

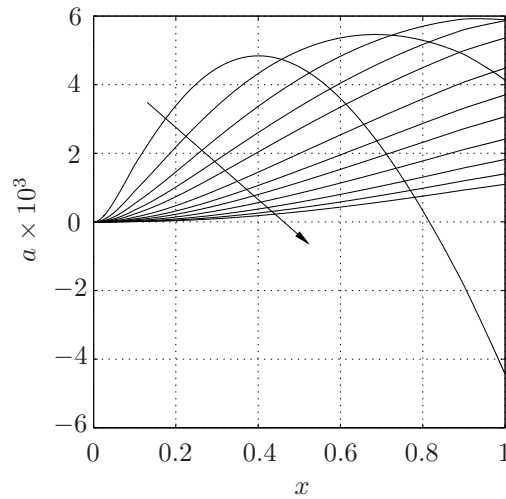


Figure 6.8.: Absolute error function a defined in (6.37) vs. the streamwise coordinate x . The parameters are those from Figure 6.6. The arrow indicates the direction of increasing Pe .

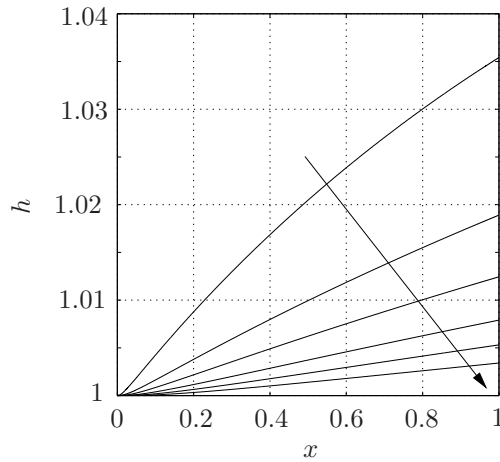


Figure 6.9.: Actual height $h(x)$ deduced from (6.36) with the parameters given in Figure 6.6. The arrow indicates the direction of increasing Pe .

Ignoring the Eckert–Schneider condition We now compare our model with the one mentioned at the beginning of this section assuming equimolar diffusion, *comparative model* called in the following. We again use the parameters from Figure 6.6 with $B = 1/8$, define $\Xi = 5$ and assume $C_0 = 0.5$ for convenience. Ignoring the effect of unidirectional diffusion implies $B^* = 1/16$ and $\varphi_m^* = -Sh\Delta C_i$, where the asterisk indicates the quantities resulting from the comparative model. The results are shown in Figure 6.10 where the black graphs refer to φ_m (linear/linear), the blue graphs to ϕ_m (linear/non-linear) and the red graphs refer to the model assuming equimolar diffusion. Even if the Sherwood number Sh remains practically unaltered, the mass flux density evaluations of our model ϕ_m and φ_m are significantly larger than the mass flux density of the comparative model φ_m^* . The findings are as expected and the comparison of the mass flux densities illustrate the importance of the Eckert–Schneider condition where our model gives an absorbed mass flux that is roughly 1.4...1.5 times larger than the absorbed mass flux from the comparative model. The driving potential ΔC_i and the mixing concentration \bar{C} are in general lower for our model even if the absorbed mass flux density is larger. To resolve this apparent paradox it is necessary to employ the varying mass flux (6.36) and not the intrinsic mass flux of our model which is $\Gamma_x \equiv 1$ for all x . This is justified by the fact that condition (6.36) is fulfilled to a high degree.

Linearization of the Eckert–Schneider condition Finally, we compare the mass flux densities ϕ_m (linear/non-linear) and φ_m (linear/linear) from the present linearized model with the mass flux density from the non-linear model ϕ_m^\dagger (non-linear/non-linear). To find ϕ_m^\dagger we use the exact version of (6.5), solve the equations iteratively and use the solution

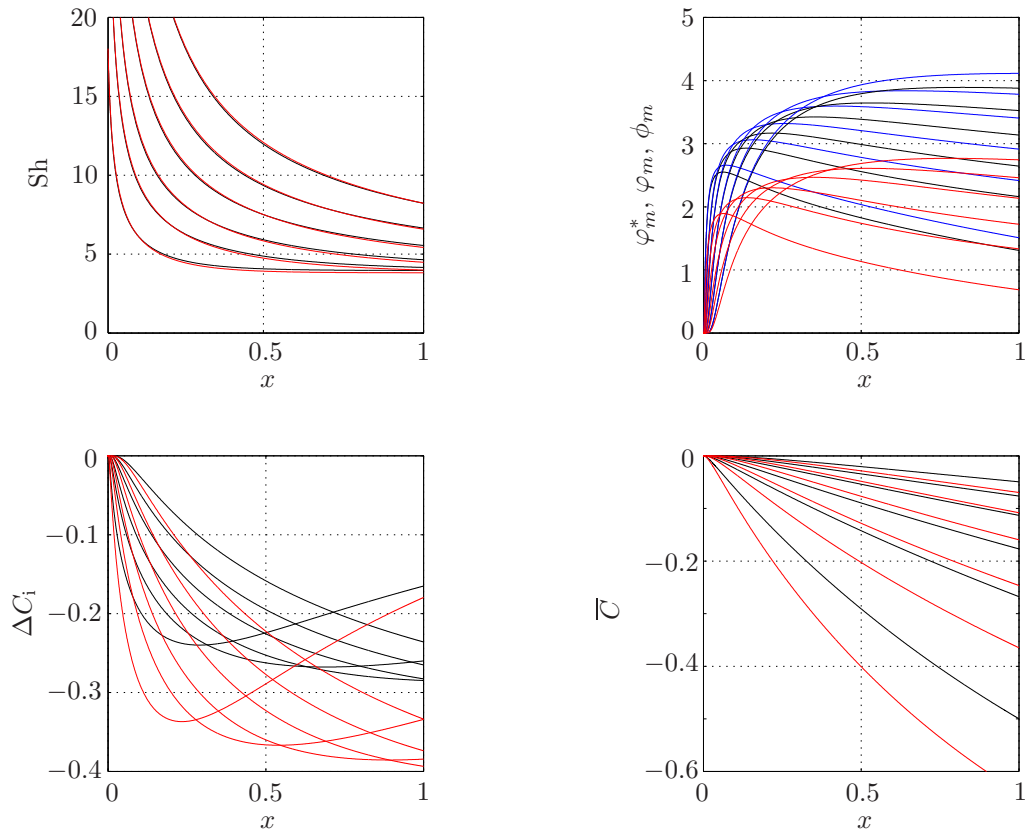


Figure 6.10.: Sherwood number Sh , mass flux densities ϕ_m (blue), φ_m (black), φ_m^* (red), driving potential ΔC_i and mixing concentration \bar{C} vs. the streamwise coordinate x . The black graphs refer to the present model and the red ones to the one assuming equimolar diffusion. The parameters are those from Figure 6.6.

to evaluate ϕ_m^\dagger in agreement with (6.31). Figure 6.11 shows the relative errors

$$e_\phi = \frac{\phi_m - \phi_m^\dagger}{\phi_m^\dagger} \quad , \quad e_\varphi = \frac{\varphi_m - \phi_m^\dagger}{\phi_m^\dagger}. \quad (6.38)$$

From the figure it becomes evident that the *real* mass flux density ϕ_m^\dagger (non-linear/non-linear) lies in between ϕ_m (linear/non-linear) and φ_m (linear/linear) from the linearized model, where the linear/linear approach underestimates and the linear/non-linear approach overestimates the *real* absorption rate by roughly 5% or less. We conclude that the linear/non-linear evaluation yields slightly better results.

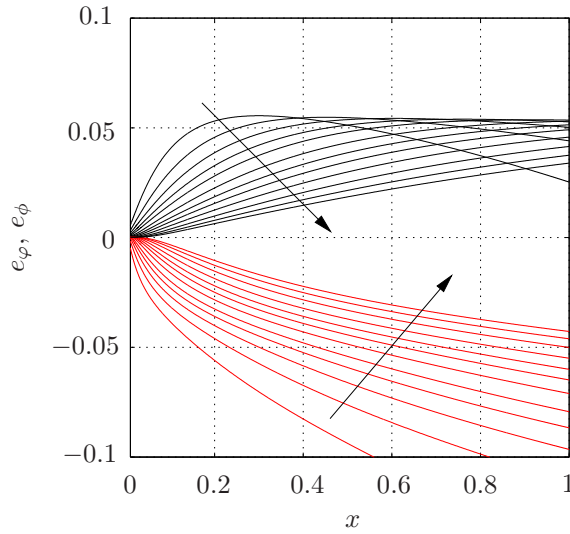


Figure 6.11.: Relative errors e_φ (red) and e_ϕ (black). The parameters are those from Figure 6.6. The arrows indicate the direction of increasing Pe.

6.4.4. Variation of the coolant Nusselt number

To deduce the most effective case with respect to Pe, we shall reduce the mass flux density to the non-dimensional averaged mass flux density

$$\bar{\phi}_m = \int_0^1 \phi_m dx. \quad (6.39)$$

Here, in contrast to the definition of Sh, the scaling factor is no longer a locally varying value so that an easy conversion between the non-dimensional and the dimensional mass flux density is guaranteed. However, from $\bar{\phi}_m$ we are still not able to deduce the most effective case with respect to Pe since the scaling factor includes $h_{\text{Nu}} \propto \text{Pe}^{1/3}$. It might, therefore, be more advantageous to choose an easier accessible scaling factor. If we do so, we have to admit, that the non-dimensional formulation becomes somewhat counterproductive and cumbersome. Nonetheless, for the task to deduce the most effective Péclet number we define the easily accessible scaling quantity for the averaged mass flux density $\bar{\eta}/L_0$ so that the non-dimensional averaged mass flux density becomes (Hofmann & Kuhlmann, 2012)

$$\bar{m} := -\bar{m}^* \left(\frac{\bar{\eta}}{L_0} \right)^{-1} = -\frac{1}{\varepsilon_0 \text{Pr Le}} \int_0^1 \frac{\partial_y C}{C + \Xi} dx = \text{Re}(\Gamma_{\text{out}} - 1). \quad (6.40)$$

Figure 6.12 shows the result for \bar{m} vs. the Péclet number Pe for several Nu_c^* and a certain parameter set (see figure caption). In addition we show the limiting case of the isothermal

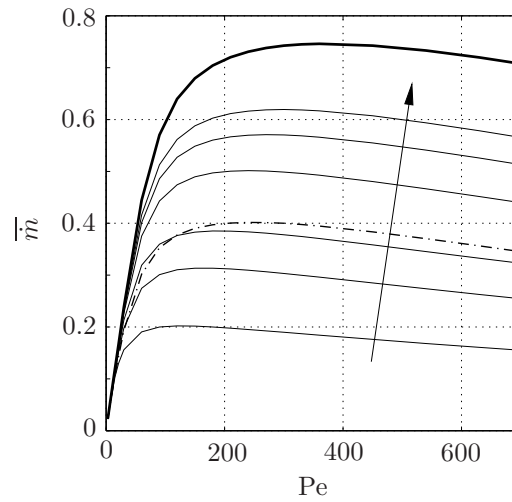


Figure 6.12.: Averaged mass flux density \bar{m} as function of the Péclet number Pe and the reduced coolant Nusselt numbers $Nu_c^* = \{500, 1000, 1500, 3000, 5000, 8000\}$. The thick curve represents the isothermal wall ($T = -1$), the dash-dotted curve the linear variation of the wall temperature ($T = -x$). The remaining parameters are $\{Le, A, B, \zeta, Pe_c^*\} = \{80, 5 \times 10^{-5}, 1/8, 0, -15000\}$. The Prandtl number is chosen as $Pr = 30$. The arrow indicates the direction of increasing Nu_c^* .

wall ($T = -1$) as a thick curve and the result for the linear variation of the wall temperature ($T = -x$) as a dash-dotted curve. From the trend of the curves within the figure it becomes evident that the coolant Nusselt number has a crucial influence on the quantitative result and the linear temperature variation may only serve as a qualitative representation of the absorption process. We can also conclude that an absorption maximum exists at relatively low Pe . With a given apparatus parameter A , the variation of Pe implies the variation of the aspect ratio ε_0 and with a given fluid this finally means a variation of the film thickness so that we can practically speak of an optimal film thickness. As mentioned by Killion & Garimella (2001) already Kawae *et al.* (1989) noticed the existence of an optimal film thickness.

To understand the appearance of this optimum we analyze the total heat flux balance of the film by integrating the transport equation yielding the heat fluxes

$$Q_s = -\frac{1}{\varepsilon_0} \int_0^1 (\partial_y T)|_{y=0} dx \quad (6.41)$$

$$Q_n = \frac{1}{\varepsilon_0} \int_0^1 (\partial_y T)|_{y=1} dx \quad (6.42)$$

$$Q_c = -Pe \int_0^1 (u_{Nu} T)|_{x=1} dy = -Pe \bar{T}_{out} \quad (6.43)$$

which are the total heat flux to the coolant Q_s , the total heat flux at the free-surface Q_n and the (negative) convected net fraction Q_c which is related to the mixing temperature at the outlet \bar{T}_{out} due to $\bar{T}_{\text{in}} = 0$. Figure 6.13 shows the total fluxes Q_i vs. the Péclet number Pe where the blue graphs represent Q_s (coolant), the red graphs Q_n (absorption), the solid black graphs Q_c (convection) and the dash-dotted line represents the sum of all fluxes confirming conservation. Thus, the coolant heat flux (blue) balances the total heat due to absorption (red) plus the convective heat transport (black). As Pe is increased, the more cooling demand stems from the convective process (the film itself) and the less remains for the absorption process (for the film surface). With the argument from above we may assume that increasing Pe causes an increasing film thickness and therefore an increasing incoming total enthalpy, where more and more cooling demand is addressed to the film (bulk) and less remains to cool the surface to drive absorption. Finally, Figure 6.14 shows the ratio Q_n/Q_s for all Nu_c^* that are given in Figure 6.13. This ratio is a measure for the efficiency where the best values are gained for vanishing Pe . The most efficient case is therefore the one with the least effectiveness since nothing is absorbed, see Figure 6.12. Again, with a given A and $Pe \rightarrow 0$ we conclude $\varepsilon_0 \rightarrow 0$ which implies either a plate that approaches an infinite length or a vanishing film thickness where the latter case is of practical relevance. A film of vanishing thickness suffers from the fact that it has no capacity to carry the absorbate and is therefore the least effective case for absorption.

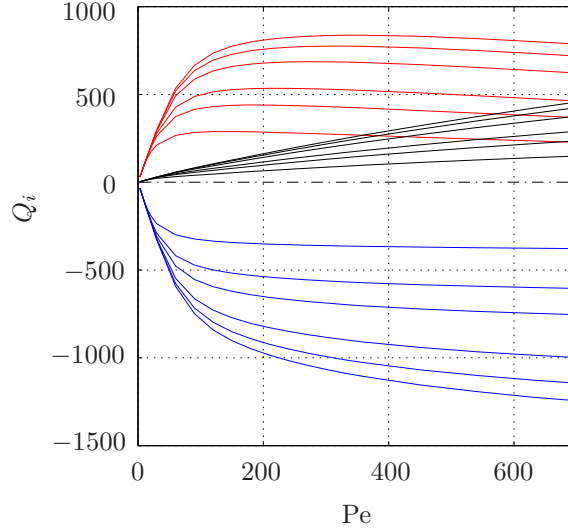


Figure 6.13.: Total heat fluxes Q_i as function of Pe and Nu_c^* . Shown are Q_n (red), Q_s (blue), Q_c (solid black) and the sum of all fluxes (dash-dotted). The parameters are $\{Le, A, B, \zeta, Pe_c^*\} = \{80, 5 \times 10^{-5}, 1/8, 0, -15000\}$ and $Nu_c^* = \{500, 1000, 1500, 3000, 5000, 8000\}$. Higher levels correspond to larger Nu_c^* .

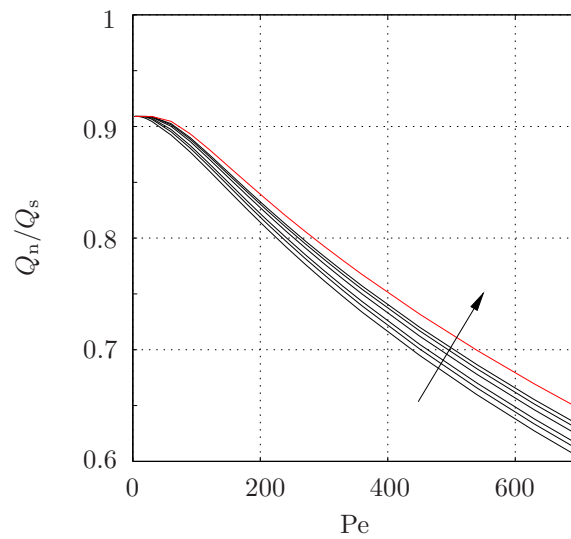


Figure 6.14.: Ratio Q_n/Q_s as function of Pe and Nu_c^* for the parameters given in Figure 6.13. The arrow indicates the direction of increasing Nu_c^* .

6.5. Interim summary

We summarize the assumptions made and comment on their validity.

1. Streamwise diffusion is a higher order effect and can be safely neglected.
2. As long as the gas is very dilute and the latent heat large, the heat loss to the gas phase can be neglected.
3. Employing a linear concentration coefficient γ seems to be justified, at least for small operating pressures for the LiBr–H₂O-system.
4. Modeling errors arising from the Eckert–Schneider condition were discussed.
 - a) The linearization of the Eckert–Schneider condition leads to a relatively small error depending on the post-processing.
 - b) Accounting for unidirectional diffusion but neglecting the increase of the film thickness results in an inconsistent formulation. However, the impact was shown to be relatively small.
 - c) Finally, the inclusion of the Eckert–Schneider condition appears to be essential. Among all different models for flat absorbing falling films the inclusion of the one-sided diffusion process seems to be by far the most important aspect, since no other simplification has a comparable impact.

5. The heat transfer at the wall has a crucial influence to the quantitative result. A linear temperature variation at the wall can only serve as a qualitative representation.
6. We find a maximum for the averaged mass flux density as function of Pe which is related to an optimal aspect ratio $\varepsilon_0 = APe^{1/3}$ since the apparatus parameter A is given. For a particular fluid this finally results in an optimal film thickness, Reynolds number or incoming mass flux, respectively.
7. We have shown that the most efficient case is in turn the least effective one.

7. The absorbing wavy film

The assumption of one-way coupling again allows to employ the solutions of the isothermal wavy film, so that $\mathbf{u} = \mathbf{u}(x, y, t)$ and $h = h(x, t)$ are known in the equations for heat and species transport. However, the free surface boundary conditions prohibit the numerical treatment of the wavy absorbing film within the moving frame and we need to change into the laboratory frame. Therefore, the problem becomes transient and a time stepping technique has to be introduced.

7.1. Governing equations

Bulk equations The transport equation for the scalar quantity $S = S(x, y, t)$ reads in the laboratory frame by neglecting streamwise diffusion

$$\left[\partial_t + \mathbf{u} \cdot \nabla - \frac{1}{\text{Pe}} \partial_{yy} \right] S(x, y, t) = 0. \quad (7.1)$$

We again introduce a coordinate transformation as for the Navier–Stokes equations, hence

$$\tau = t \quad , \quad \xi = x \quad , \quad \eta = \frac{y}{h(x, t)}. \quad (7.2)$$

Note that x and ξ represent the streamwise coordinates in the laboratory frame (we assume no longer moving coordinates in streamwise direction). The operators transform as

$$\partial_t = \partial_\tau - \frac{\eta \dot{h}}{h} \partial_\eta \quad , \quad \partial_x = \partial_\xi - \frac{\eta h'}{h} \partial_\eta \quad , \quad \partial_y = \frac{1}{h} \partial_\eta. \quad (7.3a)$$

We exploit the traveling wave solutions so that $\dot{h} = -ch'$. The transport equation (7.1) for $S = S(\xi, \eta, \tau)$ within the computational domain reads

$$\left(\partial_\tau + \frac{c\eta h'}{h} \partial_\eta \right) S + u \left(\partial_\xi - \frac{\eta h'}{h} \partial_\eta \right) S + \frac{v}{h} \partial_\eta S - \frac{1}{\text{Pe} h^2} \partial_{\eta\eta} S = 0.$$

Collection of all terms yields

$$\left[\partial_\tau + u \partial_\xi + \frac{\eta h' (c - u) + v}{h} \partial_\eta - \frac{1}{\text{Pe} h^2} \partial_{\eta\eta} \right] S = 0.$$

Since all velocity components and the surface position are given, we define the coefficients

$$f(\xi, \eta, \tau) := \frac{\eta h'(c - u) + v}{h}, \quad (7.4a)$$

$$g(\xi, \tau) := h^{-2}, \quad (7.4b)$$

and obtain

$$\left[\partial_\tau + u \partial_\xi + f \partial_\eta - \frac{g}{\text{Pe}} \partial_{\eta\eta} \right] S(\xi, \eta, \tau) = 0. \quad (7.5)$$

Wall bc For the present study it is advising to reduce the complexity of the model to a reasonable minimum. From this point of view we define the wall to be isothermal, thus $T|_{\eta=0} = -1$. The resulting deficit of this approach is a discontinuity of the temperature at the lower left corner connecting the inlet with the wall. Our numerical experiments have shown that this discontinuity induces severe oscillations of the temperature derivative at the wall. To circumvent this issue, we introduce the regularized wall boundary condition

$$T|_{\eta=0} = -\frac{1 + \tanh[s(\xi - \xi_0)]}{2}(1 - e^{-\tau}) \quad (7.6)$$

representing a smeared step function shifted by ξ_0 from the inlet $\xi = 0$ and smeared by the parameter s . The exponential term additionally guarantees a smooth onset in time. The temporal evolution of the function is shown in Figure 7.1.

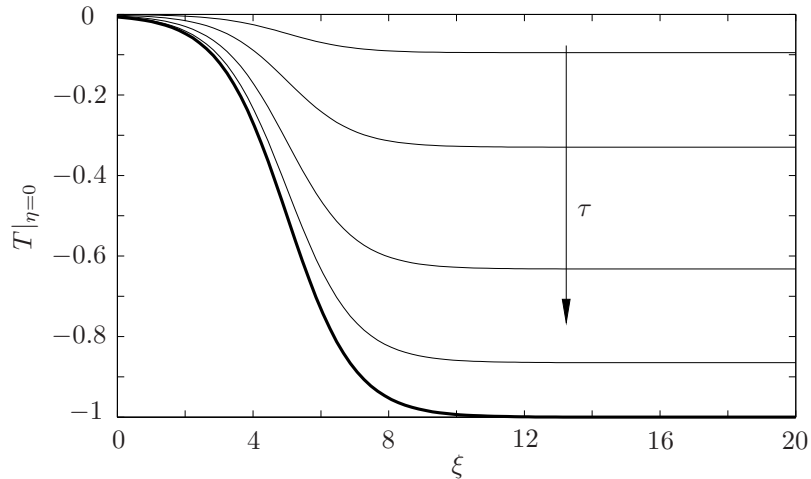


Figure 7.1.: Temporal evolution of the regularized wall bc for $\xi_0 = 5$ and $s = 1/2$. The arrow shows in the direction of increasing τ . The thick graph represents the time-asymptotic state.

Flux bc The flux boundary condition at the free surface becomes

$$(-hh'\partial_\xi + n^2\partial_\eta)(T + BC) = 0 \quad (7.7)$$

where we have used the normal derivative operator (5.5). For the later proposed marching technique it is advantageous to neglect the derivative in ξ which is small compared to the crosswise derivative so that this simplification is expected to bear no significant impact. The flux bc finally reads

$$\partial_\eta T = -B\partial_\eta C. \quad (7.8)$$

Inlet bc To avoid the steep gradient of C at the inlet, related to $\zeta \neq 0$, we simply define $\zeta = 0$ so that the inlet bc becomes $C|_{\xi=0} = 0$.

7.2. Numerical approach

On a first view the parabolic character of the equations invites to employ a simple marching technique using finite differences. Such a numerical technique works properly as long as $u \geq 0$, i.e. as long as no backflow occurs. However, for cases with a backflow region, the problem becomes a representative of the forward-backward heat equation. For these cases the marching technique becomes unstable if a region of backflow is entered since the equation is integrated in its unstable direction (Aziz *et al.*, 1999).

A potential remedy to circumvent this shortcoming is given by Phillips & Ackerberg (1973), since their problem, integration of the unsteady boundary layer equations through regions of backflow, seems to be very similar to the present one. They employ space-marching in the streamwise direction which is then followed by time-marching. Central differences are used throughout so that their method is of second order accuracy in space and time. Depending on the direction of the streamwise velocity Phillips & Ackerberg (1973) switch the stencil for the convective derivative. Unfortunately, the straightforward implementation of this method turned out to be not convergent for the present problem, so that a further modification of the backflow treatment is needed.

Several additional unsuccessful approaches to solve the numerical stability problem induced by the backflow, have finally compelled us to drop the convective term $u\partial_\xi S$ within the regions of backflow, i.e. to set $u = 0$ for $u < 0$. This idea was stimulated by Cebeci *et al.* (1979) and is called FLARE-approximation¹ from now on. Paradoxically, this crude-looking approximation yields the most promising results. The impact of the FLARE-approximation will be estimated by a benchmark simulation further below.

¹Named after the authors Flügge-Lotz and Reyhner.

Beyond that, our numerical experiments have shown that the application of the basic scheme of Phillips & Ackerberg (1973) to both transport equations leads to minor temporal oscillations of the temperature derivative at the wall. We have therefore decided to use the Crank–Nicholson scheme for the discretization of T and the basic scheme of Phillips & Ackerberg (1973) for the discretization of C .

Due to the discretization schemes used we keep the transport equation for T in its form but transform the PDE for C into a system of PDE's of first order by defining

$$w := \partial_\eta C \tag{7.9}$$

so that the transport equations become

$$(\partial_\tau + \theta u \partial_\xi) C + \left(f - \frac{g}{\text{PeLe}} \partial_\eta \right) w = 0, \tag{7.10a}$$

$$\partial_\eta C - w = 0, \tag{7.10b}$$

$$\left(\partial_\tau + \theta u \partial_\xi + f \partial_\eta - \frac{g}{\text{Pe}} \partial_{\eta\eta} \right) T = 0. \tag{7.10c}$$

where $\theta = \theta(u)$ is the Heaviside step function to account for the FLARE-approximation, setting $u = 0$ for $u < 0$. We shall point out that the FLARE-approximation is inconsistent with the original transport equation already before discretization due to the introduction of the Heaviside step function. However, for cases where the impact of the convective term is small, we expect that the solution of the original transport equation is well approximated. The set of boundary conditions reads

$$T|_{\xi=0} = 0, \tag{7.11a}$$

$$C|_{\xi=0} = 0, \tag{7.11b}$$

$$T|_{\eta=0} = -\frac{1 + \tanh[s(\xi - \xi_0)]}{2} (1 - e^{-\tau}), \tag{7.11c}$$

$$w|_{\eta=0} = 0, \tag{7.11d}$$

$$(T - C)|_{\eta=1} = 0, \tag{7.11e}$$

$$(Bw + \partial_\eta T)|_{\eta=1} = 0. \tag{7.11f}$$

As initial condition we employ the zero-state, i.e.

$$T|_{\tau=0} = 0, \tag{7.12a}$$

$$C|_{\tau=0} = 0, \tag{7.12b}$$

$$w|_{\tau=0} = 0. \tag{7.12c}$$

7.2.1. Discretization of C and w

The sketch in Figure 7.2 shows a single cell in order to introduce the notation used in the following.

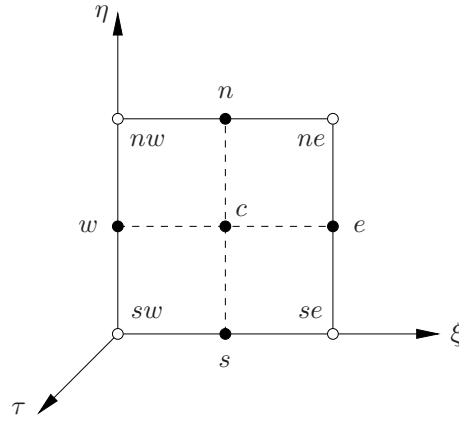


Figure 7.2.: Sketch of a single cell with the notation used. The open circles indicate the shared location of C and w .

The discretization of (7.10a) is done around the center of a cell (location c) and between the two consecutive time levels n and $n+1$ (the position is indicated as A_C in Figure 7.3) so that both time levels enter with a weight of $1/2$, hence

$$\begin{aligned}\partial_\tau C &\approx \frac{C_c^{n+1} - C_c^n}{\Delta\tau} \\ w &\approx \frac{w_c^{n+1} + w_c^n}{2} \\ \partial_\xi C &\approx \frac{1}{2} \left[\frac{C_e^{n+1} - C_w^{n+1}}{\Delta\xi} \right] + \frac{1}{2} \left[\frac{C_e^n - C_w^n}{\Delta\xi} \right] \\ \partial_\eta w &\approx \frac{1}{2} \left[\frac{w_n^{n+1} - w_s^{n+1}}{\Delta\eta} \right] + \frac{1}{2} \left[\frac{w_n^n - w_s^n}{\Delta\eta} \right].\end{aligned}$$

Centered values are interpolated by the arithmetic mean of the corner values, thus

$$C_c \approx \frac{C_{ne} + C_{se} + C_{nw} + C_{sw}}{4}.$$

In terms of the corner values, the discretized version of (7.10a) becomes

$$\partial_\tau C \approx \left[\frac{C_{ne}^{n+1} + C_{se}^{n+1}}{4\Delta\tau} \right] + \left[\frac{C_{nw}^{n+1} + C_{sw}^{n+1}}{4\Delta\tau} \right] - \left[\frac{C_{ne}^n + C_{se}^n + C_{nw}^n + C_{sw}^n}{4\Delta\tau} \right] \quad (7.13a)$$

$$\partial_\xi C \approx \left[\frac{C_{ne}^{n+1} + C_{se}^{n+1}}{4\Delta\xi} \right] - \left[\frac{C_{nw}^{n+1} + C_{sw}^{n+1}}{4\Delta\xi} \right] + \left[\frac{(C_{ne}^n + C_{se}^n) - (C_{nw}^n + C_{sw}^n)}{4\Delta\xi} \right] \quad (7.13b)$$

$$w \approx \left[\frac{w_{ne}^{n+1} + w_{se}^{n+1}}{8} \right] + \left[\frac{w_{nw}^{n+1} + w_{sw}^{n+1}}{8} \right] + \left[\frac{w_{ne}^n + w_{se}^n + w_{nw}^n + w_{sw}^n}{8} \right] \quad (7.13c)$$

$$\partial_\eta w \approx \left[\frac{w_{ne}^{n+1} - w_{se}^{n+1}}{4\Delta\eta} \right] + \left[\frac{w_{nw}^{n+1} - w_{sw}^{n+1}}{4\Delta\eta} \right] + \left[\frac{(w_{ne}^n + w_{nw}^n) - (w_{se}^n + w_{sw}^n)}{4\Delta\eta} \right] \quad (7.13d)$$

where the first brackets hold the unknowns at the new time step $n + 1$, the second brackets hold the previously computed values at $n + 1$ and the third brackets hold the values of the previous time step n .

Equation (7.10b) is discretized at the new time level $n + 1$ around the location e . The position is indicated as A_w in Figure 7.3. The discretized version of (7.10b) then becomes

$$\frac{C_{ne}^{n+1} - C_{se}^{n+1}}{\Delta\eta} - \frac{w_{ne}^{n+1} + w_{se}^{n+1}}{2} = 0. \quad (7.14)$$

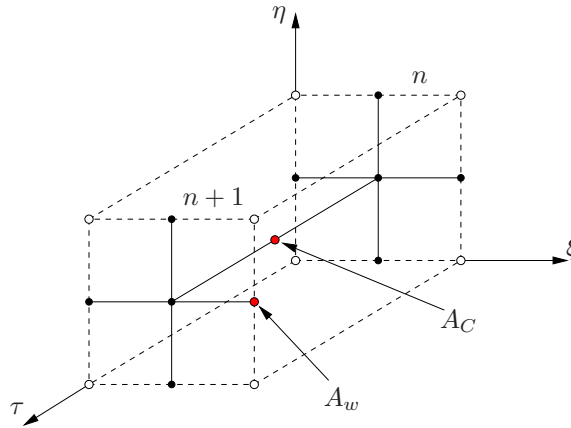


Figure 7.3.: Sketch of the numerical molecules for the discretization of C and w . The position A_C indicates the center of discretization for (7.10a) and A_w the center of discretization for (7.10b). The open circles indicate the shared location of C and w . The time levels are indicated as n and $n + 1$.

7.2.2. Discretization of T

Our numerical experiments have shown that the discretization of both transport equations with the given scheme lead to minor temporal oscillations of $(\partial_\eta T)|_{\eta=0}$. A damping of these oscillations is achieved by employing the Crank–Nicholson scheme for the discretization of T . However, keeping the introduced stencil would give us a total of $3(N_\eta + 1)$ unknowns for C, w, T that are faced to $3N_\eta + 4$ equations ($3N_\eta$ for the bulk plus 4 boundary conditions). Instead of solving an overdetermined system, we shift the given numerical

molecule by $\Delta\eta/2$ and end up at the numerical molecule for T , shown in Figure 7.4. The variable T is again evaluated at the corners, indicated by the open circles in Figure 7.4. The interpolation is carried out as in Section 7.2.1.

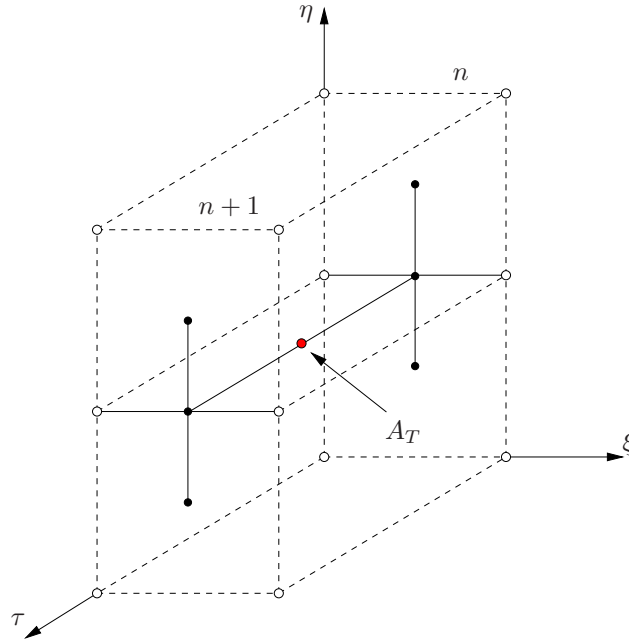


Figure 7.4.: Sketch of the numerical molecules for the discretization of T . The position A_T indicates the center of discretization for (7.10c). The time levels are indicated as n , $n + 1$ and the location of T is represented by the open circles.

7.2.3. Interpolation of u

Since it is desirable to choose the spatial step $\Delta\xi$ and the time step $\Delta\tau$ independently of the underlying flow field resolution, the coefficients u , g and f are subject to interpolation. We therefore decompose the coefficients into their Fourier spectra with respect to ξ' , hence

$$\hat{a}_n(\eta) = \frac{1}{N_\xi} \sum_{j=0}^{N_\xi-1} a_j(\eta) e^{-ik_n \xi'_j} \quad \text{with} \quad k_n = \frac{2\pi}{L} n \quad \text{for} \quad a = u, f, g \quad (7.15)$$

where $\hat{a}_n(\eta) = \hat{a}(k_n, \eta)$ are the Fourier coefficients of the corresponding data set $a_j(\eta) = a(\xi'_j, \eta)$ given in moving coordinates $\xi' = \xi - c\tau$. The number of contributors N_ξ is determined by the streamwise resolution of the underlying Navier–Stokes solution. For the evaluation of the coefficients at any location (ξ, η, τ) (with ξ now in the laboratory

frame) we recompose according to

$$a(\xi, \eta, \tau) \approx \sum_{n=-N}^N \hat{a}_n(\eta) e^{ik_n(\xi - c\tau)} \quad \text{for} \quad \hat{a} = \hat{u}, \hat{f}, \hat{g}. \quad (7.16)$$

The given approximation includes only wave numbers up to N , so that the high wave number components are neglected. To find the cut off wave number, we compare the Fourier amplitudes $|\hat{a}_n|$ with the amplitude of the fundamental $|\hat{a}_1|$, thus $r_n := |\hat{a}_n|/|\hat{a}_1|$ and set the cut off where $r_n < \varepsilon$ by defining $\varepsilon := 10^{-4}$.

We shall note that the resolution in η is inherited by the flow field resolution and $N_\eta = 50$ is used throughout.

7.2.4. Basic verification

For a partial verification of the code we apply the introduced time-stepping method to a flat film and compare it with the result of the stationary solver that was employed in Chapter 6. Since we have verified the code for the flat film with data from the literature and since the codes are fundamentally different from another, a coincidence shall indicate that the time stepping method gives correct results.

To demonstrate the influence of the regularization of the thermal wall boundary condition we employ the isothermal wall for the stationary flat film simulation. By defining $Re := 10$ all parameters are given. For now, we simply assume $\Delta\tau = \Delta\xi = 1$ and give some more thoughts about choosing the step sizes subsequently.

Figure 7.5 shows the spatio-temporal evolution of the free surface temperature or concentration, respectively. The parabolic character of the system becomes evident. The dashed line indicates the surface velocity $u_{Nu, \max} = 1.5$ and the full line represents $u_p = 1.25$ approximating the present perturbation propagation velocity. This gives us an estimate for the time span that is needed to reach a stationary solution. We shall employ this propagation velocity also for the *really* transient simulations to be discussed later to estimate the time span to reach a time periodic solution.

Figure 7.6 compares the result of the stationary solver with the final result of the time stepping method. For a better comparability we have shifted the result of the latter by $x = \xi_0$. The agreement is excellent so that our initial verification is successful and a basic functionality of the solver can be guaranteed, at least for forward flow.

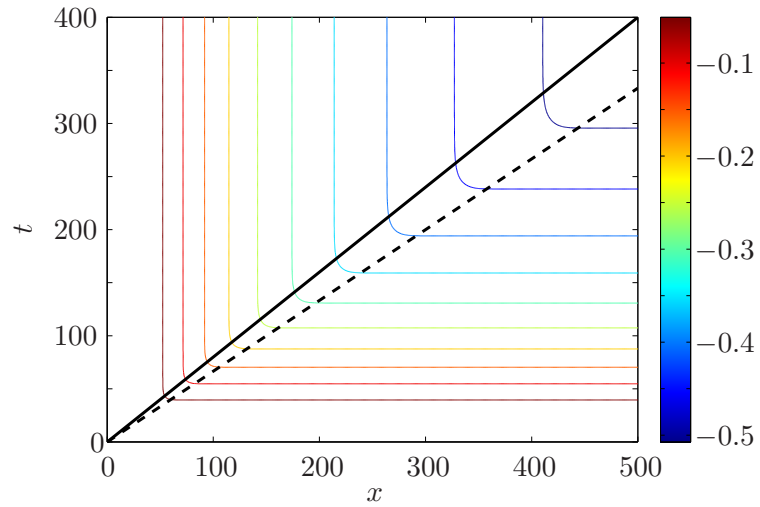


Figure 7.5.: Isolines (color) of the surface temperature (or concentration) in the xt -plane to illustrate the spatio-temporal evolution. The lines indicate the surface velocity $u = 1.5$ (dashed) and $u = 1.25$ (full) to approximate the perturbation propagation velocity.

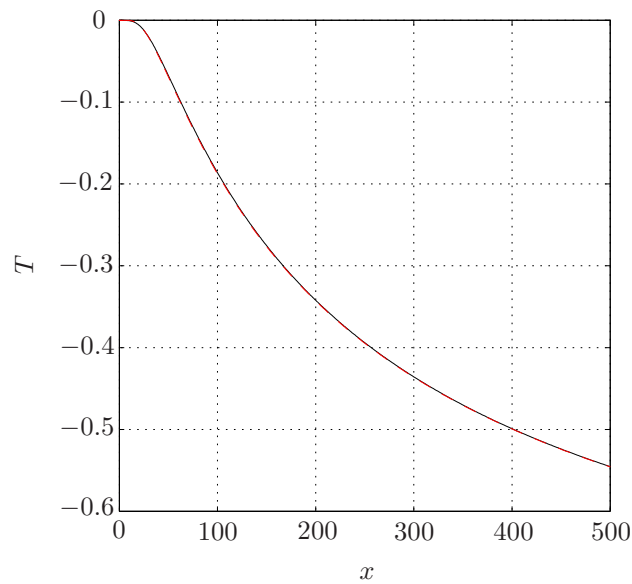


Figure 7.6.: Time-asyncotic surface temperature T (black, full) and solution of the stationary solver (red, dashed) vs. the streamwise coordinate x .

7.3. Results for the thermal case

For the final verification we reproduce the results of the thermal film of Chapter 5. We therefore change the boundary condition at the surface to $T|_{\eta=1} = C|_{\eta=1} = 0$, decoupling the fields from another. We use $T|_{\xi=0} = C|_{\xi=0} = 0$ at the inlet and apply the regularized wall boundary condition (7.6) also to C . Employing $Le = 1$ yields the identical problem for T and C so that the setup is also a verification for the discretization strategies, as both schemes shall lead to the same result. The simulation is initialized with $S(\xi, \eta, \tau = 0) = 0$ for $S = T, C, w$. The step sizes are chosen as $\Delta\tau = 1/8$ and $\Delta\xi = 1/4$. Figure 7.7 shows the contours of the temperature field for $Pr = 1$ and $Pr = 10$. The qualitative agreements with Figure 5.5 and Figure 5.6 are good. However, the case $Pr = 100$ does not converge even if the employed numerical schemes are stable in general. This is due to the FLARE-approximation and the backflow regions, respectively, since a larger Pr leads to a larger Pe and therefore to a more dominant convective term, which suffers from the discontinuous velocity field from the FLARE-approximation, see step function in (7.10).

For the verification of the discretization schemes we compare the results for T and C in the $\xi\eta$ -plane in Figure 7.8 showing the isolines for the temperature field (red) and for the concentration field (black). We clearly see that the different treatment of T and C in the discretization has no influence on the solution.

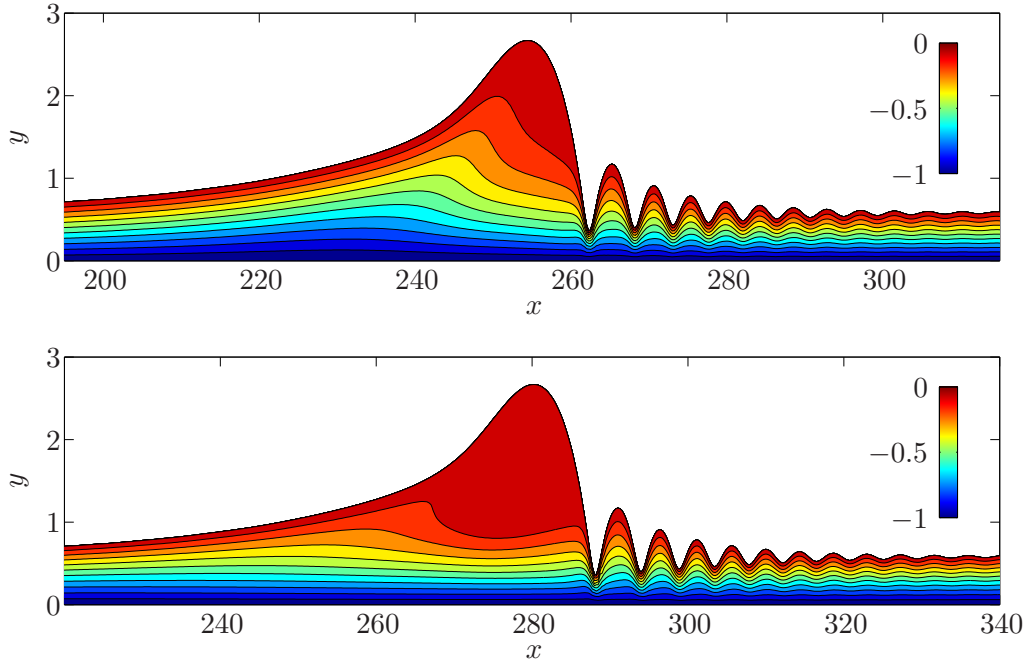


Figure 7.7.: Contours of the temperature for $Pr = 1$ (top) and $Pr = 10$ (bottom).

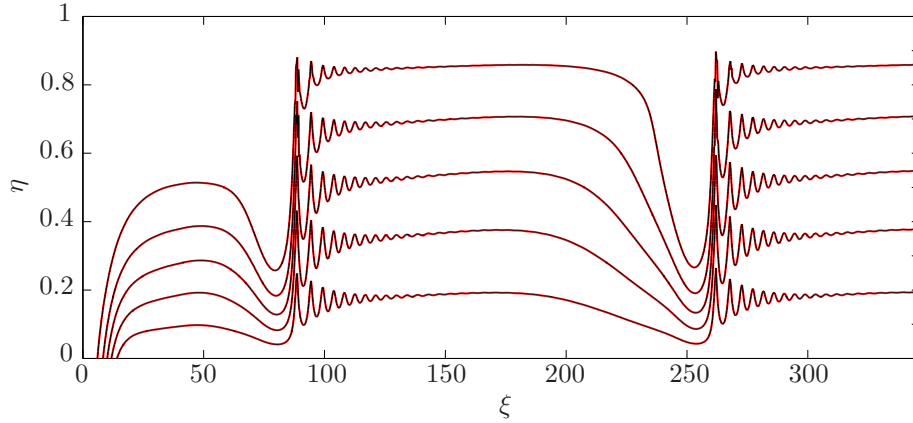


Figure 7.8.: Isolines of T (red) and C (black) in the $\xi\eta$ -plane for $\text{Pr} = 10$ and $t = 150$.

Figure 7.9 shows the height h (black), the Nusselt number bottom Nu_f (blue) and the Nusselt number free surface Nu_i (red) for $\text{Pr} = 1$ where the dashed curves refer to the result of Chapter 5 shown in Figure 5.5 and the solid curves are the present results from the marching technique by using the FLARE-approximation. The overall comparison is good, despite the minor oscillations induced by the numerical treatment of the backflow regions.

Figure 7.10 shows h (black), Nu_f (blue) and Nu_i (red) for $\text{Pr} = 10$ where the dashed curves again refer to the results from Figure 5.6. Here, the comparison is already poor giving an indication for the impact of the FLARE-approximation. Nonetheless, the overall qualitative behavior is well captured.

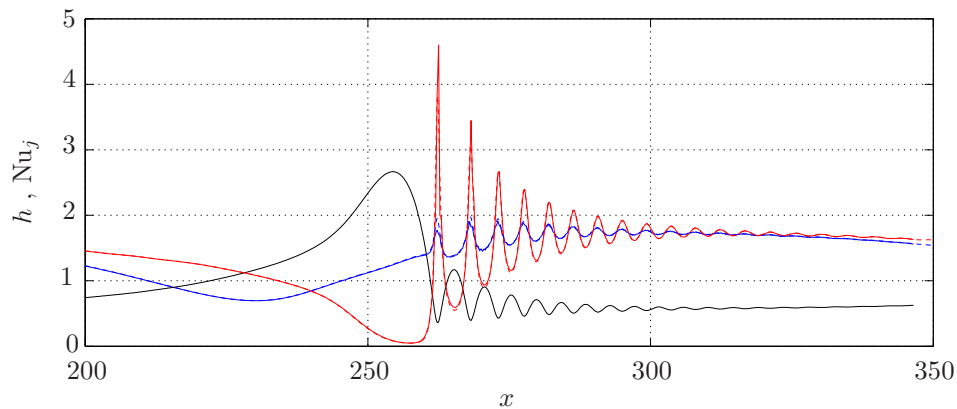


Figure 7.9.: Height h (black), Nusselt number bottom Nu_f (blue) and Nusselt number free surface Nu_i (red) for $\text{Pr} = 1$. The solid curves refer to the results from time-stepping and the dashed ones refer to the results given in Figure 5.5.

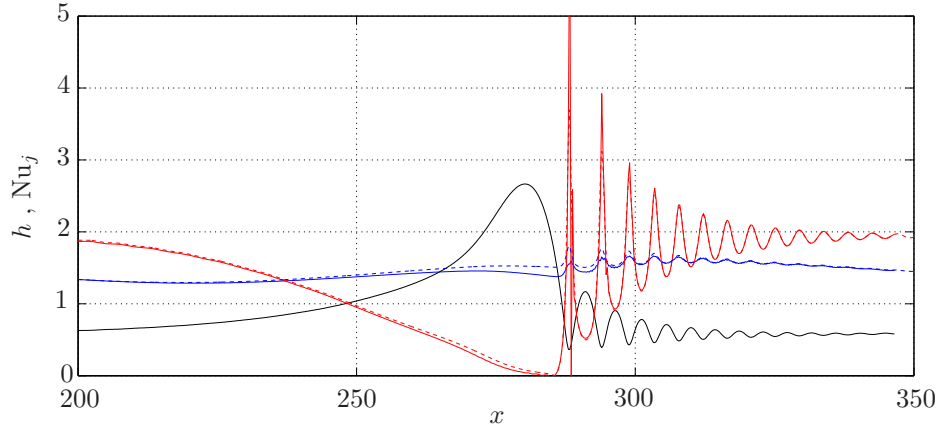


Figure 7.10.: Height h (black), Nusselt number bottom Nu_f (blue) and Nusselt number free surface Nu_i (red) for $Pr = 10$. The solid curves refer to the results from time-stepping and the dashed ones refer to the results given in Figure 5.6.

The benchmark simulation of the thermal wavy film yields the following interim results.

- The different discretization schemes of the respective transport equations have no influence to the solution.
- For forward flow, the time stepping method yields reliable results, shown by the comparison with the results from the solver of Chapter 6.
- The agreements with the results of Chapter 5 show that the time stepping method yields acceptable results with certain deviations due to the chosen approximation. However, the backflow regions, treated within the FLARE-approximation, are sources of numerical instability, in particular for large Prandtl numbers and large backflow regions.

7.4. Results for the absorbing case

In this final section we shall investigate the wavy absorbing film, again within the FLARE-approximation. The result from the previous chapter suggests that the error introduced is acceptable. However, one has to keep in mind that the approach is limited due to the inconsistent formulation. To mimic a system that is related to LiBr–H₂O we define the parameter set

$$Le := 80 \quad , \quad Pr := 30 \quad , \quad B := 1/8. \quad (7.17)$$

The boundary conditions (7.11) already imply $\zeta = 0$. For the regularized thermal wall boundary condition we define $\xi_0 := 10$ and $s := 0.2$. The remaining free parameter is Pr since Re is already inherited from the considered flow field.

7.4.1. Evaluation of step sizes

For the following test we employ the flow field of case 6 (see Table 4.4) and consider a total length of 4 wavelengths, thus $L_0 = 4L$. The step sizes $\Delta\xi$ and $\Delta\tau$ are varied and the qualitative results are examined and summarized in Table 7.1. From Table 7.1 one can easily extract that the method calls for a CFL-number Co below one, thus $\text{Co} = u\Delta\tau/\Delta\xi < 1$ (for $u \approx 1$). Secondly it seems most advantageous to employ the step size combinations for which $\Delta\tau/\Delta\xi = 0.5$.

Table 7.1.: Qualitative results for different step size combinations. A diverged solution is indicated by 0, a qualitatively reasonable solution by 1, n/a means that the simulation has not been performed and wig indicates the appearance of wiggles in T and/or C .

	$\Delta\tau = 1$	$\Delta\tau = 1/2$	$\Delta\tau = 1/4$	$\Delta\tau = 1/8$
$\Delta\xi = 1$	0	1	wig	wig
$\Delta\xi = 1/2$	0	0	1	wig
$\Delta\xi = 1/4$	0	0	0	1
$\Delta\xi = 1/8$	n/a	0	n/a	0

7.4.2. Convergence check

With $\Delta\tau/\Delta\xi = 0.5$ we perform a grid refinement study again for case 6 (Table 4.4) and $L_0 = 6L \approx 350$. The step sizes are chosen as $\Delta\xi = 1/2^n$ and $\Delta\tau = 1/2^{n+1}$ for $n = 2, 3, 4$. The results for the negative η -derivative of the concentration at the free surface

$$C'_\eta := -(\partial_\eta C)|_{\eta=1} \quad (7.18)$$

are shown in Figure 7.11 for the spatial evolution at the end of the simulation $t_{\text{end}} = 279$, and in Figure 7.12 for the temporal evolution at the end of the domain $x_{\text{end}} = 349$. The figures also show the instantaneous height $h(x, t_{\text{end}})$ and the local height $h(x_{\text{end}}, t)$, respectively. The overall convergence of the solution is good apart from the narrow oscillating regions.

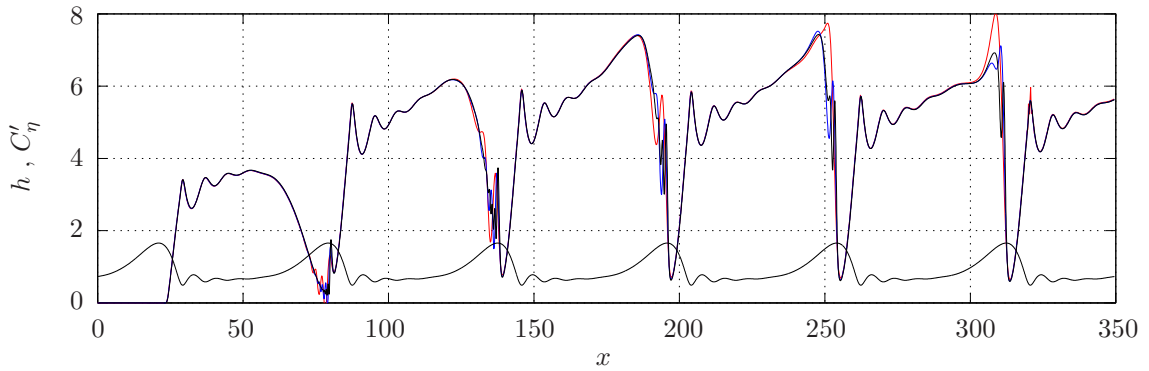


Figure 7.11.: Spatial evolution of C'_η for $t_{\text{end}} = 279$, where the step sizes are chosen as $\Delta\xi = 1/2^n$ and $\Delta\tau = 1/2^{n+1}$ for $n = 2$ (red), $n = 3$ (blue) and $n = 4$ (black). The instantaneous height $h(x, t_{\text{end}})$ is also shown (lower curve).

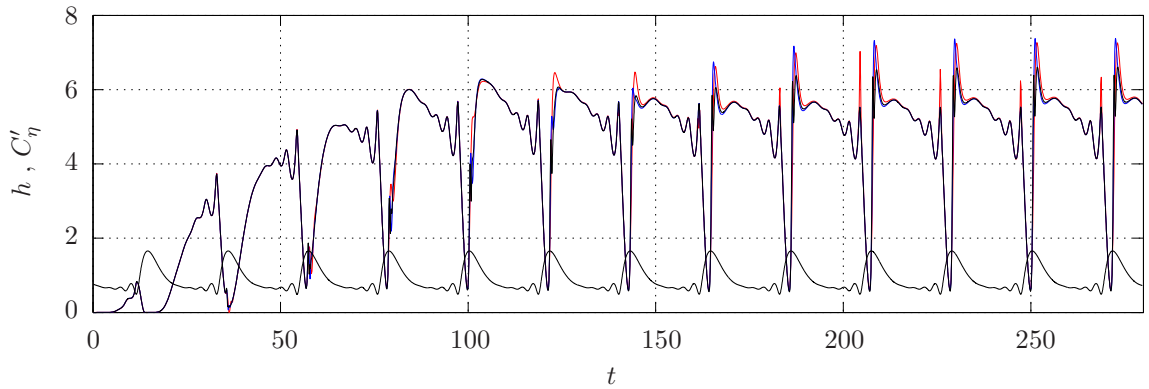


Figure 7.12.: Temporal evolution of C'_η for $x_{\text{end}} = 349$, where the step sizes are chosen as $\Delta\xi = 1/2^n$ and $\Delta\tau = 1/2^{n+1}$ for $n = 2$ (red), $n = 3$ (blue) and $n = 4$ (black). The local height $h(x_{\text{end}}, t)$ is also shown (lower curve).

7.4.3. Results for case 6

Figure 7.13 shows the temperature field and the concentration field for case 6 of Table 4.4 with the parameters given in (7.17) at the end of the simulation. In Figure 7.14 a close up of the concentration field near the 3rd and 4th wave hump including a vector plot of the velocity field (within the moving frame) is given. From the close up we clearly identify the convective species transport and the influence of the tiny separation zone within the moving frame.

The size of the separation zone can be estimated qualitatively from the central, left image and quantitatively from the central, right image of Figure 7.24. The latter shows the streamwise surface velocity $u|_{y=h}$ (in the laboratory frame) and the wave celerity c as

dashed line, so that an intersection of the surface velocity with c means the appearance of a separation zone (in the moving frame) (Albert *et al.*, 2014). Correspondingly, an intersection with the baseline indicates backflow (in the laboratory frame). Due to the almost tangential surface velocity (in fact it is intersecting c) one finds a region (within the moving frame) with almost no fluid movement. This becomes also clear from the vector plot of Figure 7.14.

Figure 7.15 shows the height h and the relevant quantity for mass flux $(-\partial_y C)_{y=h}$, scaled by $1/8$ for convenience. Due to the boundary condition and the choice of B , this quantity is equivalent to the heat flux density at the free surface $\phi_{q,i}$. From the graphs it becomes evident that absorption is largest at the deepest wave trough and drops rapidly along the steep front of the wave crest to reach its minimum at the vertex. From there it increases again to values that are close to the maximum of the first trough in front of the main hump. In a comparison with the film height it becomes clearly visible that the mass flux density and heat flux density, respectively, again scales inversely with the height. This finding agrees qualitatively very well with Albert *et al.* (2014). However, they present a local Sherwood number which differs from our non-dimensional mass flux density by a normalization with a local driving potential.

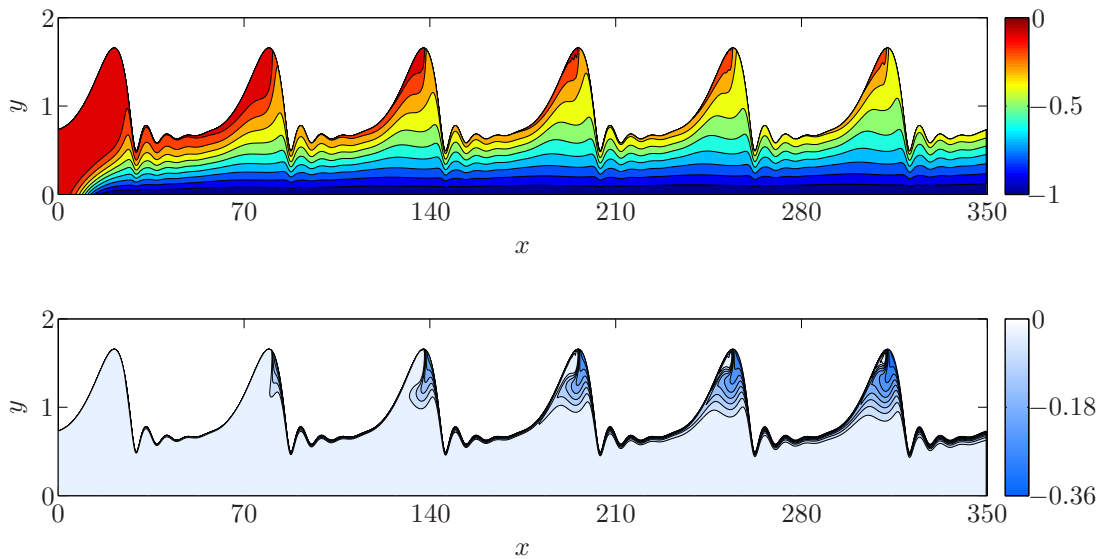


Figure 7.13.: Solution for $T(x, y, t_0)$ (top) and $C(x, y, t_0)$ (bottom) at $t_0 = 279$ for case 6 of Table 4.4.

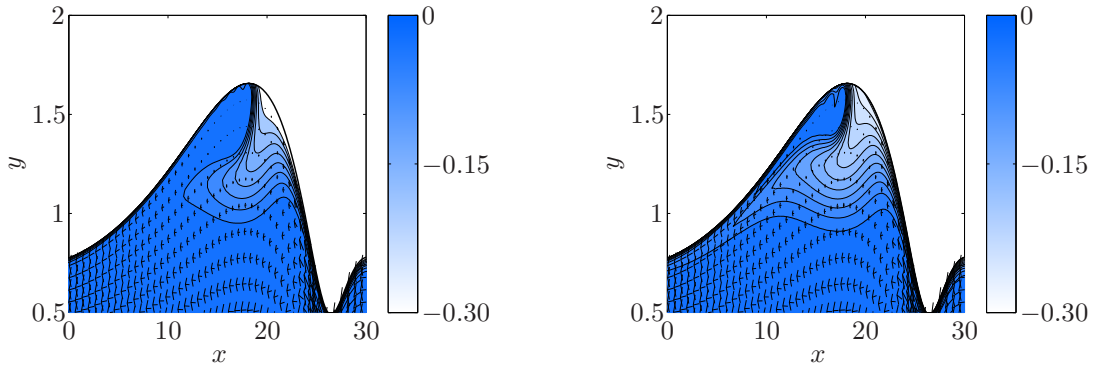


Figure 7.14.: Close up of the concentration field $C(x, y, t_0)$ at $t_0 = 279$ shown in Figure 7.13. Left: Close up of the 3rd hump. Right: Close up of the 4th hump. The vector plot shows the velocity field within the moving frame.

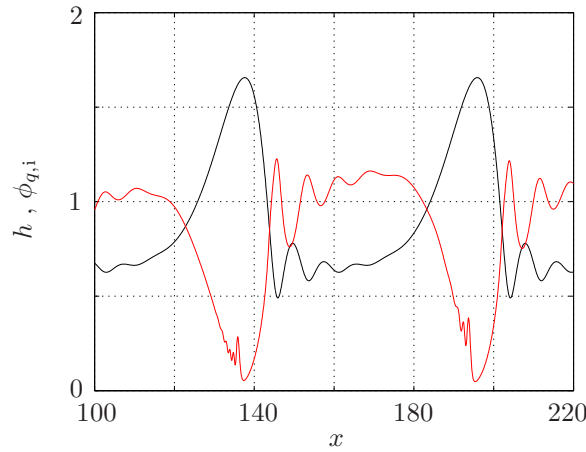


Figure 7.15.: Heat flux density at the free surface $\phi_{q,i}$ (red) and instantaneous height $h(x, t_{\text{end}})$ (black) at $t_0 = 279$. The region between the 3rd and 4th wave hump is shown.

Figure 7.16 shows the instantaneous values at $t = 279$ as function of x for the height h , the temperature difference across the film $\Delta T_x = T|_{y=h} - T|_{y=0}$, the heat flux density at the wall $\phi_{q,f} = (\partial_y T)|_{y=0}$ and the heat flux density at the free surface $\phi_{q,i} = (\partial_y T)|_{y=h}$ (all in black). By averaging over the last period we find the time averaged quantities of the respective values as functions of x , which are depicted in red. Finally, the solution of the corresponding flat film is given in blue. The enhancement of all average values becomes evident. For a better comparability of the heat flux densities, Figure 7.17 shows again the film height, the wall heat flux density and the heat flux density at the free surface.

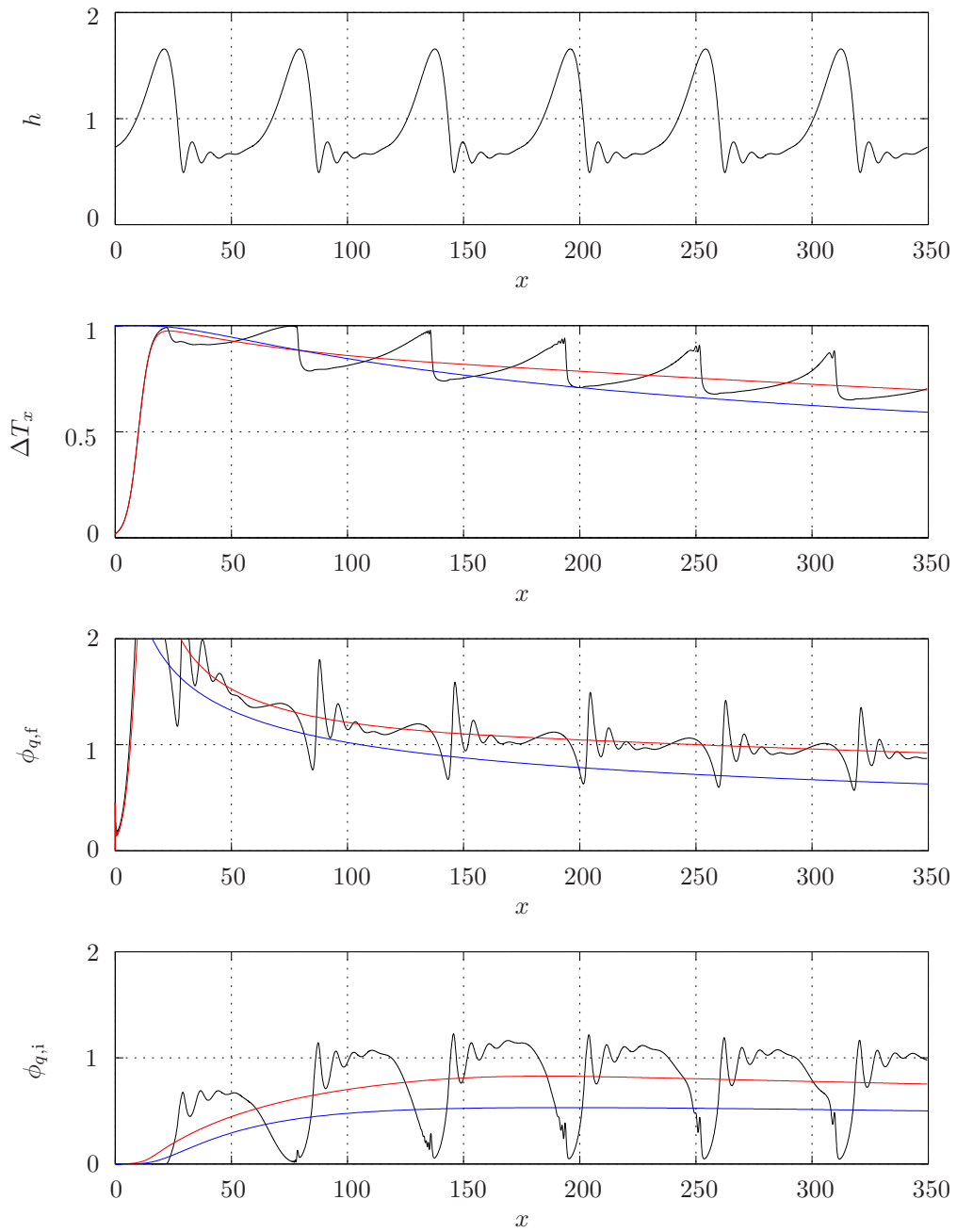


Figure 7.16.: Results for the wavy absorbing film. Local and instantaneous quantities are given in black, time averaged quantities in red and the solution of the corresponding absorbing flat film is depicted in blue.

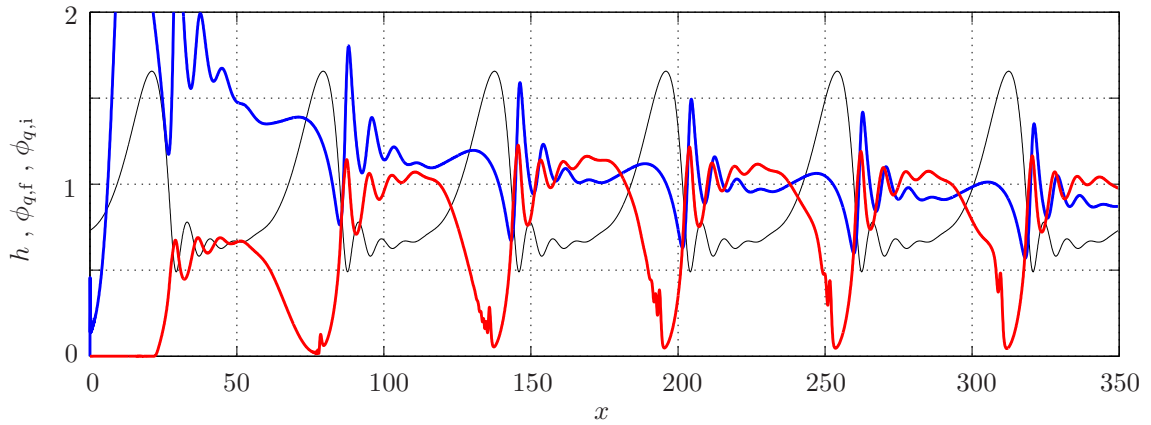


Figure 7.17.: Local and instantaneous film height h (black), wall heat flux density $\phi_{q,f}$ (blue) and heat flux density at the free surface $\phi_{q,i}$ (red).

Figure 7.18 shows the results for case 6 by employing $Le = 1$ and $B = 1/8$. Below, Figure 7.19 presents the same case also for $Le = 1$ but $B = 10$. The particular choice for B stems from the flux boundary condition that may be also written in terms of the Lewis number, i.e. $B = B^*/Le$. From our comparative simulation, presented in Figure 7.13, we find $B^* = 10$. This means that the first case is chosen such that Le is varied but B kept where in turn the lower case is chosen such that Le is varied but B^* kept. The same strategy was repeated for $Le = 10$ and the results are shown in Figure 7.20 and 7.21.

- $Le = 1$: From a comparison of the upper and lower concentration fields we easily notice that they agree qualitatively very well but differ in their concentration level (very roughly by a factor of 9). The temperature fields, however, differ also qualitatively from another.

Firstly, by comparing both cases with Figure 7.13 ($Le = 80$) it becomes evident that the smaller Lewis number results in a more pronounced bulk diffusion so that the thin boundary layers vanish. Secondly, we notice that the surface temperature does not change significantly for $B = 10$ in contrast to $B = 1/8$. This prevents the film to absorb mass as it stays close to its equilibrium state which is given by the inlet condition. The reason for this result is the huge difference in B representing the enthalpy of evaporation. Thus, for $B = 10$, already a small amount of absorbed mass leads to a much larger release of heat than for $B = 1/8$. This explains the reduced concentration level for C of the lower case.

- $Le = 10$: Comparing Figure 7.20 with 7.21 brings us to the same conclusions as before. However, the concentration boundary layer is already very much pronounced and significantly thinner than for $Le = 1$. By comparing Figure 7.18 with Figure

7.20 we notice a very good qualitative agreement for T . This is caused due to their accordance in Pr and B .

7.4.4. Results for other cases

In the following we investigate two more cases out of Table 4.4 where we again refer to Figure 7.24 showing the employed flow fields.

- $Re = 15$ (case 8): Due to convergence problems for $Le = 80$ we shall present a case for $Le = 10$ and $B = 1/8$ since we expect a qualitatively similar result. From Figure 7.22 the qualitative agreement with our reference case becomes clear. The influence of the separation zone is more pronounced but the *tears* in the concentration field already indicate numerical difficulties which become critical for larger Le . Thence, additional numerical shortcomings become manifest in the concentration field within the separation zone. This was already visible from the oscillations in Figure 7.14.
- $Re = 8.6$ (case 5): We finally investigate a case where the separation zone is totally absent and Figure 7.23 shows the result for $Le = 80$ and $B = 1/8$. The result is as expected, showing a thin concentration boundary layer and a practically untainted convective transport of the species through the main hump due to the absence of the separation zone. However, the influence of the slow fluid motion at the back of the wave crest is clearly visible.

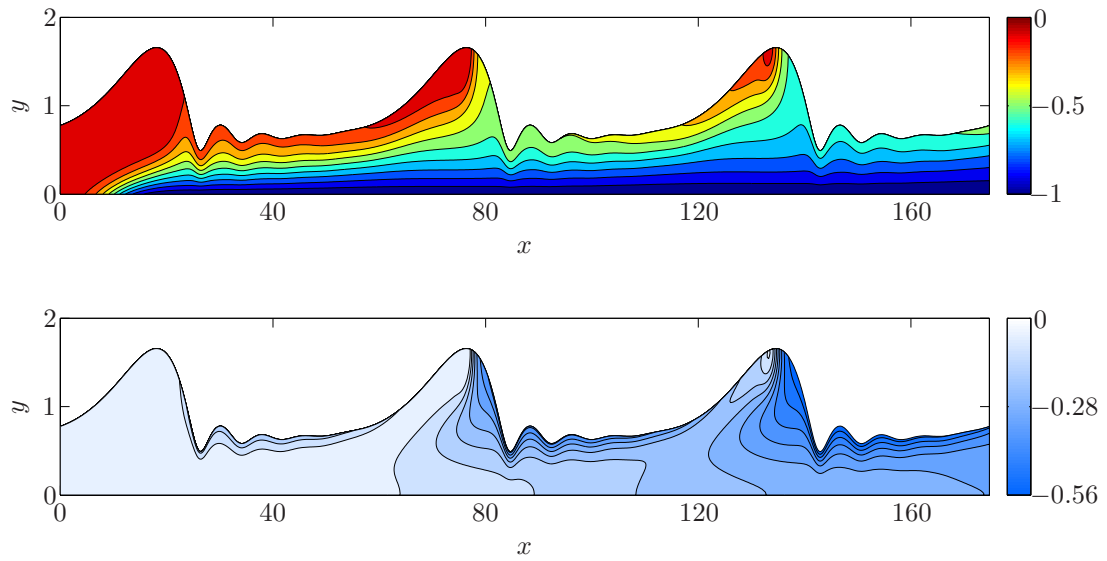


Figure 7.18.: Solution for $T(x, y, t_0)$ (top) and $C(x, y, t_0)$ (bottom) at $t_0 = 150$ for case 6 out of Table 4.4 ($\text{Re} = 10.7$) for $\text{Pr} = 30$, $\text{Le} = 1$ and $B = 1/8$ ($B^* = 1/8$).

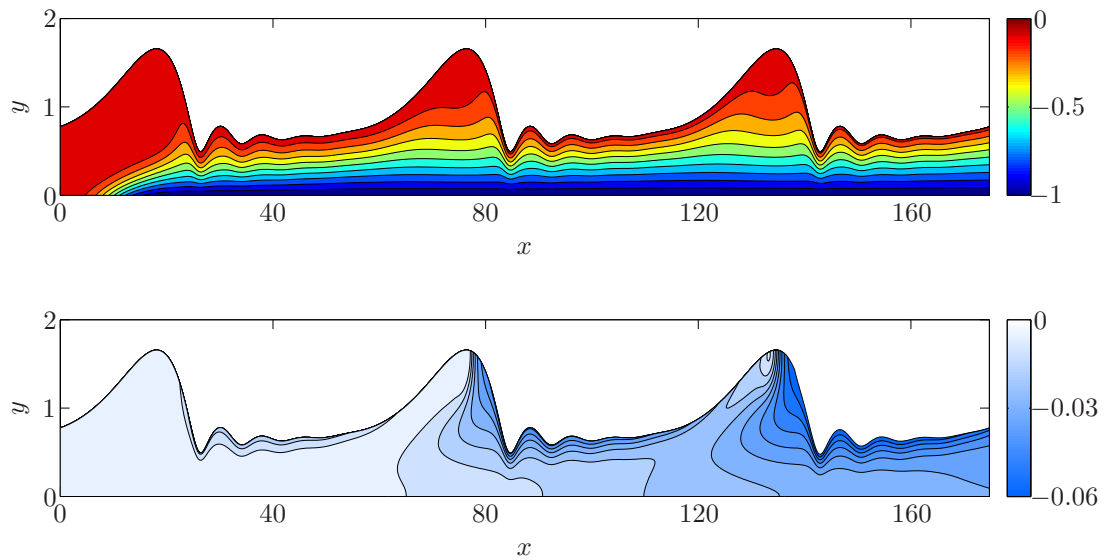


Figure 7.19.: Solution for $T(x, y, t_0)$ (top) and $C(x, y, t_0)$ (bottom) at $t_0 = 150$ for case 6 out of Table 4.4 ($\text{Re} = 10.7$) for $\text{Pr} = 30$, $\text{Le} = 1$ and $B = 10$ ($B^* = 10$).

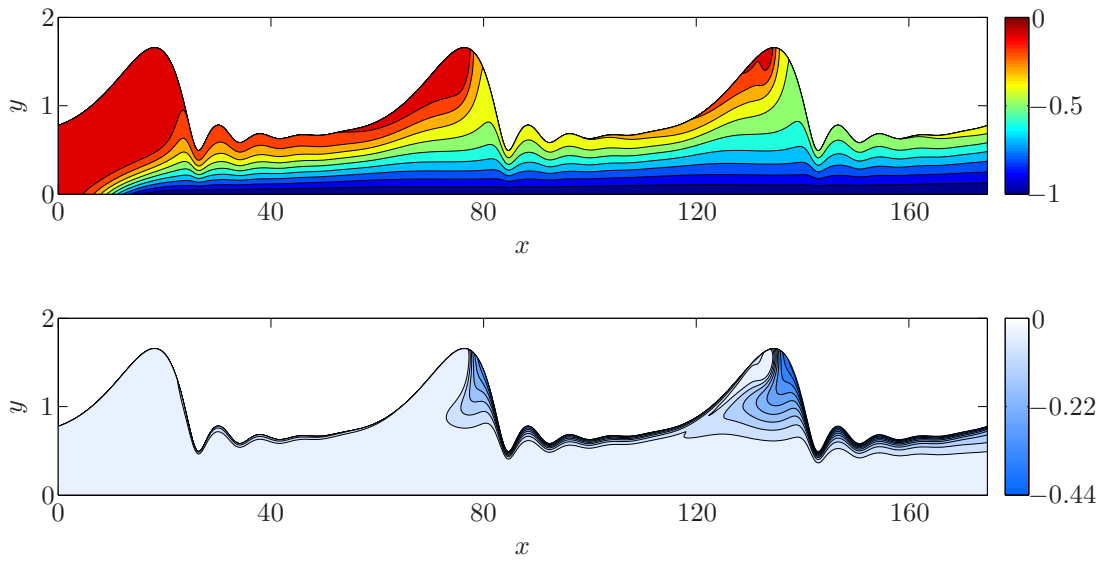


Figure 7.20.: Solution for $T(x, y, t_0)$ (top) and $C(x, y, t_0)$ (bottom) at $t_0 = 150$ for case 6 out of Table 4.4 ($\text{Re} = 10.7$) for $\text{Pr} = 30$, $\text{Le} = 10$ and $B = 1/8$ ($B^* = 10/8$).

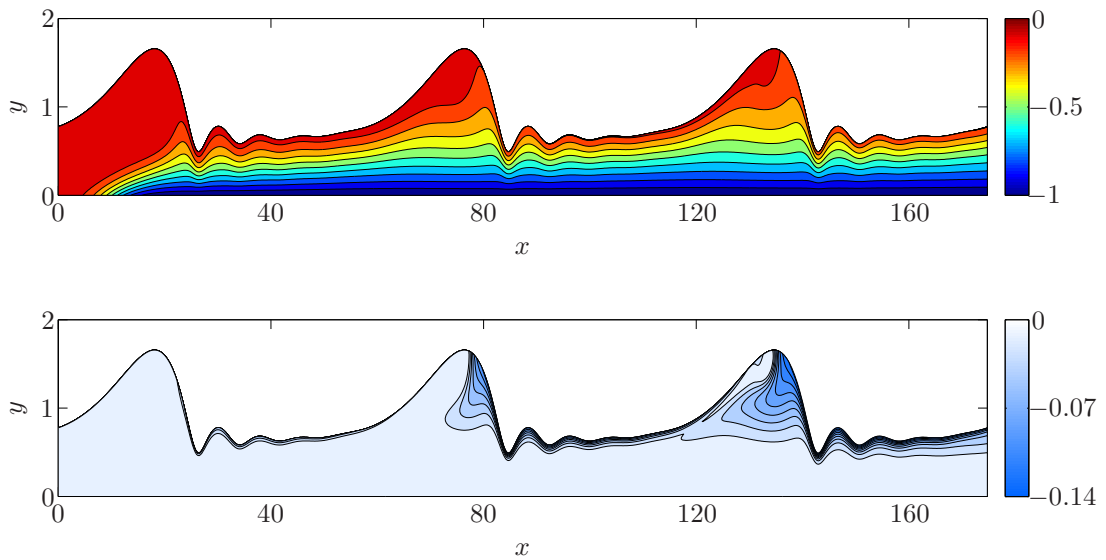


Figure 7.21.: Solution for $T(x, y, t_0)$ (top) and $C(x, y, t_0)$ (bottom) at $t_0 = 150$ for case 6 out of Table 4.4 ($\text{Re} = 10.7$) for $\text{Pr} = 30$, $\text{Le} = 10$ and $B = 1$ ($B^* = 10$).

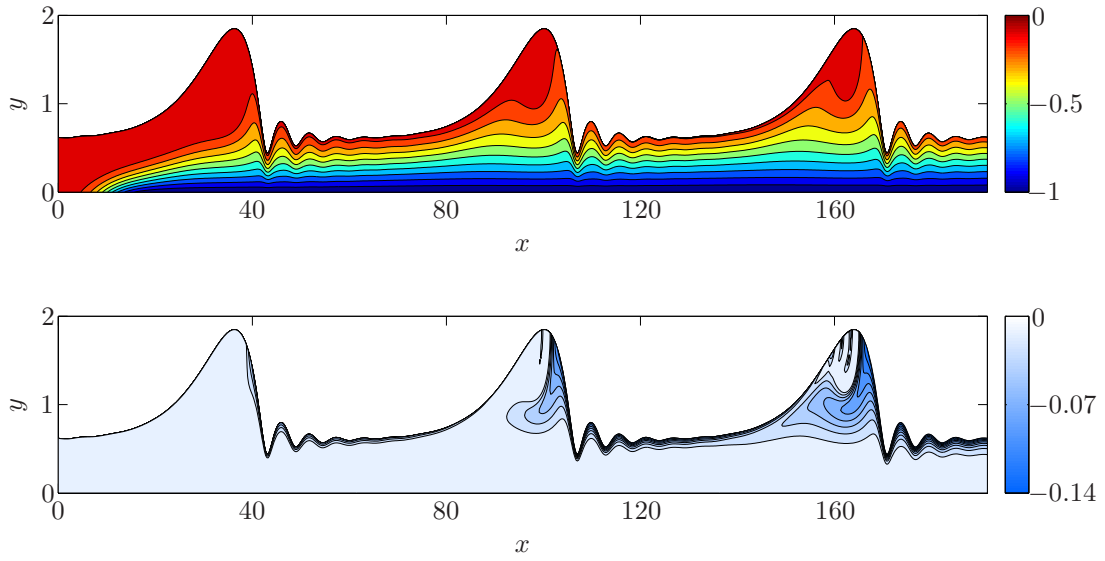


Figure 7.22.: Solution for $T(x, y, t_0)$ (top) and $C(x, y, t_0)$ (bottom) at $t_0 = 150$ for case 8 out of Table 4.4 ($Re = 15$) for $Pr = 30$, $Le = 10$ and $B = 1/8$.

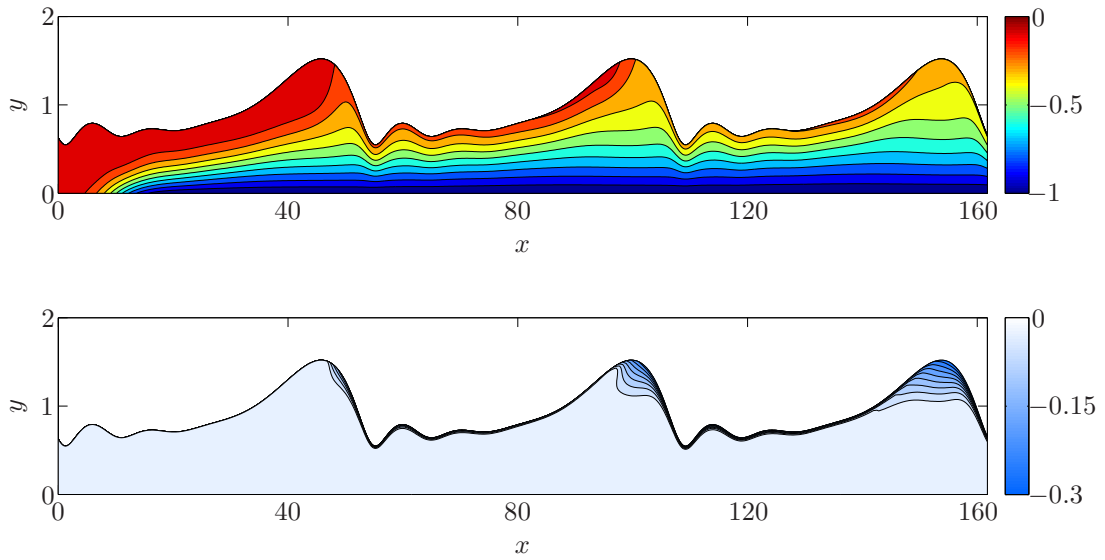


Figure 7.23.: Solution for $T(x, y, t_0)$ (top) and $C(x, y, t_0)$ (bottom) at $t_0 = 150$ for case 5 out of Table 4.4 ($Re = 8.6$) for $Pr = 30$, $Le = 80$ and $B = 1/8$.

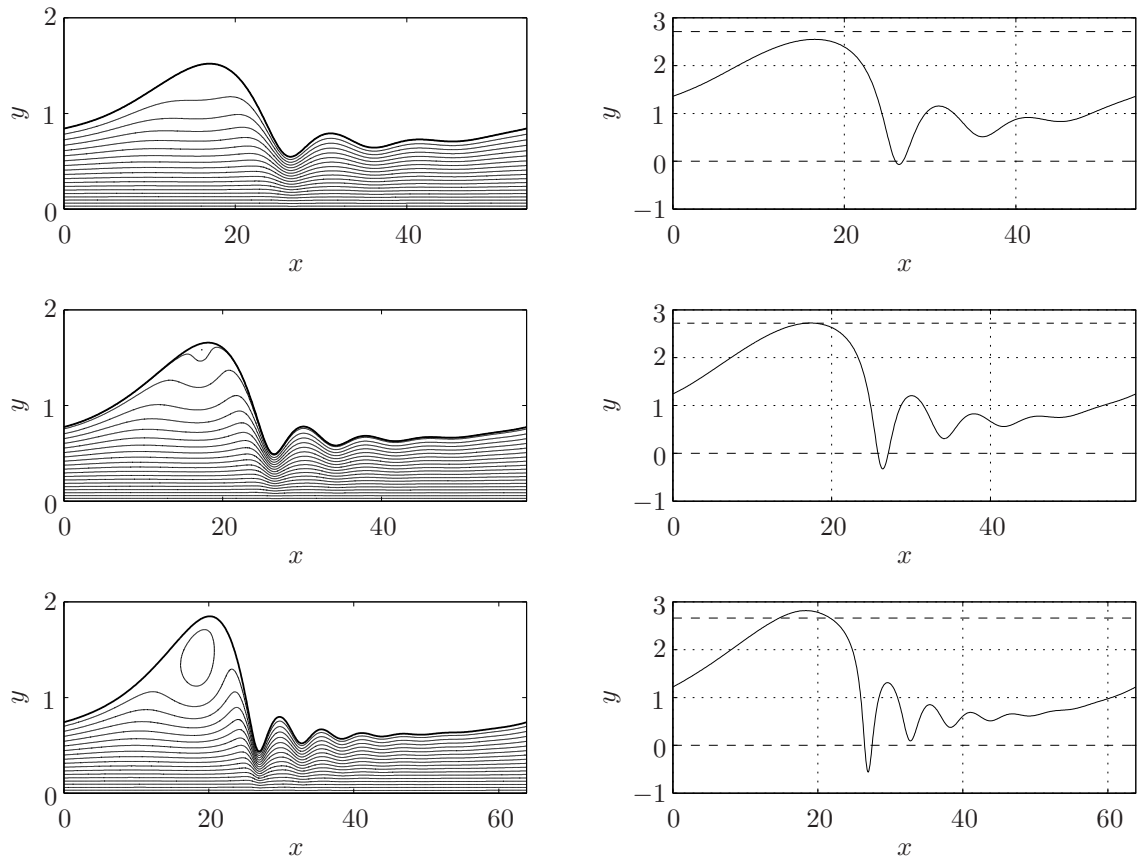


Figure 7.24.: Left column: Streamlines within the moving frame. Top: case 5 ($Re = 8.6$), center: case 6 ($Re = 10.7$), bottom: case 8 ($Re = 15$). Right column: Streamwise component of the fluid velocity at the free surface, thus $u|_{y=h}$ (within the laboratory frame). The cases agree side by side. The dashed lines indicate the wave celerity c and $u = 0$.

8. Summary and Conclusions

The present thesis considers the falling liquid film in different manifestations, the isothermal and the thermal wavy film, the absorbing flat film and the absorbing wavy film. The discussions of the numerically generated results for these four cases are given in separated chapters in the mentioned order. Preparatory to the presentation of the numerical results, a comprehensive analysis of the governing equations including the boundary conditions is given to estimate the influence of several approximations. Also, the one-way coupled formulation of the problem (the flow field remains unaffected by the species and/or heat transport) is justified. This approximation allows to solve the Navier–Stokes equations and the transport equations for heat and species consecutively, reducing the complexity to a reasonable degree. Three different solvers were developed in MATLAB by the author exclusively for this thesis.

The first discussion deals with the isothermal wavy film, where the solutions are found as sharp-interface traveling-wave solutions of the Navier–Stokes equations, corresponding to steady states within a co-moving frame of reference. The strongly coupled non-linear system, including the a priori unknown wave celerity and the shape of the free surface, is solved with Newton’s method by using the finite-volume formulation on a staggered grid. A coordinate transformation is introduced to adapt the computational mesh to the free surface in order to represent a sharp liquid–gas interface. An arclength continuation method is implemented to efficiently track the solution branches, and the resulting system of linear equations is solved using the bordering algorithm. The code is successfully verified for the constant height formulation (closed flow condition). In addition, the constant flux formulation (open flow condition) is implemented to compare the steady solutions within the moving frame with available periodically-forced transient simulations within the laboratory frame showing excellent agreements. The solutions of selected branches are evaluated for their average film height and the surface area increase. In addition, all solutions with backflow regions are marked in the respective solution branch to show that this phenomenon is the rule rather than the exception for the chosen parameter set. The falling liquid film is examined in a non-standard approach by employing Navier–Stokes equations rather than using boundary layer related model equations. This was motivated by the analysis of the strong surface tension limit for liquids like LiBr–H₂O. However, all results suggest that the selection of the Navier–Stokes equations is based on a too stringent

interpretation of the initial analysis of the strong surface tension limit. This leads to the conclusion that common model equations might be a good approximation, even for the parameters used in this thesis. The main conclusion of this chapter regarding heat and/or species transfer enhancement at the free surface is that the surface increase due to the waviness is not a relevant quantity to explain a significant transfer enhancement. It is shown that the surface increase is not more than 1% compared to the corresponding flat film.

The second numerical investigation addresses the thermal wavy film to identify the significance of convection to the enhancement of heat transfer. The analysis is again done in the moving frame of reference by employing an isothermal wall and an isothermal free surface. The local Nusselt number is analyzed for several Prandtl numbers and the average Nusselt number is derived for a wide range of Prandtl numbers. This chapter is closed by showing the lower and upper bounds for the average Nusselt numbers for all solutions of the branches generated in the preceding chapter. A measure for the convectively induced heat transfer enhancement is introduced, showing that more than 70% of the Nusselt number increase is related to the film thinning effect. The convective effects are thus only of secondary importance for the cases shown. In addition, the local Nusselt number distributions are analyzed and the vortex within the moving frame of reference is shown to act as an insulator for the heat transfer at the free surface. In turn, it compresses the thermal boundary layer below the main hump and enhances the heat transfer to the wall. The enhancement of heat transfer, which is related to the backflow regions in the capillary wave troughs, is hard to separate from the convective effect per se. From there, a selective statement to the action of the backflow regions regarding heat transfer enhancement is not given.

To create a benchmark for the absorbing wavy film, the absorbing flat film is discussed in the third investigation. The corresponding code is successfully verified with literature data. Certain modeling aspects, like the thermal wall boundary condition and the inclusion of the Eckert–Schneider condition are analyzed in detail. The latter condition is related to one-sided diffusion and appears to be the most important aspect in modeling the absorbing flat film. It is shown that the two common approaches to the absorbing flat film are either not physically sound or mathematically inconsistent. It is further proposed that ignoring the Eckert–Schneider condition is the most relevant modeling error, leading to a deviation of almost 50% between the two approaches for the cases shown. Another main conclusion of this chapter is that a falling film of finite length has an optimum film thickness at relatively low values of the Péclet number. This optimum is the result of the increasing heat capacity of the liquid film as the film thickness is increased.

In the final step, certain traveling wave solutions from the initial investigation are employed to solve the transient, coupled heat and species transfer. In the transient formu-

lation the appearance of backflow regions results in a forward-backward heat equation which causes difficulties in the numerical solution. However, for simplicity, an easy to implement marching technique is used and the so-called FLARE approximation is employed as remedy for the integration through regions of backflow. For the verification of this approximation a comparison with the thermal cases of the second numerical investigation is given. Finally, solutions for the absorbing wavy falling film are presented for several parameter revealing the influence of the separation zone of the wave hump.

The presented results of the absorbing wavy film are based on highly resolved Navier-Stokes solutions with a sharp interface and assume large Prandtl and Lewis numbers. This qualifies the results as benchmark cases for other model approaches, even if the approximative treatment of the backflow regions is a remaining deficit. This has to be left as open issue which might be resolved by a more sophisticated numerical method.

A. Thermophysical properties of LiBr–H₂O

The present chapter provides properly formatted data to construct the material parameters of LiBr–H₂O numerically.

A.1. Transport coefficients, solubility

Diffusion coefficient

Table A.1 shows the data for the binary diffusion coefficient D at $T = 25^\circ\text{C}$ given by [Gierow & Jernqvist \(1993\)](#). As mentioned there, one can employ the Stokes–Einstein equation to find D for other temperatures, thus

$$\frac{D_1 \bar{\eta}_1}{T_1} = \frac{D_2 \bar{\eta}_2}{T_2} \quad (\text{A.1})$$

with the dynamic viscosity $\bar{\eta}$, given by [Patterson & Perez-Blanco \(1988\)](#) for instance (see next section).

Table A.1.: Diffusion coefficient D for $T = 25^\circ\text{C}$.

$C / \text{wt}\% \text{ LiBr}$	$D / 10^{-9} \text{ m}^2/\text{s}$
1	1.321
5	1.349
11	1.440
17	1.539
23	1.655
29.15	1.739
35	1.822
41	1.826
47	1.809
53	1.488
59.27	1.041

Dynamic viscosity

The numerical fit for the dynamic viscosity $\bar{\eta}$ given by [Patterson & Perez-Blanco \(1988\)](#) is valid between $0^\circ\text{C} < T < 90^\circ\text{C}$ and $5 < C < 60$ with $[C] = \text{wt}\% \text{LiBr}$. The relation reads

$$\bar{\eta} = 10^{-3} \sum_{i=0}^5 \sum_{j=0}^2 E_{ij} C^i T^j \quad , \quad [\bar{\eta}] = \text{Pa s}$$

where T has to be given in degree Celsius and C in wt% LiBr.¹ The factor 10^{-3} , which is not present in [Patterson & Perez-Blanco \(1988\)](#), is due to the unit conversion from cP (centipoise) to Pa s. Table A.2 represents the coefficients E_{ij} .

Table A.2.: Coefficients E_{ij} for the dynamic viscosity $\bar{\eta}$.

1.488747E+0	-4.164814E-2	3.404030E-4
1.143975E-1	9.636832E-4	-2.794515E-5
-1.278729E-2	-5.981025E-5	2.580301E-6
6.999985E-4	-1.282435E-7	-9.737750E-8
-1.638074E-5	5.703002E-8	1.585609E-9
1.456348E-7	-9.842266E-10	-7.922925E-12

Thermal conductivity

The numerical fit for the thermal conductivity λ given by [Patterson & Perez-Blanco \(1988\)](#) reads

$$\lambda = 1.163 \sum_{i=0}^4 \sum_{j=0}^2 D_{ij} C^i T^j \quad , \quad [\lambda] = \frac{\text{W}}{\text{m K}}$$

again with T in degree Celsius and C in wt% LiBr. The factor $4187/3600 \approx 1.163$, which is not present in [Patterson & Perez-Blanco \(1988\)](#), is due to the unit conversion from kcal/h to W. Table A.3 represents the coefficients D_{ij} .

¹Note that the input value for $C = 0.60$ is 60 rather than 0.6.

Table A.3.: Coefficients D_{ij} for the thermal conductivity λ .

4.815196E-1	1.858174E-3	-7.923126E-6
-2.217277E-3	9.614755E-6	-1.869392E-7
-1.994141E-5	-1.139291E-6	1.408951E-8
3.727255E-7	2.107608E-8	-2.740806E-10
-2.489886E-9	-1.330532E-10	1.810818E-12

Solubility

The solubility curve (onset of crystallization) is given by [Boryta \(1970\)](#). Table [A.4](#) represents an excerpt for our relevant region.

Table A.4.: Solubility curve (excerpt) from [Boryta \(1970\)](#).

$T / ^\circ\text{C}$	$C / \text{wt}\% \text{ LiBr}$
9.93	58.08
18.99	58.67
24.29	60.63
33.14	62.50
38.26	63.96
44.27	65.17
50.35	65.82
57.58	66.16
63.42	66.55

A.2. Gibbs energy equation of state

The Gibbs energy equation of state for aqueous LiBr solutions can be constructed numerically from the data given by [Kim & Ferreira \(2006\)](#). The equation of state for G is then used to derive the molar enthalpy H , the molar heat capacity C_p and the molar volume V of the mixture by using

$$H = -RT^2 \left(\frac{\partial}{\partial T} \frac{G}{RT} \right)_{P,x}, \quad (\text{A.2a})$$

$$C_p = -T \left(\frac{\partial^2 G}{\partial T^2} \right)_{P,x}, \quad (\text{A.2b})$$

$$V = \left(\frac{\partial G}{\partial P} \right)_{T,x}, \quad (\text{A.2c})$$

where $x := x_1$ represents the mole fraction defined as $x_\alpha = n_\alpha/n$ with the unit kmol substance α per kmol solution. As before and in accordance to [Kim & Ferreira \(2006\)](#), subscript $\alpha = 1$ refers to LiBr, $\alpha = 2$ to H₂O and no subscript refers to the solution (mixture). The relation to our mass fraction C_α reads

$$C_\alpha = \frac{x_\alpha M_\alpha}{M} \quad (\text{A.3})$$

where we have introduced the (average) molar mass of the mixture

$$M = \left(\frac{C_1}{M_1} + \frac{1 - C_1}{M_2} \right)^{-1} \quad (\text{A.4})$$

with the molar mass of LiBr $M_1 = 86.85$ kg/kmol and the molar mass of water $M_2 = 18.02$ kg/kmol. The molar mass of the mixture is used to relate the molar quantities [\(A.2\)](#) to the specific quantities ones, thus

$$h_s = \frac{H}{M}, \quad (\text{A.5a})$$

$$c_p = \frac{C_p}{M}, \quad (\text{A.5b})$$

$$\rho = \left(\frac{V}{M} \right)^{-1}. \quad (\text{A.5c})$$

Figure [A.1](#) shows some relevant isotherms for the specific heat capacity c_p and the specific enthalpy h_s as function of the mass fraction C for the LiBr–H₂O mixture derived from G . Additionally, the absolute error of $h_s - c_p T$ and $Z/\Delta C$ defined by [\(3.24\)](#) are given.

Figure [A.2](#) shows the evaluation of the density for LiBr–H₂O derived from G including the expansion coefficients β_T and β_C , see [\(3.4\)](#).

A.3. Vapor pressure P_2

The vapor pressure of H₂O within the LiBr–H₂O solution P_2 is also given by [Kim & Ferreira \(2006\)](#) and can be constructed from

$$P_2 = \exp \left(\frac{\alpha - \ln(\theta + \sqrt{\theta^2 - 1})}{\beta} \right) \quad (\text{A.6})$$

with the intermediate variables

$$\theta = \cosh[\alpha - \beta \ln(P^*)] \exp(\phi v m M_2 \beta), \quad (\text{A.7a})$$

$$\alpha = \sum_{j=0}^2 \frac{\alpha_j}{T^j}, \quad (\text{A.7b})$$

$$\beta = \sum_{j=0}^2 \frac{\beta_j}{T^j}, \quad (\text{A.7c})$$

$$\phi = 1 + \sum_{i=1}^6 a_i m^{i/2}, \quad (\text{A.7d})$$

$$a_i = \sum_{j=0}^2 \frac{a_{ij}}{T^j}, \quad (\text{A.7e})$$

deduced from the constants given in Table A.5. The pressure term in (A.7d) is already neglected as suggested by Kim & Ferreira (2006). We have further introduced the dissociation number ν , which is $\nu = 2$ for LiBr, the molality

$$m = \frac{x_1}{(1 - x_1)M_2}$$

and the saturation pressure of pure water P^* , which can be derived from the relation given in Kim & Ferreira (2006) or from the simple and well known Magnus-formula

$$P^* = 0.611 \text{ kPa} \exp\left(\frac{17.62 T}{243.12^\circ\text{C} + T}\right). \quad (\text{A.8})$$

Table A.5.: Constants given by Kim & Ferreira (2006) for the evaluation of (A.7).

	$j = 0$	$j = 1$	$j = 2$
α_j	1.1375E+01	-3.8590E+03	5.1319E+05
β_j	8.6010E-01	-1.9575E+02	2.3136E+04
a_{1j}	-2.1963155E+01	+4.9372316E+03	-6.5548406E+05
a_{2j}	-3.8104752E+03	+2.6115345E+06	-3.6699691E+08
a_{3j}	+1.2280854E+05	-7.7187923E+07	+1.0398560E+10
a_{4j}	-1.4716737E+06	+9.1952848E+08	-1.1894502E+11
a_{5j}	+7.7658213E+06	-4.9375666E+09	+6.3175547E+11
a_{6j}	-1.5118922E+07	+9.8399744E+09	-1.2737898E+12

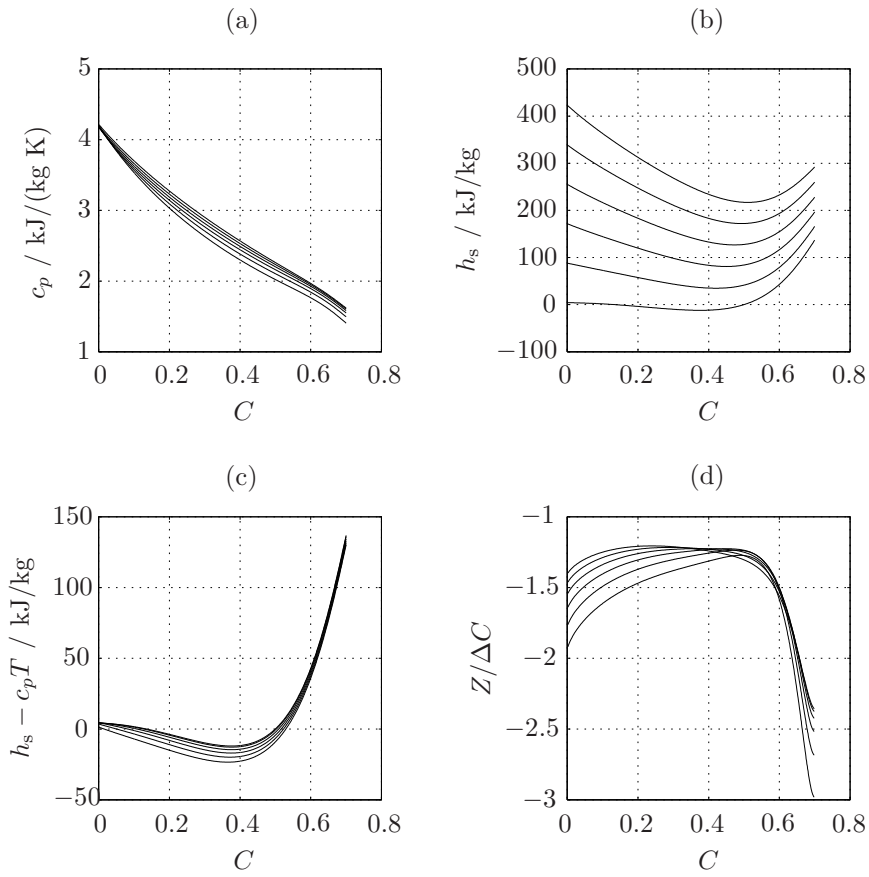


Figure A.1.: Representative isotherms as function of the mass fraction C for (a) specific heat capacity c_p , (b) specific enthalpy h_s , (c) abs. error of $h_s - c_p T$ and (d) scaled interdiffusion number $Z/\Delta C$ defined by (3.24). All data is extracted from the equation of state.

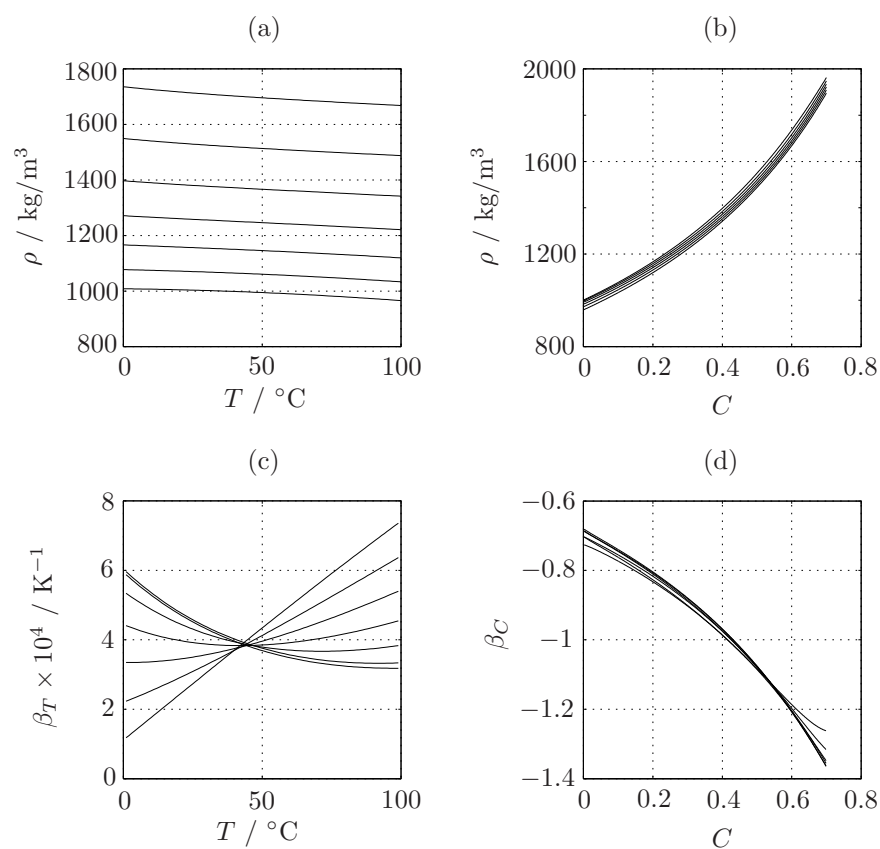


Figure A.2.: Density ρ and expansion coefficients deduced from G (a) isoconcentrations for ρ as function of T , (b) isotherms for ρ as function of C , (c) isoconcentrations of the thermal expansion coefficient β_T as function of T (d) isotherms of the solutal expansion coefficient β_C as function of C .

Bibliography

- AKTERSHEV, S. & ALEKSEENKO, S. 2013 Nonlinear waves and heat transfer in a falling film of condensate. *Physics of Fluids* **25** (8), 083602.
- ALBERT, C., MARSCHALL, H. & BOTHE, D. 2014 Direct numerical simulation of interfacial mass transfer into falling films. *International Journal of Heat and Mass Transfer* **69**, 343–357.
- ALBERT, C., RAACH, H. & BOTHE, D. 2012 Influence of surface tension models on the hydrodynamics of wavy laminar falling films in volume of fluid-simulations. *International Journal of Multiphase Flow* **43**, 66–71.
- AZIZ, A., FRENCH, D., JENSEN, S. & KELLOGG, R. 1999 Origins, analysis, numerical analysis, and numerical approximation of a forward-backward parabolic problem. *ESAIM: Mathematical Modelling and Numerical Analysis* **33** (05), 895–922.
- BACH, P. & VILLADSEN, J. 1984 Simulation of the vertical flow of a thin, wavy film using a finite-element method. *International Journal of Heat and Mass Transfer* **27** (6), 815–827.
- BENJAMIN, T. B. 1957 Wave formation in laminar flow down an inclined plane. *Journal of Fluid Mechanics* **2** (6), 554–573.
- BO, S., MA, X., LAN, Z., CHEN, J. & CHEN, H. 2010 Numerical simulation on the falling film absorption process in a counter-flow absorber. *Chemical Engineering Journal* **156** (6), 607–612.
- BORYTA, D. A. 1970 Solubility of lithium bromide in water between -50°C and $+100^{\circ}\text{C}$ (45 to 70% lithium bromide). *Journal of Chemical & Engineering Data* **15** (1), 142–144.
- BOTHE, D., KOEBE, M., WIELAGE, K. & WARNECKE, H.-J. 2003 VOF-simulations of mass transfer from single bubbles and bubble chains rising in the aqueous solutions. In *Proceedings of FEDSM03: Fourth ASME-JSME Joint Fluids Engineering Conference, Honolulu, Hawaii, USA*.
- BRACKBILL, J., KOTHE, D. & ZEMACH, C. 1992 A continuum method for modeling surface tension. *Journal of Computational Physics* **100** (2), 335–354.

- CEBECI, T., KELLER, H. B. & WILLIAMS, P. G. 1979 Separating boundary-layer flow calculations. *Journal of Computational Physics* **31** (3), 363–378.
- CHANG, H.-C. 1994 Wave evolution on a falling film. *Annual Review of Fluid Mechanics* **26**, 103–136.
- CHANG, H.-C., CHENG, M., DEMEKHIN, E. A. & KOPELEVICH, D. I. 1994 Secondary and tertiary excitation of three-dimensional patterns on a falling film. *Journal of Fluid Mechanics* **270**, 251–275.
- CHANG, H.-C. & DEMEKHIN, E. A. 2002 *Complex Wave Dynamics on Thin Films*, 1st Ed., *Studies in Interface Science*, vol. 14. Elsevier.
- CHANG, H.-C., DEMEKHIN, E. A. & KOPELEVICH, D. I. 1993 Nonlinear evolution of waves on a vertically falling film. *Journal of Fluid Mechanics* **250**, 433–480.
- CHENG, M. & CHANG, H.-C. 1995 Competition between subharmonic and sideband secondary instabilities on a falling film. *Physics of Fluids* **7** (1), 34–54.
- DAI, Y. J. & ZHANG, H. F. 2004 Numerical simulation and theoretical analysis of heat and mass transfer in a cross flow liquid desiccant air dehumidifier packed with honeycomb paper. *Energy Conversion and Management* **45**, 1343–1356.
- DIETZE, G. 2010 Flow separation in falling liquid films. PhD thesis, RWTH Aachen.
- DIETZE, G., LEEFKEN, A. & KNEER, R. 2008 Investigation of the backflow phenomenon in falling liquid films. *Journal of Fluid Mechanics* **595**, 435.
- ELPERIN, T. & FOMINYKH, A. 2008 Effect of thermal diffusion on absorption during dissolution of short gas plugs. *International Journal of Heat and Mass Transfer* **51** (11), 3251–3254.
- FERZIGER, J. H. & PERIĆ, M. 2002 *Computational Methods for Fluid Dynamics*, 3rd Ed. Springer.
- GAO, D., MORLEY, N. & DHIR, V. 2003 Numerical simulation of wavy falling film flow using vof method. *Journal of Computational Physics* **192** (2), 624–642.
- GIEROW, M. & JERNQVIST, A. 1993 Measurement of mass diffusivity with holographic interferometry for H₂O/NaOH and H₂O/LiBr working pairs. In *Proceedings of the International Heat Pump Conference, AES*, , vol. 31, pp. 525–532. Int. Abs. Heat Pump Conf.

- GRIGOR'EVA, N. I. & NAKORYAKOV, V. E. 1977 Exact solution of combined heat- and mass-transfer problem during film absorption. *Journal of Engineering Physics* **33** (5), 1349–1353.
- GROSSMAN, G. 1983 Simultaneous heat and mass transfer in film absorption under laminar flow. *International Journal of Heat and Mass Transfer* **26** (3), 357–371.
- GROSSMAN, G. 1987 Analysis of interdiffusion in film absorption. *International Journal of Heat and Mass Transfer* **30** (1), 205–208.
- GROSSMAN, G. & GOMMED, K. 1997 Heat and mass transfer in film absorption in the presence of non-absorbable gases. *International Journal of Heat and Mass Transfer* **40** (15), 3595–3606.
- HOFMANN, E. & KUHLMANN, H. C. 2012 On the optimum mass transfer of flat absorbing falling films. *International Journal of Heat and Mass Transfer* **55** (25–26), 7686–7697.
- JASAK, H. & RUSCHE, H. 2009 Dynamic mesh handling in OpenFOAM. In *Proceeding of the 47th Aerospace Sciences Meeting Including The New Horizons Forum and Aerospace Exposition, Orlando, Florida*.
- KALLIADASIS, S., RUYER-QUIL, C., SCHEID, B. & VELARDE, M. G. 2012 *Falling Liquid Films*, 1st Ed., *Applied Mathematical Sciences*, vol. 176. Springer.
- KAPITZA, P. L. & KAPITZA, S. P. 1949 Wave flow of thin layers of a viscous fluid. *Zh. Eksp. Teor. Fiz* **19**, 105.
- KARAMI, S. & FARHANIEH, B. 2009 A numerical study on the absorption of water vapor into a film of aqueous LiBr falling along a vertical plate. *Heat and Mass Transfer* **46** (2), 197–207.
- KARAMI, S. & FARHANIEH, B. 2011 Numerical modeling of incline plate LiBr absorber. *Heat and Mass Transfer* **47** (3), 259–267.
- KAWAE, N., SHIGECHI, T., KANEMARU, K. & YAMADA, T. 1989 Water vapor evaporation into laminar film flow of a lithium bromide-water solution (influence of variable properties and inlet film thickness on absorption mass transfer rate). *Heat Transfer Japanese Research* **32** (10).
- KELLER, H. B. 1977 Numerical solution of bifurcation and nonlinear eigenvalue problems. *Applications of bifurcation theory* pp. 359–384.
- KELLER, H. B. 1986 Lectures on numerical methods in bifurcation problems. *Applied Mathematics* **217**.
-

- KILLION, J. D. & GARIMELLA, S. 2001 A critical review of models of coupled heat and mass transfer in falling-film absorption. *International Journal of Refrigeration* **24** (8), 755–797.
- KIM, D. S. & FERREIRA, C. A. I. 2006 A gibbs energy equation for LiBr aqueous solutions. *International Journal of Refrigeration* **29** (1), 36–46.
- KIM, D. S. & FERREIRA, C. A. I. 2009 Analytic modelling of a falling film absorber and experimental determination of transfer coefficients. *International Journal of Heat and Mass Transfer* **52** (21–22), 4757–4765.
- LANDAU, L. D. & LIFSHITZ, E. M. 1987 *Fluid Mechanics*, 2nd Ed., *Course Of Theoretical Physics*, vol. 6. Pergamon.
- LANZERSTORFER, D. 2012 On the global instabilities of incompressible plane-channel flows with geometric discontinuities. PhD thesis, TU Wien.
- LIU, J. & GOLLUB, J. P. 1993 Onset of spatially chaotic waves on flowing films. *Physical Review Letters* **70** (15).
- MALAMATARIS, N., VLACHOGIANNIS, M. & BONTOZOGLOU, V. 2002 Solitary waves on inclined films: Flow structure and binary interactions. *Physics of Fluids* **14**, 1082.
- MALAMATARIS, N. A. & BALAKOTAIAH, V. 2008 Flow structure underneath the large amplitude waves of a vertically falling film. *AIChE Journal* **54** (7), 1725–1740.
- MATLAB 2010 Matlab 7.10.0.499 (r2010a) documentation.
- MITTERMAIER, M., SCHULZE, P. & ZIEGLER, F. 2014 A numerical model for combined heat and mass transfer in a laminar liquid falling film with simplified hydrodynamics. *International Journal of Heat and Mass Transfer* **70**, 990–1002.
- MIYARA, A. 1999 Numerical analysis on flow dynamics and heat transfer of falling liquid films with interfacial waves. *Heat and Mass Transfer* **35** (4), 298–306.
- MORIOKA, I. & KIYOTA, M. 1991 Absorption of water vapor into a wavy film of an aqueous solution of LiBr. *JSME International Journal. Ser. 2* **34** (2), 183–188.
- NUSSELT, W. 1916 Die Oberflächenkondensation des Wasserdampfes. *VDI-Zeitschrift* **60**, 541–546.
- ORON, A., DAVIS, S. H. & BANKOFF, S. G. 1997 Long-scale evolution of thin liquid films. *Reviews of modern physics* **69** (3), 931.

- PATNAIK, V. & PEREZ-BLANCO, H. 1996 A study of absorption enhancement by wavy film flows. *International Journal of Heat and Fluid Flow* **17** (1), 71–77.
- PATTERSON, M. R. & PEREZ-BLANCO, H. 1988 Numerical fits of the properties of lithium-bromide water solutions. *ASHRAE Transactions* **94**, 2059–2077, oT-88-20-2.
- PHILLIPS, J. H. & ACKERBERG, R. C. 1973 A numerical method for integrating the unsteady boundary-layer equations when there are regions of backflow. *Journal of Fluid Mechanics* **58**, 561–579.
- PRIELING, D. & STEINER, H. 2013*a* Analysis of the wall mass transfer on spinning disks using an integral boundary layer method. *Chemical Engineering Science* **101**, 109–119.
- PRIELING, D. & STEINER, H. 2013*b* Unsteady thin film flow on spinning disks at large ekman numbers using an integral boundary layer method. *International Journal of Heat and Mass Transfer* **65**, 10–22.
- RAACH, H., SOMASUNDARAM, S. & MITROVIC, J. 2011 Optimisation of turbulence wire spacing in falling films performed with openfoam. *Desalination* **267** (1), 118–119.
- RUYER-QUIL, C., SCHEID, B., KALLIADASIS, S., VELARDE, M. & ZEYTOUNIAN, R. K. 2005 Thermocapillary long waves in a liquid film flow. Part 1. Low-dimensional formulation. *Journal of Fluid Mechanics* **538**, 199–222.
- SALAMON, T. 1995 Finite element simulations of steady viscoelastic free-surface flows. PhD thesis, Massachusetts Institute of Technology.
- SALAMON, T. R., ARMSTRONG, R. C. & BROWN, R. A. 1994 Traveling waves on vertical films: Numerical analysis using the finite element method. *Physics of Fluids* **6**, 2202–2220.
- SCHEID, B., RUYER-QUIL, C., KALLIADASIS, S., VELARDE, M. & ZEYTOUNIAN, R. K. 2005 Thermocapillary long waves in a liquid film flow. Part 2. Linear stability and nonlinear waves. *Journal of Fluid Mechanics* **538**, 223–244.
- SCHEID, B., RUYER-QUIL, C. & MANNEVILLE, P. 2006 Wave patterns in film flows: modelling and three-dimensional waves. *Journal of Fluid Mechanics* **562**, 183–222.
- SCHLICHTING, H. & GERSTEN, K. 1997 *Boundary Layer Theory*. Springer.
- SEYDEL, R. 1994 *Practical Bifurcation and Stability Analysis*, 2nd Ed., *Interdisciplinary applied mathematics*, vol. 5. Springer.
- SHAH, R. & LONDON, A. 1978 *Laminar Flow Forced Convection in Ducts: a source book for compact heat exchanger analytical data*. Academic press New York.

-
- SQUIRE, W. & TRAPP, G. 1998 Using complex variables to estimate derivatives of real functions. *Siam Review* **40** (1), 110–112.
- THURSTON, G. A. 1980 Newton’s method: A link between continuous and discrete solutions of nonlinear problems. *Res. in Nonlinear Struct. and Solid Mech.* pp. 27–46.
- TRIFONOV, Y. 2012 Stability and bifurcations of the wavy film flow down a vertical plate: the results of integral approaches and full-scale computations. *Fluid Dynamics Research* **44** (3), 031418.
- TRUESDELL, C. & TOUPIN, R. 1960 *The Classical Field Theories, Encyclopedia of Physics: Principles of Classical Mechanics and Field Theory*, vol. III/1. Springer.
- TUKOVIĆ, Z. 2011 Private communication.
- TUKOVIĆ, Z. & JASAK, H. 2008 Simulation of free-rising bubble with soluble surfactant using moving mesh finite volume/area method. In *Proceedings of 6th International Conference on CFD in Oil & Gas, Metallurgical and Process Industries*, no. CFD08-072.
- VDI-GVC 2010 *VDI Heat Atlas*. Springer.
- WASSENAAR, R. H. 1996 Measured and predicted effect of flowrate and tube spacing on horizontal tube absorber performance. *International Journal of Refrigeration* **19** (5), 347–355.
- WESSELING, P. 2001 *Principles of Computational Fluid Dynamics, Springer Series in Computational Mathematics*, vol. 29. Springer.
- YANG, R. & JOU, T.-M. 1998 Non-absorbable gas effect on the wavy film absorption process. *International Journal of Heat and Mass Transfer* **41**, 3657–3668.
- YIH, C.-S. 1955 Stability of parallel laminar flow with a free surface. In *Proceedings of 2nd US Congress on Applied Mechanics ASME*, pp. 623–628.
- YOON, J.-I., PHAN, T.-T., MOON, C.-G. & BANSAL, P. 2005 Numerical study on heat an mass transfer characteristics of plate absorber. *Applied Thermal Engineering* **25**, 2219–2235.

Curriculum Vitae

Personal Data

Name Ernst Hofmann
Date of birth February 17, 1979
Place of birth Gmunden, Austria
Address Attemsgasse 43/19, 1220 Wien
Phone +43 699 10 70 10 87
E-Mail ernst_hofmann@yahoo.de

Academic Studies

2010/04 – 2015/04 University of Technology Vienna
Doctoral Programme in Technical Sciences
2007/10 – 2010/03 University of Technology Vienna
Master Programme in Technical Physics
2004/10 – 2007/10 University of Technology Graz
Bachelor Programme in Technical Physics

Employment

2013/08 – present Simulation Engineer at Liebherr-Transportation, Korneuburg
2010/04 – 2013/07 Project Assistant at University of Technology Vienna
2002/09 – 2004/08 Quality Engineer at STIWA, Attnang-Puchheim
1999/06 – 2002/08 Design Engineer at TCG Unitech, Kirchdorf a. d. Krems

Education and Military Service

1998 – 1999 Military Service, Austrian Armed Forces, Salzburg
1993 – 1998 Federal Secondary College (HTL) for Mechanical Engineering
1985 – 1993 Primary and Secondary School